FINAL REPORT

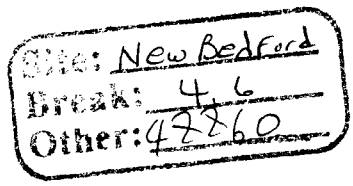

SDMS DocID 48860

for

MODELING OF THE TRANSPORT, DISTRIBUTION, AND FATE OF PCBs AND HEAVY METALS IN THE ACUSHNET RIVER/ NEW BEDFORD HARBOR/BUZZARDS BAY SYSTEM

VOLUME II

Under Contract No. 4236-MOD-0019

to

EBASCO SERVICES, INC.
211 Congress Street
Boston, MA 02110

September 21, 1990

from

BATTELLE MEMORIAL INSTITUTE
Duxbury Operations
397 Washington Street
Duxbury, MA 02332

VOLUME II
TABLE OF CONTENTS

VOLUME II
TABLE OF CONTENTS
(Continued)

VOLUME II
LIST OF TABLES

VOLUME II
LIST OF TABLES
(Continued)

VOLUME II
LIST OF FIGURES

VOLUME II
LIST OF FIGURES
(Continued)

VOLUME II
LIST OF FIGURES
(Continued)

VOLUME II
LIST OF FIGURES
(Continued)

VOLUME II
LIST OF FIGURES
(Continued)

VOLUME II
LIST OF FIGURES
(Continued)

VOLUME II
LIST OF FIGURES
(Continued)

VOLUME II
LIST OF FIGURES
(Continued)

5.0 HYDRODYNAMIC AND SEDIMENT/CONTAMINANT TRANSPORT MODEL

5.1 INTRODUCTION

As part of the New Bedford Harbor feasibility study, a three-dimensional hydrodynamic and sediment/contaminant transport model (the TEMPEST/FLESCOT code) was applied to New Bedford Harbor. The objective of the modeling is to analyze the transport and fate of PCBs within the system. The model is a tool that can be used to comparatively evaluate the no-action and remedial-action alternatives over a future period. The model estimates water column and bed sediment total-PCB concentrations, which in turn can be used in risk assessment studies and in modeling total PCBs in the food chain.

The formulation of the TEMPEST/FLESCOT model for the New Bedford Harbor system is presented in this chapter. Included are discussions of the physical setting, the governing equations and numerical procedures, model testing, and calibration of the model.

5.2 PHYSICAL SETTING

5.2.1 Introduction

New Bedford Harbor, shown in Figure 5.1, is located on the north shore of Buzzards Bay. The harbor is a small urban estuary composed of the drowned valley of the Acushnet River, which trends north-northwest-south-southeast and empties into Buzzards Bay. The Acushnet River bed is a smooth-floored valley with the steep-sided, relatively low-lying ridges of New Bedford, reaching elevations of less than 55 m, and Fairhaven, reaching elevations of less than 15 m, on the west and east, respectively.

New Bedford Harbor can be divided into two main basins: the outer harbor and the inner harbor. The outer harbor is defined as that area south of the hurricane barrier but north of the line connecting Wilbur Point on the east and Round Hill Point on the west. The outer harbor is connected to Buzzards Bay along this line. Several natural 9-m channels and one dredged 9-m channel, in otherwise shallow water, characterize the bathymetry of the outer harbor. The dredged channel connects the shallow water of the inner harbor to the deeper water of Buzzards Bay.

The inner harbor is defined as that portion of the Acushnet River estuary north of the hurricane barrier. The inner harbor is approximately 6.4 km long from the hurricane barrier to the Wood Street Bridge. Three structures in the inner harbor severely restrict tidal flows. The Coggeshall Street Bridge, the uppermost of these constrictions, has a maximum opening width of approximately 33.5 m and a depth of 5.8 m. The Interstate 195 Bridge constricts the harbor approximately 100 m downstream from the Coggeshall Street Bridge. The hurricane barrier, constructed in 1966, constricts the entrance to the inner harbor to a width of 45.7 m and a depth of 8.5 m. North of Popes Island, the water depth decreases to 7 m and continues to decrease to 4.6 m near the Coggeshall Street Bridge. North of the Coggeshall Street Bridge, the estuary

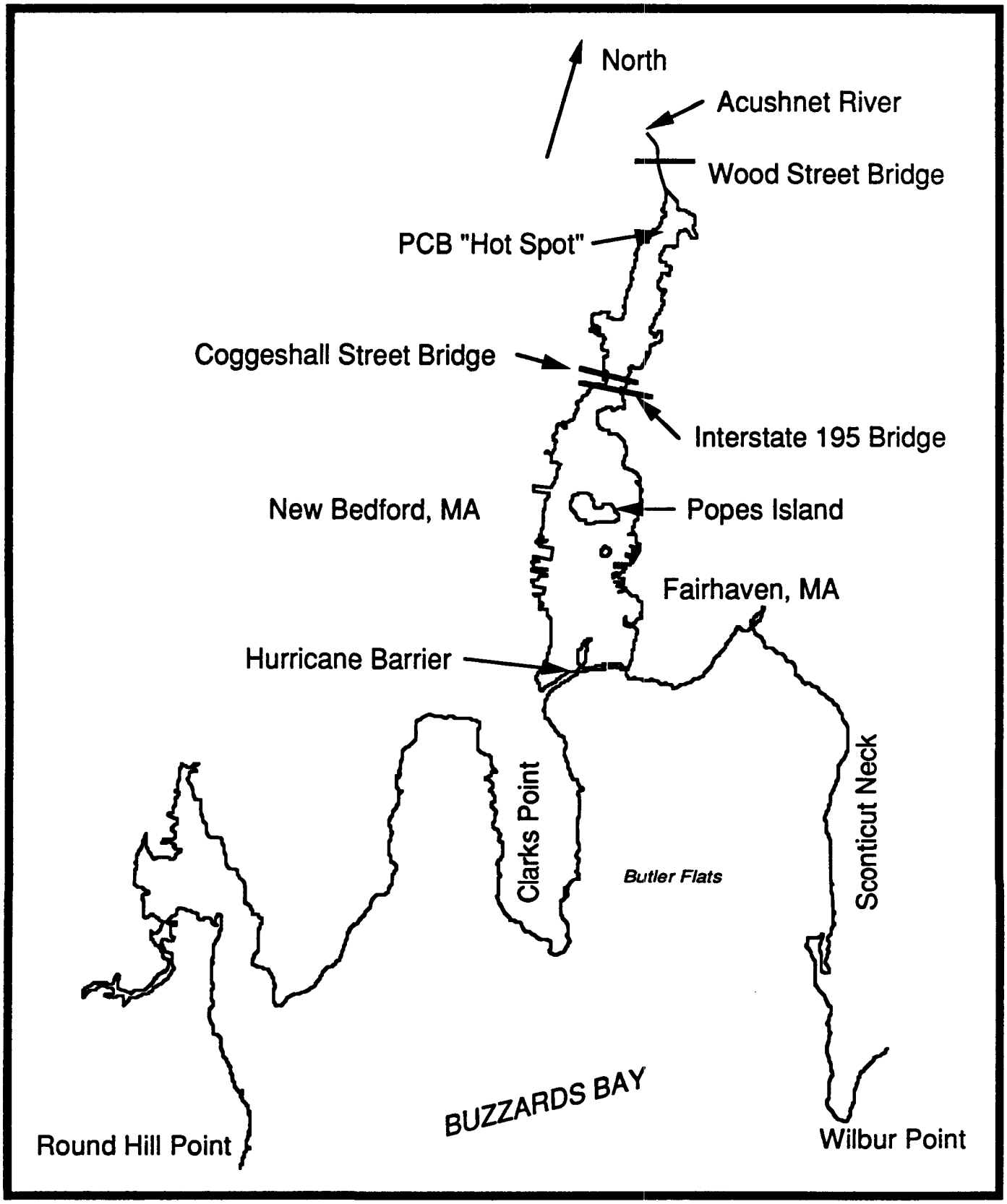

FIGURE 5.1. NEW BEDFORD HARBOR STUDY AREA

becomes a non-navigable stream, with depths typically less than 0.3 m (mean low water) near the Wood Street Bridge.

5.2.2 Climatology

The New Bedford area has a variable climate. Sea breezes moderate both summer and winter temperatures. The mean annual temperature, based on 77 years of records at New Bedford, is 10°C. The highest average monthly temperature is 22°C in July, and the lowest is -1°C in January.

The New Bedford area is characterized by frequent but short periods of heavy precipitation. The average annual precipitation, based on 151 years of records at New Bedford, is 114 cm (USACE 1982, in ASA 1986). Precipitation is distributed approximately uniformly throughout the year, with approximately 10 cm/mo. The maximum monthly precipitation at New Bedford was 48 cm, in August 1826, and the minimum monthly precipitation was 0.025 cm, in June 1949.

Winds at New Bedford predominate from the northwest in winter and from the southwest in summer. The average wind speed at Green Airport in Warwick, Rhode Island, approximately 45 km to the west-northwest, is 4.8 m/s. The highest average monthly winds occur in March and April and the lowest in August. The fastest winds occur in August, with speeds up to 40.3 m/s. For the rest of the year, the fastest winds are typically up to 22.3 m/s.

Severe weather conditions at New Bedford can result from short-duration thunderstorms during May through August, coastal storms, such as the "Nor'easters" of late winter, and hurricanes during the summer and fall. Thunderstorms are usually of short duration, and are also accompanied by high winds for short periods of time. Coastal storms with high winds produce the most severe weather at New Bedford. These storms may occur in any month of the year, but generally occur from late fall through spring. The hurricane season is from June to November. It has been observed during storms that

winds predominate from the south, with gusts reaching 31.3 m/s, tides of 0.3 to 0.9 m above normal, and average rainfall of 1.3 cm.

Based on meteorological records at the Buzzards Bay Light Tower, Graber (1986b) reported that October through April is the stormy season for Buzzards Bay. Storm events, with wind speeds in excess of 15 m/s lasting for approximately 1 to 2 days, occur approximately once or twice per month.

5.2.3 Freshwater Inflows

The only major source of freshwater inflows to New Bedford Harbor is the Acushnet River. The Acushnet River drains a small, 47.7-km^2 basin above Saw Mill Dam, 700 m upstream from the Wood Street Bridge and the point of greatest freshwater inflow. The Wood Street Bridge is the approximate upstream limit of tidal influence.

No long-term stream gauge records exist for the Acushnet River, but freshwater inflow is small. Cortell (1982, in ASA 1986) estimates the mean annual discharge of the Acushnet River to be 0.85 m^3/s. Signell (1986, in ASA 1986) estimated the average runoff to be 0.79 m^3/s. U.S. Geological Survey measurements of the discharge of the Acushnet River from 1972 through 1974 near the Leonard Street Bridge indicate a maximum (monthly) flow of approximately 0.70 m^3/s and a minimum (monthly) flow of 0.02 m^3/s.

The standard project flood for the basin at Saw Mill Dam is 37.7 m^3/s peak flow, based on estimates by the U.S. Army Corps of Engineers. NUS (1984) estimates the 10-, 25-, 50-, and 100-year storm events for the Acushnet River to be 17.0, 20.5, 22.7, and 38.2 m^3/s, respectively.

5.2.4 Tides and Currents

Tides in New Bedford Harbor are semidiurnal, two high waters and two low waters occurring each lunar day. Mean tide range is 1.1 m, and the spring tide range is 1.40 m. The tides display a standing-wave behavior, with maximum flood/ebb currents occurring approximately 3 h before high/low water. Based on measured flows at the Coggeshall Street Bridge versus predicted tides (EPA 1983), there appears to be little tidal damping or phase shift between the lower and upper harbor and Buzzards Bay.

Currents vary considerably throughout New Bedford Harbor. In the outer harbor, the currents are generally less than 0.50 m/s. Within the inner harbor, currents vary sharply because of the constrictions. At the hurricane barrier, currents have been estimated at 1.22 m/s (Ellis 1977). At the Coggeshall Street Bridge, currents were approximately 1.83 m/s maximum ebb, 0.91 m/s maximum flood, 0.52 m/s average ebb, and 0.34 m/s average flood (EPA 1983). Current speeds north of the Coggeshall Street Bridge averaged approximately 0.09 m/s, with a maximum of 0.26 m/s (EPA 1983). Current speeds over two tidal cycles south of the Coggeshall Street Bridge averaged approximately 0.06 m/s at two stations, with a maximum of 0.18 m/s (Summerhayes et al. 1977).

5.2.5 Salinities and Temperatures

New Bedford Harbor is a weakly stratified, partially mixed estuary. Salinities typically vary from 26 to 30 ppt but have been reported as low as 12 ppt at the surface during heavy rains (EPA 1983). At the Coggeshall Street Bridge, vertical salinity differences as great as 18 ppt have been reported. South of the Coggeshall Street Bridge, the harbor is generally vertically well-mixed, with top-to-bottom salinity differences seldom exceeding 1 to 2 ppt. There do not appear to be any significant longitudinal gradients in salinities (Ellis 1977).

Water temperatures in New Bedford Harbor range from a low of 0.5°C in winter to a high of 19.0°C in summer.

5.2.6 Waves

The outer New Bedford Harbor is exposed to wind-generated waves from the southwest through southeast, with a wind fetch of over 14 km. Even with this fetch, the waves within the outer harbor would seldom exceed 1 m because of the generally shallow water depths. Graber (1986a) estimated the severity of storm-generated surface waves in Buzzards Bay using a numerical, deep-water, parametric-wave model. He found that the outer harbor is most vulnerable to waves from the southwest, reaching estimated heights as great as 2 m with a wind speed of 40 m/s.

The inner New Bedford Harbor is well protected from most wind-generated waves. The narrow width of the inner harbor, its generally shallow depths, and the presence of constrictions at the hurricane barrier and the Interstate 195 and Coggeshall Street Bridges greatly restrict the wind fetch. Teeter (1988) reported waves as high as 0.92 m just upstream of the Coggeshall Street Bridge during a storm with wind speeds up to 48 km/h. However, these waves were restricted to the deeper channel, and the wave heights decreased rapidly in the shallower areas outside the main channel.

5.2.7 Bottom Sediments

The surficial sediments of New Bedford Harbor are composed mostly of silty material of glacial origin, with varying amounts of clay and sand. The silt and clay content of the shallow estuary landward of the Coggeshall Street Bridge varies from 10% to 80%, with the higher percentages being found along the west margins of the estuary and in the extreme upper portions of the estuary. The sand content of the surficial sediments in this area varies from 20% to 80%, is most predominant along the east margin, and increases seaward toward the Coggeshall Street Bridge.

Seaward of the Coggeshall Street Bridge, the sediments of the deeper portions of the harbor are composed primarily of silt and clay. The sand content is generally less in this area, except around the constrictions at the Coggeshall Street and Interstate 195 Bridges and at the hurricane barrier, where the higher currents prohibit finer material from depositing.

The surficial sediments seaward of the hurricane barrier are generally coarser than in the inner harbor, with the sand content being higher along the margins of the outer harbor. The silt and clay content of the surficial sediments is higher along the deeper western margins of the outer harbor. The sand content along the shallow, east shore varies from 50% to 90%.

5.2.8 Suspended Sediment

Suspended sediment concentrations range from less than 10 to approximately 40 mg/L, the higher values being associated with the passage of storm events (EPA 1983). A three- to four-fold increase in suspended sediment can occur during these storms. Ellis (1977) found that over a 2-year period the suspended sediment concentrations were generally less than 10 mg/L, with a maximum of 26 mg/L. After the passage of Hurricane Belle on August 10, 1976, the maximum suspended sediment concentration was 32 mg/L, at the Interstate 195 Bridge.

Suspended sediment concentrations are generally one and one-half to two times higher in the bottom waters than in the surface waters. The highest suspended sediment concentrations are found during the flood phase of the tidal cycle (EPA 1983, Teeter 1988). The maximum concentrations occur as the flood tide decreases in velocity approximately 1 h after the velocity maximum.

Seasonally suspended sediment concentrations tend to be lowest during the winter and highest during early spring, remaining moderately high through early summer. Resuspension of bottom sediment from storm waves appears to be the major source of the seasonally suspended sediment. The Acushnet River appears to be a relatively unimportant source of suspended sediment, except during severe storms (Summerhayes et al. 1977).

5.2.9 Field Data Analysis

Various field data were collected and used to establish initial and boundary conditions for the TEMPEST/FLESCOT model, and to develop a conceptual description of circulation and contaminant transport in New Bedford Harbor.

5.2.9.1 Bathymetry

Bathymetric data and shoreline location information were obtained from National Ocean Survey (NOS) charts, surveys performed for the U.S. Army Corps of Engineers (USACE), and unpublished surveys performed by Tibbetts Engineering Company as summarized below:

NOS: Chart No. 13230

USACE: Acushnet River, New Bedford Project 110, Sheets 1 and 2

USACE: New Bedford-Fairhaven Condition Survey, NB 331 Sheets 5 and 6, December 1978

Tibbetts: New Bedford-Fairhaven Master Plan Study Area Revision, January 17, 1979.

Depth data from these sources were used to generate the bathymetric chart shown in Figure 5.2, which was then used for the initial depth conditions in the TEMPEST/FLESCOT model. Depth data were digitized from the best available charts, and spot elevation charts were made of the digitized data at the same scale as the source chart. Spot elevation charts from each source were then compared to identify digitizing errors. The individual spot elevation charts were then combined into a master depth file containing 7,622 values of x (easting), y (northing), and z (depth).

Shoreline data were digitized in a similar fashion from the same source charts.

FIGURE 5.2. NEW BEDFORD HARBOR BATHYMETRY. DEPTHS IN METERS (MLW).

5.2.9.2 Sediment Data

Five sources of sediment data, summarized below, were used to develop the initial conditions of grain size for the TEMPEST/FLESCOT model:

- 110 samples reported in Ellis (1977)
- 66 samples reported in Huidobro and De Lorenzo (1983)
- 22 samples reported in Condike (1986)
- 18 samples reported in Woodward-Clyde Consultants (1987)
- Battelle Ocean Sciences database.

Only the surface sediment data from these sources were used to generate the grain-size database used in the TEMPEST/FLESCOT model. The grain size and location data were collected into a single data file and a grain size contour map were developed for the clay, silt, sand and gravel fractions (Figures 5.3 through 5.6).

5.2.9.3 Polychlorinated Biphenyl (PCB) Data

Information on the distribution of PCBs in bottom sediments, used as initial conditions, was obtained from the Battelle Ocean Sciences, Alliance, and GCA databases. The Battelle Ocean Sciences PCB database was designed specifically to provide additional information for the TEMPEST/FLESCOT model. These data were collected on three sampling cruises in 1984 and 1985. The Alliance database was originally constructed for the U.S. Environmental Protection Agency by Metcalf & Eddy (1983) and was transferred to GCA in 1986. The data from the Alliance database were also incorporated into a master database maintained at Battelle Ocean Sciences. The Alliance database consisted of over 5,000 entries of PCB and metals concentrations in water, sediments, biota, waste water, and air from the New Bedford Harbor area. Only those entries on sediments were used to develop the initial-condition map for the TEMPEST/FLESCOT model. The GCA database provided the most information on PCBs for the generation of initial conditions for the TEMPEST/FLESCOT model because of its complete coverage in the inner harbor. Subsequent to development of the TEMPEST/FLESCOT model initial PCB conditions, additional PCB data were collected by the U.S. Army Corps of Engineers and others. These data were not

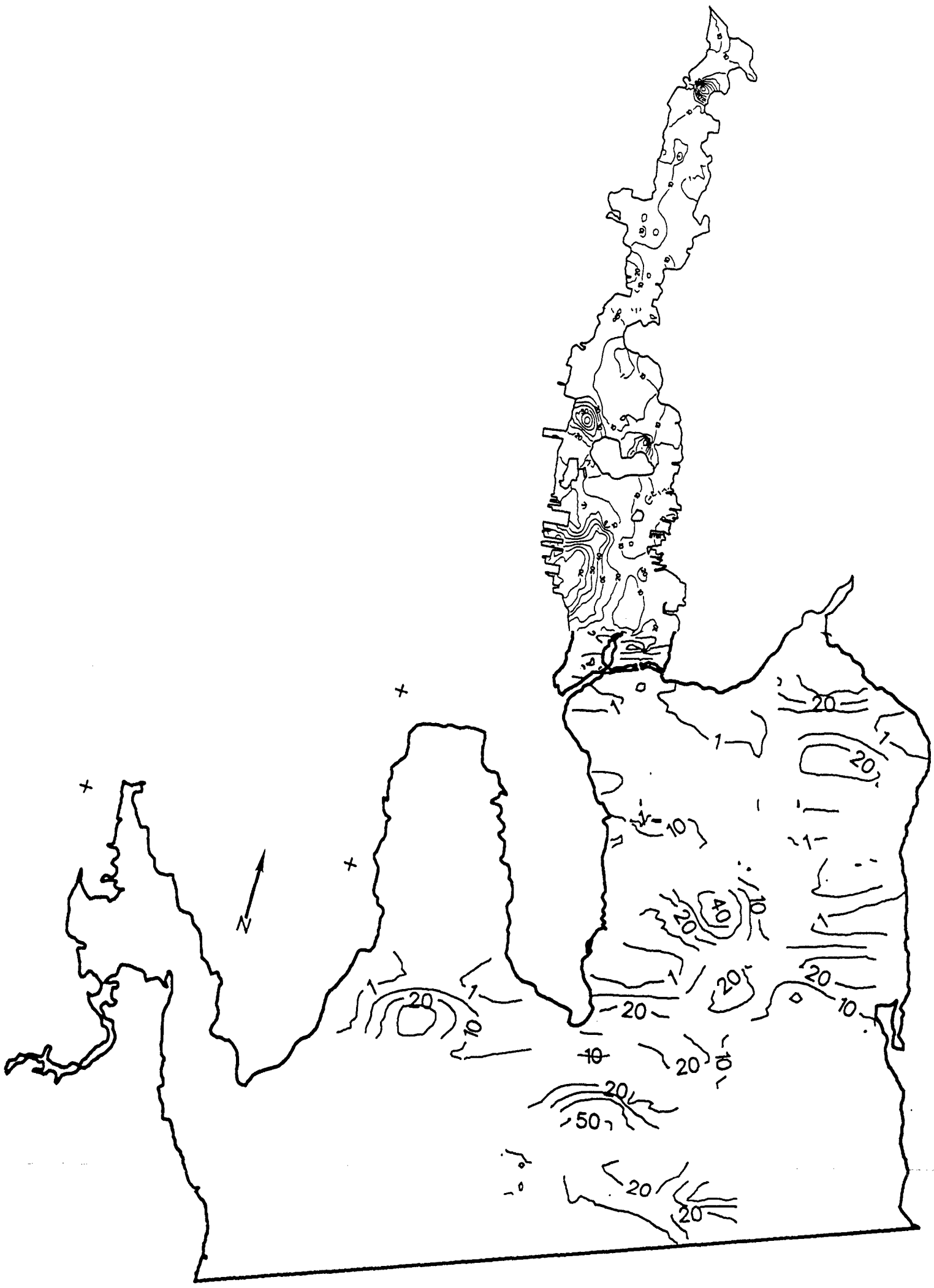

FIGURE 5.3. BED SEDIMENT GRAIN SIZE DISTRIBUTION CLAY FRACTION

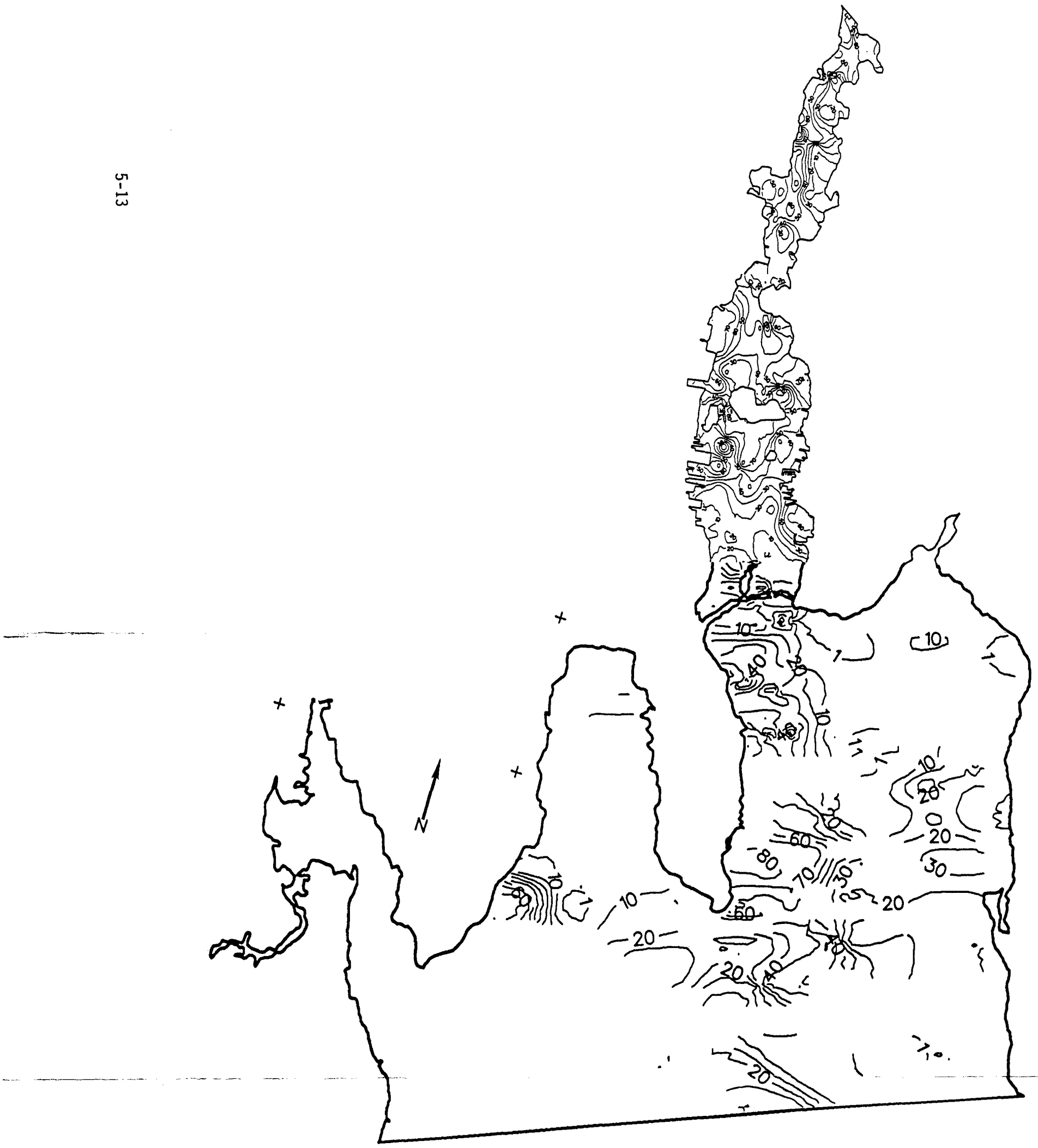

FIGURE 5.4. BED SEDIMENT GRAIN SIZE DISTRIBUTION SILT FRACTION

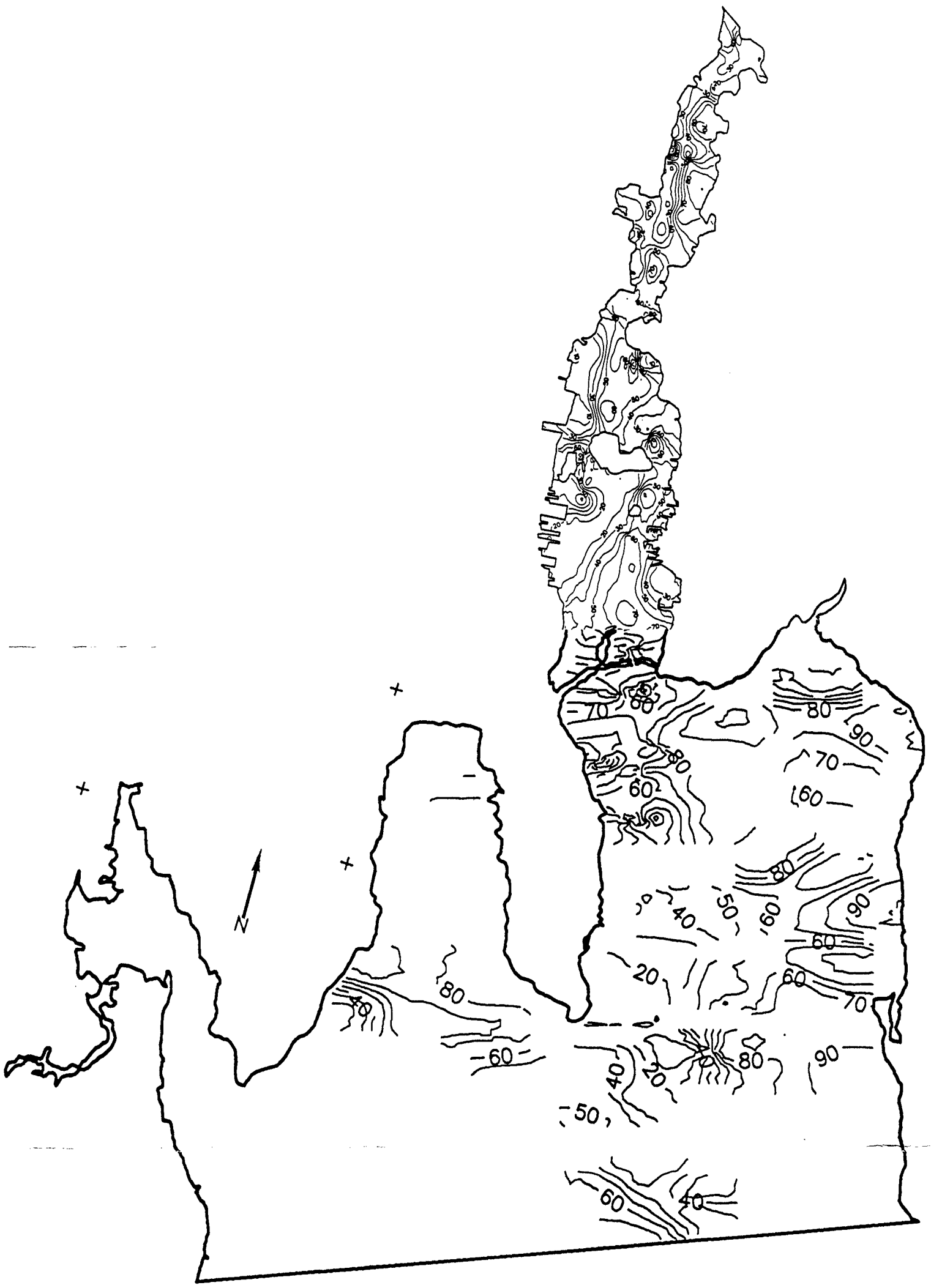

FIGURE 5.5. BED SEDIMENT GRAIN SIZE DISTRIBUTION SAND FRACTION

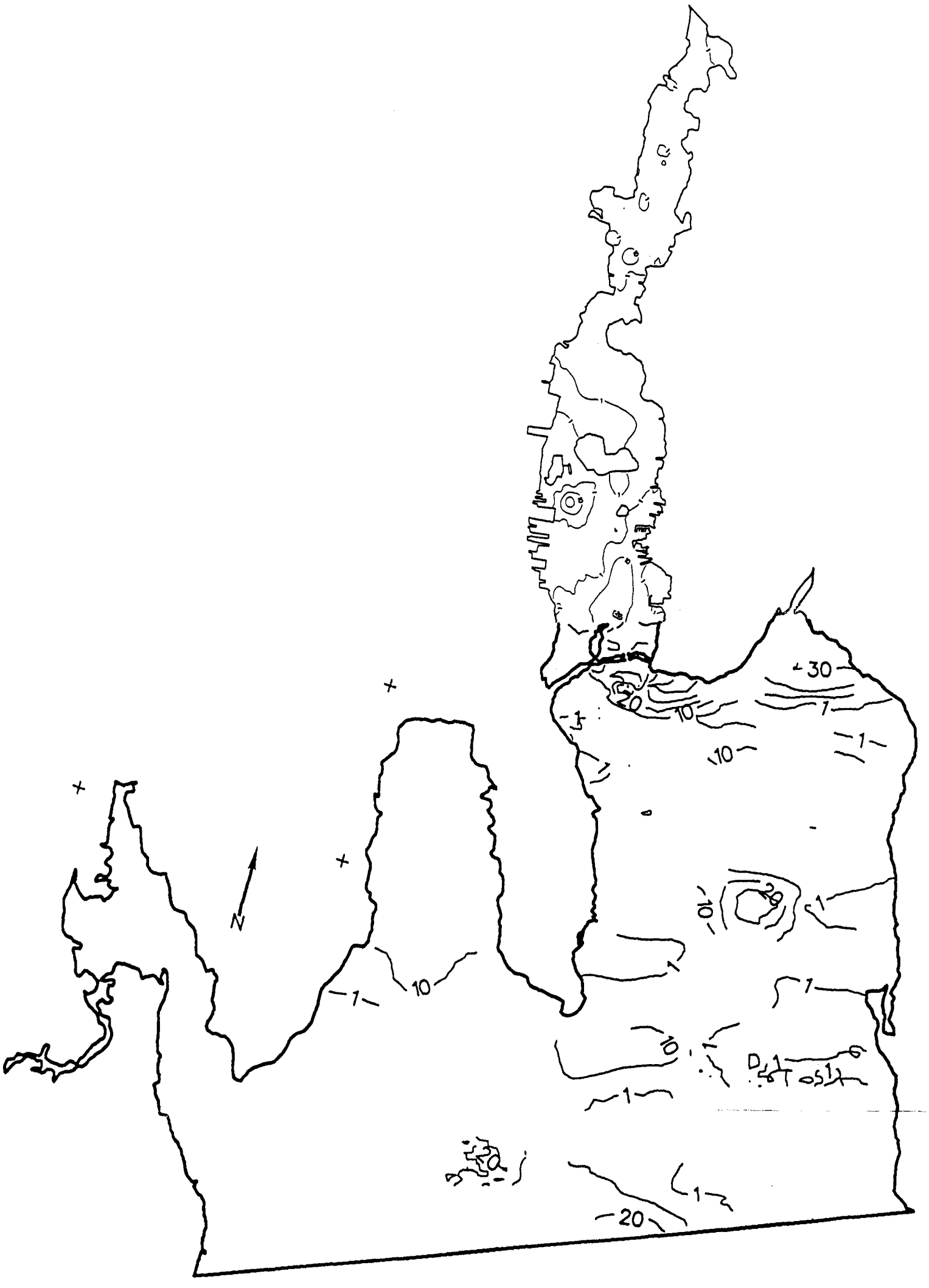

FIGURE 5.6. BED SEDIMENT GRAIN SIZE DISTRIBUTION GRAVEL FRACTION

incorporated into the TEMPEST/FLESCOT model because modeling efforts had progressed too far by the time the additional PCB data had become available.

The PCB data from the three databases represented many depth intervals. Only the surface samples reported in the three databases, representing the upper 20 cm of a sediment core, or results from surface grab samples were used in generating the initial PCB bottom sediment conditions for the TEMPEST/FLESCOT model. The initial conditions for the TEMPEST/FLESCOT model were generated from the PCB contour map shown in Figure 5.7. A total of 388 data points were used to generate this figure. A scatter plot of the sample locations used to generate the contours is presented as Figure 5.8.

The PCB data from the three databases were compiled into a single file, along with the source of the data, sample number, location, total PCB concentration, units for PCB concentration, and number of samples summed to produce the total concentration for the surface sediment value (0 to 20 cm). The randomly spaced PCB data from the three databases were interpolated onto a 30 x 30 m grid covering the inner and outer harbor (Sampson 1975). A quadrant-search gridding algorithm was employed, where for each grid location the algorithm used up to two data points from each of four quadrants centered about the grid location to calculate the grid PCB value. At least one data point closer than 244 m to the grid was required to produce a PCB value for that grid. Any additional data points (up to a maximum of eight) within a 457-m radius were used to calculate the PCB value. The PCB value at each grid was estimated as the inverse distance-weighted average of the eight (or fewer) data points. A digital shoreline was incorporated, and a contour map of the surface sediment PCB concentrations was then prepared.

5.2.9.4 Conceptual Model of New Bedford Harbor

The time-varying distribution of PCBs in New Bedford Harbor depends on a number of factors, including the source of the PCBs, physical-chemical properties of PCBs--especially their affinity to bind to sediments--resuspension of PCB-contaminated bottom sediments, and circulation patterns

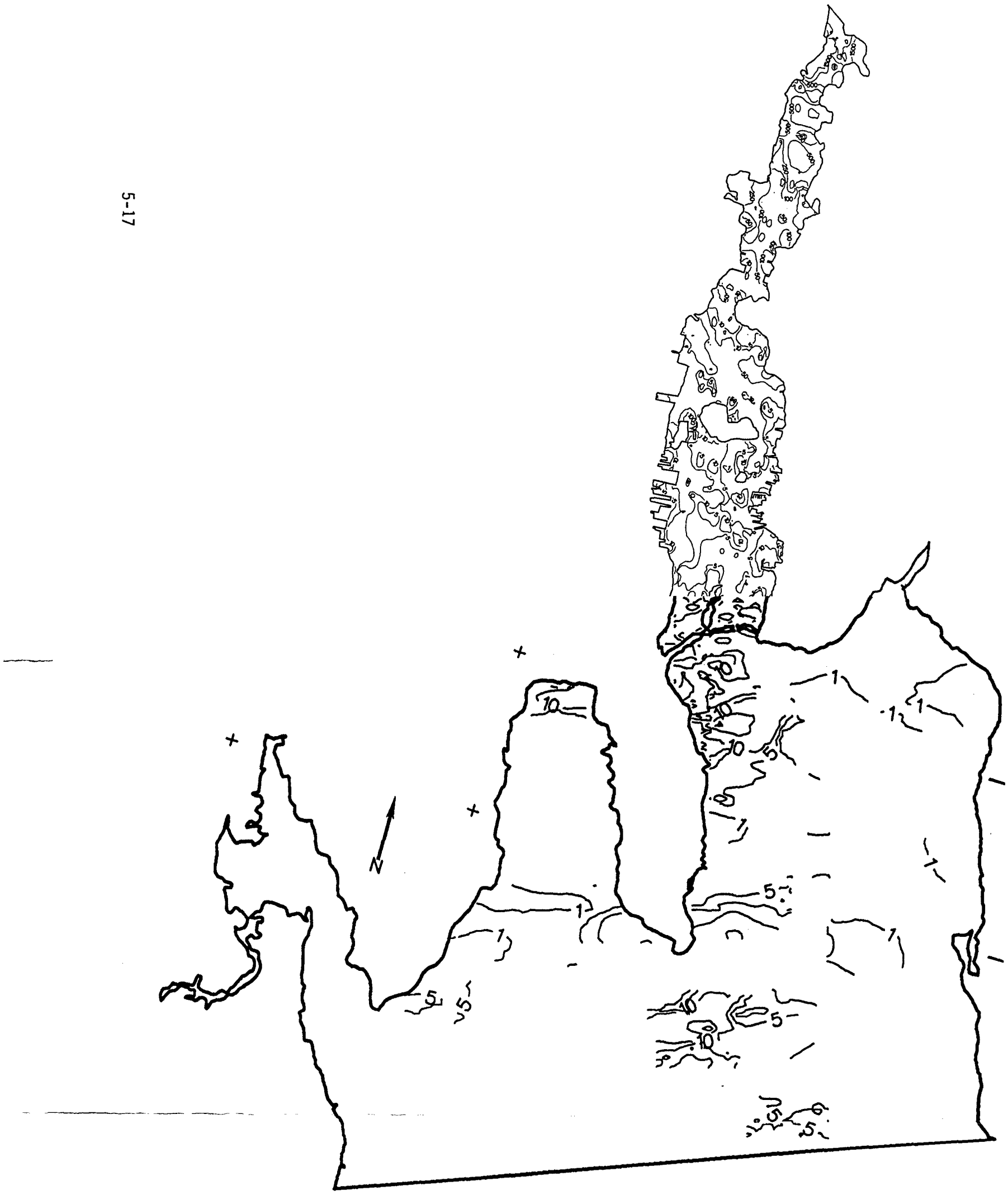

FIGURE 5.7. MEASURED PCB CONCENTRATIONS IN SURFICIAL BED SEDIMENTS (mg/kg)

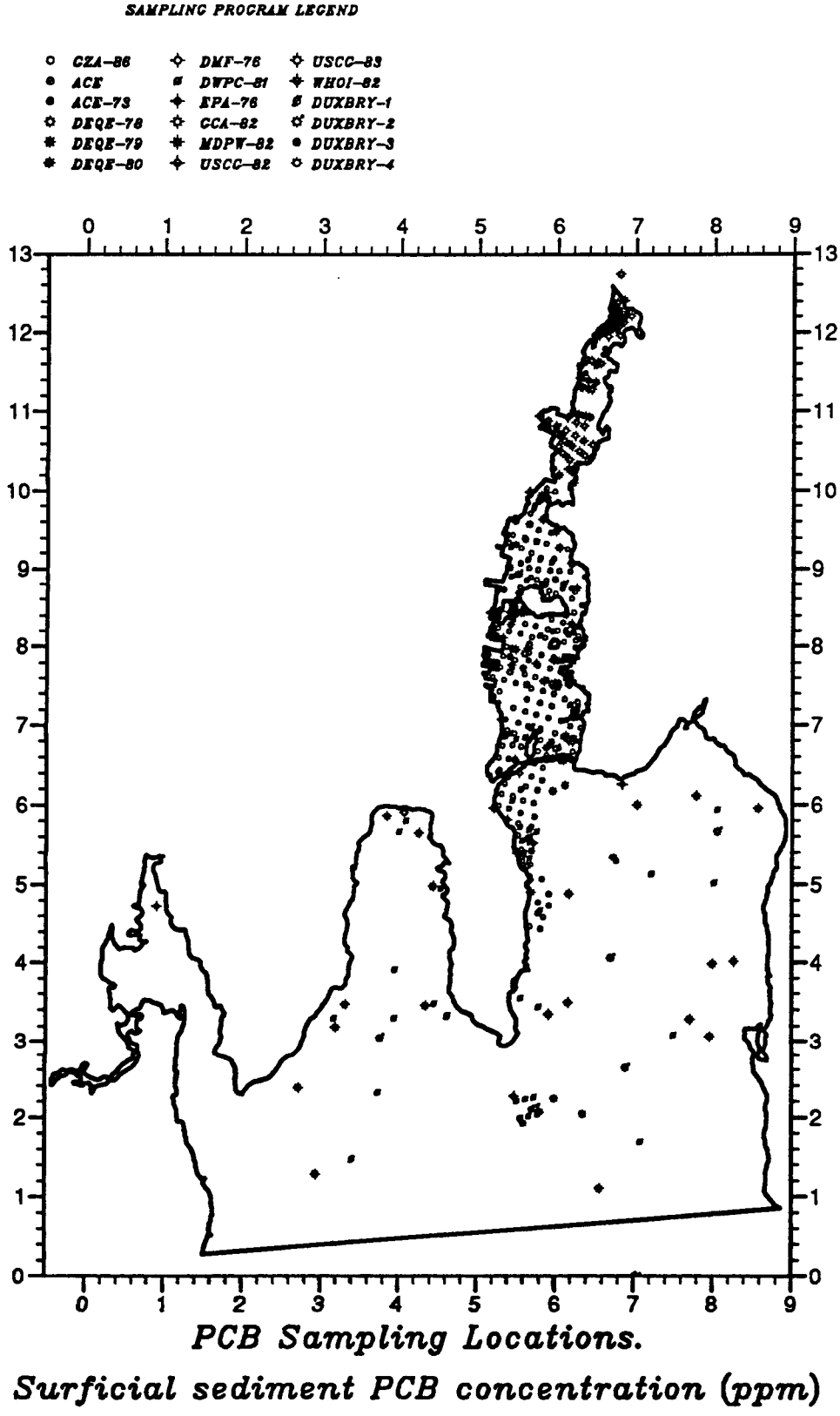

FIGURE 5.8. PCB BED SEDIMENT SAMPLING LOCATIONS

and intensity for transporting dissolved and sediment-bound PCBs within the harbor.

Because PCBs are chemically and thermally stable, they persist in aquatic environments for long periods. They are also relatively insoluble and have a strong tendency to attach to particulates or to lipids of aquatic organisms (Larsson and Södergren 1987). Thus, after being discharged to an aquatic environment in the dissolved phase, PCBs quickly bind to sediments or bioaccumulate in organisms. This does not mean, however, that the PCBs become immobile once deposited in bottom sediments. Remobilization into the overlying water column can occur from bioturbation of sediments by benthic organisms, upward convection with gases produced in anaerobic sediments, direct desorption into the sediment pore water or the overlying water column, diffusive transport from sediment to the overlying water column, uptake and bioaccumulation by organisms, or physical resuspension of sediment-bound PCBs. Using a quantitative water, air, and sediment interaction model for Lake Ontario, Mackay and Diamond (1989) estimated that with major inputs of PCBs from inflowing water (1329 kg/yr) and atmospheric deposition (45 kg/yr) a net PCB flux of 1140 kg/yr from the water to the sediments occurs. They further estimated that the main losses of PCBs from the surficial sediments are from burial in deeper layers (41.4%), sediment resuspension (40.9%), diffusion from the sediment into the overlying water (11.6%), and biotic and abiotic degradation in the sediment (6.1%). The behavior of PCBs in an estuarine system such as New Bedford Harbor is likely to be qualitatively similar to that observed in this freshwater system.

Many of the factors described by Mackay and Diamond (1989) relative to the dynamics of PCBs in Lake Ontario apply to New Bedford Harbor. Based on their model, the main losses of PCBs in the upper harbor, in decreasing order of importance, should be burial in deeper sediment layers (deposition of relatively uncontaminated sediments over the contaminated sediments), resuspension of PCB-contaminated sediment, diffusion of PCBs to overlaying water, and biotic and abiotic degradation in the sediment. The relative importance of these factors, however, may be different in New Bedford Harbor.

Within New Bedford Harbor, bottom sediments contain the greatest mass of PCBs. Estimates of PCBs in the harbor's bottom sediments vary from 110,000 kg (Farrington 1982) to approximately 374,000 kg (ASA 1987, mean estimate), with the majority being located in the shallow portion of the harbor landward of the Coggeshall Street Bridge. Field measurements indicate that these PCBs are mobile. Based on field measurements, ASA (1987) estimated that the water column contains approximately 10 kg of PCBs at any given time and that the suspended particulate mass is from two to four times that of the dissolved mass. Approximately 46% of the water column PCBs are estimated to be in the upper harbor (landward of the Coggeshall Street Bridge). This corresponds to the location of the largest mass of PCBs in bottom sediments. Estimates of the total flux of PCBs have also been made (EPA 1983, Teeter 1988). These mass PCB flux estimates were based on actual field measurements at the Coggeshall Street Bridge (EPA 1983, Teeter 1988). In both cases a net seaward flux of PCBs was observed. The flux estimates range from a net seaward transport of 0.86 to 1.55 kg of PCBs per tidal cycle, most being transported as PCBs attached to suspended particulates.

Within the bottom sediments in the upper harbor, the highest concentrations of PCBs generally are not found in the surface sediments (EPA 1983) but are situated at some depth (e.g., 10 to 15 cm below the surface at Balsam Site FX, Thibodeaux 1989), indicating that either (1) the primary source of PCBs has greatly diminished, (2) there is a high sedimentation rate of relatively uncontaminated sediments in the upper harbor, (3) contaminated sediments in the bioturbation zone have been selectively removed, or (4) that some combination of these has occurred. The first two conditions are known generally and are substantiated by field measurements, respectively. Because PCB production was terminated in the late 1970s, the direct input of PCBs to New Bedford Harbor has greatly diminished. Secondary sources of PCBs, such as inputs from temporary terrestrial holding areas, atmospheric deposition, or resuspension, transport and deposition of previously contaminated sediments, probably are still occurring and can be expected to continue for some time. Teeter (1988) estimates that the sedimentation rate in the upper harbor is about 3 mm/yr and that the origin of these sediments is Buzzards Bay. This estimate was based on field measurements of suspended sediment flux at the

Coggeshall Street Bridge that showed a net landward flux of 2,200 kg per tidal cycle, with at least one-third of this settling out during the tidal cycle.

Field measurements of PCBs in the water column indicate a substantial mass of PCBs in transit at all times (EPA 1983, ASA 1987, Teeter 1988). The mobility of PCBs in the presence of ongoing deposition in the upper harbor implies that PCBs can migrate upward in the sediment column by some mechanism and then release to the overlying water by diffusion of a soluble phase, by erosion (resuspension) of surficial sediments, or by a particle exchange mechanism (Teeter 1988).

The mobility of PCBs in bottom sediments of the upper harbor cannot be accounted for strictly by the resuspension of bottom sediments, which occurs as a result of current or wave action. Tidal currents in the upper harbor are small, with magnitudes less than 9 cm/s, and the upper estuary is well protected from wind-generated waves and currents. ASA (1986) reported that current velocities on the order of 20 to 30 cm/s are required for significant resuspension of the upper harbor sediments to occur. There is evidence, however, that the seaward flux of PCBs past the Coggeshall Street Bridge increases during storms conditions (EPA 1983), suggesting that critical erosion velocities can be exceeded during storms.

New Bedford Harbor is a weakly stratified, partially mixed estuary with very small freshwater inflows. The inner harbor is small, shallow, and well protected from most wind events. With such estuaries, tides are normally the dominating process for water mass exchange and are the main mechanism for dispersion and mixing within the estuary. Density and wind-driven circulation is secondary to that of tides under most conditions. Only under abnormal events, such as storms, can density and wind-driven circulation temporarily dominate circulation. The resuspension and transport of PCB-contaminated bottom sediments should increase during storm conditions, which may represent the major PCB transport and redistribution episodes during a year. Storms with wind speeds in excess of 15 m/s occur once or twice per month, with durations of 1 to 2 days during October through April.

Dispersion and mixing within New Bedford Harbor is complicated, as has been illustrated by dye dispersion studies (ASA 1987). These studies showed a net seaward transport of dissolved constituents released in the upper harbor. The travel time between the upper harbor (near the Aerovox plant) and the hurricane barrier was 2 days, and relatively steady-state conditions were reached in the estuary after 6 days. Large vertical, lateral, and longitudinal dye concentration gradients were observed, especially in the upper harbor near the dye release point. Vertical stratification was observed, with the surface dye concentrations typically being 5 to 10 times higher than the bottom values in the upper harbor. Stratification decreased in the down-estuary direction but was still prevalent in the lower harbor. Based on these limited data, one can suggest that the upper harbor is not well mixed laterally and that flow and eddy diffusion are highly three-dimensional processes.

The three severe physical constrictions in the harbor, the hurricane barrier and the Coggeshall Street/Interstate 195 Bridges, can affect dispersion and mixing within the estuary. These constrictions do not appear to affect the tidal wave, since little tidal damping or phase shift between the upper and lower harbors and Buzzards Bay occurs (Teeter 1988). The most obvious effects of the constrictions are their effects on the circulation within the harbor. The constrictions will tend to cause secondary circulation cells, thereby short-circuiting the exchange of water between cells. Because there will be a greater degree of recirculation of water within the cells, the presence of secondary circulation cells in an estuary will generally increase the residence time of contaminants within the estuary.

The upper harbor also has a central channel with adjacent subtidal flats on both sides. The volume transport of water and advection of dissolved and suspended contaminants in the upper harbor therefore varies across the estuary with the stage of the tide. These flow features and the associated lateral dispersion are highly three-dimensional.

In summary, the migration of PCB contamination from the source area in the upper harbor to adjacent environments (Buzzards Bay and the atmosphere) is conceptually modeled as follows:

- PCBs migrate from the highly contaminated bottom sediments into the overlying water column as a result of 1) desorption from fine-grained sediment particles and upward diffusion in interstitial (pore) water, 2) erosion and resuspension of sediment particles by boundary layer currents (steady and/or wind-wave generated) and 3) benthic organisms. The latter two processes are likely responsible for the majority of the PCB transport from the sediments.

- Dissolved PCBs in the water column readsorb to "clean" fine-grained sediment particles exported to the harbor from Buzzards Bay and upland sources. The fate of these adsorbed PCBs then depends on subsequent advection or diffusion and deposition and resuspension of the scavenging particles. Particles which depart the harbor with adsorbed PCB and do not return represent a net loss from the system. Scavenging particles that remain in the source area and sequester PCBs from the water column prevent evaporation and transport mechanisms from removing PCBs from the system for at least one adsorption/desorption cycle.

- Gains and losses of particle-bound PCBs from New Bedford Harbor represent a sediment transport problem involving erosion and deposition (particle settling) and advective and diffusive transport of suspended particles. The flow field and eddy diffusion regimes in time and space must be known to estimate instantaneous sediment transport reliably. In aggregate, they determine the rate at which the contaminated particles in the source area exchange with cleaner particles in Buzzards Bay.

- Transport and losses of dissolved PCB from the water column depend on the balance between the rates at which the chemical evolves diffusively from contaminated bottom sediments, advects to and from the system, and evaporates to the atmosphere. In New Bedford Harbor, the rate-limiting process appears to be mass transfer from the sediments, although vertical diffusivities in the water column may be important as well.

Conceptually, a comprehensive model must simulate all these diverse processes. Practically, the dominant ones are the most important to the present analysis. These are discussed in more detail below, in the context of the numerical simulations.

5.3 DESCRIPTION OF THE TEMPEST/FLESCOT COMPUTER CODE

5.3.1 Computer Code History

The TEMPEST computer code was originally developed as a three-dimensional computer code to model hydrothermal applications in engineered systems (Trent and Eyler 1989). The code is based on the Navier-Stokes equations. The marine version of TEMPEST was designed to handle the special requirements of large-scale marine hydrodynamic simulations. Such simulations include three-dimensional, time-dependent flows in bays, estuaries, coastal zones, lakes, and oceans.

The FLESCOT constituent transport routines are operationally embedded in the marine version of TEMPEST. The FLESCOT routines account for sediment transport, contaminant transport, and sediment-contaminant geochemistry in the water column and bed.

Since the development of the marine version of TEMPEST in 1982, TEMPEST has been used in five major modeling projects:

- Hudson River Estuary, New York - A 106-km reach of the Hudson River estuary between Chelsea, New York, and the mouth of the river was modeled to predict time-varying, three-dimensional distributions of tidal flow, salinity, sediment, and radionuclides in both dissolved and sediment-sorbed form for a 40-day period (Onishi and Trent 1982).
- Beaufort Sea, Alaska - A 15- x 75-km area, which included Prudhoe Bay and Stefansson Sound, was modeled to predict changes in circulation patterns and water quality after construction of the 4000-m-long Lisburne causeway (Onishi et al. 1985a).
- Sequim Bay, Washington - A 5- x 9-km area in the Strait of Juan de Fuca was modeled to predict the tidally varying flow and migration of sewage effluent from a proposed outfall near Sequim Bay (Onishi et al. 1985b).
- Diablo Canyon, California - A coastal zone was modeled to predict the evolution of a thermal plume caused by the release of hot water from a nuclear power plant (PG&E 1989).

- New Bedford Harbor, Massachusetts - Circulation and mass transport modeling was performed in support of a sewage outfall siting project (Yabusaki et al. 1989).

In this study, the TEMPEST/FLESCOT code was modified to include 1) the calculation of a time-varying water surface, 2) solution of the transport equations using a decoupled mode, and 3) a wave-enhanced bottom friction model. The numerical procedures associated with each modification are described below.

5.3.2 TEMPEST Hydrodynamics

The governing equations employed in the TEMPEST hydrodynamics model are the following:

- conservation of fluid mass (the continuity equation)
- conservation of momentum (the Navier-Stokes equations)
- conservation of energy (the first law of thermodynamics)
- conservation of mass for constituents, including salt.

The fundamental assumptions underlying the TEMPEST hydrodynamics model are the following:

- governing equations describe time-averaged mean flow (i.e., Reynolds averaging has been done)
- a Boussinesq eddy viscosity formulation defines the Reynolds stresses
- the Boussinesq approximation holds (i.e., fluid density variations are much smaller than the fluid density itself).

The effects of temperature and salinity on density are factored into the calculation of model hydrodynamics through a sea water equation of state (i.e., NHO 1952). Note that the water density is not a function of pressure when the incompressible assumption is made.

5.3.2.1 Continuity Equation

$$\frac{\partial u}{\partial x}+\frac{\partial v}{\partial y}+\frac{\partial w}{\partial z}=0 \tag{1}$$

where u, v, and w = velocity components in the x, y, and z directions

x, y, and z = longitudinal, lateral, and vertical (upward) directions, respectively.

5.3.2.2 Momentum Equations

X-Component Momentum Equation

$$\frac{\partial u}{\partial t}+\frac{\partial uu}{\partial x}+\frac{\partial uv}{\partial y}+\frac{\partial uw}{\partial z}+f_x=\frac{-1}{\rho_0}\frac{\partial P}{\partial x}+\frac{\partial}{\partial x}\left(\epsilon_x\frac{\partial u}{\partial x}\right)+\frac{\partial}{\partial y}\left(\epsilon_y\frac{\partial u}{\partial y}\right)$$
$$+\frac{\partial}{\partial z}\left(\epsilon_z\frac{\partial u}{\partial z}\right)-\frac{1}{\rho_0}\left(F_x^b+F_x^s\right) \tag{2}$$

Y-Component Momentum Equation

$$\frac{\partial v}{\partial t}+\frac{\partial uv}{\partial x}+\frac{\partial vv}{\partial y}+\frac{\partial vw}{\partial z}+f_y=\frac{-1}{\rho_0}\frac{\partial P}{\partial y}+\frac{\partial}{\partial x}\left(\epsilon_x\frac{\partial v}{\partial x}\right)+\frac{\partial}{\partial y}\left(\epsilon_y\frac{\partial v}{\partial y}\right)$$
$$+\frac{\partial}{\partial z}\left(\epsilon_z\frac{\partial v}{\partial z}\right)-\frac{1}{\rho_0}\left(F_y^b+F_y^s\right) \tag{3}$$

Z-Component Momentum Equation

$$\frac{\partial w}{\partial t}+\frac{\partial uw}{\partial x}+\frac{\partial vw}{\partial y}+\frac{\partial ww}{\partial z}+f_z=\frac{\rho g}{\rho_0}-\frac{1}{\rho_0}\frac{\partial P}{\partial z}+\frac{\partial}{\partial x}\left(\epsilon_x\frac{\partial w}{\partial x}\right)+\frac{\partial}{\partial y}\left(\epsilon_y\frac{\partial w}{\partial y}\right)$$
$$+\frac{\partial}{\partial z}\left(\epsilon_z\frac{\partial w}{\partial z}\right)-\frac{1}{\rho_0}F_z^b \tag{4}$$

where t = time

$f_x = 2\Omega$ (w cos Φ - v sin Φ); Coriolis acceleration in x direction

$f_y = 2\Omega$ u sin Φ; Coriolis acceleration in y direction

f_z = -2Ω u cos Φ; Coriolis acceleration in z direction

F_i^b = boundary shear force per unit volume in direction i; i = x, y, z

F_i^s = surface (e.g., wind) shear force per unit volume in direction i; i = x, y

g = gravitational acceleration

P = pressure

ρ = water density

ρ_o = reference water density

Φ = planetary latitude

Ω = rate of Earth's rotation (7.29×10^{-5}/s)

ϵ_x, ϵ_y, ϵ_z = eddy viscosity components in the x, y, and z directions, respectively.

5.3.2.2.1 Boundary Processes

Wind Shear Stress. The wind stress at the water surface is formulated using a standard wind-friction drag correlation. Using this relationship, the force per unit volume is computed and applied to the surface cells. This force is computed at each time step and applied as time- and space-dependent quantities in the lateral momentum equation solution procedure. In the TEMPEST formulation, wind stress is applied uniformly over the water surface in the model domain.

The form of the wind stress correlation is given as the following:

X-Component Wind Shear Stress

$$F_x^s = C_d \rho_a W^2 \sin\psi \; A_s / \forall \qquad (5)$$

Y-Component Wind Shear Stress

$$F_y^s = C_d \rho_a W^2 \cos\psi \; A_s / \forall \tag{6}$$

where C_d = wind stress drag coefficient

W = wind speed measured at some specified height (e.g., 10 m)

ρ_a = air density

ψ = angle between the wind and coordinate directions

A_s = surface cell area

$\forall$ = cell elemental volume.

The drag coefficient is computed from the linear function

$$C_d = c_1 + c_2 W \tag{7}$$

where the constants, c_1 and c_2, are based on wind data.

Boundary Resistance. In a manner analogous to wind stress at the water surface, bottom friction is commonly expressed by the following:

X-Component Boundary Friction

$$F_x^b = C_f \rho_0 u \left(u^2 + v^2\right)^{\frac{1}{2}} A_s / \forall \tag{8}$$

Y-Component Boundary Friction

$$F_y^b = C_f \rho_0 v \left(u^2 + v^2\right)^{\frac{1}{2}} A_s / \forall \tag{9}$$

Z-Component Boundary Friction

$$F_z^b = C_f \rho_0 w\left(u^2 + w^2\right)^{\frac{1}{2}} A_s / \forall$$

or (10)

$$F_z^b = C_f \rho_0 w\left(v^2 + w^2\right)^{\frac{1}{2}} A_s / \forall$$

where C_f = drag coefficient

ρ_0 = fluid density.

The model globally applies bottom friction, whereas form drag can be specified at any particular location in the model by increasing the drag coefficient.

Open-Flow Boundaries. Boundary conditions along any open-flow boundary are difficult to set properly. Tidal-height data are necessary but must be carefully implemented in the computational procedure for free-surface simulations. For instance, the tidal wave is only part of the total wave component that will be generated in the simulation. Other components are generated from wind and boundary reflections. At the open boundary, care must be taken so that reflected waves and wind-generated waves pass unimpeded through the open boundary and out of the modeled region. That is, one must ensure that these shorter waves do not undergo nonphysical reflections off an open boundary. On the other hand, tidal-stage data reveal little about short-wavelength waves that are generated outside of the modeled region and will be passing into the physical region.

Therefore, the modeling approach used in TEMPEST is to allow short waves to pass out of the region and to not consider such waves as entering the modeled region. In this type of boundary condition, the boundary flow is entirely driven by the computed elevation change at the boundary if the flow is out of the system and is entirely driven by the tidal stage if flow is into the system. The boundary elevation is never allowed to drop below the tidal data, but it can be computed to be above the tidal data. If the tidal elevation were always to be enforced at the boundary, a short-wavelength wave would

sense the fixed elevation as a barrier and be partially reflected, which, on physical grounds, is unreasonable.

Under other conditions the boundary flow may be "mixed." That is, it may consist of both a persistent current and a tidal component. It is possible that both tidal-stage and current data would be available. If one were to impose both the boundary tidal stage and the current, nonphysical waves would most likely be computed, because of inconsistency. The modeler could never specify the surface height and current to match exactly physical conditions along the boundary. Thus, this type of boundary condition presents a considerable modeling difficulty.

5.3.2.2.2 Initial Conditions. In this study, all hydrodynamic simulations were initiated from a cold start (i.e., motionless water with a uniform surface elevation). Primary forcing functions for the model hydrodynamics were provided by water surface elevation changes at the open boundary and by wind shear stress applied to the water surface.

Simulated depth and velocity fields were considered to be fully developed after a model spinup period of at least one tidal cycle (i.e., 12.417 h). Testing during the calibration phase indicated that less than half of one tidal cycle was necessary for model spin-up.

5.3.2.3 Dissolved Mass Transport Equation

$$\frac{\partial \phi}{\partial t} + u\frac{\partial \phi}{\partial x} + v\frac{\partial \phi}{\partial y} + w\frac{\partial \phi}{\partial z} = \frac{\partial}{\partial x}\left(k_x \frac{\partial \phi}{\partial x}\right) + \frac{\partial}{\partial y}\left(k_y \frac{\partial \phi}{\partial y}\right) + \frac{\partial}{\partial z}\left(k_z \frac{\partial \phi}{\partial z}\right) + q_\phi \qquad (11)$$

where ϕ = concentration of mass per unit volume

q_ϕ = mass generation/dissipation (including surface and bottom fluxes)

k_x, k_y, k_z = dispersion coefficients in the x, y, and z directions, respectively.

In the context of the modeled hydrodynamics, the dissolved mass transport equation relates specifically to a constituent that can affect the density of the modeled fluid. In this study, salinity (and heat) transport is coupled to the hydrodynamics through the seawater equation-of-state. Neutrally buoyant constituents are modeled in the FLESCOT transport routines using the same dissolved mass transport equation without coupling to the model hydrodynamics.

Boundary Processes. Boundary conditions for constituent (e.g., salinity) transport are similar to those discussed for thermal boundary conditions. They must be implemented at a tidal or any continuative boundary in much the same way as for the tidal elevation boundary condition. That is, one can predict what is flowing out, but one cannot predict how much of the constituent that has flowed out of the model will flow back into the same region. Thus, a boundary condition is set for each constituent, the value of which is used only if at the boundary the flow is into the modeled system. If the boundary flow is out of the system, a concentration simulated by the TEMPEST computation is transported out of the modeled region.

Initial Conditions. Initial salinity conditions were based on hydrographic surveys conducted during the modeled hydrodynamic episodes. The field data were laterally extrapolated from the cruise transects to distribute the initial conditions over the entire volume of the model domain.

5.3.2.4 Model Options

The marine version of the TEMPEST hydrodynamics model has several user options. The following is a discussion of the invoked options for turbulence closure, hydrostatic pressure, free-surface calculations, and Coriolis acceleration.

Turbulence Closure. In this study, the turbulent diffusion of heat, mass, and momentum is modeled as an anisotropic process, using constant diffusion coefficients. Turbulence associated with surface water is generated by a

variety of conditions, including interaction with the bottom boundary layer, wind-and wave-action, and interior shearing currents. Generally, the nature of the turbulence is both inhomogeneous and anisotropic, the lateral scales of turbulence being much larger than the vertical scales.

Eddy Viscosity. The TEMPEST code models eddy viscosity diffusion using two components, a lateral component, ϵ_l, and a vertical component, ϵ_v. These two models are each a composite. The lateral and vertical components of turbulence are modeled

$$\epsilon_l = \epsilon_i + \epsilon_{l0}$$
$$\epsilon_v = \epsilon_i \qquad (12)$$

where ϵ_{l0} = large-scale lateral component of eddy viscosity and

ϵ_i = isotropic component

The isotropic component is given by

$$\epsilon_i = \epsilon_m + \epsilon_0 \qquad (13)$$

where ϵ_m = molecular viscosity

ϵ_0 = constant component.

Thermal and Mass Diffusion. In the current application, thermal- and mass-diffusion coefficients are related to the eddy viscosity coefficients by a constant ratio expressed as the Prandtl (Pr) or Schmidt (Sc) number:

$$Pr = \frac{\epsilon}{\sigma} \quad ; \quad Sc = \frac{\epsilon}{k} \qquad (14)$$

where ϵ = eddy viscosity coefficient

σ = thermal diffusion coefficient

k = mass diffusion coefficient.

Hydrostatic Pressure Approximation. The hydrostatic pressure approximation is valid only for shallow-water waves or for cases where the wave length is large compared to the water depth, such as for tidal flows in estuaries and bays. In these cases, flow fields have negligible temporal and spatial accelerations and shear stress changes (eddy viscosity terms) in the vertical, as compared to the gravitational, term. This approach replaces the vertical component of the momentum equations with the hydrostatic equation:

$$\frac{\partial P}{\partial z} = - \rho g. \tag{15}$$

The vertical component of the Coriolis acceleration is also neglected in this case.

The hydrostatic-pressure approximation permits a simple vertical integration of the flow field to determine the pressure field. Additionally, this assumption implies that pressures are disconnected from lateral communication at any one time step in the simulation. This is a good approximation if the lateral scale of the flow is large compared to the water depth.

Free-Surface Calculation. The kinematic free-surface boundary condition is simplified by dropping the water surface gradient terms in the x and y directions. Continuity is enforced by vertically integrating the continuity equation using the lateral components of velocity computed in the solution to the momentum equation. This procedure begins at a bottom cell, where the net difference in the lateral flows becomes the mass flux out of the top of the cell. This vertical mass flux (or velocity) is then the flow through the bottom of the layer of cells above. In the surface layer, the net difference between the lateral inflow and the vertical upflow through the bottom of the surface cell is interpreted as a change of surface elevation.

To increase computational efficiency, TEMPEST requires that the free-surface configuration remain in one level of cells, the surface layer. This means that the free surface cannot cross grid lines or fall beneath the center line

of the surface cell. The surface layer, however, is constructed so that it can accommodate any thickness of fluid above the surface-cell center line. Applications allowed by the surface-layer restrictions include typical tidal currents in bays and estuaries, wind-driven currents, wind setup, and other mild long waves. Phenomena such as tidal bores, hydraulic jumps, flood waves, cascades, and flooding of tidal flats cannot be modeled with the marine version of TEMPEST.

Planetary Coriolis Forces. Geophysical flows are influenced by the rotation of the Earth. This effect, the Coriolis force, is caused by the motion of the water relative to a rotating reference frame (the spinning Earth). The magnitude of the Coriolis force is a function of both latitude and flow velocity. For an invariant flow field, the Coriolis force would vary from zero at the equator to a maximum value at the North or South Pole. The Coriolis force, F_C, is given in vector form,

$$F_C = 2\Omega \times V, \tag{16}$$

or in component form (eliminating second-order terms):

$$\begin{aligned} F_x &= -2\Omega \sin\Phi \; v \\ F_y &= 2\Omega \sin\Phi \; u \end{aligned} \tag{17}$$

where Φ = planetary latitude

The Coriolis force causes deflections to the right-hand side of the flow direction in the Northern Hemisphere, resulting in clockwise rotational drift. In the Southern Hemisphere, the Coriolis force has an opposite directional sense.

5.3.3 Flescot Sediment/Contaminant Transport

The FLESCOT constituent transport routines are operationally embedded in the marine version of TEMPEST. The FLESCOT routines account for sediment

transport, contaminant transport, and sediment-contaminant interaction in the water column and bed.

The governing equations employed in the FLESCOT transport routines are:

- conservation of sediment mass
- conservation of dissolved-constituent mass
- conservation of sorbed-constituent mass.

These three equations are coupled to account for changes in three size fractions of bed- and suspended-sediment, changes in dissolved contaminant concentrations, and changes in sorbed-contaminant concentration for each sediment size fraction.

The fundamental assumptions underlying the FLESCOT transport routines are:

- dissolved contaminants are neutrally buoyant
- sediment transport has no effect on model hydrodynamics
- linear isotherms for sediment sorption and desorption are applicable.

5.3.3.1 Sediment Transport Equation

The sediment transport submodel includes the mechanisms of 1) advection and dispersion of sediments, 2) fall velocity and cohesiveness, 3) deposition on the seabed or ocean bottom, 4) erosion from the bed (bed erosion and armoring), and 5) sediment contributions from point/nonpoint sources and subsequent mixing. This submodel also calculates changes in bed conditions, including bed elevation changes caused by scouring and/or deposition, and it gives a distribution of sediment sizes within each bed cell.

The migration of sediment through transport, deposition, and scouring is solved for each size fraction of cohesive and noncohesive sediments separately, up to a total of three size fractions. This approach recognizes

that the movements and adsorption capacities of sediments vary significantly with sediment sizes and types.

$$\frac{\partial C_j}{\partial t} + \frac{\partial}{\partial x}\left(uC_j\right) + \frac{\partial}{\partial y}\left(vC_j\right) + \frac{\partial}{\partial z}\left[\left(w - w_{sj}\right)C_j\right]$$

$$= \frac{\partial}{\partial x}\left(k_x \frac{\partial C_j}{\partial x}\right) + \frac{\partial}{\partial y}\left(k_y \frac{\partial C_j}{\partial y}\right) + \frac{\partial}{\partial z}\left(k_z \frac{\partial C_j}{\partial z}\right) \qquad (18)$$

$$+ \frac{1}{\Delta Z}\left(S_{Rj} - S_{Dj}\right) + {}^{q}C_j$$

Boundary Conditions for Sediment Transport

$$\frac{\partial C_j}{\partial x} = 0 \quad or \quad C_j = C_{j0} \qquad at \quad x = 0 \quad or \quad L$$

$$\frac{\partial C_j}{\partial y} = 0 \quad or \quad C_j = C_{j0} \qquad at \quad y = 0 \quad or \quad B \qquad (19)$$

$$\left(w - w_{sj}\right)C_j - k_z \frac{\partial C_j}{\partial z} = 0 \qquad at \quad z = H$$

$$(1-\gamma)w_{sj}C_j + k_z \frac{\partial C_j}{\partial z} = 0 \qquad at \quad z = 0$$

where γ = reentrainment coefficient

B = estuarine width

C_j = sediment concentration of j^{th} sediment

H = flow depth

L = longitudinal distance of a simulation area

ΔZ = vertical thickness of bottom water column cell

q_{Cj} = lateral influx or other source strength of j^{th} sediment

S_{Dj} = j^{th} sediment deposition rate per unit surface area

S_{Rj} = j^{th} sediment erosion rate per unit surface area

w_{sj} = fall velocity of j^{th} sediment.

A zero concentration gradient is set at lateral and longitudinal model boundaries. The effect of this condition is to prevent dispersion through open and solid boundaries; consequently, sediment can only be advected through open boundaries. At the open boundary, internally computed sediment concentrations are used to determine the sediment mass leaving the system during outflowing conditions. Inflowing sediment mass is based on the specified sediment concentration at the open boundary.

Sand Sediment Transport. Because of the simplicity of the formulation, FLESCOT uses the DuBoys formula (Vanoni 1975) to estimate the noncohesive sediment transport capacity of flow:

$$Q_T = \psi_D \tau_b (\tau_b - \tau_c) \tag{20}$$

where Q_T = total sediment transport capacity of flow per unit width

ψ_D = DuBoys coefficient (function of sediment size)

τ_b = bed shear stress

τ_c = critical shear stress (function of sediment size).

To obtain the sediment concentration, sediment-erosion and -deposition rates are calculated separately for each sediment size fraction. If the amount of sediment actually being transported is less than the flow can carry for the given hydrodynamic conditions, the flow will scour sediment from the bed. This process will increase the rate of sediment transport, which is based on the difference between the sediment transport capacity of the flow and the actual sediment transport rate:

$$S_{Dj} = \frac{Q_{TA} - Q_T}{\Delta x}$$

$$S_{Rj} = \frac{Q_T - Q_{TA}}{\Delta x} \tag{21}$$

where Q_{TA} = actual sand transport per unit width

Δx = longitudinal increment from computational grid.

The process continues until the actual sediment transport rate becomes equal to the carrying capacity of the flow or until all the available bottom sediment is scoured, whichever occurs first.

Cohesive Sediment Transport. The formulas of Partheniades (1962) and of Krone (1962) are used to calculate cohesive sediment erosion and deposition rates:

$$S_{Dj} = w_{sj} C_j \left(1 - \frac{\tau_b}{\tau_{cDj}}\right)$$

$$S_{Rj} = M_j \left(\frac{\tau_b}{\tau_{cRj}} - 1\right) \qquad (22)$$

where τ_{cDj} = critical shear stress for deposition of the j^{th} sediment

τ_{cRj} = critical shear stress for erosion of the j^{th} sediment

M_j = erodibility coefficient for the j^{th} sediment.

Boundary Processes

Wave-Enhanced Bottom Stress. Wave effects, especially during storms, interact with currents, resulting in enhanced shear stress at the bed. To account for this effect, a form of the Grant and Madsen (1979) wave-enhanced bottom stress calculation was implemented after Graber (1987). In this calculation, an iterative procedure is used to correct the bottom stress to include wave effects. In addition to water depth and velocity, calculated by the hydrodynamic model, this iterative procedure requires significant wave height and period to compute the near-bottom orbital velocity. Bottom roughness, z_0, is represented by the grain-size diameter, d_{50}.

Processing of the input data follows the following procedure:

1. Calculate near-bottom orbital wave velocity, u_b:

$$u_b = \frac{Hw}{2 \sinh kh} \qquad (23)$$

where H = significant wave height

w = wave frequency (2π/wave period)

k = wave number based on $w^2 = gk \tanh(kh)$

h = water depth.

2. Compute the Nikuradse bottom roughness height, k_b:

$$k_b = 30\ z_0 \tag{24}$$

where $z_0 = d_{50}$, the nominal sediment diameter.

3. Compute the current velocity 100 cm above the bed, u_{100}:

$$u_{100} = \bar{u}\ \frac{\ln \frac{3000}{k_b}}{\ln \frac{11.04h_1}{k_b}} \tag{25}$$

where $\bar{u}$ = average velocity in the bottom layer of the model

h_1 = thickness of the bottom computational layer.

Once this information is entered, an iterative procedure is initiated:

- The pure wave friction factor, f_w, is determined from a table lookup, using $k_b w/u_b$.
- The wave shear velocity, u_{*w}, is computed to be $(0.5f_w)^{\frac{1}{2}}u_b$.
- The wave boundary layer thickness, δ_w, is computed to be $2ku_{*w}/w$.
- The wave-induced apparent roughness, z_{0c}, is computed to be $z_0(\delta_w/z_0)^{0.8}$.
- The drag coefficient, C_d, is calculated to be $[k/\ln(100/z_{0c})]^2$.
- The current-induced shear velocity, u_{*c}, is computed to be $C_d^{\frac{1}{2}}u_{100}$.
- The total shear velocity, u_{*cw}, is computed to be $(u_{*w}^2 + u_{*c}^2)^{\frac{1}{2}}$. The boundary layer thickness is recomputed to be $2ku_{*cw}/w$.
- The apparent roughness is recomputed to be $z_0(\delta_w/z_0)^{\beta}$, where $\beta = 1 - (u_{*c}/u_{*cw})$.

- The drag coefficient is recomputed and compared with previous iterations for adequate convergence.
- If converged, the total shear stress, t_b, is computed to be ru_{*cw}^2.

Initial Conditions. Initial conditions for sediment transport in FLESCOT require that the following suspended- and bed-sediment concentrations be specified:

- a distribution of suspended sediment concentrations for sand, silt, and clay fractions for each cell in the water column
- a spatial distribution of bed sediment concentrations for sand, silt, and clay fractions.

The initial conditions were based on field sampling surveys throughout the inner and outer harbors. Grain-size analysis was available to distinguish the modeling size fractions.

5.3.3.2 Dissolved-Contaminant Transport Equation

The governing equation for the transport and fate of the dissolved contaminant in three dimensions includes mechanisms of 1) advection and dispersion of the dissolved contaminant, 2) adsorption (uptake) of the dissolved contaminant by sediments (cohesive and noncohesive sediments) or desorption of the contaminant from the sediments into water, 3) volatilization of the dissolved contaminant, and 4) contaminant contributions from point and nonpoint sources to the system, and subsequent mixing.

$$\begin{aligned}
&\frac{\partial G_w}{\partial t} + \frac{\partial}{\partial x}\left(uG_w\right) + \frac{\partial}{\partial y}\left(vG_w\right) + \frac{\partial}{\partial z}\left(wG_w\right) \\
&\quad = \frac{\partial}{\partial x}\left(k_x \frac{\partial G_w}{\partial x}\right) + \frac{\partial}{\partial y}\left(k_y \frac{\partial G_w}{\partial y}\right) + \frac{\partial}{\partial z}\left(k_z \frac{\partial G_w}{\partial z}\right) - \lambda G_w + Q_w \\
&\qquad + \sum_j K_j\left(C_j K_{dj} G_w - G_j\right) + \sum_j K_j'\left(C_j K_{dj}' G_w - G_j\right) \\
&\qquad - \frac{1}{\Delta Z}\sum_j \gamma_j (1 - POR) D_j K_{Bj}\left(K_{dj} G_w - G_{Bj}\right) \\
&\qquad - \frac{1}{\Delta Z}\sum_j \gamma_j (1 - POR) D_j K_{Bj}'\left(K_{dj}' G_w - G_{Bj}\right)
\end{aligned} \tag{26}$$

Boundary Conditions for Dissolved Contaminant Transport

$$\frac{\partial G_w}{\partial x} = 0 \quad or \quad G_w = G_{w0} \qquad at \ x = 0 \ or \ L$$

$$\frac{\partial G_w}{\partial y} = 0 \quad or \quad G_w = G_{w0} \qquad at \ y = 0 \ or \ B$$

$$wG_w - k_z \frac{\partial G_w}{\partial z} = 0 \qquad at \ z = H \qquad (27)$$

$$\frac{\partial G_w}{\partial z} = 0 \qquad at \ z = 0$$

where D_j = diameter of j^{th} sediment size fraction

K_j, K_j' = transfer rate of contaminants for adsorption and desorption, respectively, with j^{th} sediment in the water column

K_{Bj}, K_{Bj}' = transfer rate of contaminants for adsorption and desorption, respectively, with j^{th} nonmoving sediment in the bottom

K_{dj}, K_{dj}' = distribution (or partition) coefficient between dissolved contaminant and particulate contaminant associated with j^{th} sediment for adsorption and desorption, respectively

G_{Bj} = particulate-contaminant concentration per unit weight of sediment in j^{th} sediment size fraction in the bottom

G_j = particulate-contaminant concentration associated with j^{th} sediment (radionuclide activity or weight of contaminant) per unit volume of water

G_w = dissolved-contaminant concentration (radionuclide activity or weight of contaminant) per unit volume of water

G_{w0} = constant concentration of dissolved contaminant

POR = porosity of bottom sediment

Q_w = lateral influx or other source of dissolved contaminant

γ_j = specific weight of j^{th} sediment

λ = rate of radionuclide decay or chemical and biological degradation.

A zero concentration gradient is set at lateral and longitudinal model boundaries. The effect of this condition is to prevent dispersion through open and solid boundaries; consequently, dissolved contaminant can only be advected through open boundaries. At the open boundary, internally computed

dissolved concentrations are used to determine the contaminant mass leaving the system during outflowing conditions. Inflowing contaminant mass is based on the specified sediment concentration at the open boundary.

At the water surface, the dispersion of contaminant mass must be balanced by the vertical advection of contaminant in the water column. A zero concentration gradient is specified at the bottom of the water column to prevent dispersion through the bed.

Note that the particulate-contaminant concentration associated with sediment in a water column, G_j in the above equation, is expressed in terms of the contaminant weight per unit volume of water instead of per unit weight of sediment.

Boundary Processes

Volatilization. The model computes volatilization as an internal sink in the surface water column cell. The user-specified input is a volatilization rate that is typically measured in a controlled laboratory setting.

Initial Conditions. Initial concentrations of dissolved constituent are required for all water column cells. In this study, a comprehensive, synoptic data set for water column concentrations was not available. Consequently, the distribution of initial conditions was based on available laboratory analyses from several sampling episodes. The long-term (i.e., months) transport simulations were sufficiently long to minimize the effect of inaccurate initial water column concentrations.

5.3.3.3 Particulate-Contaminant Transport

The migration (transport, deposition, and erosion) and fate of contaminants attached to sediments are solved separately for those adsorbed by each sediment size fraction of cohesive and noncohesive sediments. The governing

equation for the transport of particulate contaminant adsorbed by the j^{th} sediment includes mechanisms of 1) advection and dispersion of particulate contaminant, 2) adsorption (uptake) of dissolved contaminant by sediments or desorption from sediments into water, 3) deposition of particulate contaminant on estuarine bed or erosion from the bed, 4) erosion of particulate contaminant from the estuarine bed, and 5) contaminant contributions from point and nonpoint sources to the surface-water system and subsequent mixing.

$$\begin{aligned}
&\frac{\partial G_j}{\partial t} + \frac{\partial}{\partial x}\left(uG_j\right) + \frac{\partial}{\partial y}\left(vG_j\right) + \frac{\partial}{\partial z}\left[\left(w - w_{sj}\right)G_j\right] \\
&\quad = \frac{\partial}{\partial x}\left(k_x \frac{\partial G_j}{\partial x}\right) + \frac{\partial}{\partial y}\left(k_y \frac{\partial G_j}{\partial y}\right) + \frac{\partial}{\partial z}\left(k_z \frac{\partial G_j}{\partial z}\right) - \lambda G_j + Q_j \\
&\qquad + K_j\left(C_j K_{dj} G_w - G_j\right) + K_j'\left(C_j K_{dj}' G_w - G_j\right) \\
&\qquad - \frac{S_{Dj}}{\Delta Z} G_j + \frac{S_{Rj}}{\Delta Z} G_{Bj}
\end{aligned} \tag{28}$$

Boundary Conditions for Sediment-Sorbed Contaminant Transport

$$\begin{aligned}
&\frac{\partial G_j}{\partial x} = 0 \quad or \quad G_j = G_{j0} && at \ \ x = 0 \ \ or \ \ L \\
&\frac{\partial G_j}{\partial y} = 0 \quad or \quad G_j = G_{j0} && at \ \ y = 0 \ \ or \ \ B \\
&\left(w - w_{sj}\right)G_j - k_z \frac{\partial G_j}{\partial z} = 0 && at \ \ z = H \\
&k_z \frac{\partial G_j}{\partial z} = 0 && at \ \ z = 0
\end{aligned} \tag{29}$$

where G_{j0} = constant concentration of sediment-sorbed contaminant associated with the j^{th} sediment.

As for the sediment transport boundary conditions, a zero sediment-sorbed contaminant concentration gradient is set at lateral and longitudinal model boundaries. The effect of this condition is to prevent dispersion through open and solid boundaries; consequently, sediment-sorbed contaminants can only be advected through open boundaries. At the open boundary, internally computed sediment-sorbed contaminant concentrations are used to determine the sediment-sorbed contaminant mass leaving the system during outflowing

conditions. The mass of inflowing sediment-sorbed contaminant is based on the specified sediment-sorbed contaminant concentration at the open boundary.

At the water surface, the dispersion of sediment-sorbed contaminant mass must be balanced by the vertical advection of sediment in the water column.

Boundary Processes. Boundary processes for sediment-sorbed contaminant are controlled by the deposition and erosion of sediment to and from the bed and by the transfer of contaminant mass between the bed and the water column.

Initial Conditions. Sediment-sorbed contaminant concentrations must be specified in the bed- and water-column cells as an initial condition for the transport simulation. These concentrations are expressed as mass of contaminant per mass of sediment. Volumetric concentrations are thus dependent on initial conditions for sediment.

5.3.4 Numerical Methods

5.3.4.1 Solution Procedure

The TEMPEST/FLESCOT code uses a finite-difference discretization scheme to solve three-dimensional marine hydrodynamics and transport. The solution procedure incorporates alternating direction implicit (ADI) methods and standard linear algebraic techniques. The code has been heavily vectorized to take advantage of Cray[(a)] computer architectures.

The TEMPEST solution procedure is a semi-implicit time-marching finite difference procedure with all governing equations solved sequentially. At each time step, the momentum equations are solved explicitly and the pressure equations implicitly; temperature, turbulent kinetic energy and dissipation,

---

(a) Cray Research, Minneapolis, Minnesota.

and other scalar transport equations are solved using an implicit continuation procedure. Thus, the solution proceeds in the three phases as follows:

- Phase I - Tilde Phase. The three momentum equations are advanced in time ($t + \Delta t$) to obtain (tilde) velocities, $\tilde{U}$, $\tilde{V}$, and $\tilde{W}$, based on the previous time values of pressure and density, P and ρ. Although these values of the velocity components satisfy the momentum equations based on current values of P and ρ, continuity will usually not be satisfied.

- Phase II - Implicit Phase. The velocity component and pressure corrections, U', V', W', and P', are obtained such that the equations $U^{n+1} = \tilde{U} + U'$, $V^{n+1} = \tilde{V} + V'$, $W^{n+1} = \tilde{W} + W'$, and $P^{n+1} = \tilde{P} + P'$ satisfy continuity.

- Phase III - Scalar Phase. Using the previously computed values of U^{n+1}, V^{n+1}, and W^{n+1}, the advanced time ($t + \Delta t$) values of temperature, T^{n+1}, and other scalar quantities are computed as required.

The solution is advanced step-by-step in time by continually applying the three solution phases above. Under the assumption of hydrostatic pressure, Phases I and II can be combined into a direct solution of velocity and depth that preserves continuity.

Specifically, TEMPEST/FLESCOT uses the following solution techniques:

- nonlinear momentum terms computed with Courant-number-limited time steps
- linear momentum terms computed using shallow-water wave speed time step limitation
- implicit procedure used for computing transport of heat and constituents
- upwind differencing for the advective terms of the transport equation constant, variable, or automatically adjusted time steps.

The following are limitations of the numerical solution procedure:

- Cartesian coordinates
- surface fluctuation limits to surface layer (surface layer cannot cross grid lines)

- momentum solution limited by Courant number and shallow-water wave speed.

5.3.4.2 Model Testing

The TEMPEST/FLESCOT computation capabilities and modeled physics have been verified with several analytical solutions and benchmark problems (Eyler et al. 1983). This has been done through extensive verification of critical coding logic and analysis of computed results. Because of the code's generality, several operational modes are available. Many of these have been exercised to ensure proper operation of user-selectable options.

Engineered Systems. Solution of the thermal-energy equation was confirmed with several tests of conductive heat transfer. Transient and steady-state temperature distributions were compared to analytical solutions in one-, two- and three-dimensional systems. Fixed-temperature and modeled constant-heat-flux boundary conditions were tested, as were spatial distribution of initial conditions and heat generation.

Features of variable grid spacing, such as coordinate system, boundary conditions, and drag coefficient specifications, were confirmed as working correctly. Comparing predictions of plane-channel flow, duct flow, and pipe flow with analytical velocity profiles, experimental results, and other code predictions further confirmed that the numerics were programmed correctly and that the physics were modeled correctly.

Heated laminar flows were tested to assess computation of thermally coupled flows. Coupling was tested for flow over a flat plate, buoyancy-induced single-cavity convection, double-cavity convection, and combined convection in a vertical pipe. Other simulations of buoyancy-induced oscillation (internal waves) and full polar convection in a horizontal pipe tested features of time-stepping logic and coordinate systems and orientation. Temperature-dependent viscosity was modeled to ensure that the differencing logic was correct.

Wall boundary conditions for the turbulence model were verified with a modified law-of-the-wall model, using numerous simple simulations and a comparison with hand calculations of turbulent-induced wall shear and pressure drop. The wall boundary condition for turbulent heat transfer that is incorporated utilizes a modified universal temperature law-of-the-wall model. Modifications were made to handle low and high Prandtl number fluids. The model was confirmed by comparing heated turbulent flows in pipes using air, water, mercury, and sodium as test fluids.

Environmental Systems. In developing the marine version of TEMPEST, a number of verification and benchmark problems were performed to demonstrate the accuracy of the formulation. The hydrodynamics submodel was initially tested with one-dimensional problems for continuity and simple-flow regimes. Simple multidimensional problems were used to address potential flow solutions, wave propagation, Coriolis effect, and boundary conditions. The heat and mass transport submodel was verified against one- and two-dimensional analytical solutions of heat conduction and advection-diffusion. Benchmark problems were used to test the simulation of the flow field where temperature-and salinity-based density effects are coupled to the hydrodynamics. In particular, the hydrodynamic model was tested for one-dimensional wave propagation, the Ippen (1966) two-dimensional seiche basin solution, and the Leendertse et al. (1973) three-dimensional wind-driven velocity benchmark. Constituent transport was tested against one-and two-dimensional analytical solutions for coupled advection, dispersion, and decay.

Testing of the FLESCOT sediment/contaminant transport processes is documented in Onishi and Trent (1982) and Onishi et al. (1989).

5.3.4.3 Decoupled Mode

The TEMPEST/FLESCOT code can simulate sediment- and constituent-transport either coupled or decoupled from the hydrodynamics. For the long-term (i.e., months) transport simulations required by this study, it was not feasible to

generate a hydrodynamic time series of equivalent duration. Consequently, the relatively short time series (i.e., tidal cycles) of computed hydrodynamics were saved at time intervals consistent with the transport time step (i.e., minutes). The lengthier transport simulations were driven by a repeated cycle of computed hydrodynamics.

The advantage of using a saved time series of hydrodynamics is that a variety of transport scenarios can be simulated and subsequently compared using the same hydrodynamic data set. The major assumptions for using the decoupled mode are that 1) transport processes have negligible influence on the hydrodynamics with regard to fluid density and/or changes in the model geometry and 2) temporal discontinuities in the velocity field that occur when the end of one saved hydrodynamic time series is linked to the beginning of another are small. To reduce the effect of these temporal discontinuities, M2 (principal lunar, semi-diurnal tidal constituent) tides were used to generate the hydrodynamics that drove the transport-modeling studies. Symmetric tides (i.e., M2) minimized the temporal discontinuities and the cumulative bias caused by the repetition of a particular velocity time series.

5.3.5 Model Output

The TEMPEST/FLESCOT code allows the user to select the type, frequency, and format for data to be saved from a simulation. The bulk of the detailed model results are stored in binary files for post-processing. The results include time-dependent information at specified locations and spatial distributions at specified times. A text file generated with each TEMPEST/FLESCOT run summarizes a variety of user-specified information.

The types of information that can be generated are given below:

5.3.5.1 Binary Files

The following binary files were generated:

- computational grid specification

- dependent variables at every grid point at selected times: velocity (x, y, and z components), depth, salinity, temperature, density, suspended-sediment concentration (sand, silt, clay), bed-sediment concentration (sand, silt, clay), dissolved-constituent concentration, constituent concentration sorbed to suspended sediment (sand, silt, clay), constituent concentration sorbed to bed sediment (sand, silt, clay).

5.3.5.2 Summary Output

The following output is generated for input file verification:

- time parameters: simulation length, time-stepping criteria, central processing unit (CPU) time limits, restart control, iteration control.
- output control: print intervals and formats, data types, data dump control
- model options invoked: dynamic or hydrostatic pressure procedure, free surface or rigid lid, boundary slip, mass transport, sediment transport
- lookup tables for salinity/temperature equation of state
- computational grid specification: coordinate system, orientation for Coriolis, length units, boundary types,
- definition of model parameters: turbulence closure, diffusion, wind shear, bottom friction, form drag, adsorption/desorption, volatilization
- initial and boundary conditions: velocity, water surface elevation, salinity and temperature, bed and suspended sediment, constituent, distribution coefficients, wind
- source terms: water, salinity, heat, sediment, constituent.

5.3.5.3 Output

The following are generated as output:

- dependent variables at specified locations
- dependent variables at specified times
- zonal averages and fluxes
- mass balance
- convergence
- computational time profile

5.4 TESTS OF WATER SURFACE CALCULATIONS: COMPARISON WITH ANALYTICAL SOLUTIONS

Modifying the TEMPEST/FLESCOT code to compute the time-dependent motion of a free water surface added a new and untested capability to the model. To evaluate the free surface, calculation procedures were simulated for two test cases with well-known analytical solutions.

Computations of free oscillations in a three-dimensional, closed, rectangular basin were compared with the analytical solutions that were derived from the linear wave theory of Ippen (1966). This type of computation was selected to test the solution scheme without the complicating effects of an open boundary. Consistent with the assumptions used in the analytical solution, the advective, viscous, and Coriolis terms in the momentum equations were neglected. The simulations were performed using the hydrostatic pressure assumption, and the results were compared to the approximate, shallow-water form of the general analytical solution. The computational domain consisted of a 20-m-deep, 2500-m^2 basin, shown in Figure 5.9. Grid cell sizes of 100 m in the horizontal and 2 m in the vertical were used. Zero initial velocity and water depth, determined from the analytical solution using a 0.5-m wave amplitude, were assigned as starting conditions. The simulations were carried out for 240 s, using a time step of 15 s at the locations noted on Figure 5.9. Representative examples of the analytical water surface displacements and horizontal velocity components at location 4,4 are compared in Figures 5.10 through 5.12. Good agreement between the computations and the analytical solution was obtained at each comparison location. Figures showing additional comparisons are contained in Appendix E.

Simulations of a wave entering a closed-end channel were performed to test the assignment of tidal conditions at an open-boundary condition. The calculations were compared to the shallow-water analytical solutions given in Ippen (1966). A definition sketch of the problem is shown in Figure 5.13. The following dimensions were used in the test: channel length, l = 2400 m; wave amplitude, a = 0.5 m; and mean water depth, h = 13 m. The length of the

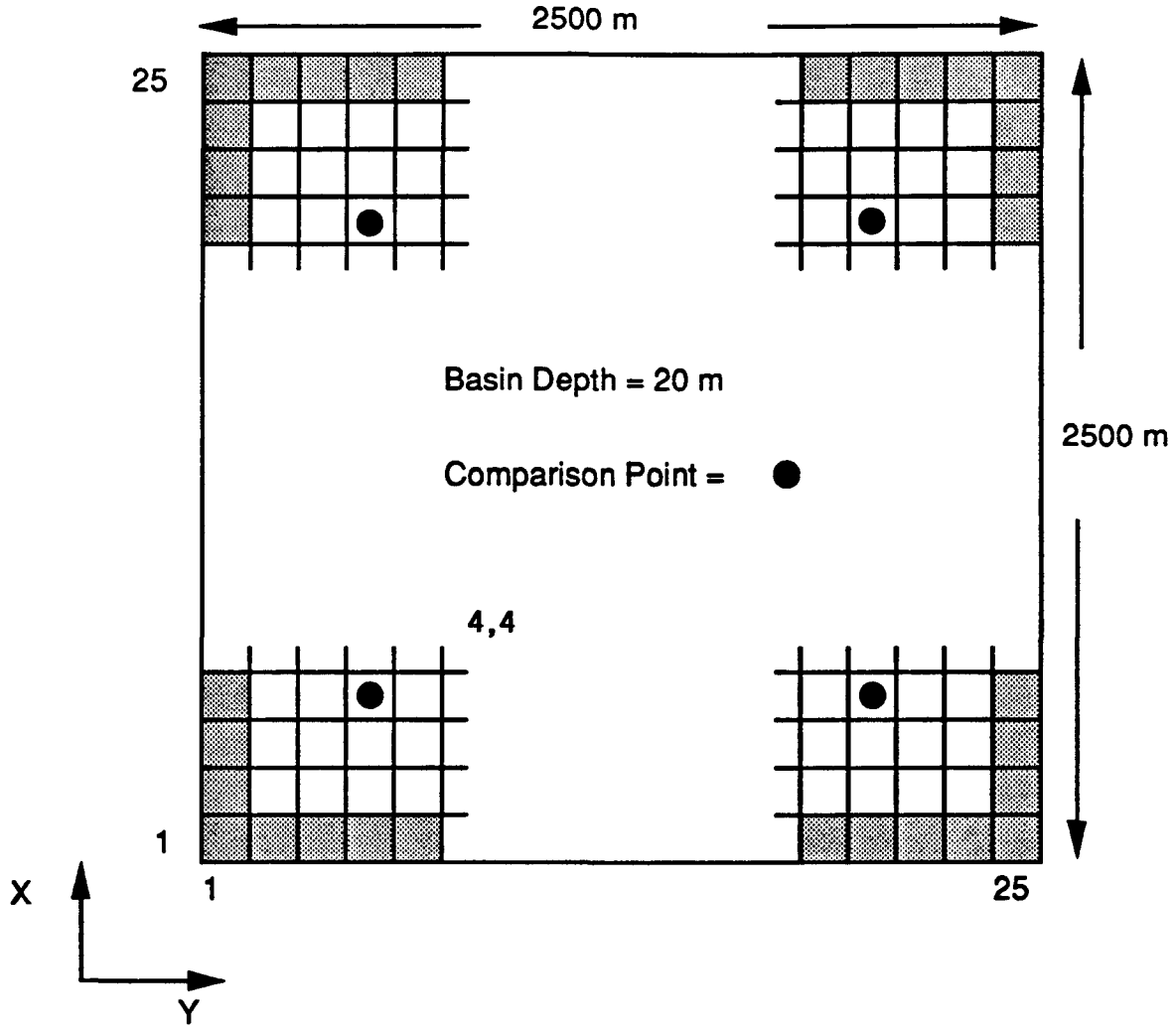

FIGURE 5.9. TEST CONFIGURATION FOR THREE-DIMENSIONAL OSCILLATIONS IN A RECTANGULAR BOX. SHADED CELLS ARE USED BY TEMPEST/FLESCOT TO SET BOUNDARY CONDITIONS.

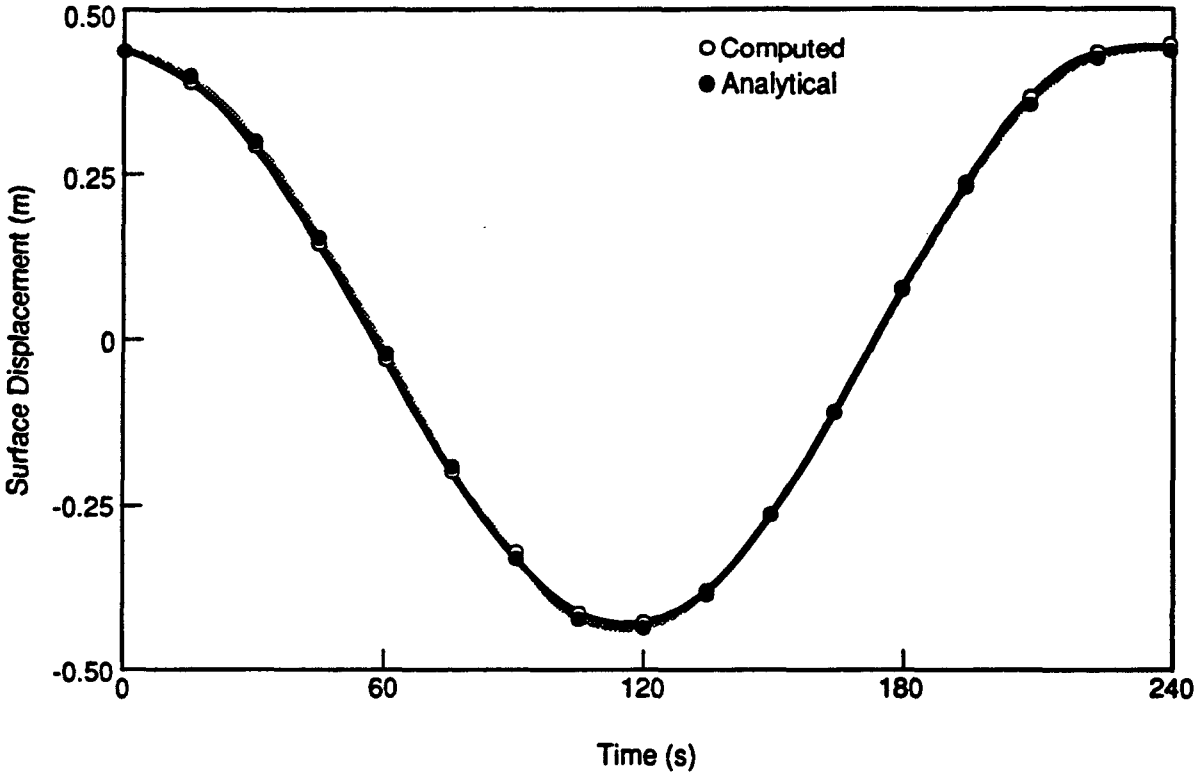

FIGURE 5.10. WATER SURFACE DISPLACEMENT AT LOCATION 4,4 FOR THREE-DIMENSIONAL OSCILLATION IN A RECTANGULAR BOX

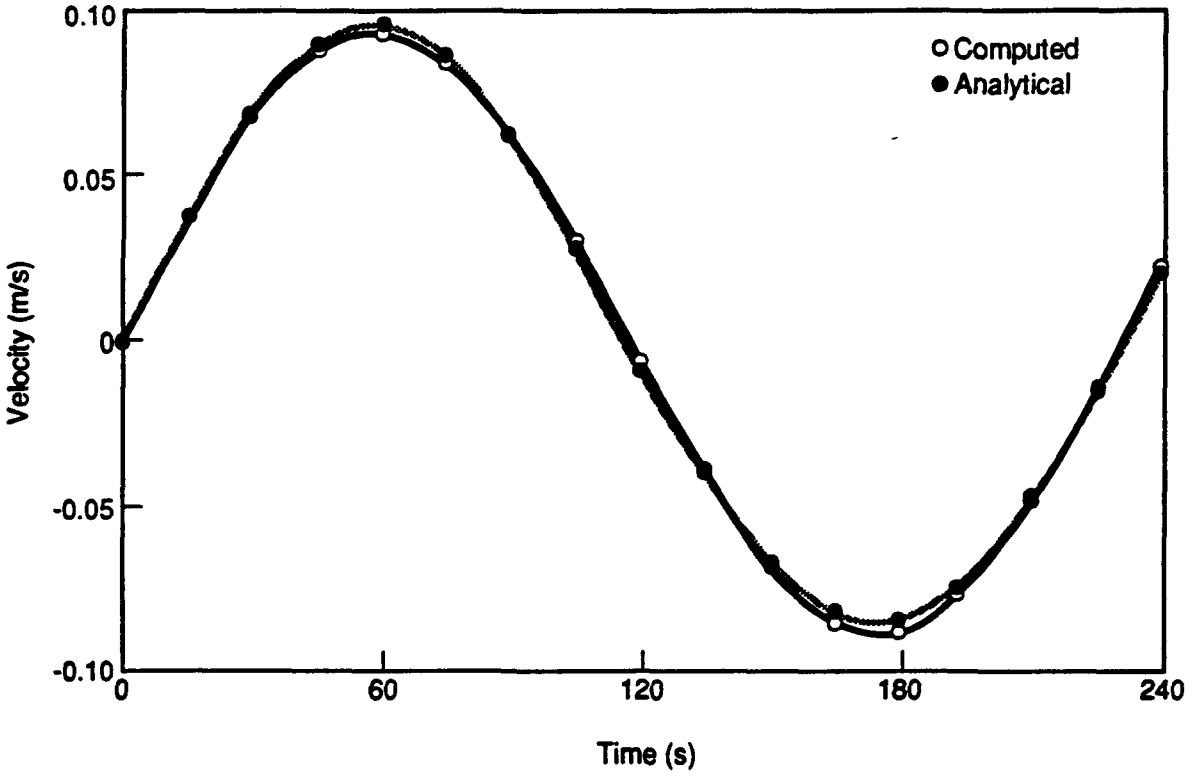

FIGURE 5.11. THE Y DIRECTION VELOCITY AT LOCATION 4,4 FOR THREE-DIMENSIONAL OSCILLATIONS IN A RECTANGULAR BOX

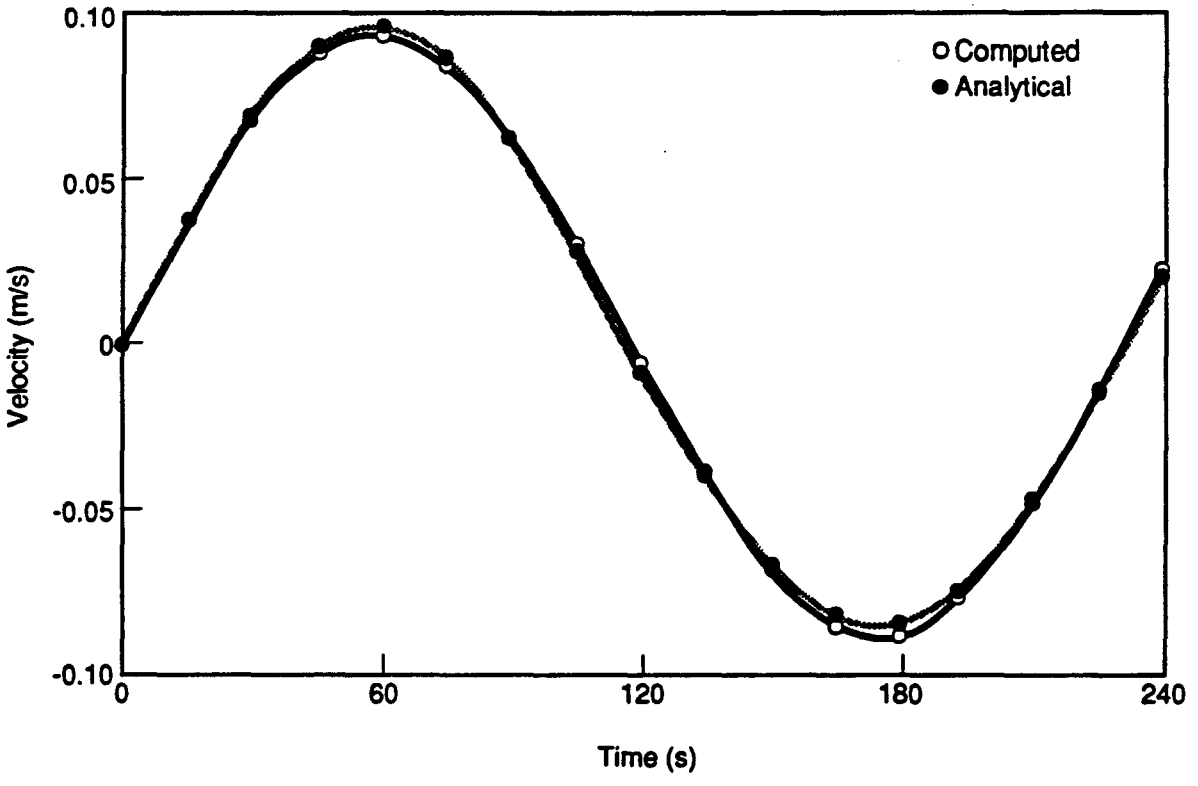

FIGURE 5.12. THE X DIRECTION VELOCITY AT LOCATION 4,4 FOR THREE-DIMENSIONAL OSCILLATIONS IN A RECTANGULAR BOX

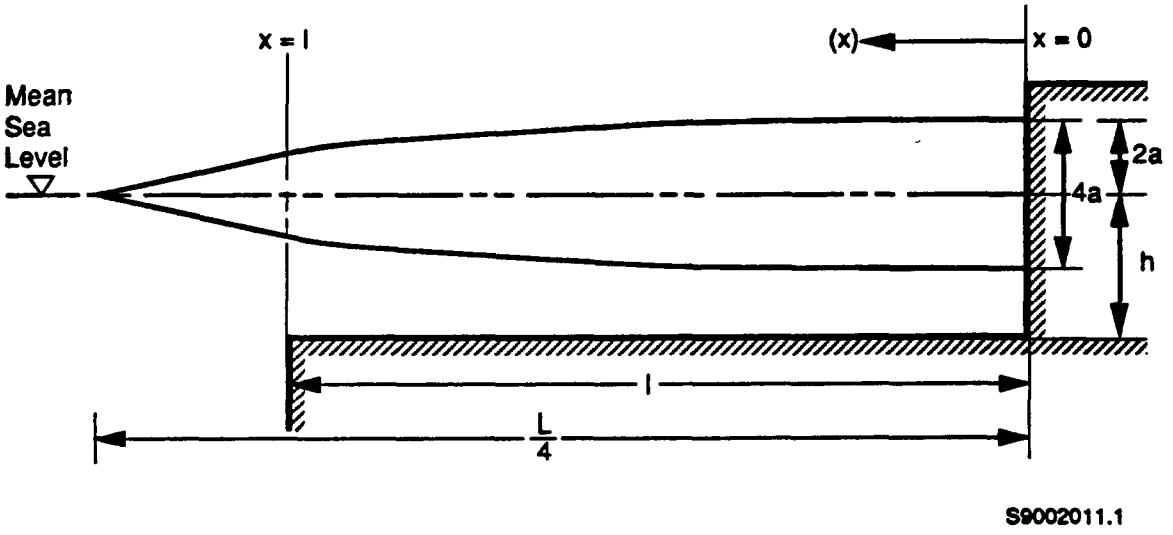

FIGURE 5.13. WAVE ENTERINE A CHANNEL OF FINITE LENGTH, L = 10,000 m (AFTER IPPEN 1966)

channel was discretized into 50-m grid cells, and 1-m cells were used in the vertical direction. A wavelength of 10,000 m, with a corresponding period of approximately 886 s, was imposed. The velocity and water surface initial conditions were set in accordance with the analytical solution at time zero. The simulation was forced with a time-dependent tidal boundary condition, developed from the analytical solution and assigned at x = 2400 m. The hydrostatic-pressure assumption was invoked, and the advective, viscous, and Coriolis terms were neglected. The results of the calculations, computed using a 50-s time step, are compared with the analytical solution at time intervals of 1/8 the wave period. Example for the velocity and water surface elevation are shown in Figures 5.14 and 5.15. The figures demonstrate good agreement between the calculations and the analytical solution. Figures showing results at other times are given in Appendix E.

In addition to the cases described above, the tests of wind-driven flow in a three-dimensional rectangular box [reported in Onishi and Trent (1982)] were repeated. The results obtained from the current version of the code were in agreement with the Onishi and Trent (1982) computations and with those of Leendertse et al. (1973). Further tests of wind forcing are described in Section 5.5.

The modification of the code to compute the motion of a free surface was judged to be successful, based on the positive results of the tests reported in this section. For each test case, the model was able to simulate the essential hydrodynamic features.

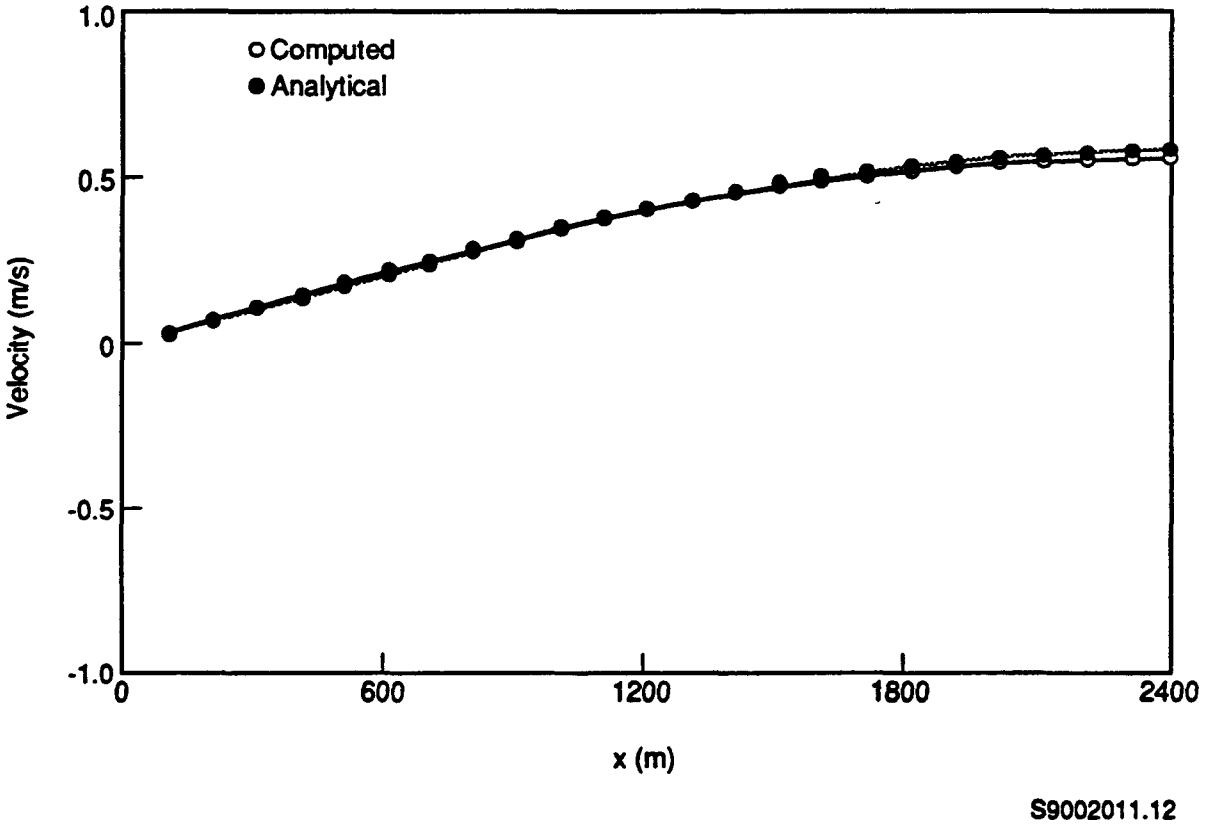

FIGURE 5.14. VELOCITY PROFILE ALONG THE CHANNEL AT TIME = 3/8T FOR A WAVE ENTERING A CHANNEL OF FINITE LENGTH

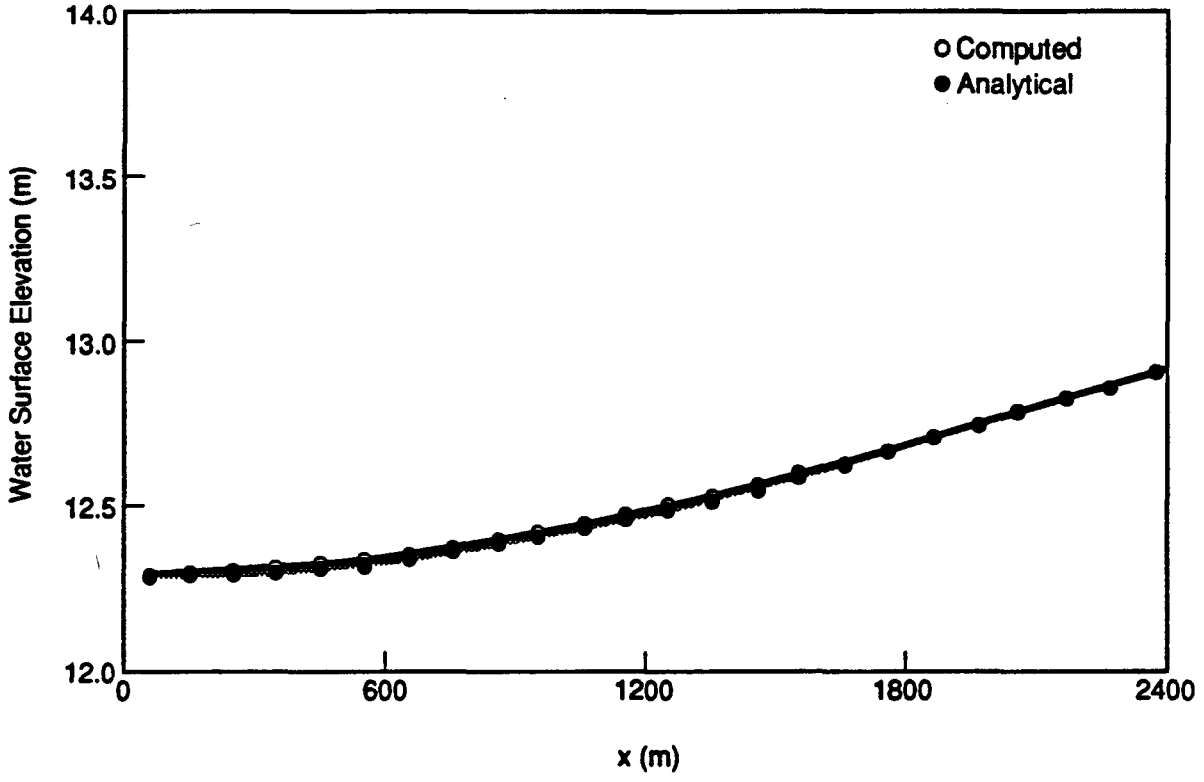

FIGURE 5.15. WATER SURFACE PROFILE ALONG THE CHANNEL AT TIME = 3/8T FOR A WAVE ENTERING A CHANNEL OF FINITE LENGTH

5.5 NEW BEDFORD HARBOR MODEL FORMULATION AND TESTING

The TEMPEST/FLESCOT model requires that one define a rectangular grid on which the numerical calculations are to be performed. To capture the important geographic features of the study area (see Figure 5.1), a grid with nonuniform spacing in the horizontal and vertical directions was generated. After the numerical grid was defined, several preliminary tests to qualify the performance of the model were done prior to calibration. Test results are described below for the following cases: M_2 tide forcing, forcing by a constant-speed and -direction wind, tide and wind forcing together, and the dispersion of a tracer released from a point source.

5.5.1 Grid Formulation

A three-dimensional, nonuniform, rectangular grid was constructed using the minimum number of grid cells required to describe the study area adequately. The grid was defined using the bathymetric (see Figure 5.2) and topographic data described in Section 5.2.1. The vertical grid structure is shown in Figure 5.16. Although eight grid layers are defined, TEMPEST/FLESCOT performs calculations only for layers 2 through 7. Grid layers 1 and 8 are used by the model to set internal boundary conditions. Figures 5.17 through 5.22 are plan views of the study area, showing the distribution of cells in each grid layer. Note that model grid north is rotated 16.5 degrees counterclockwise from true north to better align the grid with the site topography.

The model grid (Figure 5.22) covers an approximate area of 9 x 12 km. The location of the southern grid boundary was chosen to allow the use of U.S. Geological Survey tidal data for open-boundary conditions on model simulations within the hurricane barrier. The northern extent of the grid is defined by the Acushnet River at Wood Street Bridge. Depths in the model range from 10 m in Buzzards Bay and shipping lanes to less than 1 m in shallow zones such as the tidal flats between Coggeshall Street and Wood Street Bridges. The horizontal dimensions of the grid vary from 300 x 500 m for the largest to

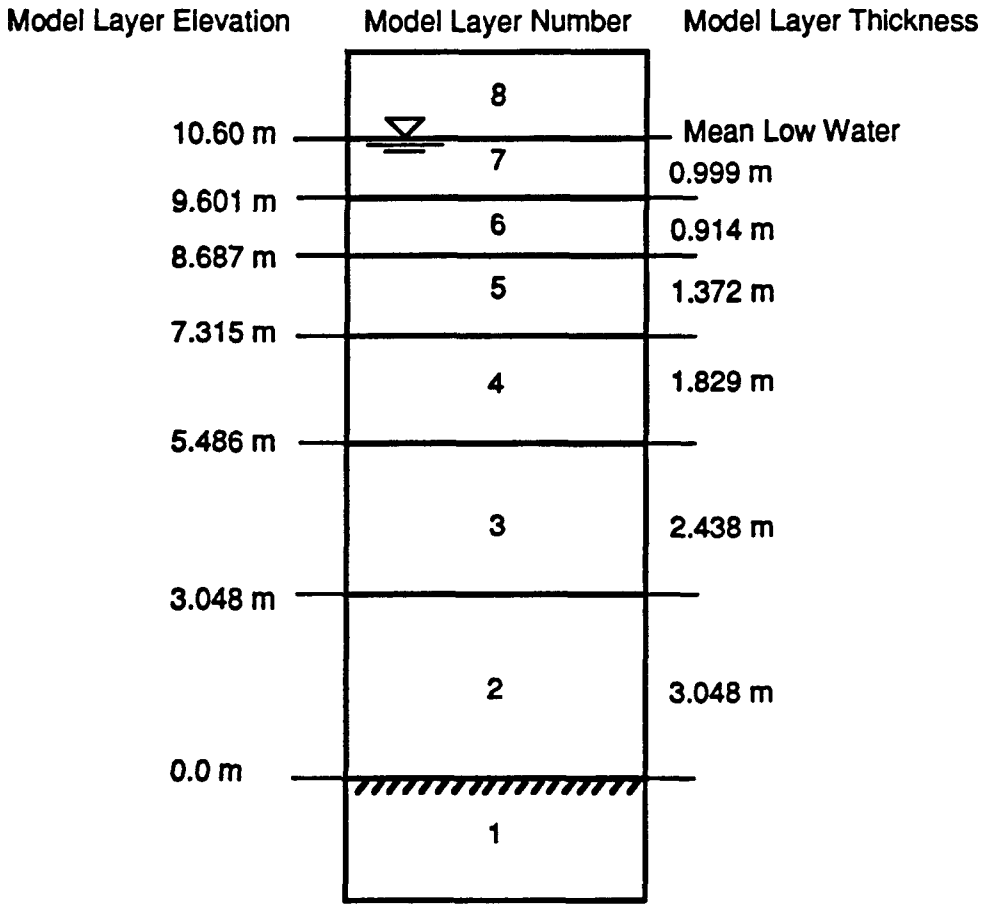

FIGURE 5.16. VERTICAL GRID STRUCTURE FOR THE NEW BEDFORD HARBOR MODEL. LAYERS 1 AND 8 ARE USED INTERNALLY BY TEMPEST/FLESCOT TO ASSIGN BOUNDARY CONDITIONS

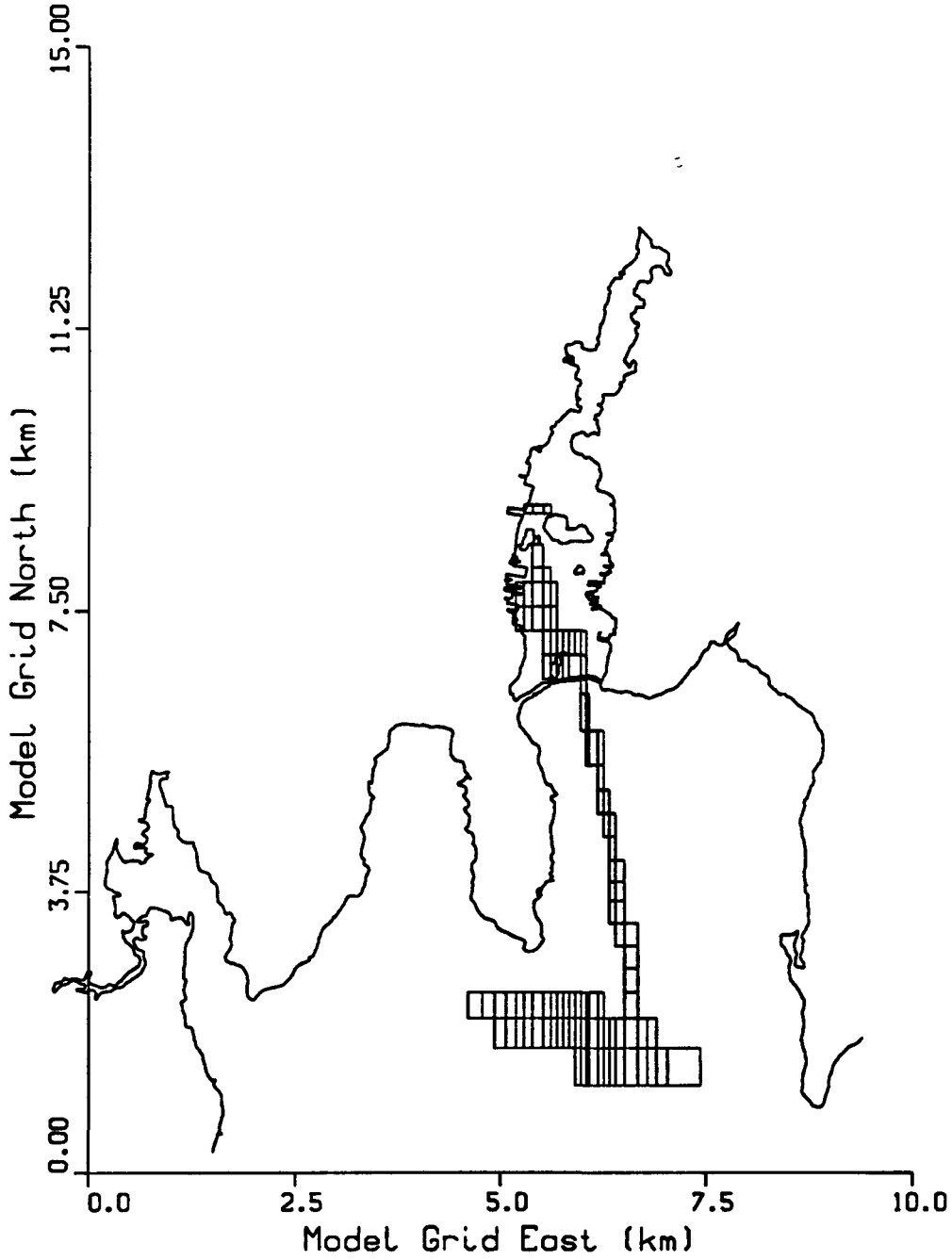

FIGURE 5.17. PLAN VIEW OF THE NEW BEDFORD HARBOR MODEL GRID. GRID LAYER 2.

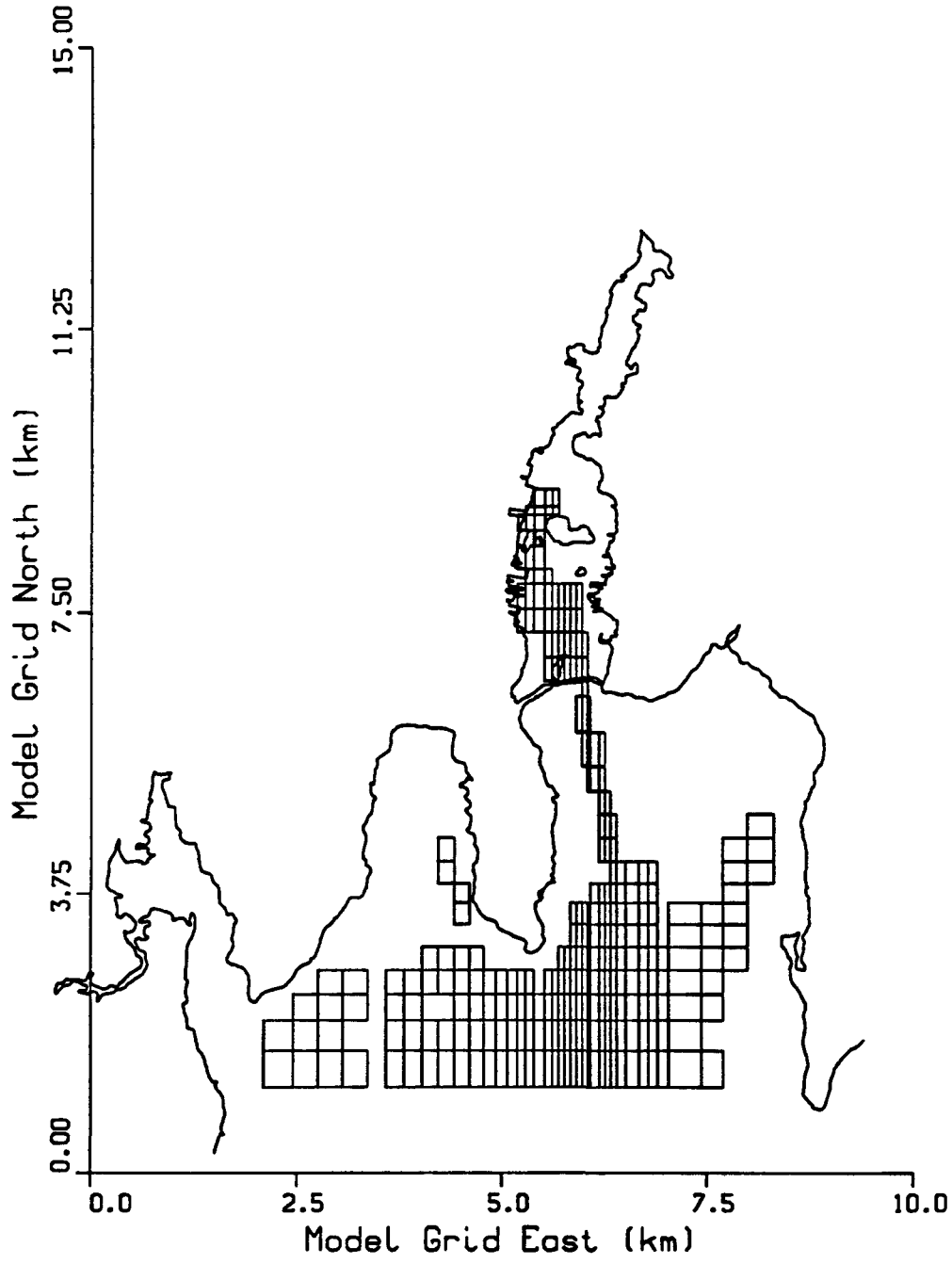

FIGURE 5.18. PLAN VIEW OF THE NEW BEDFORD HARBOR MODEL GRID. GRID LAYER 3.

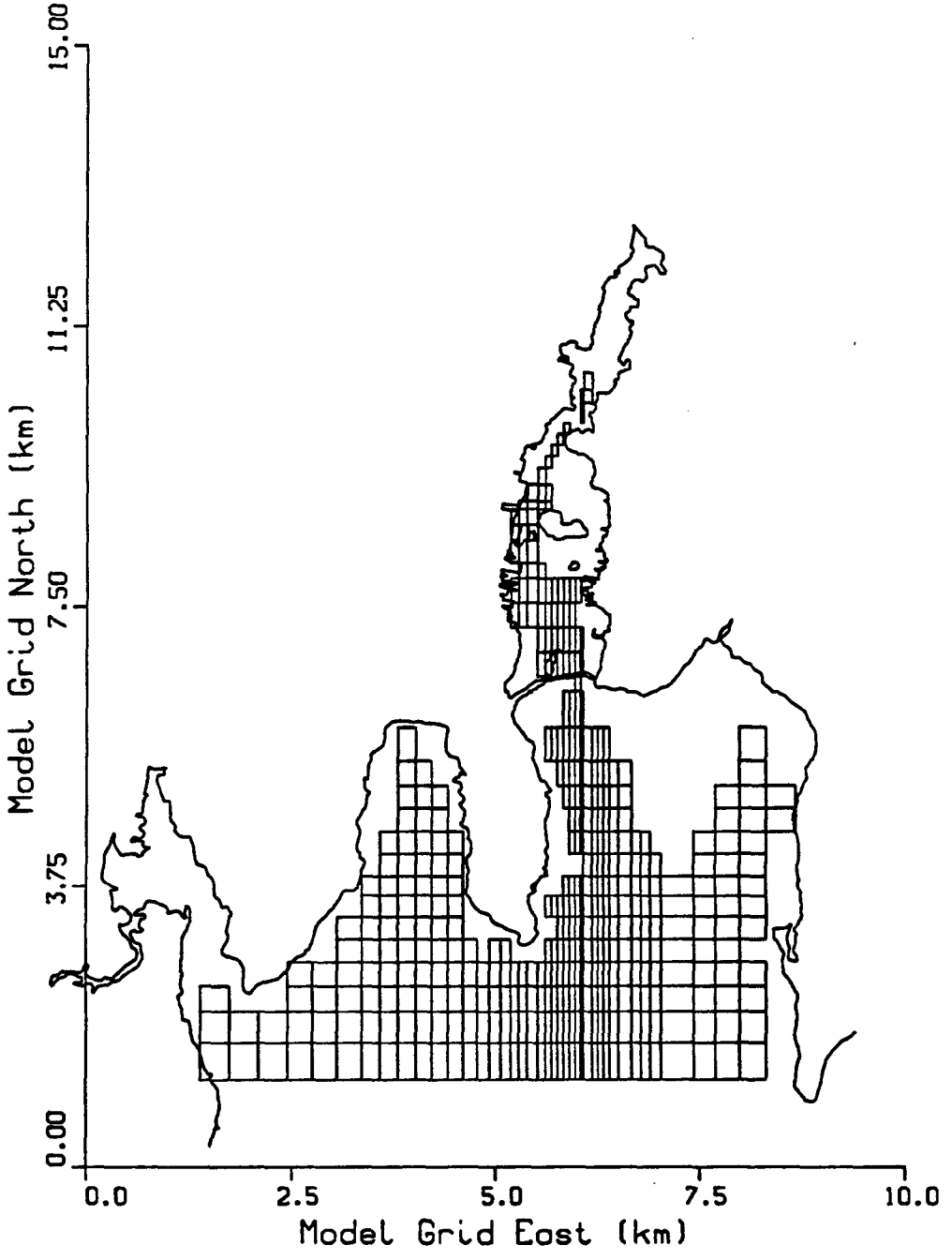

FIGURE 5.19. PLAN VIEW OF THE NEW BEDFORD HARBOR MODEL GRID. GRID LAYER 4.

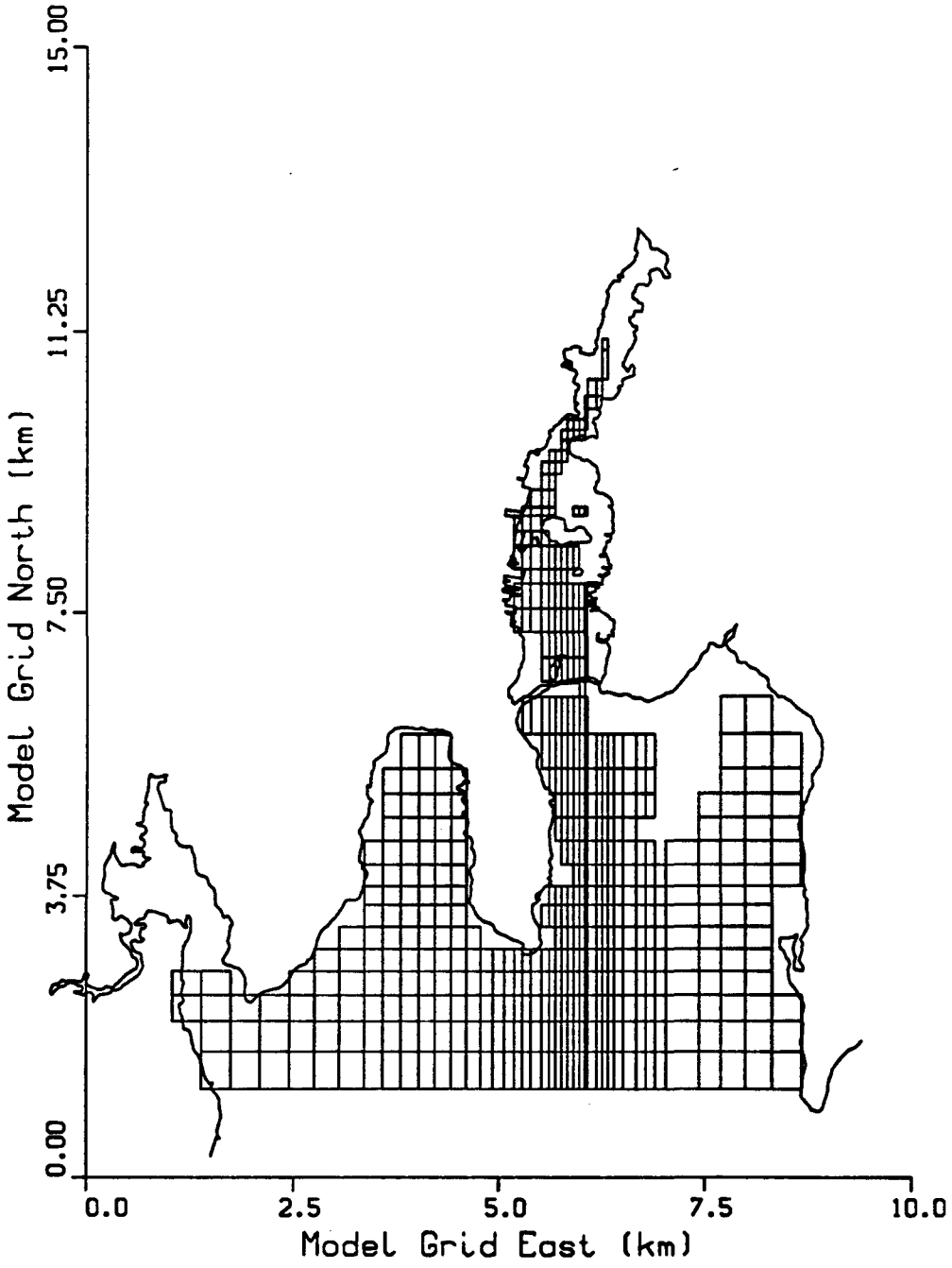

FIGURE 5.20. PLAN VIEW OF THE NEW BEDFORD HARBOR MODEL GRID. GRID LAYER 5.

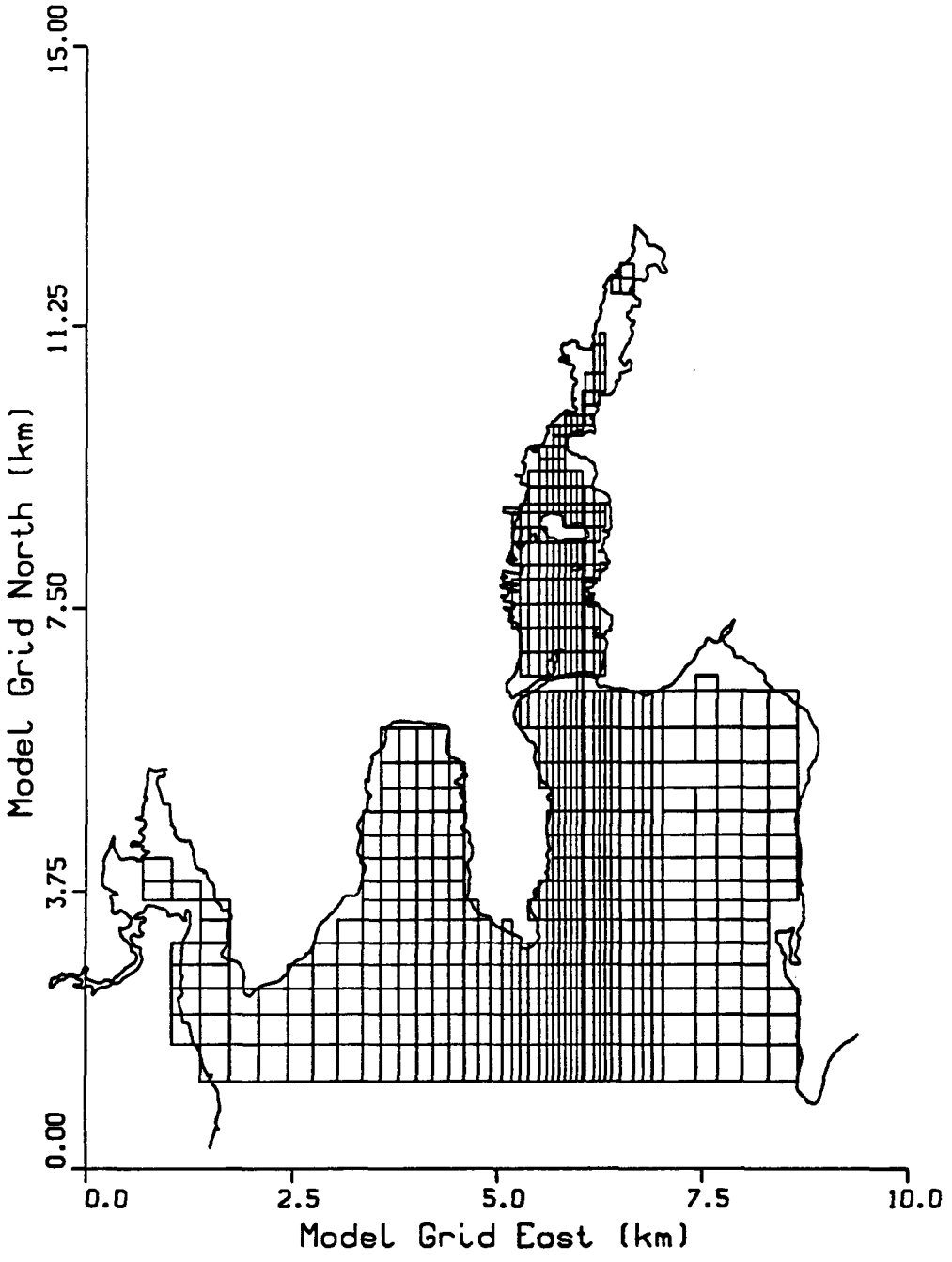

FIGURE 5.21. PLAN VIEW OF THE NEW BEDFORD HARBOR MODEL GRID. GRID LAYER 6.

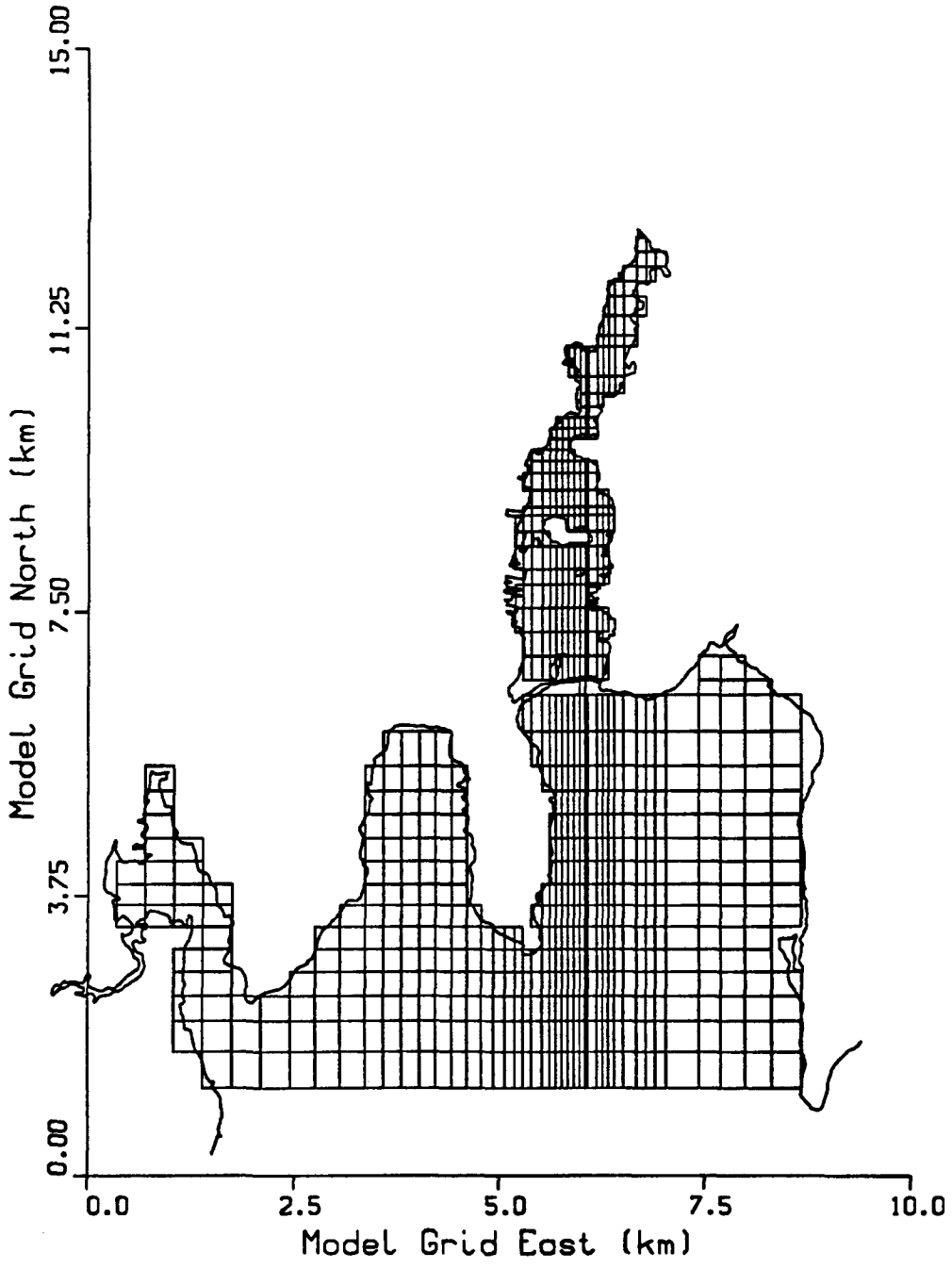

FIGURE 5.22. PLAN VIEW OF THE NEW BEDFORD HARBOR MODEL GRID. GRID LAYER 7.

33 x 100 m for the smallest cells. The horizontal grid spacing was selected to provide good resolution of the features of the study area such as the hurricane barrier and Popes Island.

5.5.2 Tide- and Wind-Forcing Tests

Following the preliminary tests of the free-surface calculation procedure using analytical solutions, the code was tested using the New Bedford Harbor grid. The purposes of the tests were twofold: to check the capability of the code to simulate free-surface flows with complex topography and bathymetry, and to gain insight into how the New Bedford Harbor model would respond to tide-and wind-forcing prior to the model calibration exercise. The following cases were simulated: a constant-speed and -direction wind case, an M_2 tide case, a test combining the previous two cases, and a quasi-steady-state stabilization test. Selected water surface height, current speed, and current direction time series data are presented for each case at the locations shown in Figure 5.23. For all of these cases, the density of the water mass was held constant.

The response of the model to a constant-speed and -direction wind was tested by applying a wind of 5 m/s blowing toward true north, where the wind vector is oriented 16.5 degrees clockwise from model grid north. The test was run with the following parameter values: a vertical eddy viscosity of 0.001 m^2/s, a horizontal eddy viscosity of 1.0 m^2/s, and a bottom friction coefficient of 0.0026. The duration of the simulation was 12.42 h, which corresponds to the period of the M_2 tide. Initial conditions for the velocity field and water surface elevation were zero and 10.6 m, respectively. Time-series results in Figures 5.24 and 5.25 show that the model reaches steady state after 4 h of simulation. Vector plots (Figures 5.26 and 5.27) are shown at 12 h, well after the model reached a steady-state condition. In the open-water areas off Clarks Point, the surface layer speed is approximately 5 cm/s (Figures 5.24 and 5.26), which is 1% of the wind speed. As shown in Figure 5.24, the velocity direction is approximately 45 degrees clockwise from the wind direction of true north (0 degree), as expected from the Ekman layer theory.

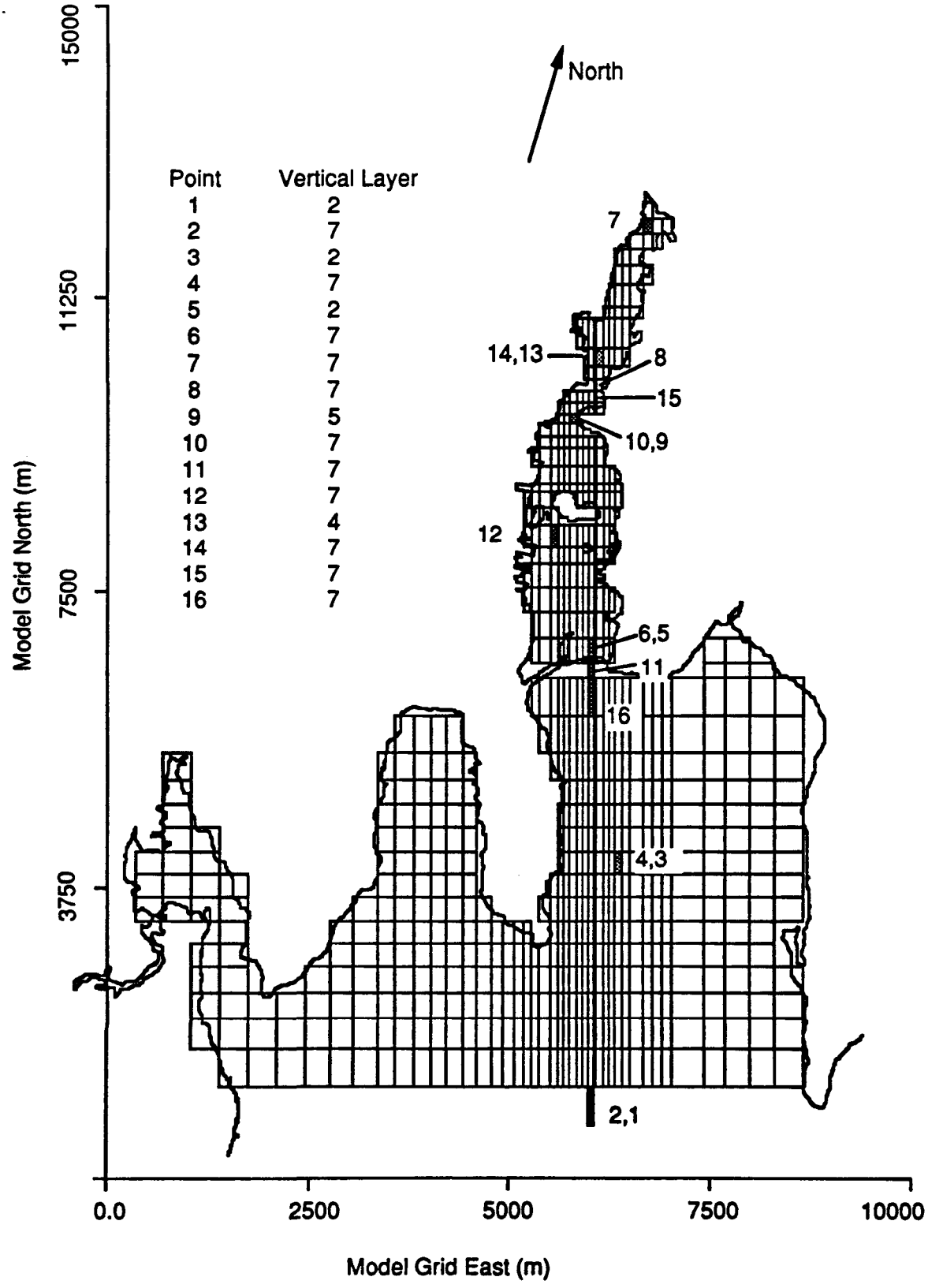

FIGURE 5.23. LOCATION OF MODEL TIME-SERIES OUTPUT POINTS FOR M_2 TIDE AND CONSTANT WIND TESTS

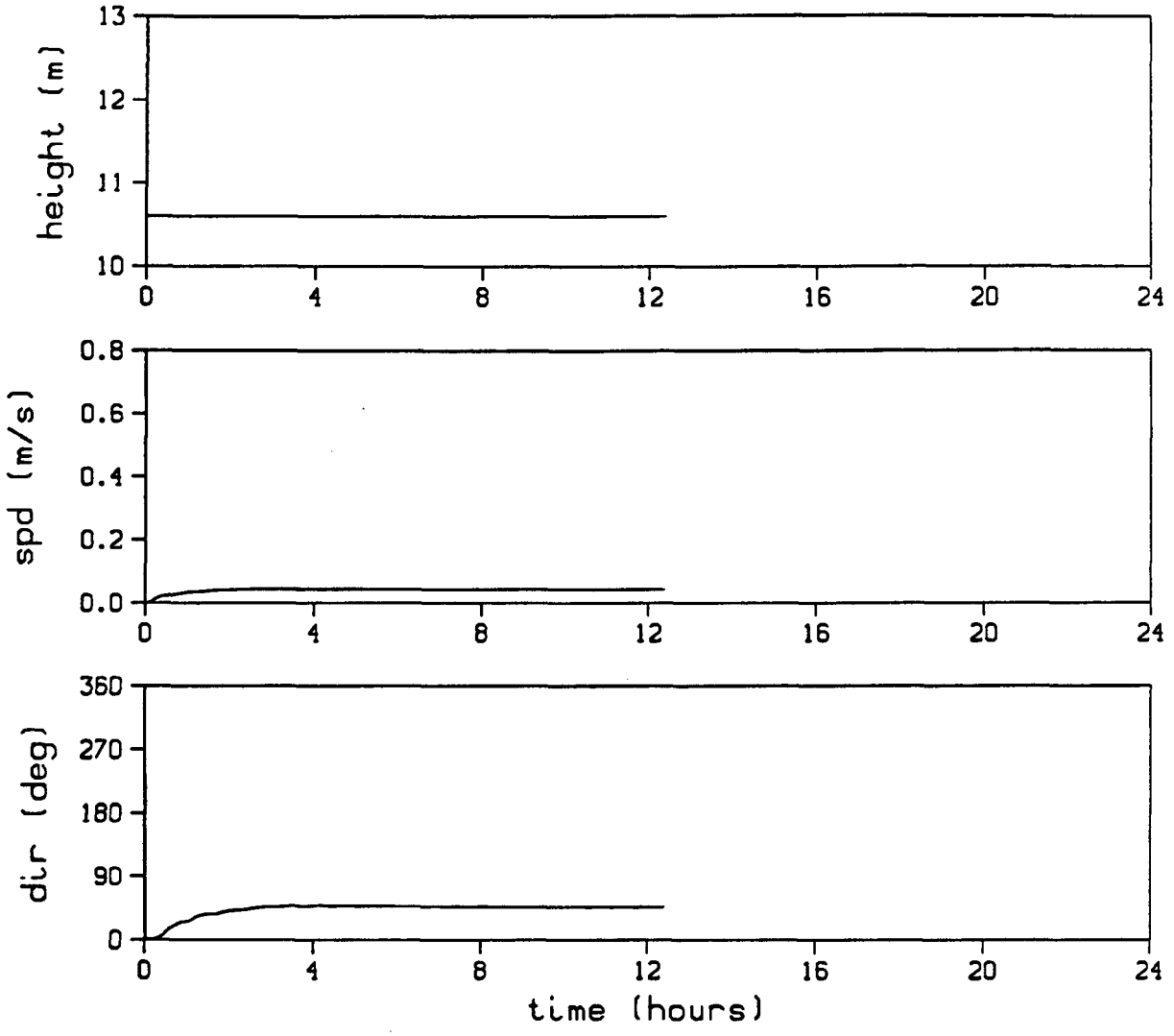

FIGURE 5.24. WATER SURFACE HEIGHT, CURRENT SPEED, AND CURRENT DIRECTION AT TIME-SERIES LOCATION 4 FOR THE WIND FORCING TEST

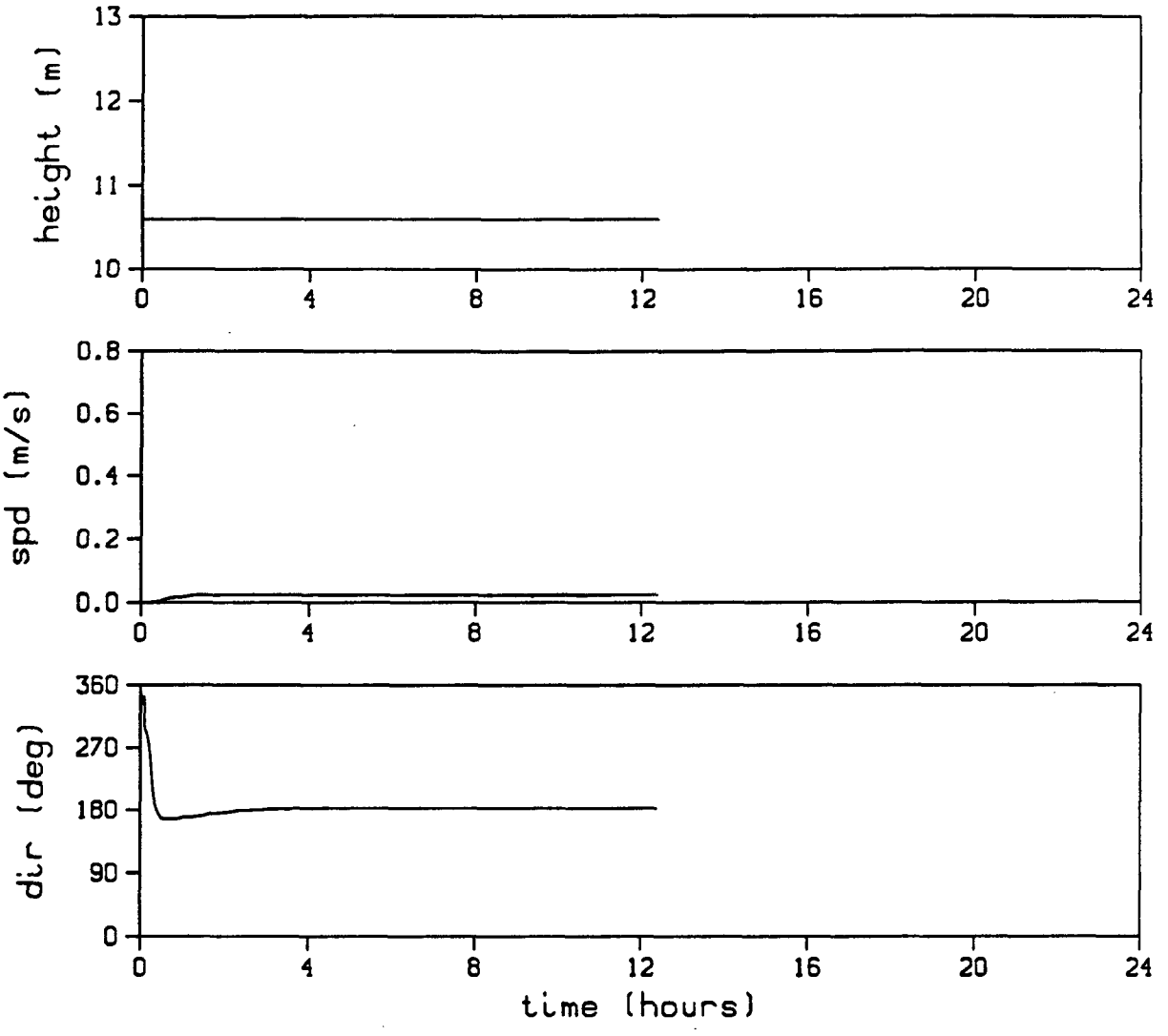

FIGURE 5.25. WATER SURFACE HEIGHT, CURRENT SPEED, AND CURRENT DIRECTION AT TIME-SERIES LOCATION 3 FOR THE WIND FORCING TEST

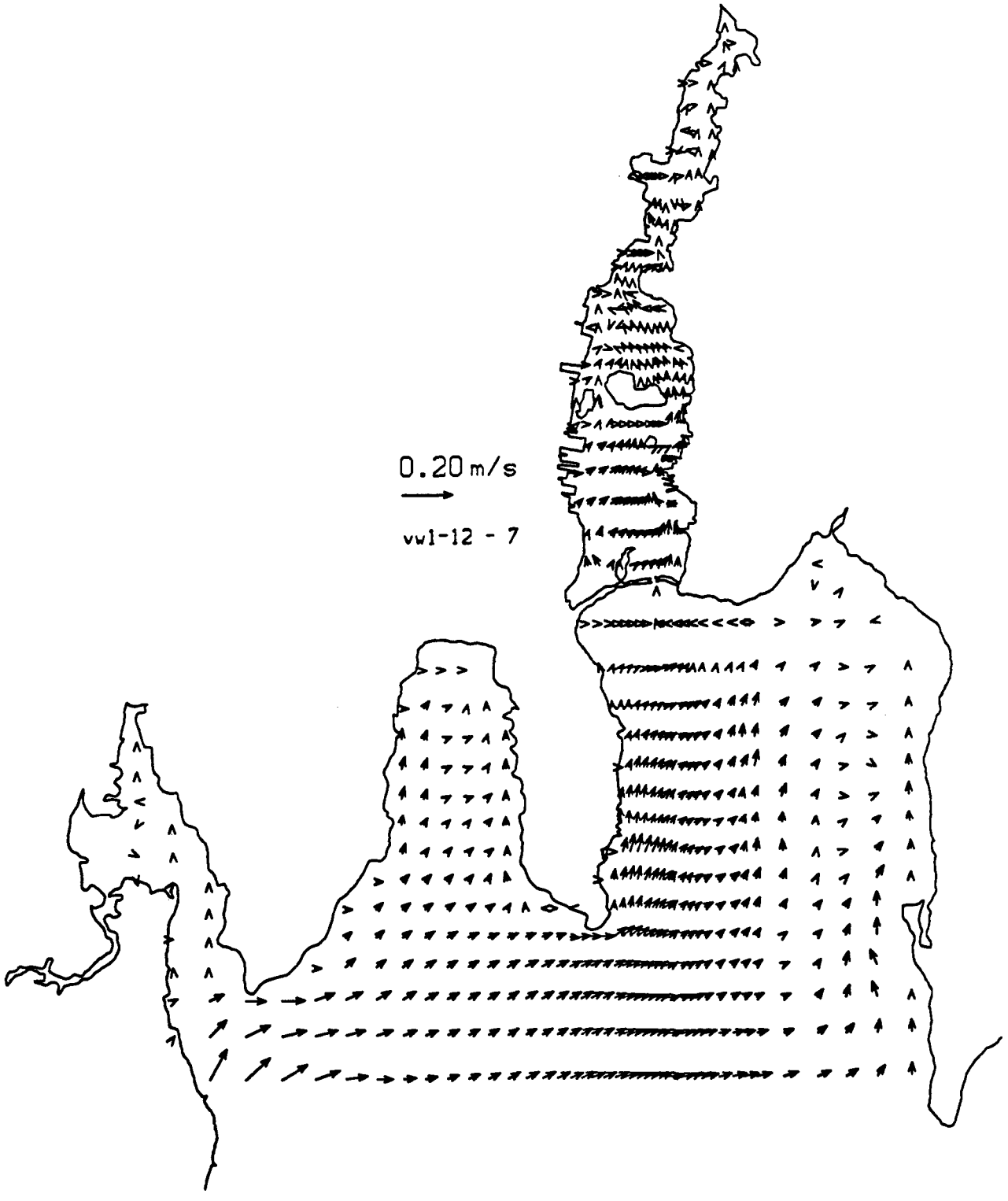

FIGURE 5.26. WIND FORCING TEST. VELOCITY VECTORS FOR GRID LAYER 7 AT TIME = 12 h.

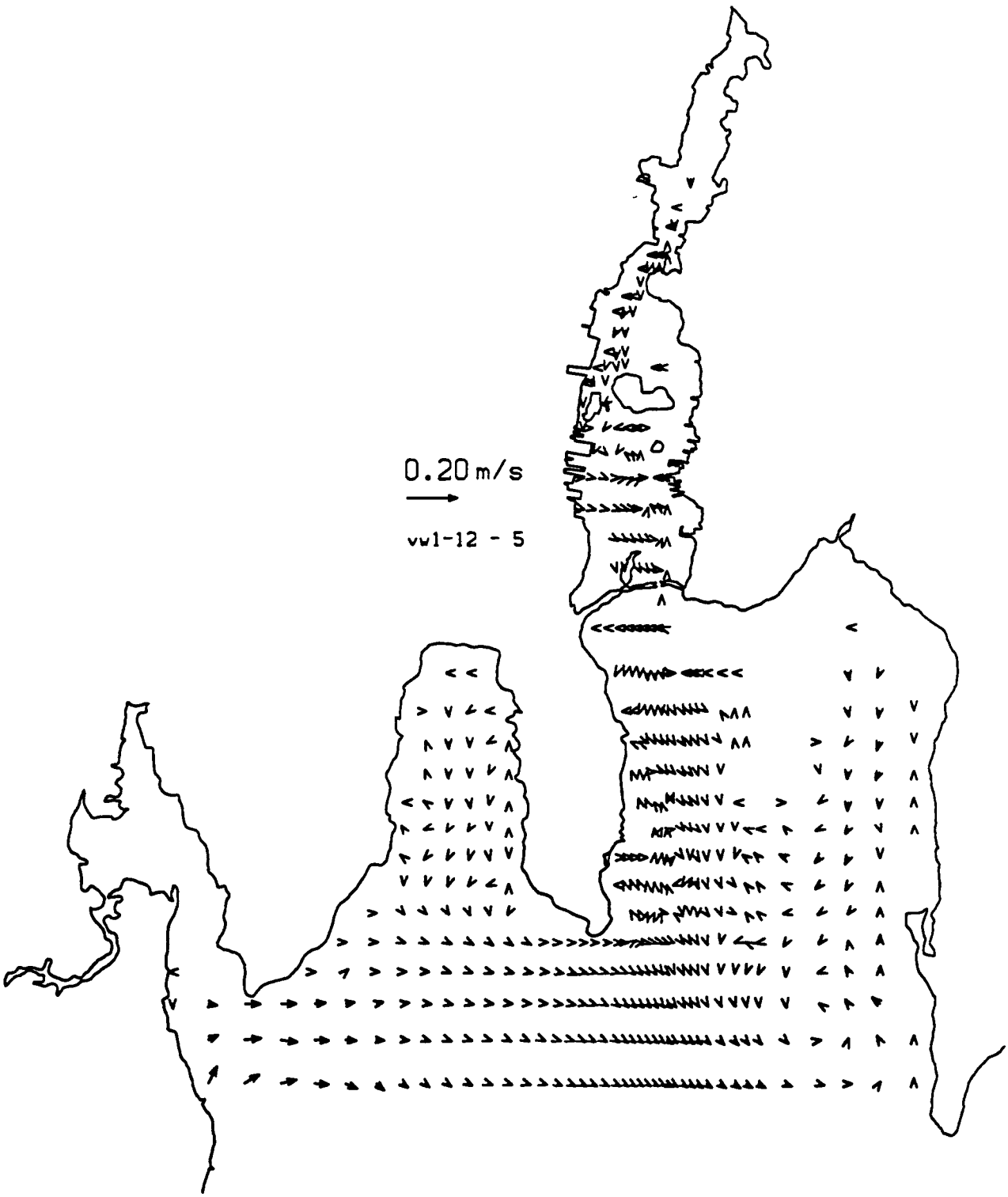

FIGURE 5.27. WIND FORCING TEST. VELOCITY VECTORS FOR GRID LAYER 5 AT TIME = 26 h.

Within the hurricane barrier, the surface speeds tend to be lower than 5 cm/s, and the direction of flow is strongly influenced by local topography. Deeper in the water column a counter flow is set up in an opposite direction to the wind. This is illustrated in Figure 5.25, which shows that the flow direction in the bottom grid layer (layer 2) is at 180 degrees. In Figure 5.27, which shows a vector plot for layer 5, a counter flow between Popes Island and Coggeshall Street Bridge is evident.

The effects of tidal forcing alone were studied by running the model with an M_2 tide imposed at the open boundary. The amplitude and period of the sinusoidal M_2 tide boundary condition were 0.70 m and 12.42 h, respectively. The eddy viscosities and bottom friction parameters were the same as those used in the wind-forcing test. Time-series results for a select number of locations are shown in Figures 5.28 through 5.33. As expected, tidal forcing creates much higher velocities and causes the flow to be oscillatory compared with constant wind forcing. At time-series locations 4 and 3 (Figures 5.28 and 5.29), the peak tidal-flow velocity is approximately three times greater than the wind-induced flow speed; however, the flow direction oscillates with the tide, the surface-layer velocity rotating in a clockwise direction and the bottom layer rotating counterclockwise. Peak velocities at the hurricane barrier and Coggeshall Stream Bridge constrictions, respectively shown in Figures 5.30 and 5.32, are nearly 60 cm/s. Lower peak velocities, approximately 10 cm/s, are calculated in areas removed from the constrictions (Figures 5.31 and 5.33). Vector plots of the surface layer (layer 7) and layer 5 velocity fields on the flood and ebb tides are displayed in Figures 5.34 through 5.37. Water tends to enter and leave the model along a northeast-southeast axis, turning toward the north as it flows around Clarks Point. The hurricane barrier causes a noticeable jet effect, especially on the ebb tide (see Figure 5.36). Maximum velocities within the harbor tend to follow the dredged shipping channel, especially below the surface in layer 5 (see Figures 5.35 and 5.37).

The two cases described above were combined to investigate the effects of tide- and wind-forcing. Time-series results are shown in Figures E.1 through

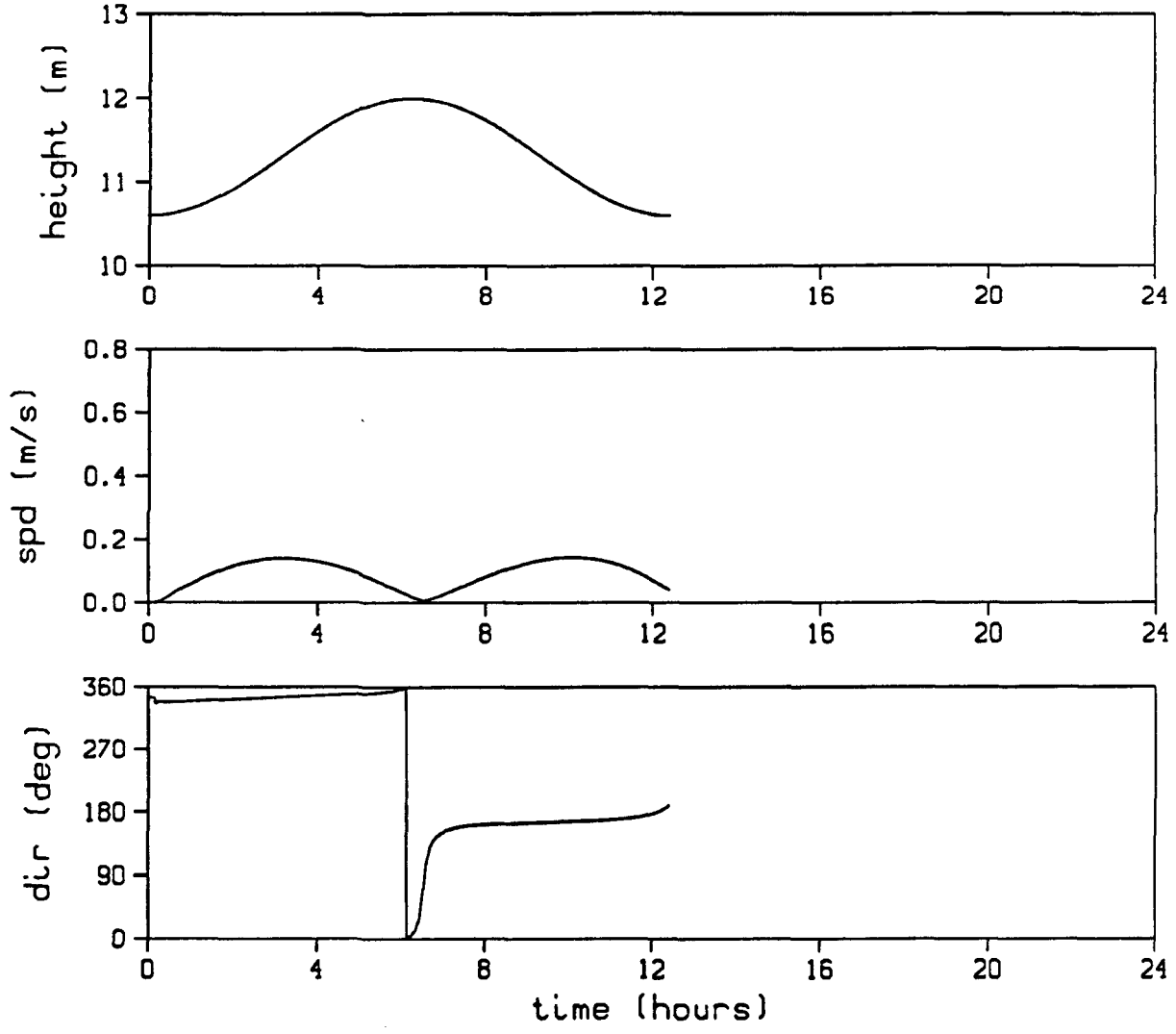

FIGURE 5.28. WATER SURFACE HEIGHT, CURRENT SPEED, AND CURRENT DIRECTION AT TIME-SERIES LOCATION 4 FOR THE M_2 TIDE FORCING TEST

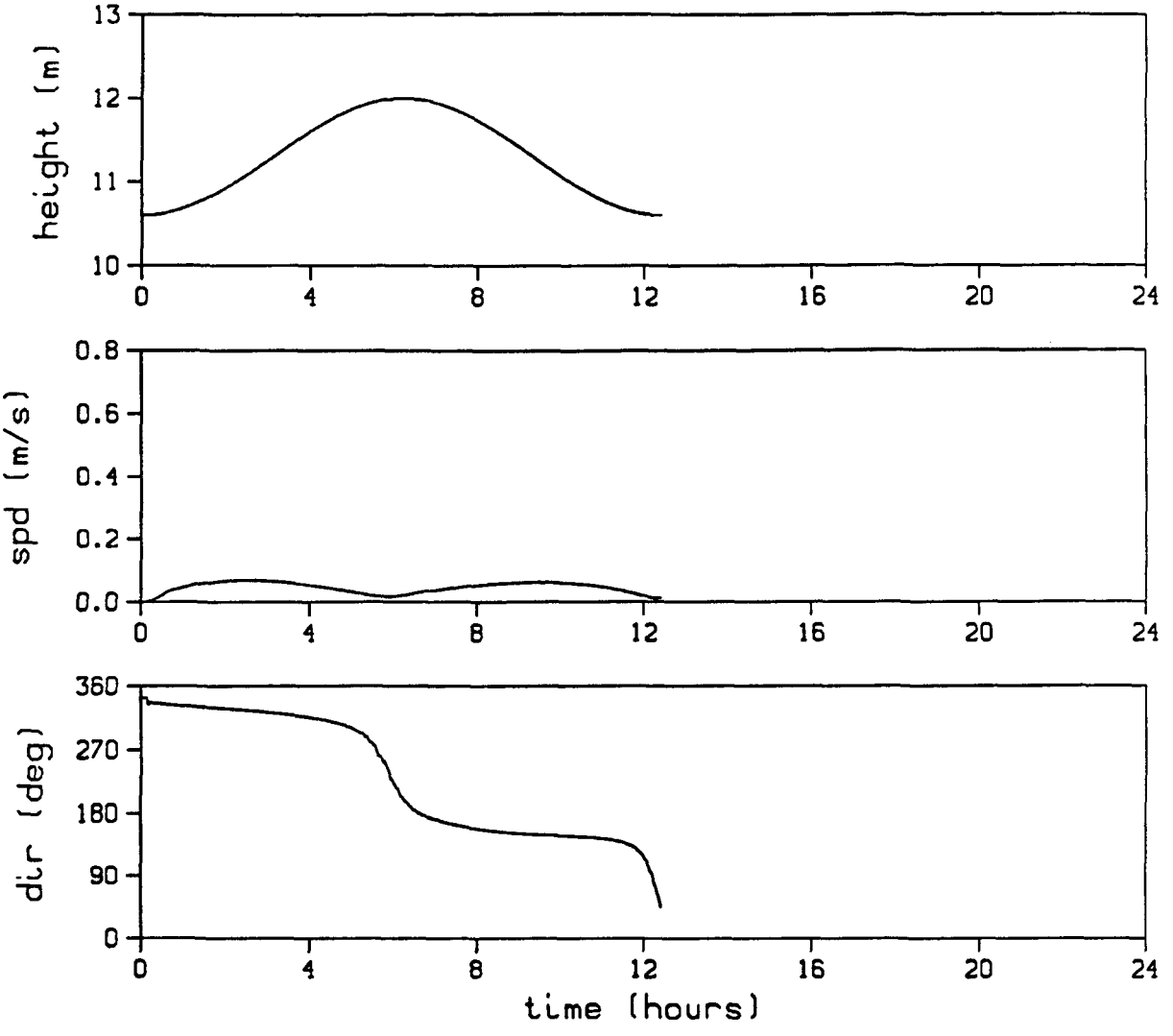

FIGURE 5.29. WATER SURFACE HEIGHT, CURRENT SPEED, AND CURRENT DIRECTION AT TIME-SERIES LOCATION 3 FOR THE M_2 TIDE FORCING TEST

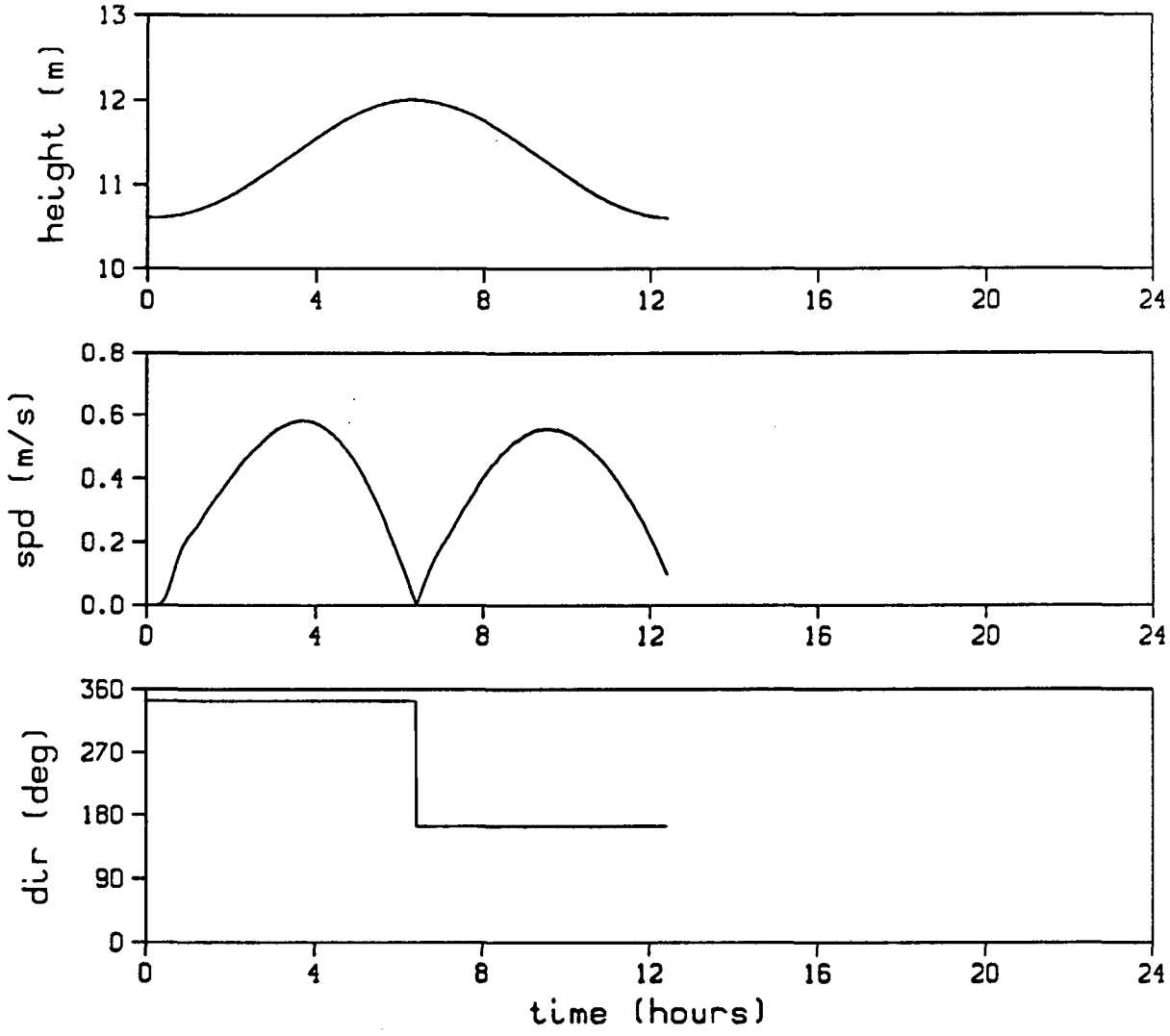

FIGURE 5.30. WATER SURFACE HEIGHT, CURRENT SPEED, AND CURRENT DIRECTION AT TIME-SERIES LOCATION 11 FOR THE M_2 TIDE FORCING TEST

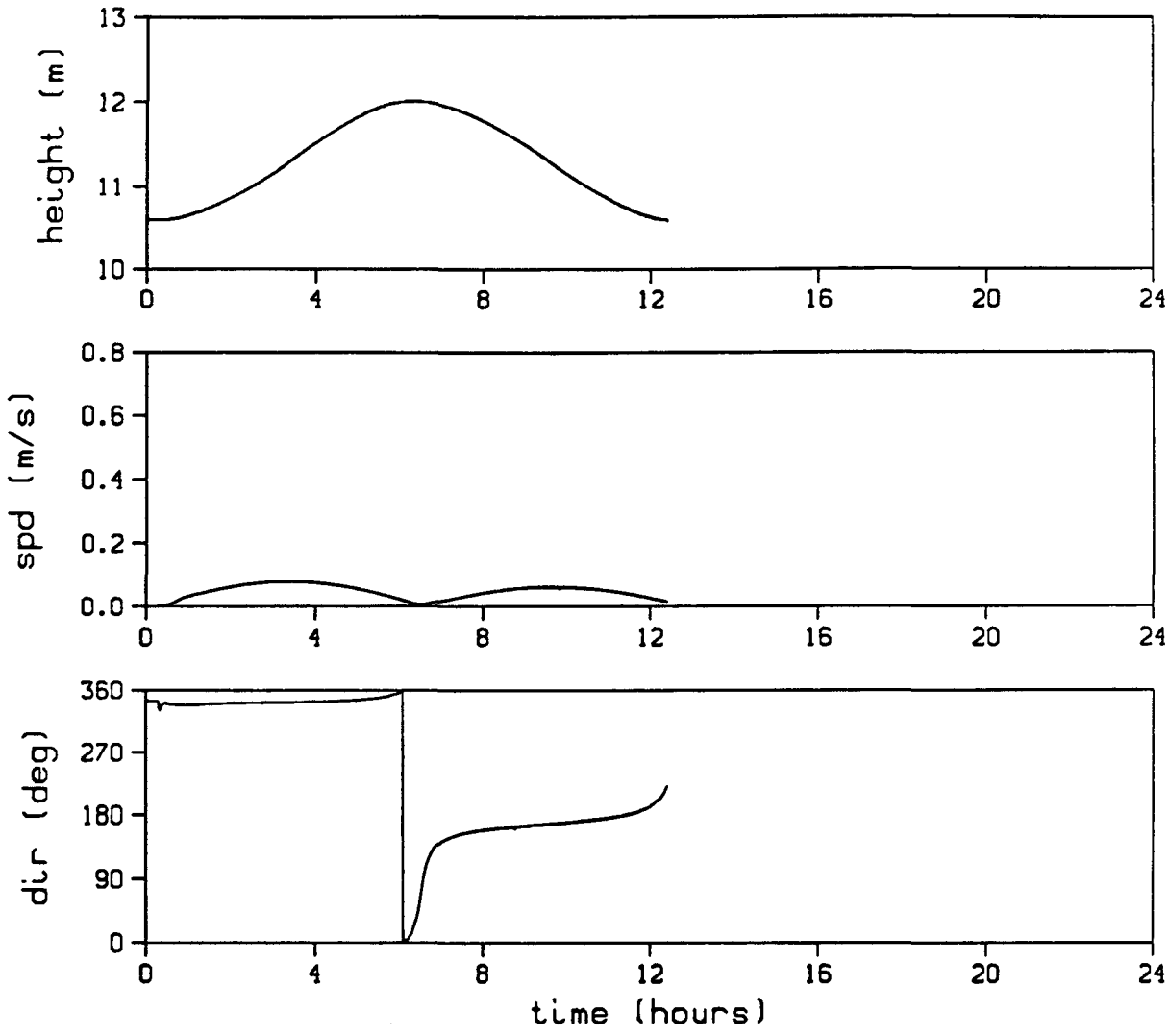

FIGURE 5.31. WATER SURFACE HEIGHT, CURRENT SPEED, AND CURRENT DIRECTION AT TIME-SERIES LOCATION 12 FOR THE M_2 TIDE FORCING TEST

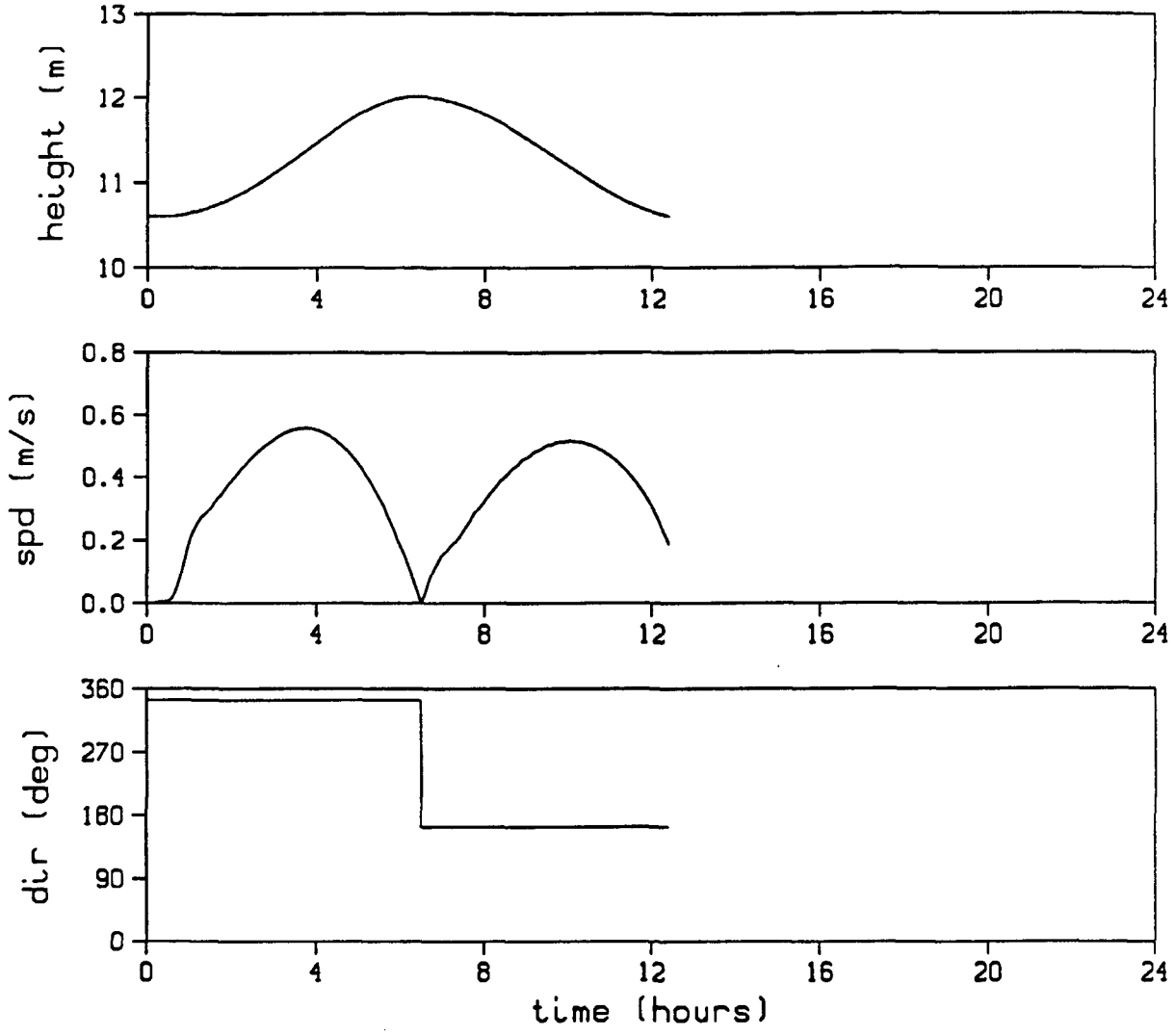

FIGURE 5.32. WATER SURFACE HEIGHT, CURRENT SPEED, AND CURRENT DIRECTION AT TIME-SERIES LOCATION 8 FOR THE M_2 TIDE FORCING TEST

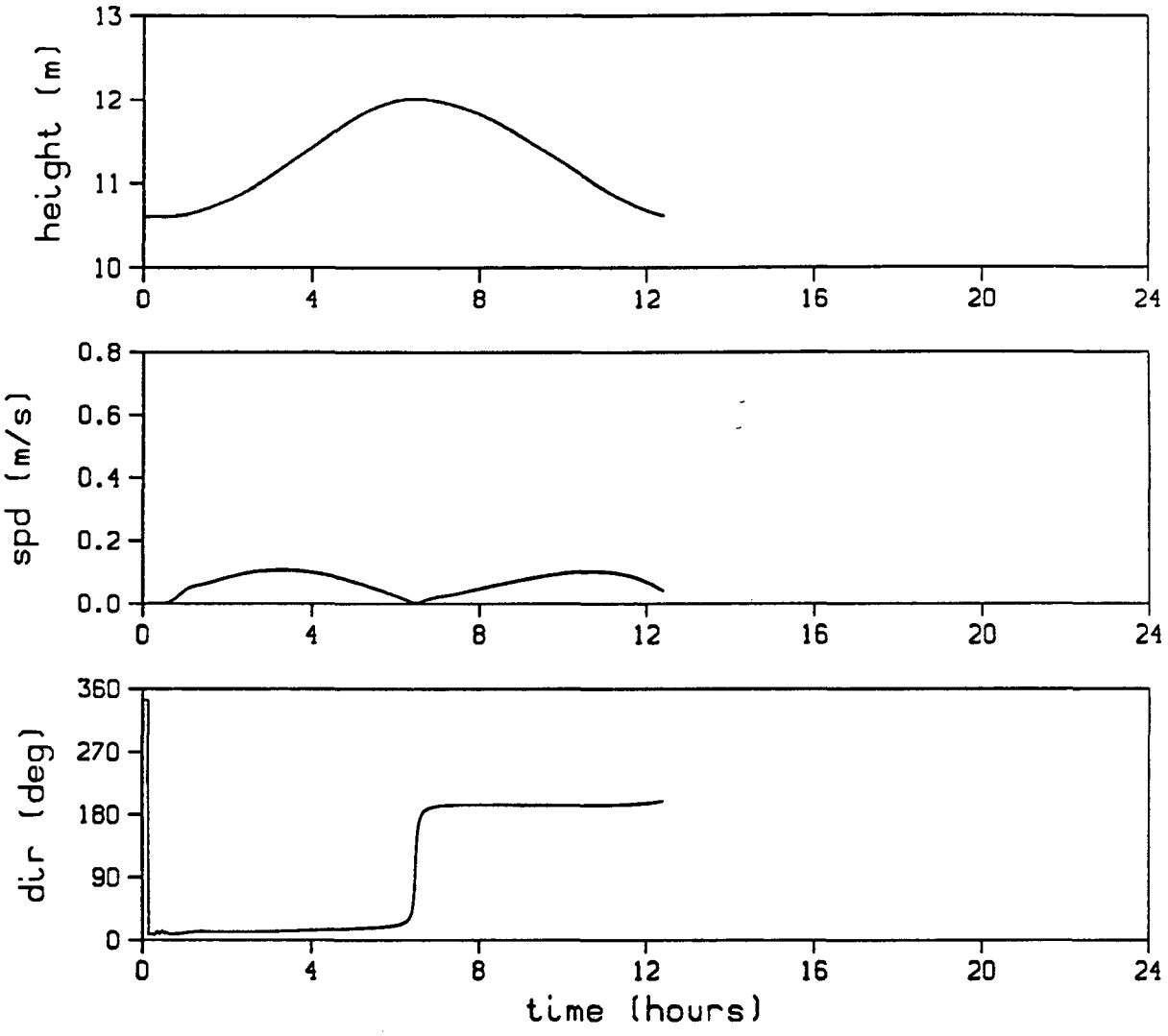

FIGURE 5.33. WATER SURFACE HEIGHT, CURRENT SPEED, AND CURRENT DIRECTION AT TIME-SERIES LOCATION 14 FOR THE M_2 TIDE FORCING TEST

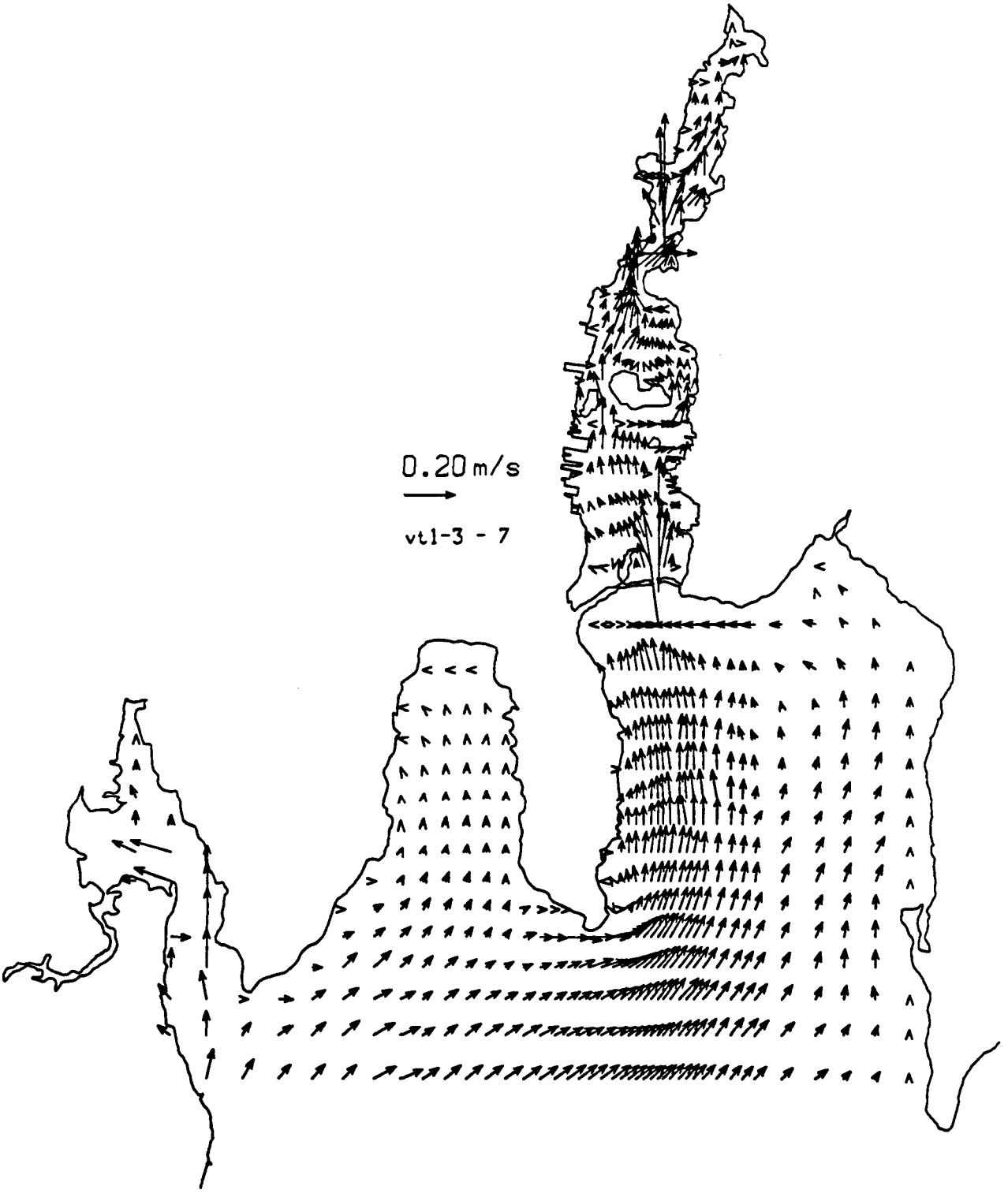

FIGURE 5.34. M_2 TIDE FORCING TEST. VELOCITY VECTORS FOR GRID LAYER 7 AT TIME = 3 h.

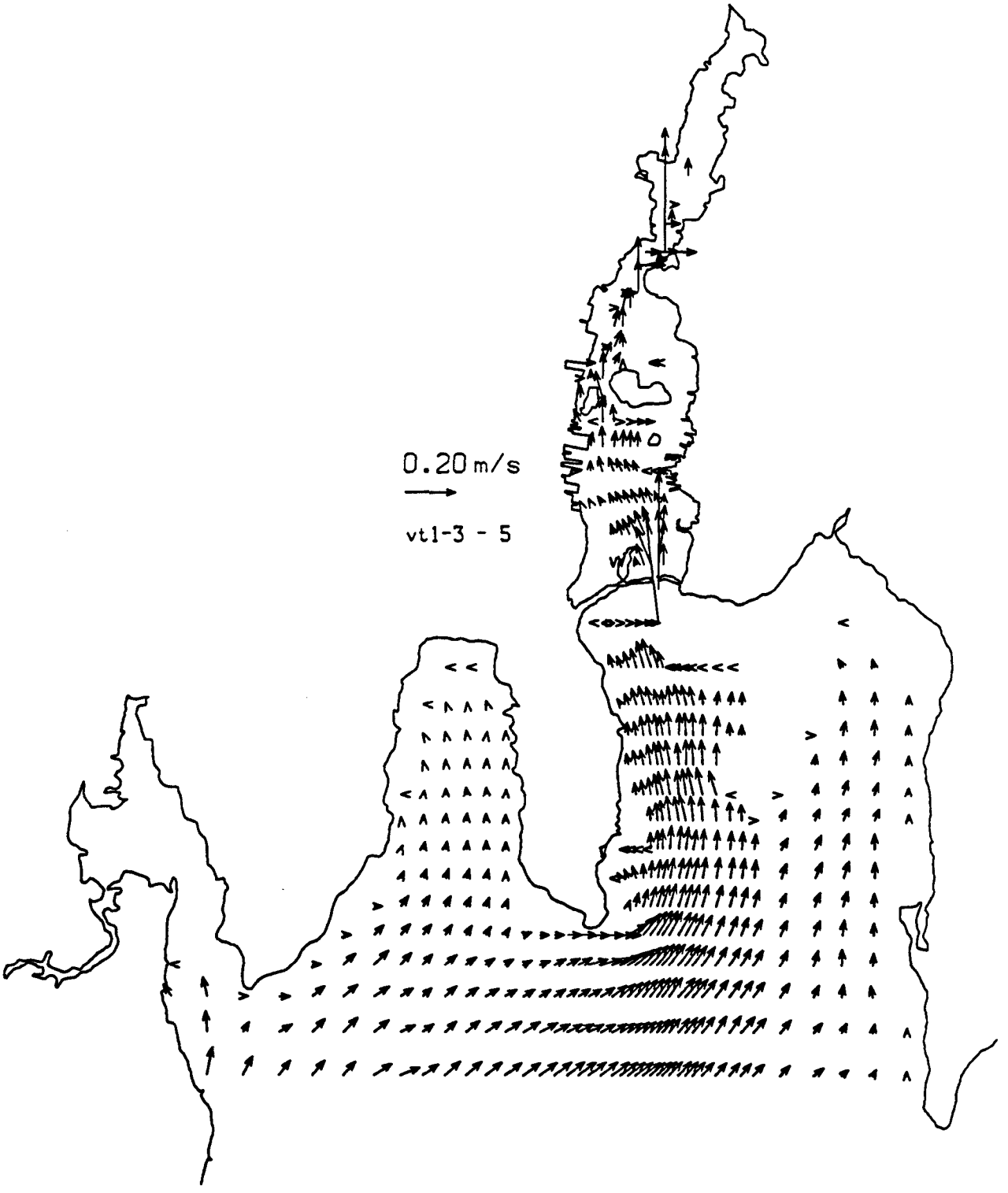

FIGURE 5.35. M_2 TIDE FORCING TEST. VELOCITY VECTORS FOR GRID LAYER 5 AT TIME = 3 h.

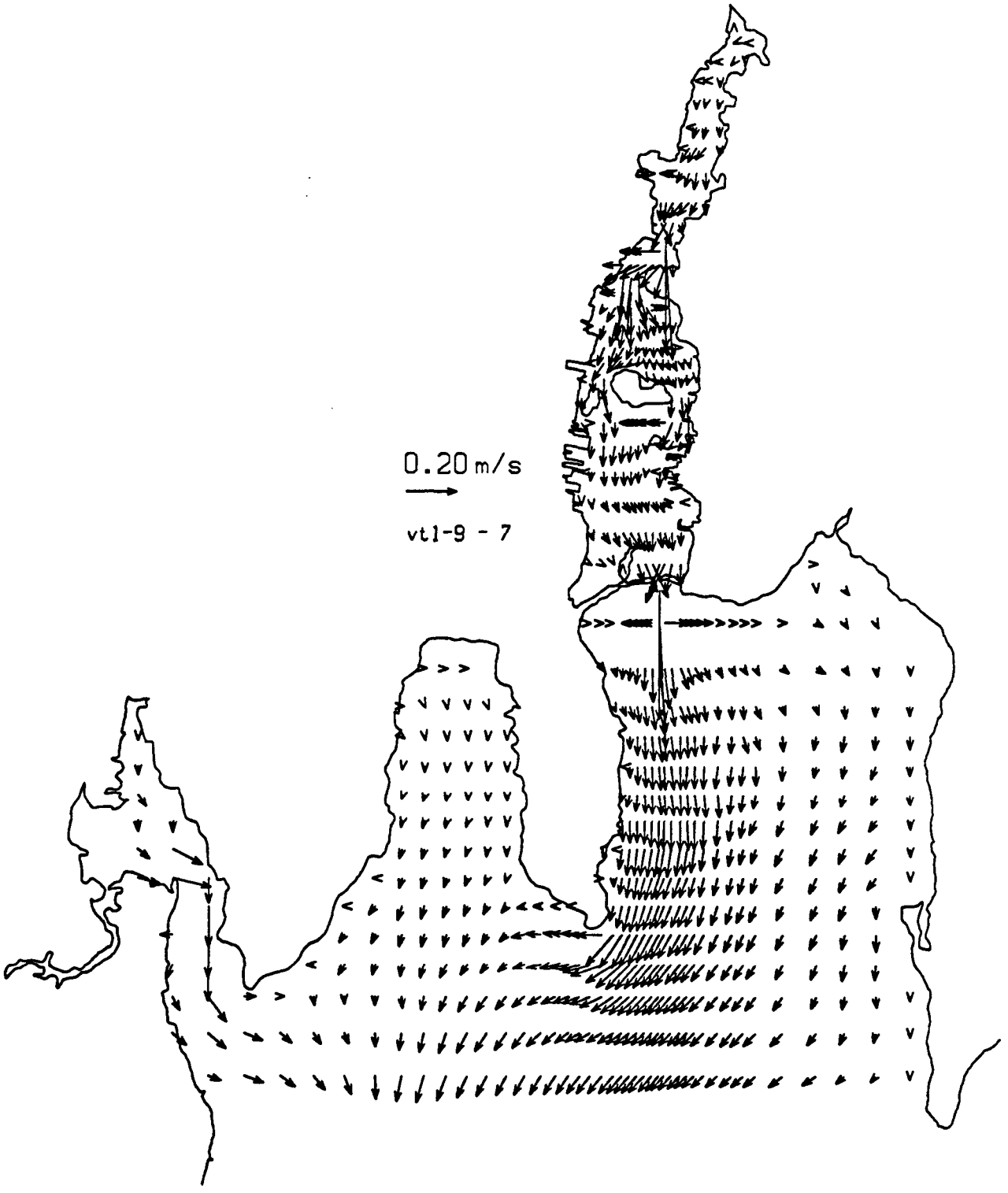

FIGURE 5.36. M_2 TIDE FORCING TEST. VELOCITY VECTORS FOR GRID LAYER 7 AT TIME = 9 h.

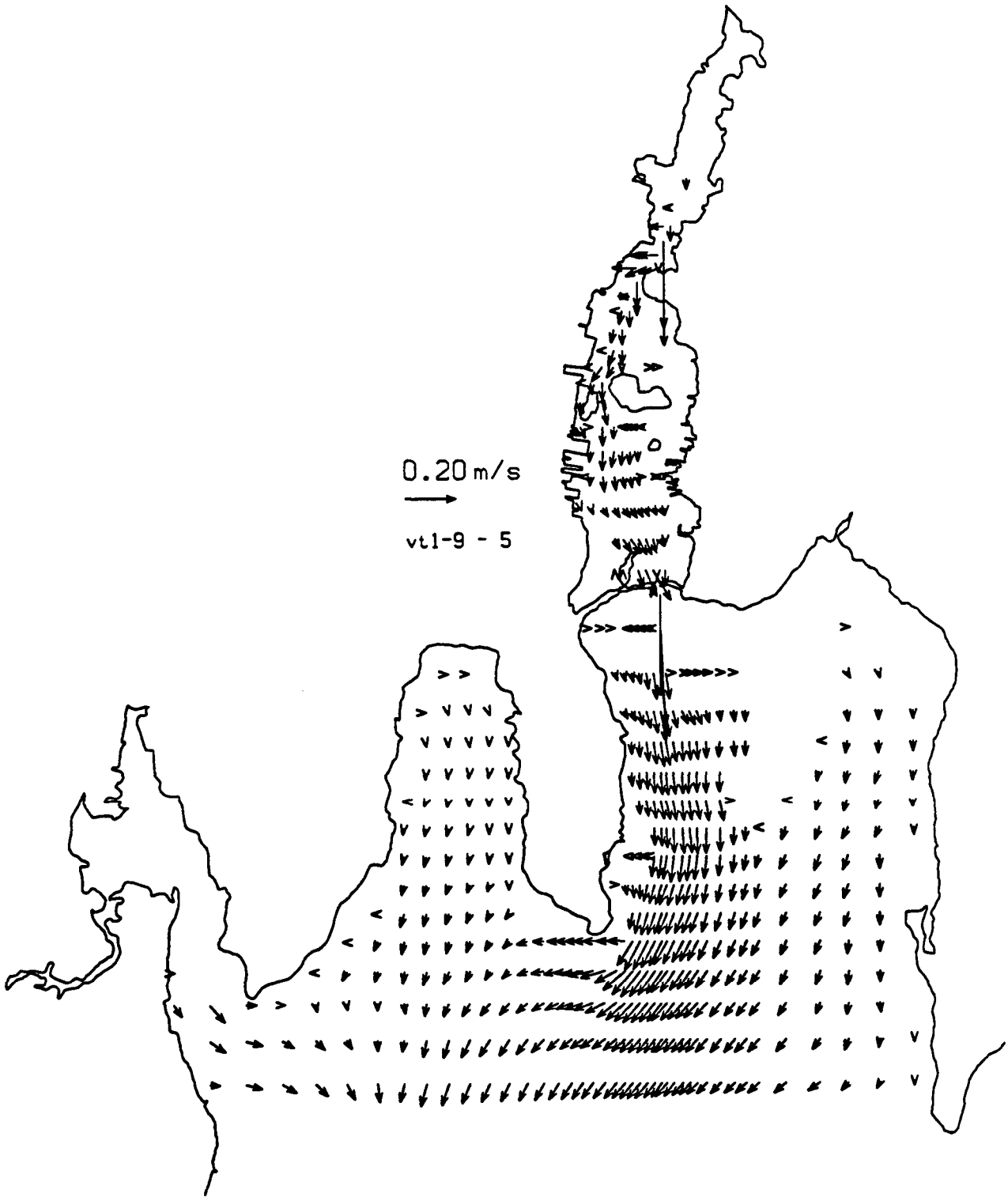

FIGURE 5.37. M_2 TIDE FORCING TEST. VELOCITY VECTORS FOR GRID LAYER 5 AT TIME = 9 h.

E.6, and velocity vector plots in Figures E.7 through E.11 of Appendix E. In general, the computed results for the combined tide- and wind-forcing case are quite similar to the results obtained in the tide-forcing case. The combined wind and tide has a nonzero minimum velocity, and the turning of the velocity vector is slowed by the wind resistance. Flows through the hurricane barrier and the Coggeshall Street Bridge are subject to strong acceleration and are, therefore, relatively unaffected by the addition of the wind component. The results of this test support the conclusion that, for winds of 5 m/s or less, the velocity field in the model is dominated by tidal forcing, although winds may act to produce residual flows.

The time required for the model to reach a quasi-steady state, from a zero velocity initial condition (referred to as the spin-up time), was evaluated by forcing the model with an M_2 tide for three consecutive tidal cycles (37.26 h). In this case, a vertical eddy viscosity of 0.0002 m^2/s and a horizontal eddy viscosity of 2.0 m^2/s were used. The bottom friction coefficient remained as in the previous test cases. The results of the test are shown in the time-series plots (Figures 5.38 through 5.41). These results demonstrate that the model reaches a quasi-steady state very quickly; i.e., the computed tidal height, velocity, and direction are duplicated after the first tidal cycle. In fact, just 4 h of simulation are required for the computed hydrodynamics to spin up from a dead-start condition and become independent of the initial conditions, ignoring any density effects.

The foregoing results qualitatively demonstrate that the model responds correctly to wind- and tide-forcing. The tests indicate that the model is able to simulate the flow field for the topography and bathymetry of the New Bedford Harbor site. Further analysis of the simulated hydrodynamics will be presented with the calibration results in Section 5.6.1.

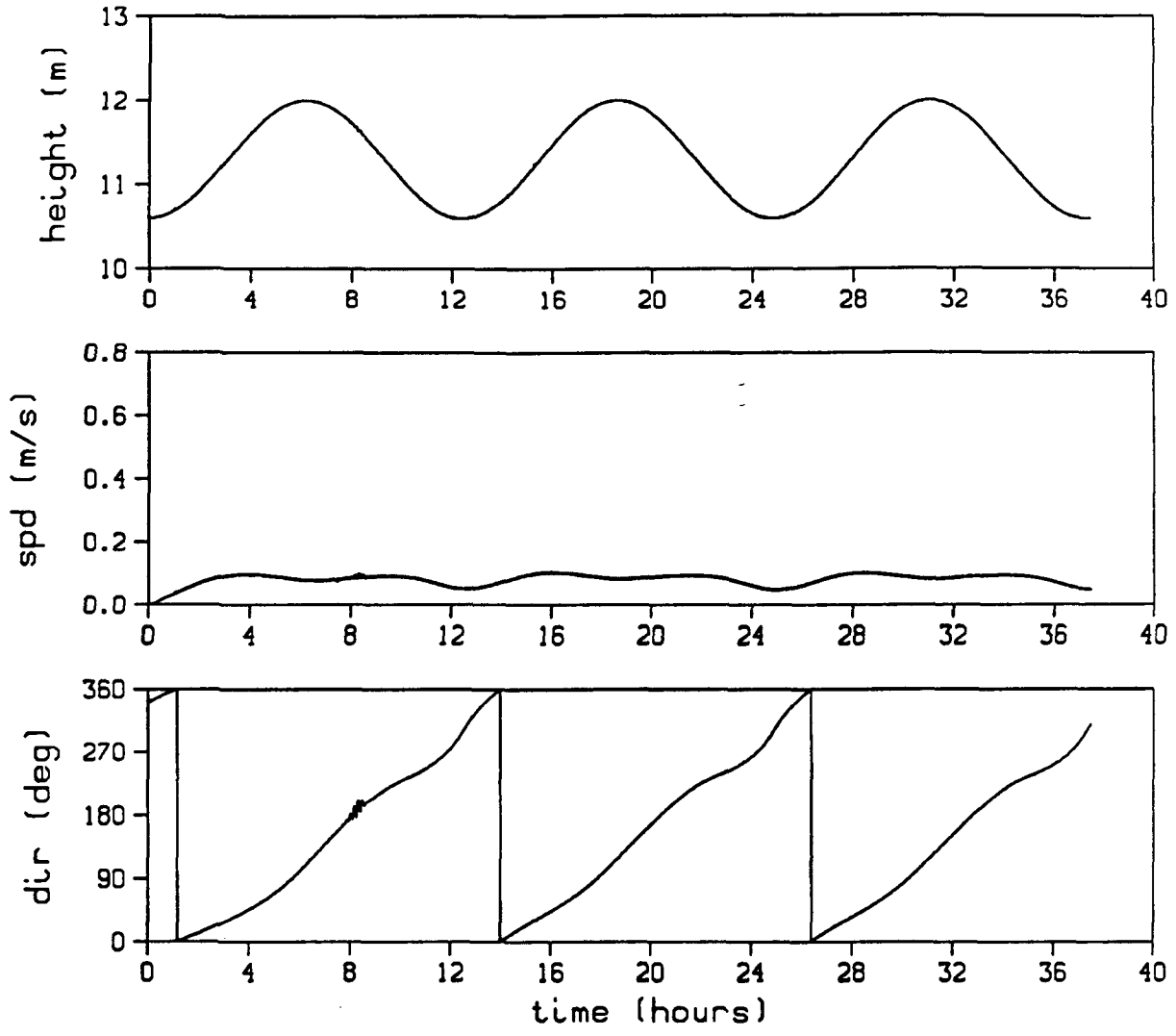

PLOT 1 13.04.06 TUES 23 JAN, 1990 JOB-marshall, ISSCO DISSPLA 10.0

FIGURE 5.38. WATER SURFACE HEIGHT, CURRENT SPEED, AND CURRENT DIRECTION AT TIME-SERIES LOCATION 2 FOR THE QUASI-STEADY STABILIZATION TEST

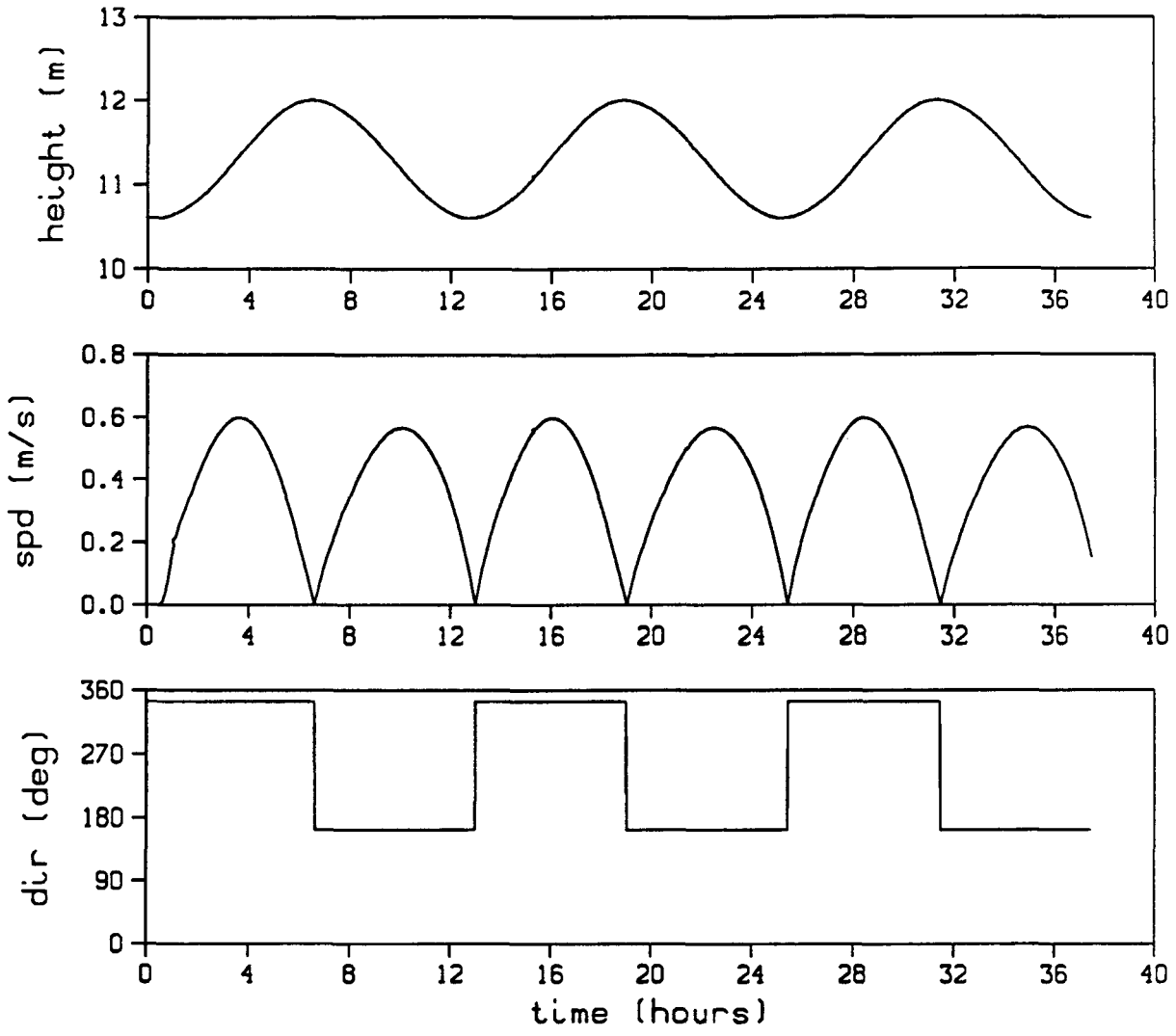

FIGURE 5.39. WATER SURFACE HEIGHT, CURRENT SPEED, AND CURRENT DIRECTION AT TIME-SERIES LOCATION 8 FOR THE QUASI-STEADY STABILIZATION TEST

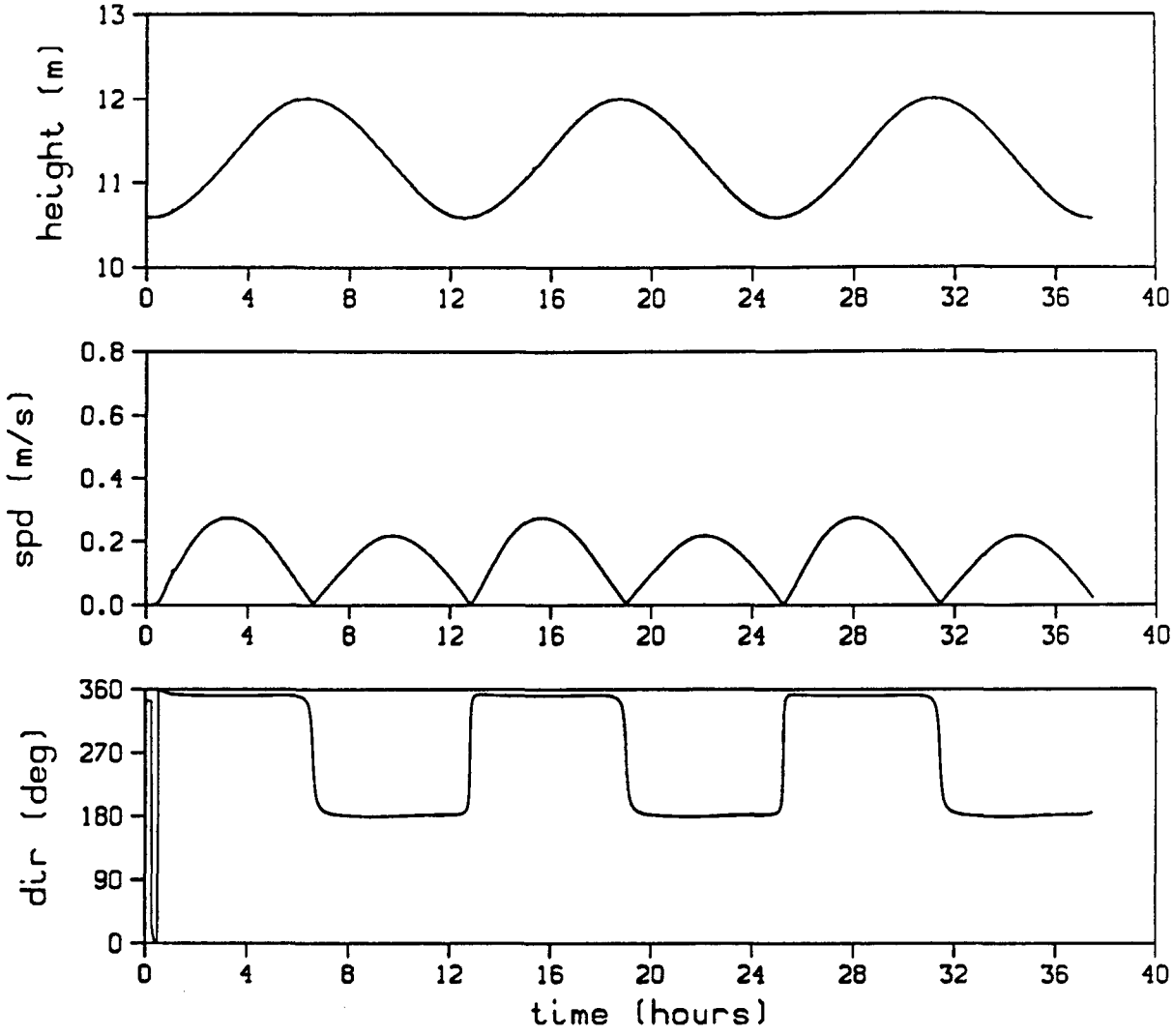

FIGURE 5.40. WATER SURFACE HEIGHT, CURRENT SPEED, AND CURRENT DIRECTION AT TIME-SERIES LOCATION 6 FOR THE QUASI-STEADY STABILIZATION TEST

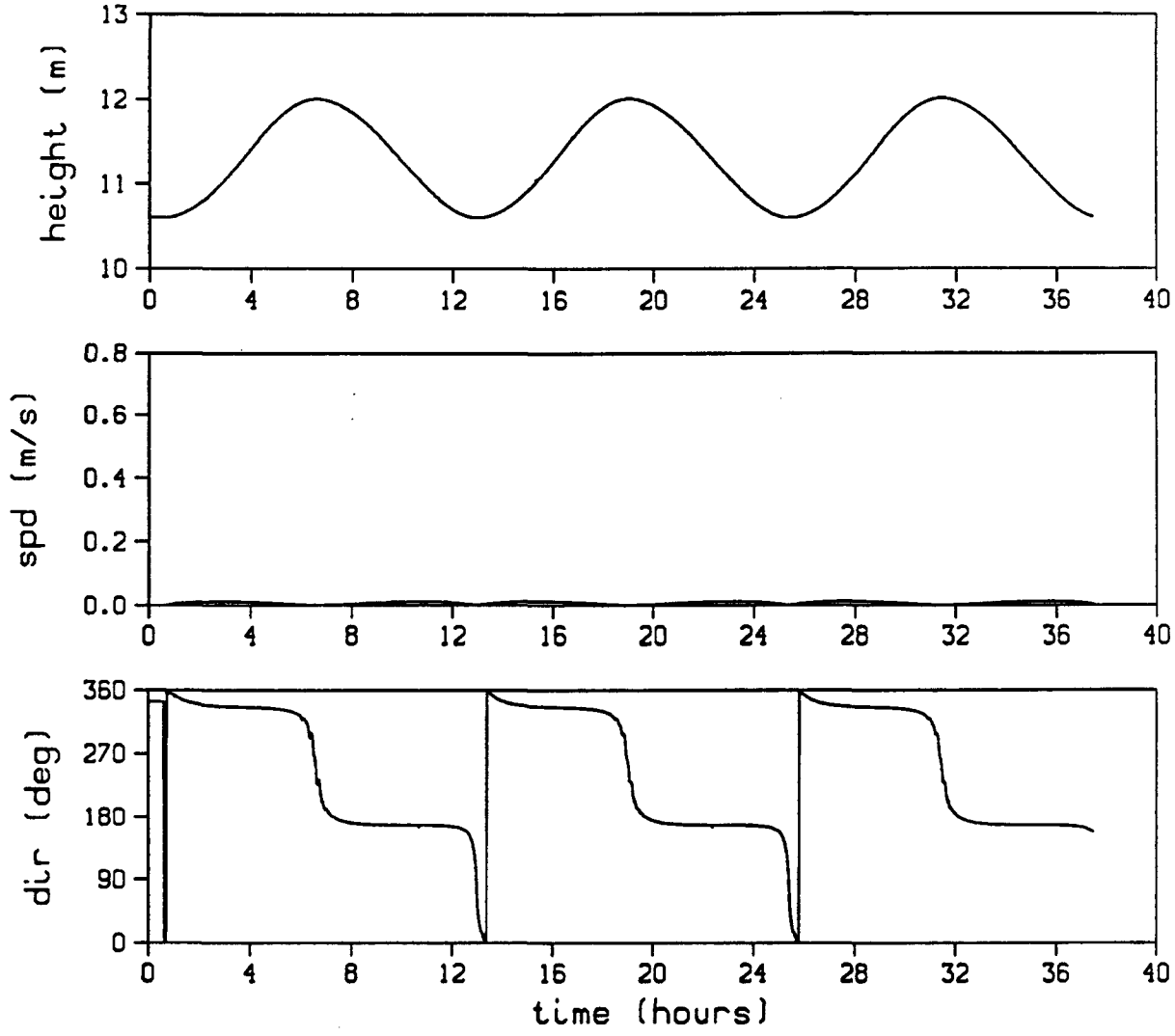

FIGURE 5.41. WATER SURFACE HEIGHT, CURRENT SPEED, AND CURRENT DIRECTION AT TIME-SERIES LOCATION 7 FOR THE QUASI-STEADY STABILIZATION TEST

5.5.3 Tracer Dispersion Test

A constant release of a conservative, neutrally buoyant tracer was simulated to qualitatively assess the capability of the model to calculate dispersion processes in New Bedford Harbor. The release location, mass-flow rate, and duration of the release correspond to those reported by ASA (1987) in their field study of the dispersion of Rhodamine WT dye released near the Aerovox Plant. Because of the long release duration and measurement period following the end of the release--approximately 14 days total--the model was simulated using the decoupled, transport-only mode described in Section 5.3.4.3. Since the decoupled-mode hydrodynamics used in the tracer simulation do not correspond to the actual tide and wind conditions during the ASA (1987) field study, only a qualitative comparison between the computed results and the measurements can be made.

The hydrodynamics used for the tracer simulation are the general-case hydrodynamics, fully described in Section 5.6.2.1. In summary, the general-case hydrodynamics (i.e., velocity field and water surface elevation) result from forcing the model with an M_2 tide and a wind blowing generally toward the north with a speed ranging from 2.5 to 10.0 m/s. The hydrodynamics were computed using the calibrated parameter set (see Section 5.6.1) and the vertical and horizontal eddy viscosities of 0.001 and 1.0 m^2/s, respectively. In this test the hydrodynamics do not include the potential effects of the Acushnet River inflow.

In the test simulation, the tracer was released at a constant rate of 29.1 mg/s into the surface- layer cell (layer 7) nearest to the Aerovox Plant site. The location of the tracer release is at point 1 (Figure 5.42). Tracer was released for a period of 192 h (8 days), then the release was stopped and the calculations were continued for an additional 144 h (6 days), resulting in a total simulation time of 336 h (14 days). The calculations were done using a Schmidt number of 1.0; that is, the turbulent diffusivity of the tracer was assumed to be equal to the eddy viscosities noted above. The initial conditions for the tracer were zero throughout the water column, and a

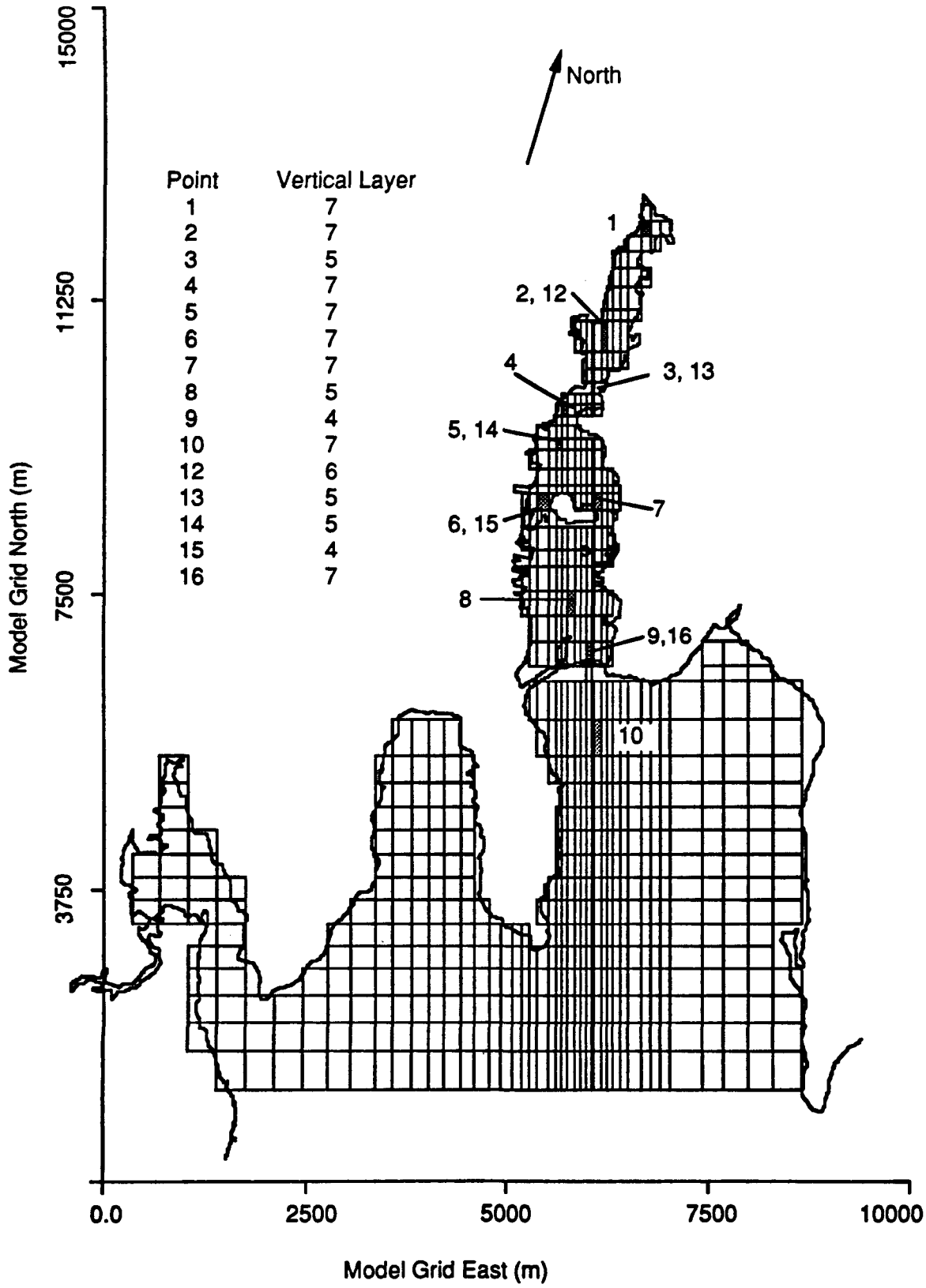

FIGURE 5.42. LOCATION OF THE MODEL TIME-SERIES OUTPUT FOR THE TRACER DISPERSION TEST.

boundary condition of zero dye concentration was maintained at the open boundary.

The results of the tracer test were plotted as time series at discrete locations and as contour plots of the concentration distribution at specific times. The horizontal and vertical locations of the time-series output points on the model grid are shown in Figure 5.42. Representative results are shown in this section, additional results are given in Figure E.89 through E.114 of Appendix E. The tracer disperses rapidly in the lateral and longitudinal directions in the upper estuary. Six hours after the start of the release, the concentration at the release point exceeds 5 ppb and has spread across the upper estuary. After approximately 48 h, the tracer has reached the Coggeshall Street Bridge and begins to move into the lower harbor. The time-series results shown in Figure 5.43 indicate that the tracer arrives at the hurricane barrier in approximately 100 h. The time-series plots also show that the concentrations oscillate as tidal currents advect higher tracer concentrations down the estuary during the ebb tide and, conversely, that water with lower tracer concentration is advected up the estuary on the flood tide. The tracer distribution at 192 h, the end point of the release, is shown in Figure 5.5.3-16. The concentration distribution is fairly uniform across the upper estuary, but the lower harbor is not laterally mixed; higher concentrations occur in the deeper water on the west side of Popes Island. Overall, the tracer concentration decreases by approximately two orders of magnitude from the release point to the hurricane barrier. The concentration distribution has not reached steady state by the time the release has stopped; the time-series results clearly show that concentrations, especially in the lower harbor, are still increasing with time. The contour plots and time-series results at various locations, typified in Figures 5.44 and 5.45, show that the tracer is well mixed vertically in the water column throughout the upper estuary and lower harbor. Following the cessation of the tracer release, concentrations in the upper estuary decrease slowly over the next 6 days of the simulation. By extrapolating the rate of decrease at location 2, approximately 15 more days will be required for the concentrations in the system to fall to negligible levels. Concentrations in the lower harbor

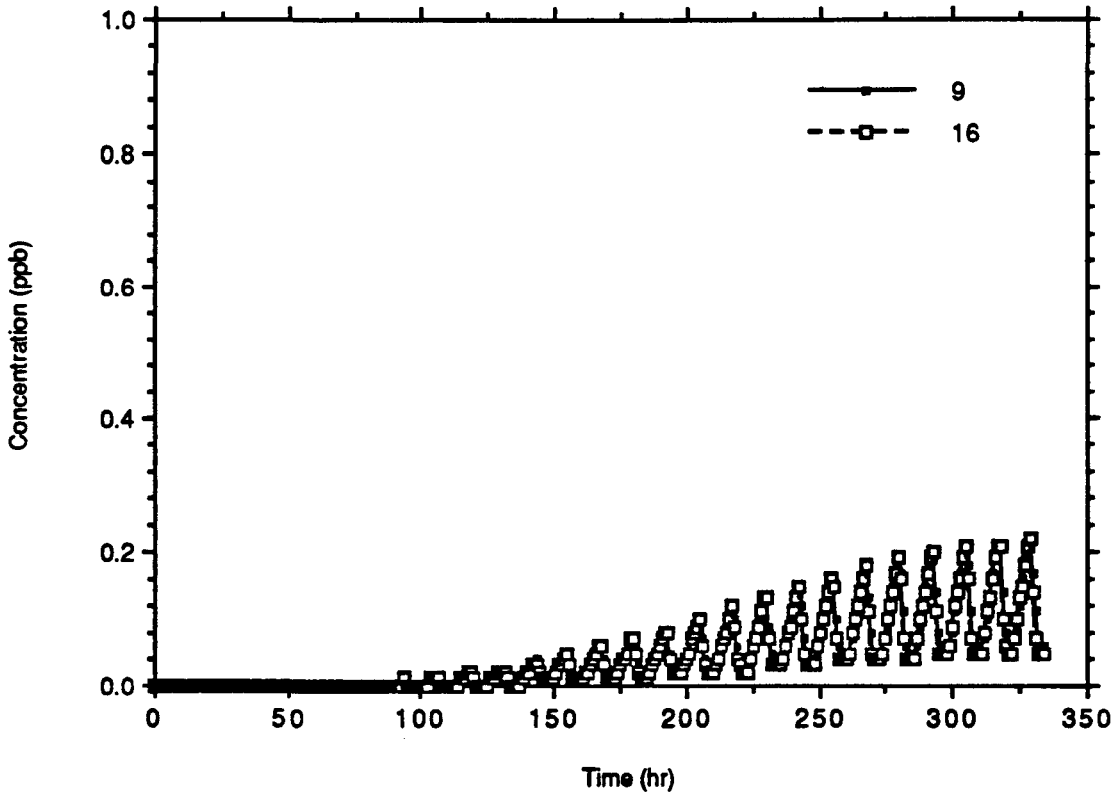

FIGURE 5.43. COMPUTED CONCENTRATION TIME-SERIES AT LOCATIONS 9 AND 16. LOCATION 16 IS IN LAYER 7 AND LOCATION 9 IS IN LAYER 4.

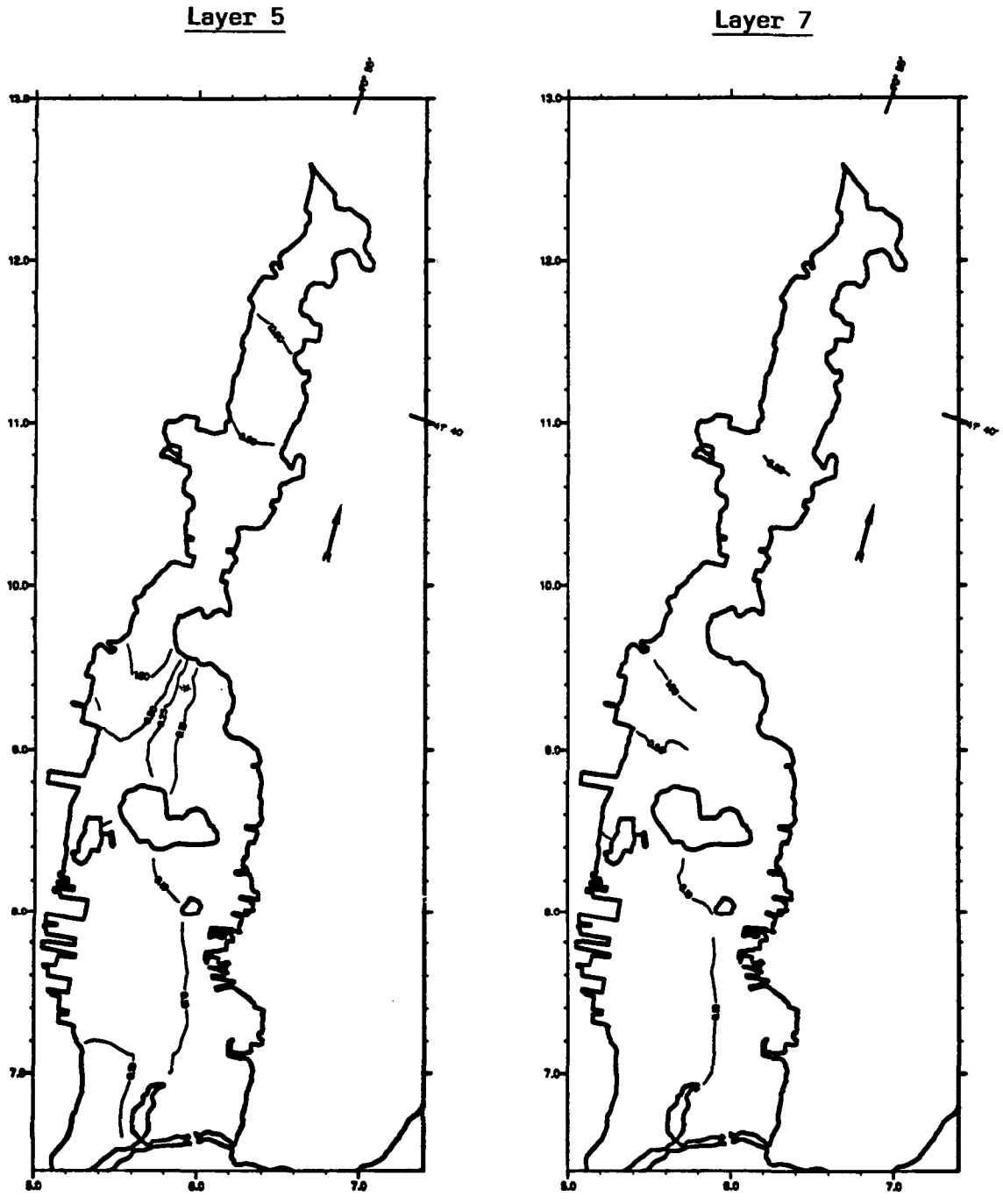

FIGURE 5.44. CONCENTRATION (ppb) DISTRIBUTION IN LAYERS 5 AND 7 AT TIME = 192 h AFTER START OF RELEASE. THE TRACER RELEASE HAS STOPPED AT TIME = 192 h.

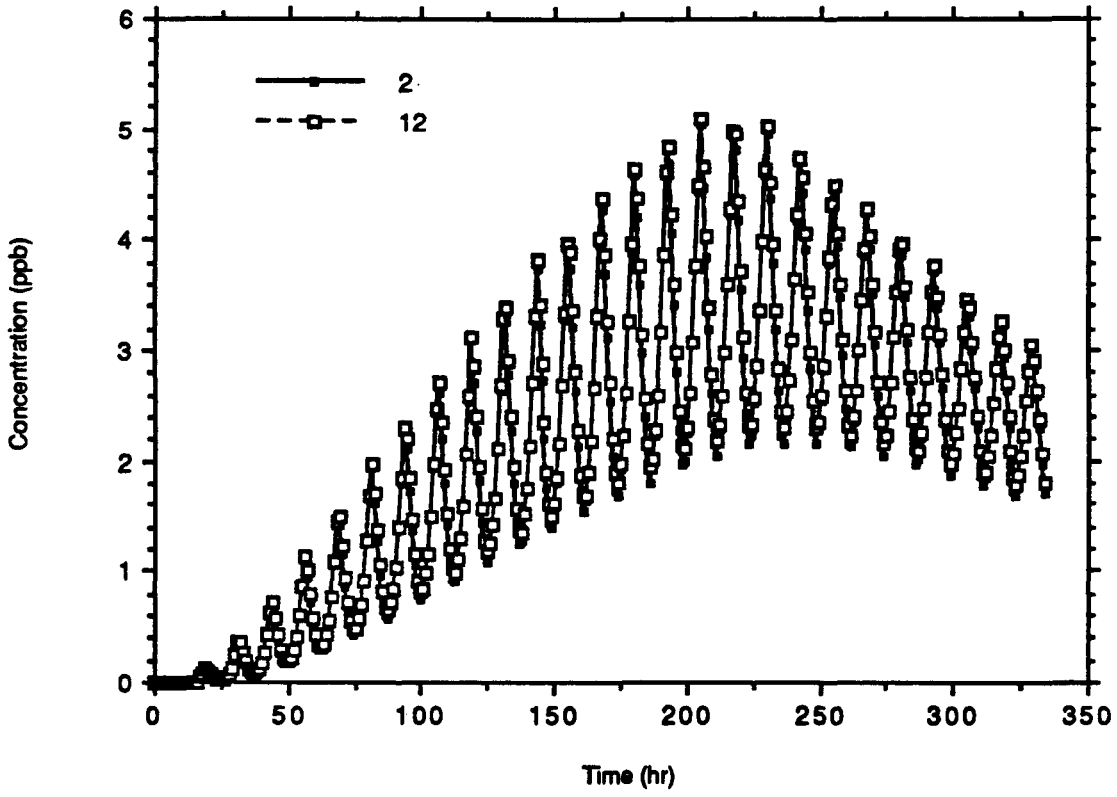

FIGURE 5.45. COMPUTED CONCENTRATION TIME-SERIES AT LOCATIONS 2 AND 12. LOCATION 2 IS IN LAYER 7 AND LOCATION 12 IS IN LAYER 5.

continue to increase after the release is stopped because higher-concentration water from the upper estuary is advected down the estuary.

As noted above, a detailed comparison of the model results to the ASA (1987) field measurements was not completed, because the hydrodynamics used in the tracer simulations were not calculated using the tide- and wind-conditions present during the field study. Nevertheless, the main features of the simulations and measurements can be qualitatively compared. The ASA results show that dye reached the hurricane barrier after 2 days and that a steady state was attained after 6 days. The computations showed the tracer arriving at the hurricane barrier after 4 days, and a steady state was approaced after 14 days. In addition, the ASA measurements show that concentrations decrease rapidly, reaching a value of approximately 0.1 ppb throughout the system 6 days after the dye release is stopped where as the model results suggest that up to 15 days are required. A contributing factor to these differences is that the tracer concentration in the computations is vertically mixed while the field measurements show that the dye maintains a definite vertical structure, with the highest concentrations occurring generally in the upper 2 m of the water column. Vertical mixing during the field measurements may have been inhibited by strong density stratification caused by freshwater runoff during two precipitation events that occurred during the study. Because of the coarse grid resolution in the vertical direction (see Figure 5.16), the computations will tend to overestimate the amount of vertical mixing, especially since the surface layer is a minimum of 1 m thick. Another important difference was that the measurements showed strong lateral mixing in the lower harbor, dye concentrations being similar on the east and west sides of Popes Island, while the computations show weak lateral mixing, with concentrations highest on the west side of Popes Island. Because the area on the east side of Popes Island is shallow, these variations are probably caused by differences in the circulation pattern resulting from differences in the wind field. Although computed and measured concentration behavior differ significantly in many ways, the discrepancies are most likely the result of using generic hydrodynamics in the calculations and the possible influences of the unmodeled river runoff event.

5.6 MODEL CALIBRATION

Application of the TEMPEST/FLESCOT model to the New Bedford Harbor site requires that the model, namely the key parameters in the governing equations, be calibrated such that the simulation results represent site-specific conditions. Calibration to measured conditions at the site is required because of the approximations inherent in a numerical model, especially one that attempts to model a phenomenon, such as sediment transport, for which the fundamental physics governing the process are not well understood. For New Bedford Harbor, the model was calibrated for two main classes of processes: hydrodynamics and sediment/contaminant transport. Hydrodynamics were calibrated first, because they are independent of the sediment/contaminant transport calculations--bed level and friction factor changes resulting from sediment transport are assumed to have negligible effects on the hydrodynamics. Following the calibration of the hydrodynamics, the sediment/contaminant transport processes were calibrated, using the decoupled mode of operation driven by previously computed and stored velocity and water level fields. In each case, the model results are compared to available field data.

5.6.1 Hydrodynamics

Velocities and water surface elevation, the model hydrodynamics, were calibrated by adjusting the parameters in the model to produce the most reasonable agreement with the field measurements available. During the calibration simulations the model was driven by tidal elevations measured near the open boundary and wind velocity measured at the hurricane barrier. The simulation results were then compared to the current-meter and tide-gage data gathered during the same period. The simulation results are also compared to other sets of field measurements collected during different tide and wind conditions representative of general conditions at the site.

As was noted in Section 5.2, New Bedford Harbor is a weakly stratified estuary, with currents dominated by wind- and tide-forcing (Geyer and Dragos,

1988), so that the influence of density-driven flow should be minimal. For this reason, and because data to perform a more quantitative calibration were lacking, the temperature and salinity fields were not simulated. The density field was accounted for by specifying, in a diagnostic manner, a temperature and salinity distribution measured from a field survey. Inflow of freshwater from the Acushnet River was not incorporated, because of its low average annual flow rate and the observations of weak stratification in the upper estuary.

The model hydrodynamics were calibrated for two 24-h periods: 0330 July 23 to 0330 July 24, 1986 and 0900 July 31 to 0900 August 1, 1986. In each case, the model was forced by tidal-elevation data near the open boundary, shown in Figure 5.46, measured by Geyer and Grant (1986). Wind forcing was uniformly applied over the model grid using wind-speed and -direction data collected at the hurricane barrier by the U.S. Army Corps of Engineers, New England Division. These tide and wind conditions are shown in Figures 5.47 and 5.48. The tide range is approximately 1.4 m and 0.8 m for the July 23 and July 31 cases, respectively. During the July 23 simulation the wind speed varied from 2 to 7 m/s, and the direction was generally toward the west. For the first 12 h of the July 31 simulation the wind speed was decreasing from 6 to 1 m/s toward the northeast. In the second 12 h the speed remained fairly constant at 1 m/s but shifted toward the northwest.

For each simulation, an initial uniform water surface elevation (10.6 m) and zero-velocity conditions, referred to as dead-start conditions, were assigned throughout the model domain. This should not adversely affect the calibration simulations because, as was demonstrated in Section 5.5.2, the simulated hydrodynamics become independent of the dead-start conditions very quickly. As noted above, a density field was assigned by interpolating onto the model grid the synoptic temperature and salinity data collected by Geyer and Grant (1986).

The model calibration parameters for this study were the following: vertical eddy viscosity, horizontal eddy viscosity, bottom friction coefficient, and

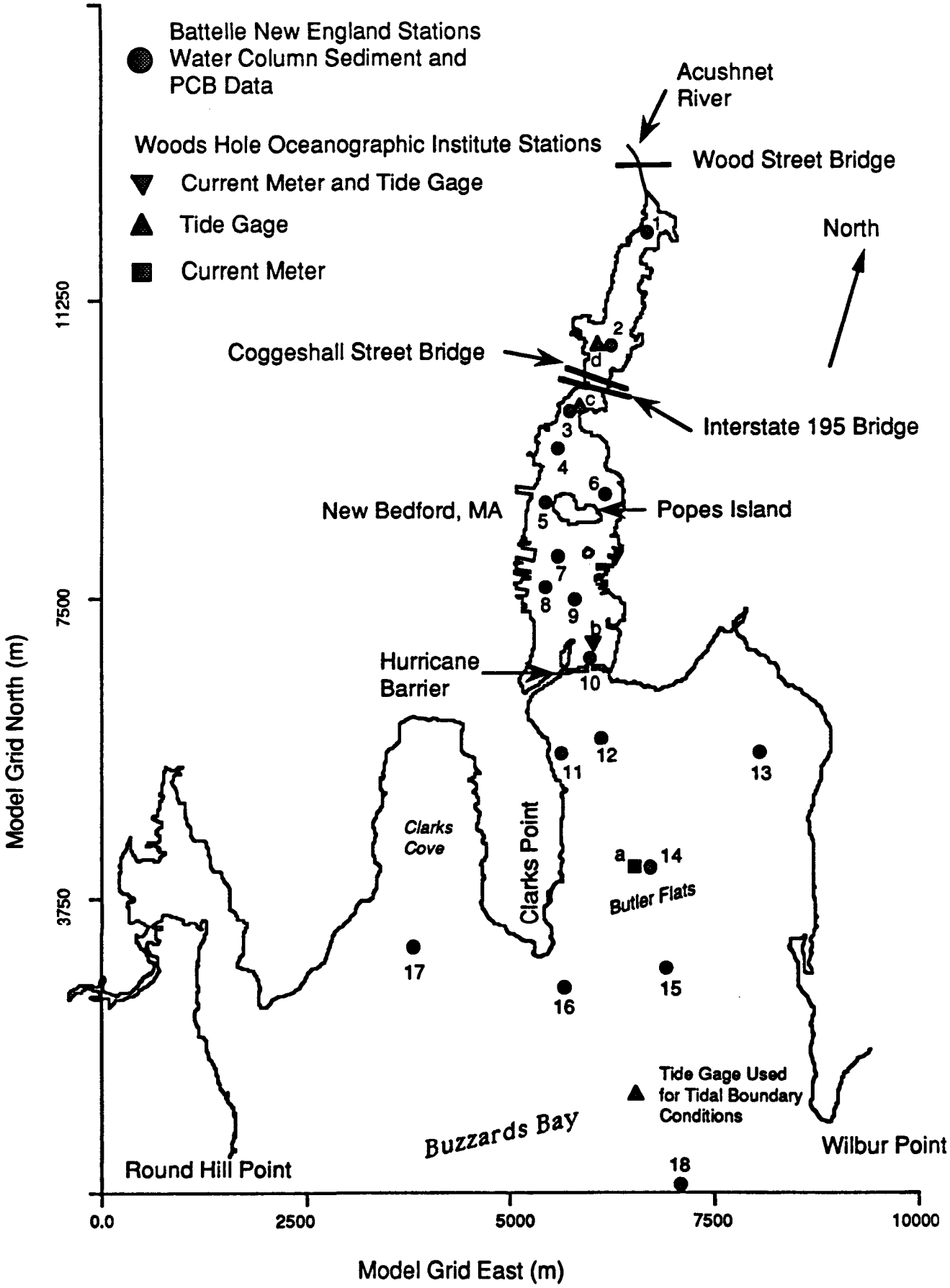

FIGURE 5.46. LOCATIONS OF FIELD MEASUREMENT STATIONS

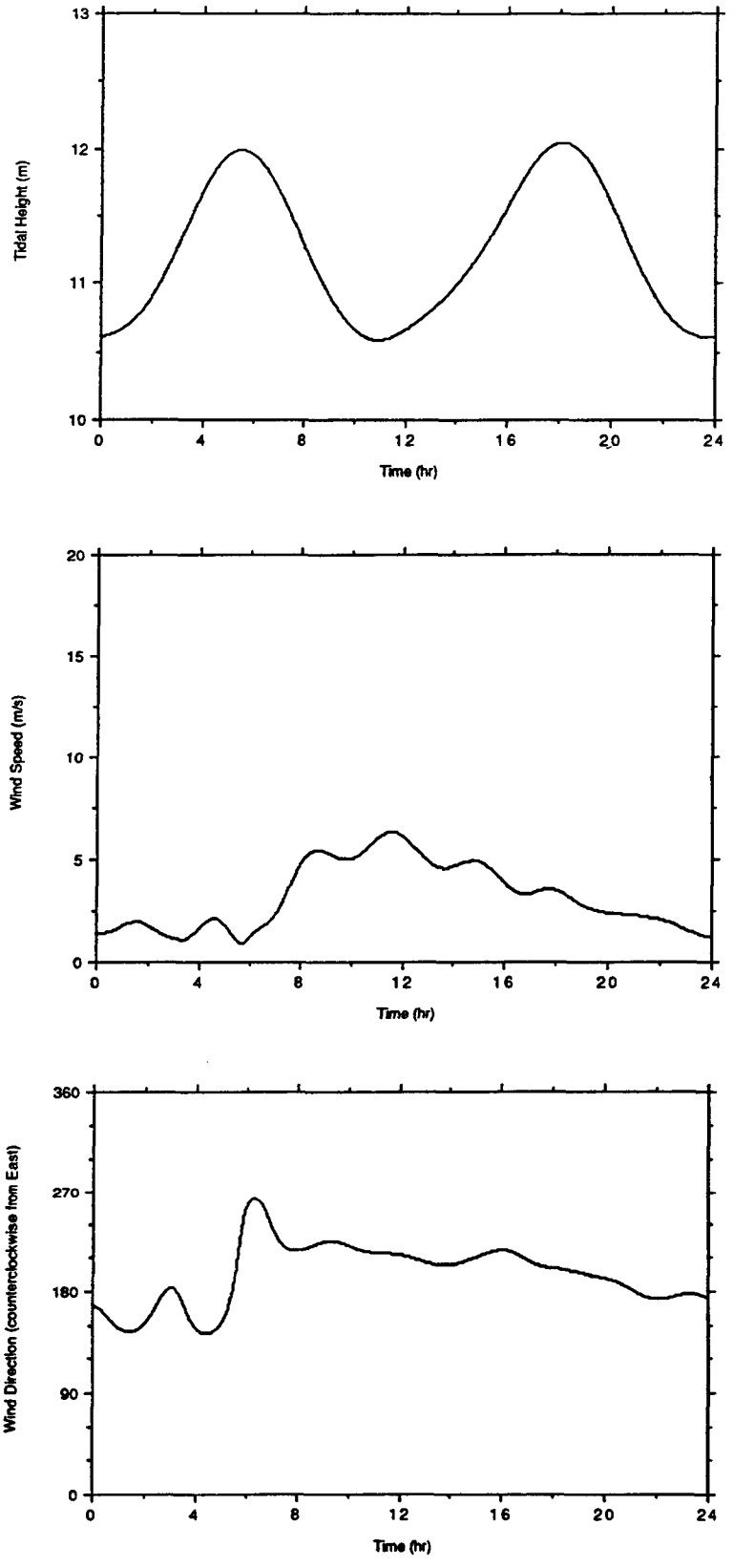

FIGURE 5.47. TIDAL HEIGHT (OPEN BOUNDARY), WIND SPEED, AND WIND DIRECTION IMPOSED FOR THE JULY 23, 1986 CALIBRATION CASE

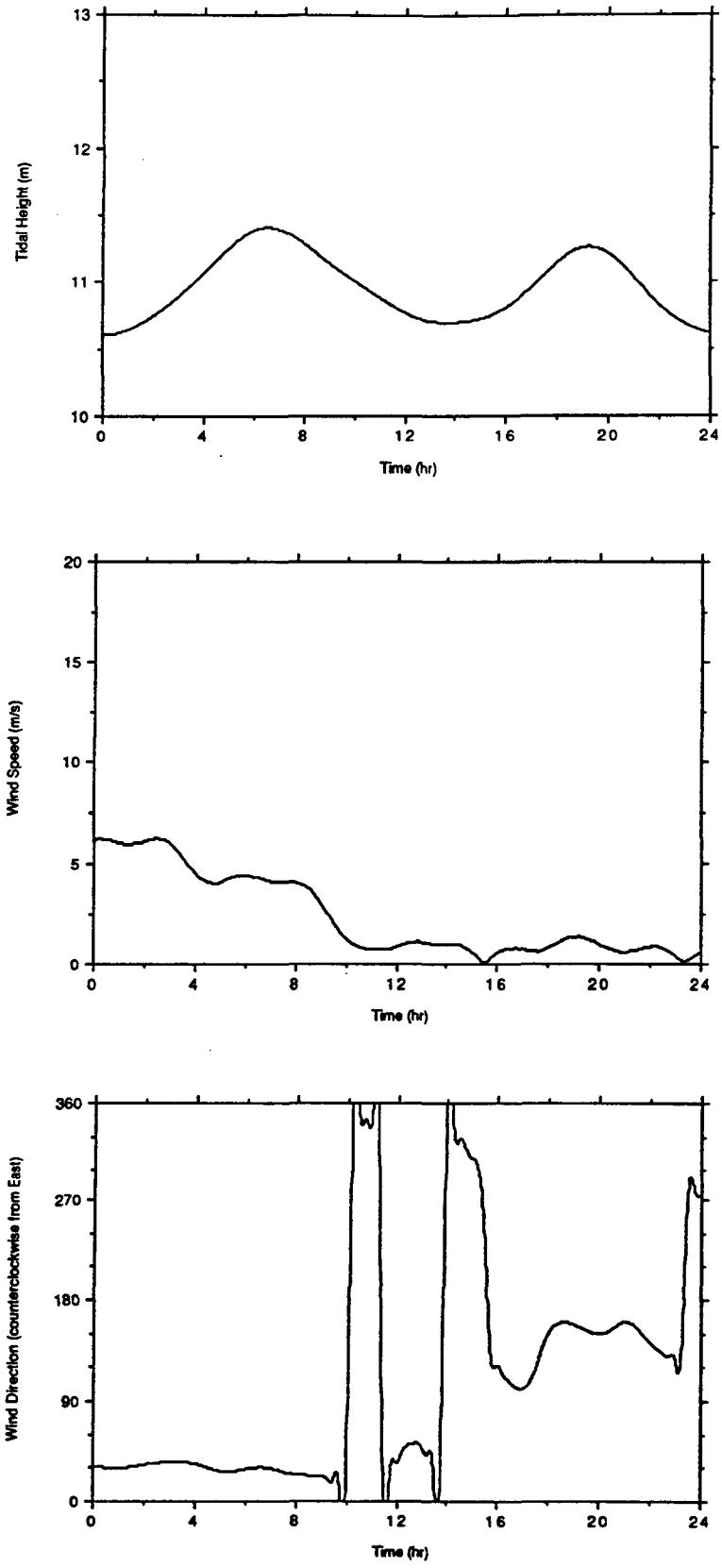

FIGURE 5.48. TIDAL HEIGHT (OPEN BOUNDARY), WIND SPEED, AND WIND DIRECTION IMPOSED FOR THE JULY 31, 1986 CALIBRATION CASE

form drag coefficient at flow constrictions. Coriolis forces were included in the simulations. Although the wind stress coefficient could be viewed as an additional calibration parameter, the following correlation proposed by Wu (1982) was used without modification:

$$C_d = (0.8 + 0.065\ W) \times 10^{-3}.$$

This wind drag coefficient is used to compute the wind shear stress discussed in Section 5.3.2.2.

The most sensitive hydrodynamic parameter was found to be the vertical eddy viscosity coefficient. Several values of the vertical eddy viscosity were tested, from 0.0001 to 0.01 m^2/s. A final value of 0.001 m^2/s was selected based on a comparison of the computed tidal heights and current velocities with the field measurements. This value also ensured that the surface-layer velocity would be no more than 2 to 3% of the wind speed in tests of wind forcing only (Section 5.5.2). The model results were not sensitive to the value of the horizontal eddy viscosity, which was varied between 0.01 and 10 m^2/s. A final value of 1.0 m^2/s was chosen.

The model results were not sensitive to the bottom friction factor, which was varied from 0.0005 to 0.01. Therefore, the bottom friction coefficient for the Buzzards Bay area recommended by Graber (1987), 0.0026, was adopted. This value is in the range of a large number of field observations reported by Sternberg (1972). The wave-enhanced bottom friction model was not used in the hydrodynamics calibration simulations.

Form drag, assigned similarly to wind- and bottom-friction, must be applied at the hurricane barrier and Coggeshall Street Bridge constrictions. Additional flow resistance must be introduced, because these constrictions are represented in the model by single grid cells. Form drag coefficients of 2.0 and 0.5 were assigned at hurricane barrier and Coggeshall Street Bridge, respectively. Using these form drag coefficients yielded nearly uniform vertical-velocity profiles, typical of flows accelerated through constrictions.

The results of the model calibration simulations using the final set of parameters are compared with the field measurements reported by Geyer and Grant (1986). The locations of the current-meter and tide-gage stations are shown in Figure 5.46. The field instruments were deployed approximately 1 m above the bottom. The number of measurement stations is limited, especially for velocity data. The computed velocities and water surface heights are compared with the measured values in Figures 5.49 through 5.56. In all cases, the computed water surface height agrees well with the measurements. Despite the number of constrictions within the harbor, both the model and the field data show that very little damping and phase shifting of the tidal wave occurs. These results are in agreement with the findings of other investigators (e.g., Teeter 1988). Velocity magnitudes and directions near Butler Flats, at Location a, are in fair agreement with the measurements (Figures 5.49 and 5.53). The computed current rotates clockwise, as do the data, but the timing of the direction changes can differ by as much as 2 h. The agreement of the computed and measured velocity at Location b is not nearly as good (Figures 5.50 and 5.54). Some of the discrepancies are the result of the coarse grid resolution at the location of this current meter. Maximum differences in the current speed are approximately 20 cm/s. The poor agreement in the current direction is caused primarily by the grid configuration, which only allows the flow to move in a grid-north or -south direction.

Computed time-series results for the calibration simulations are available at a number of different locations on the model grid. The horizontal and vertical position of the time-series output is shown in Figure 5.57, and the computed results at representative locations in Figures 5.58 through 5.65. The computed results at the other locations are shown in Figures E.131 through E.162 of Appendix E. The time-series results at locations 1 and 2 should be viewed with caution, because these locations are on the open boundary. Vector plots of the velocity field for grid layers 7 and 5 are shown for each case at one selected time in Figures 5.66 through 5.69. It should be noted that the

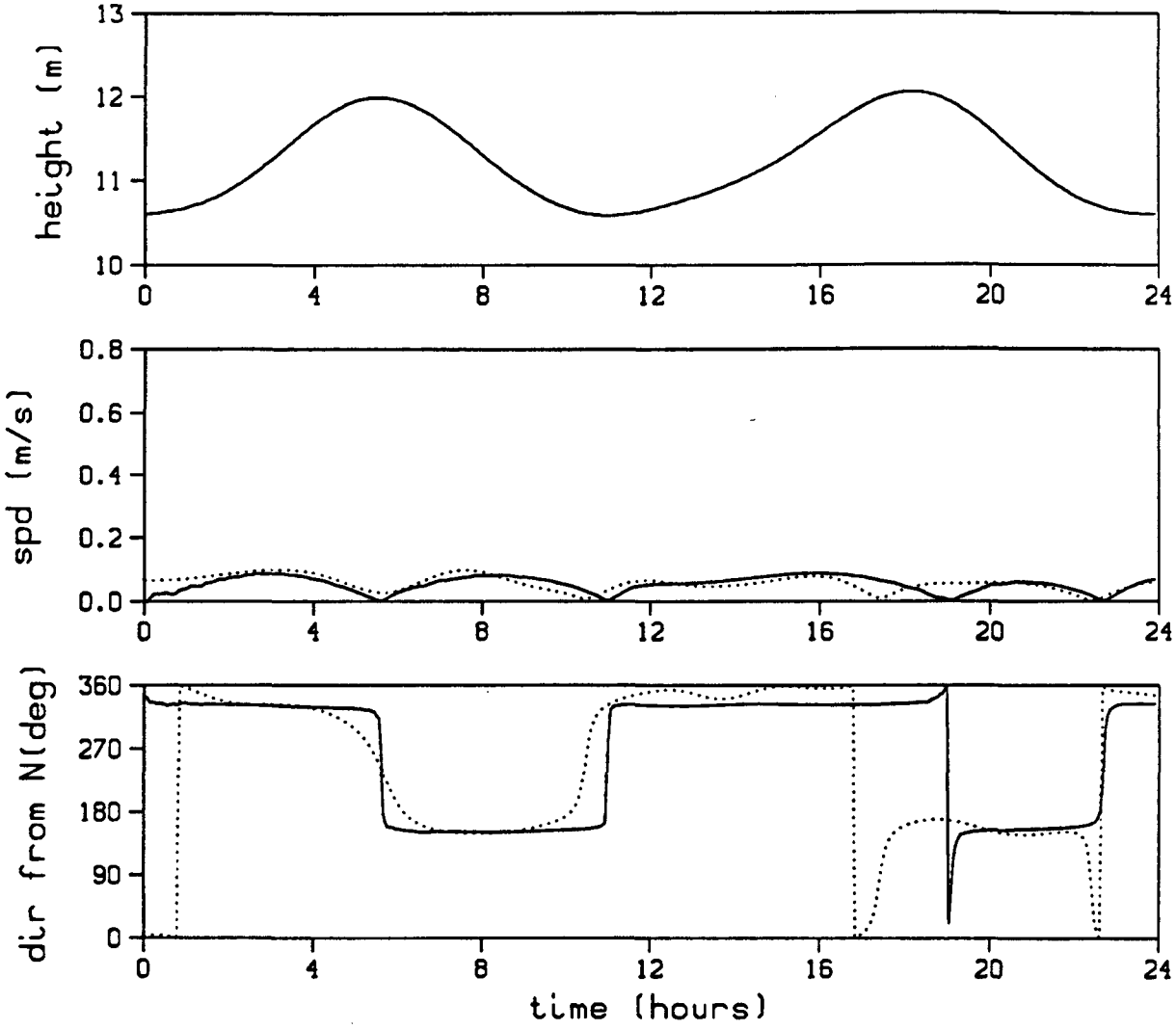

FIGURE 5.49. WATER SURFACE HEIGTH, CURRENT SPEED, AND CURRENT DIRECTION AT WOODS HOLE OCEANOGRAPHIC INSTITUTE (WHOI) STATION A FOR THE JULY 23, 1986 CALIBRATION CASE. (——) = COMPUTED AND (.....) = MEASURED BY WHOI.

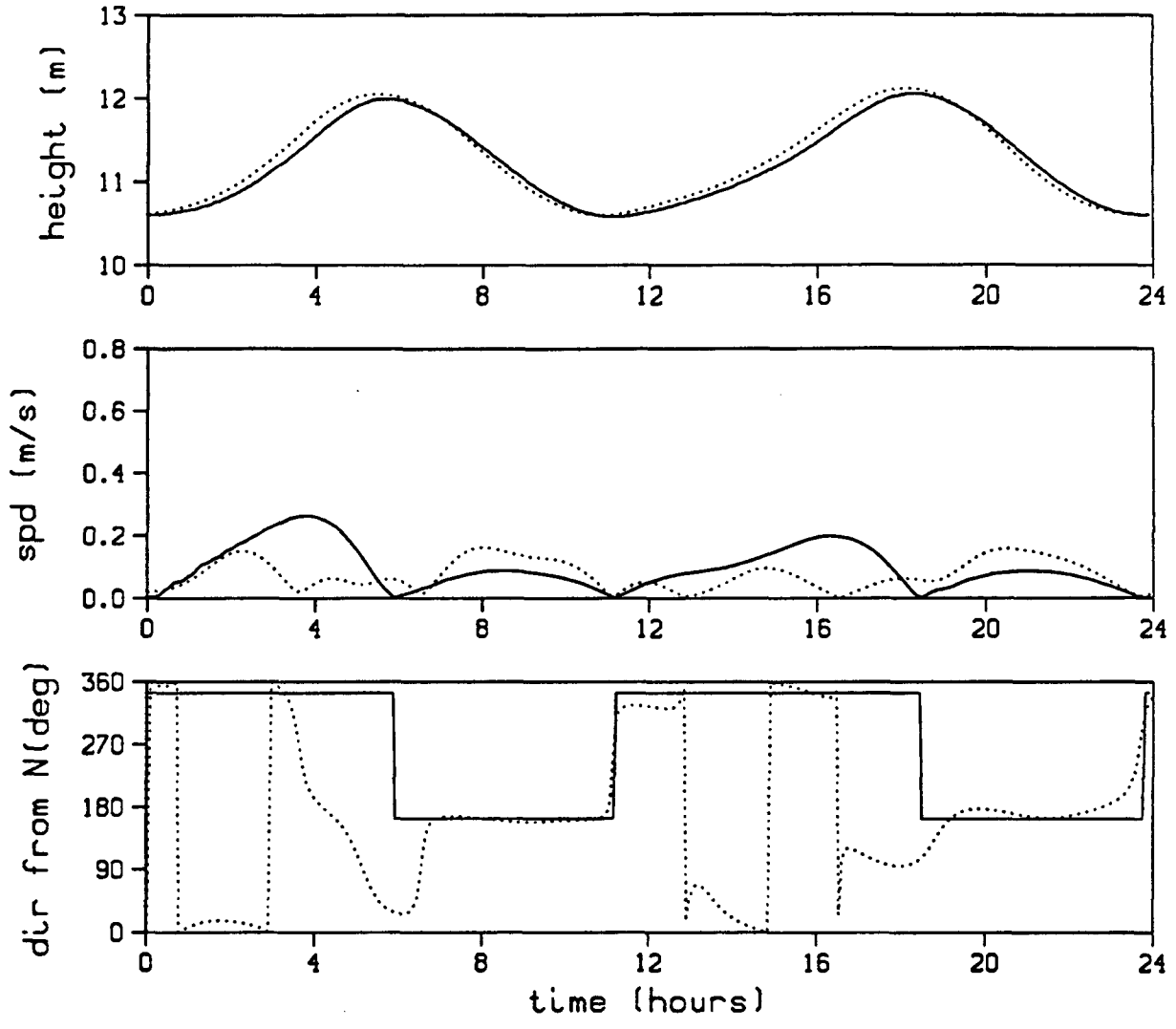

FIGURE 5.50. WATER SURFACE HEIGHT, CURRENT SPEED, AND CURRENT DIRECTION AT WOODS HOLE OCEANOGRAPHIC INSTITUTE (WHOI) STATION B FOR THE JULY 23, 1986 CALIBRATION CASE. (——) = COMPUTED AND (.....) = MEASURED BY WHOI.

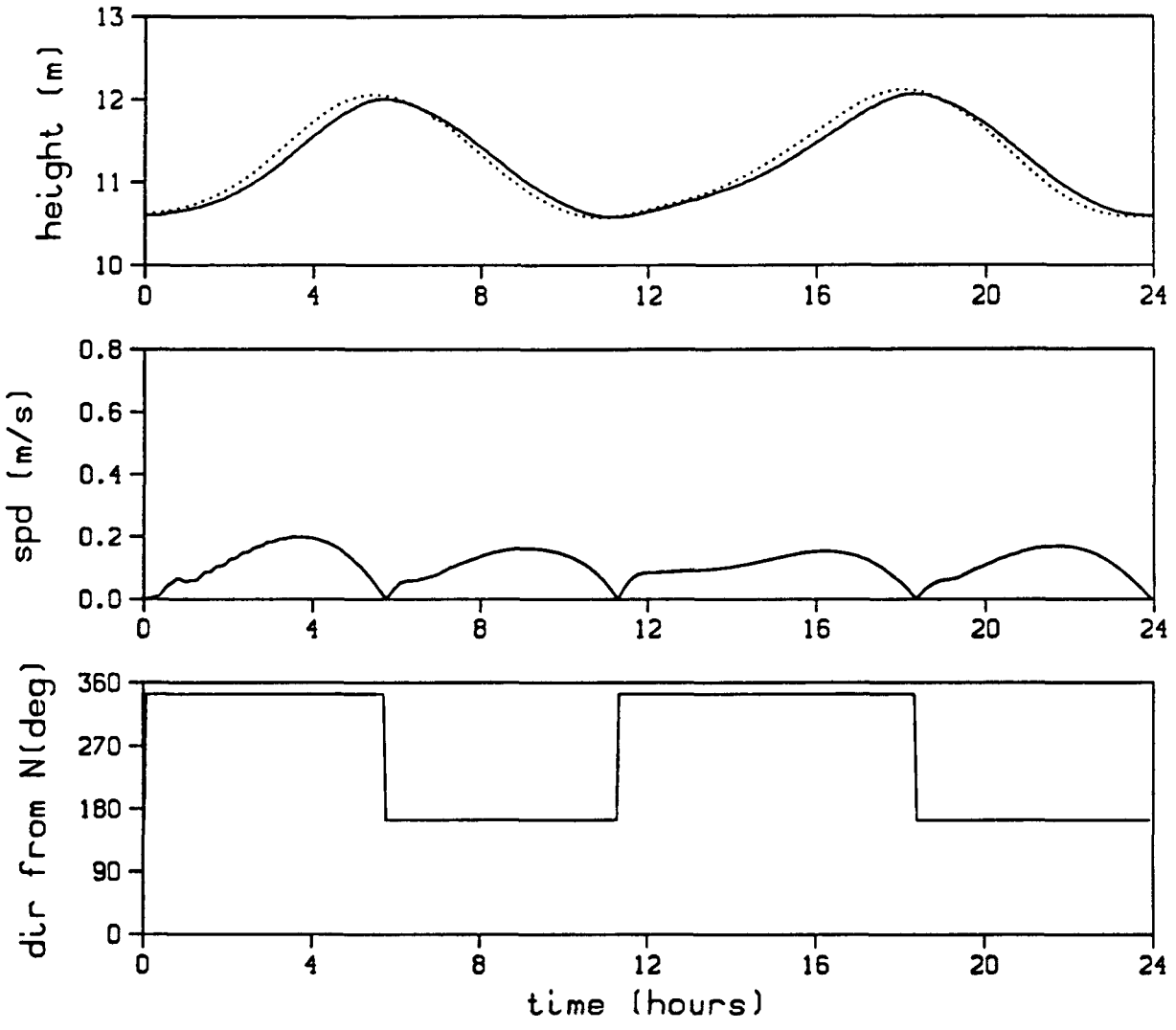

FIGURE 5.51. WATER SURFACE HEIGHT, CURRENT SPEED, AND CURRENT DIRECTION AT WOODS HOLE OCEANOGRAPHIC INSTITUTE (WHOI) STATION C FOR THE JULY 23, 1986 CALIBRATION CASE. (——) = COMPUTED AND (.....) = MEASURED BY WHOI.

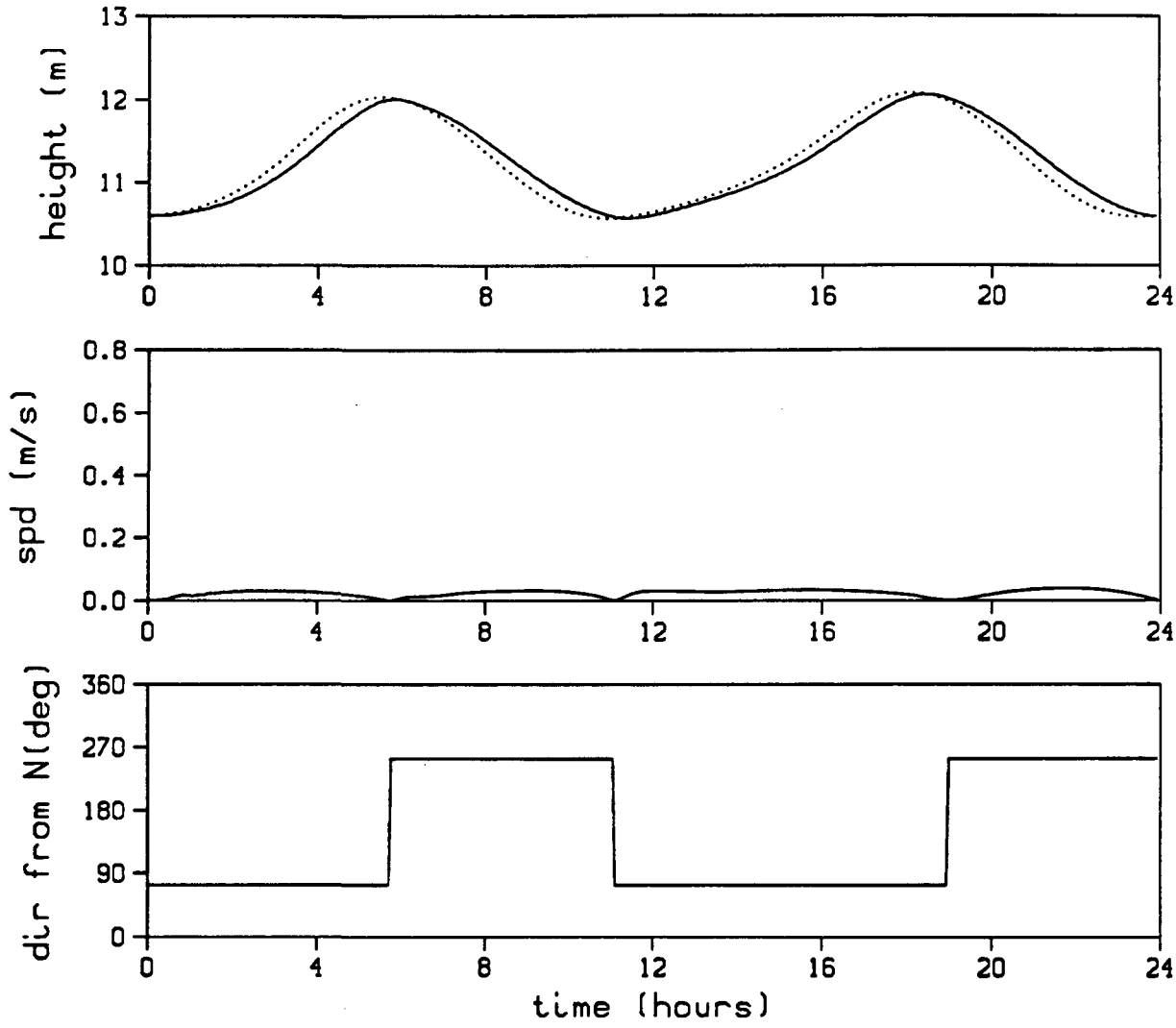

FIGURE 5.52. WATER SURFACE HEIGHT, CURRENT SPEED, AND CURRENT DIRECTION AT WOODS HOLE OCEANOGRAPHIC INSTITUTE (WHOI) STATION D FOR THE JULY 23, 1986 CALIBRATION CASE. (——) = COMPUTED AND (.....) = MEASURED BY WHOI.

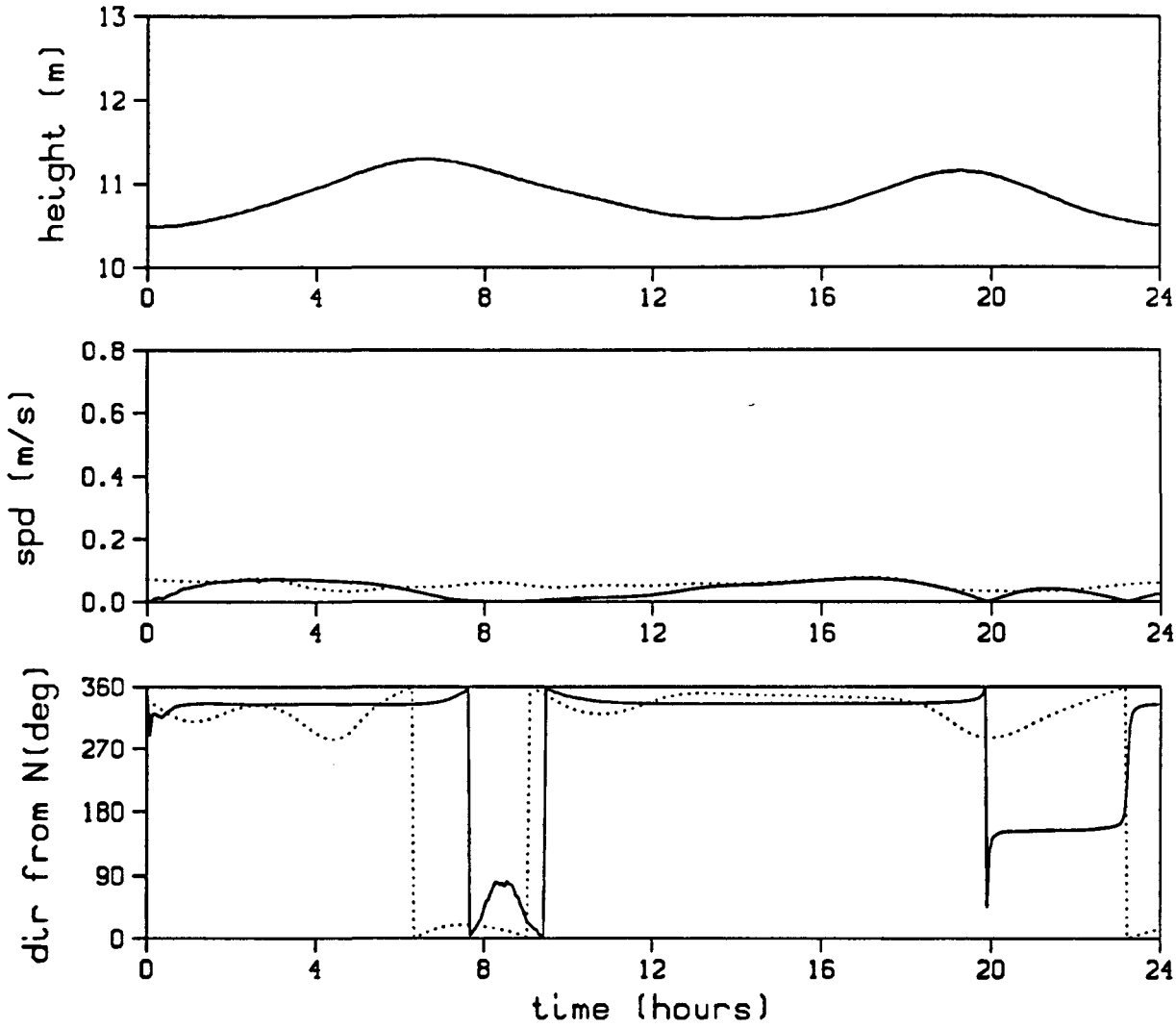

FIGURE 5.53. WATER SURFACE HEIGHT, CURRENT SPEED, AND CURRENT DIRECTION AT WOODS HOLE OCEANOGRAPHIC INSTITUTE (WHOI) STATION A FOR THE JULY 31, 1986 CALIBRATION CASE. (——) = COMPUTED AND (.....) = MEASURED BY WHOI.

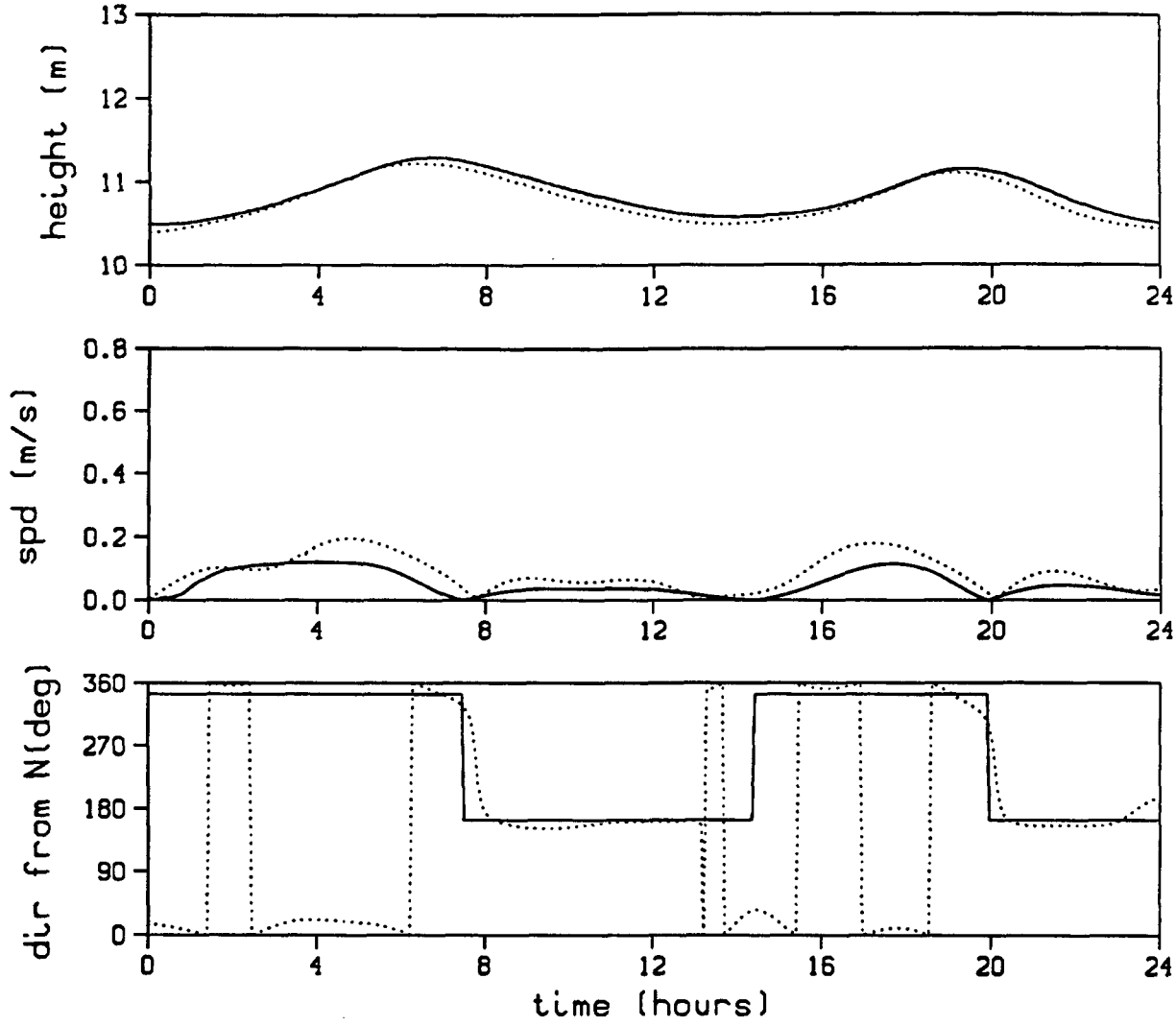

FIGURE 5.54. WATER SURFACE HEIGHT, CURRENT SPEED, AND CURRENT DIRECTION AT WOODS HOLE OCEANOGRAPHIC INSTITUTE (WHOI) STATION B FOR THE JULY 31, 1986 CALIBRATION CASE. (——) = COMPUTED AND (.....) = MEASURED BY WHOI.

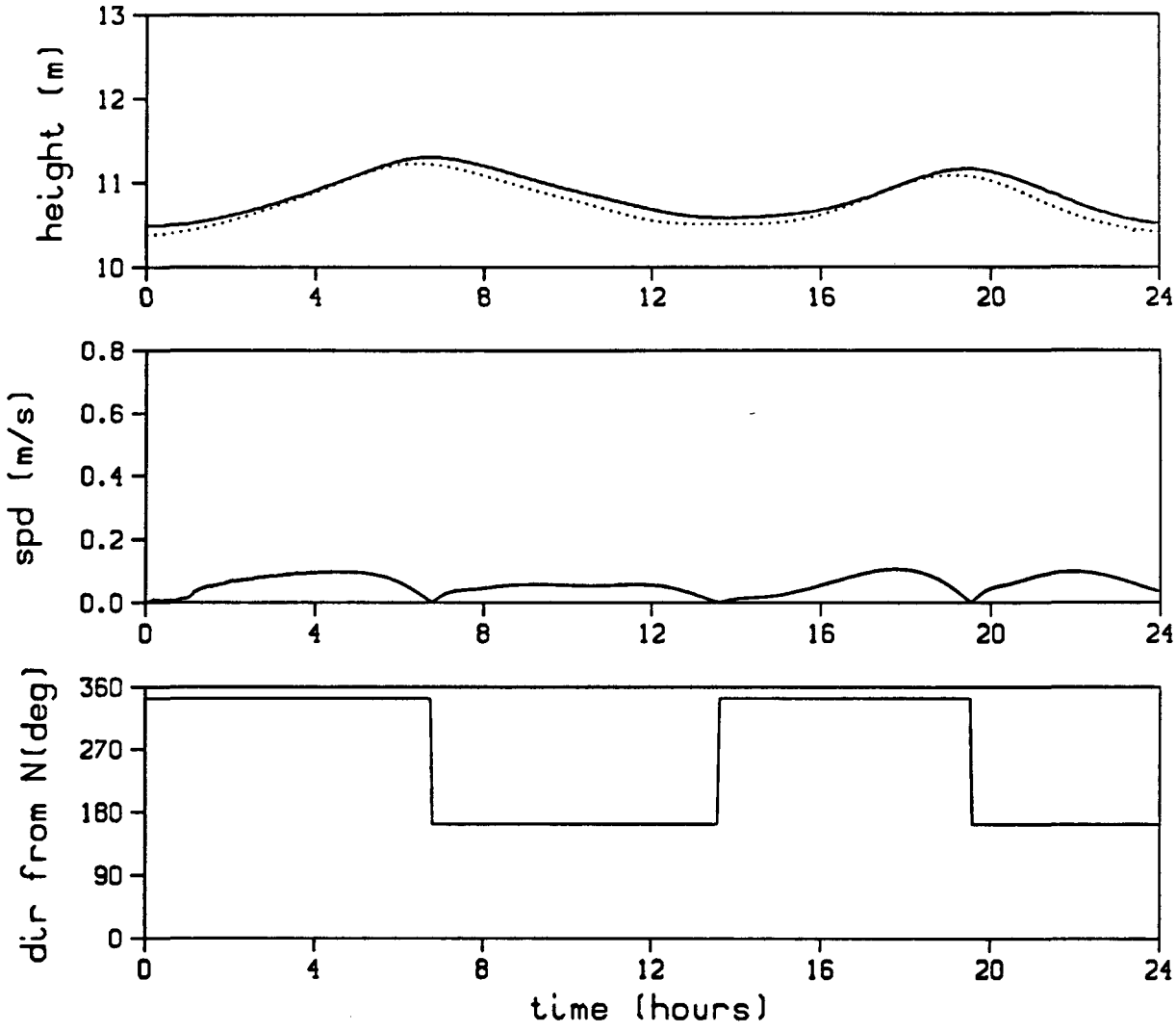

FIGURE 5.55. WATER SURFACE HEIGHT, CURRENT SPEED, AND CURRENT DIRECTION AT WOODS HOLE OCEANOGRAPHIC INSTITUTE (WHOI) STATION C FOR THE JULY 31, 1986 CALIBRATION CASE. (——) = COMPUTED AND (.....) = MEASURED BY WHOI.

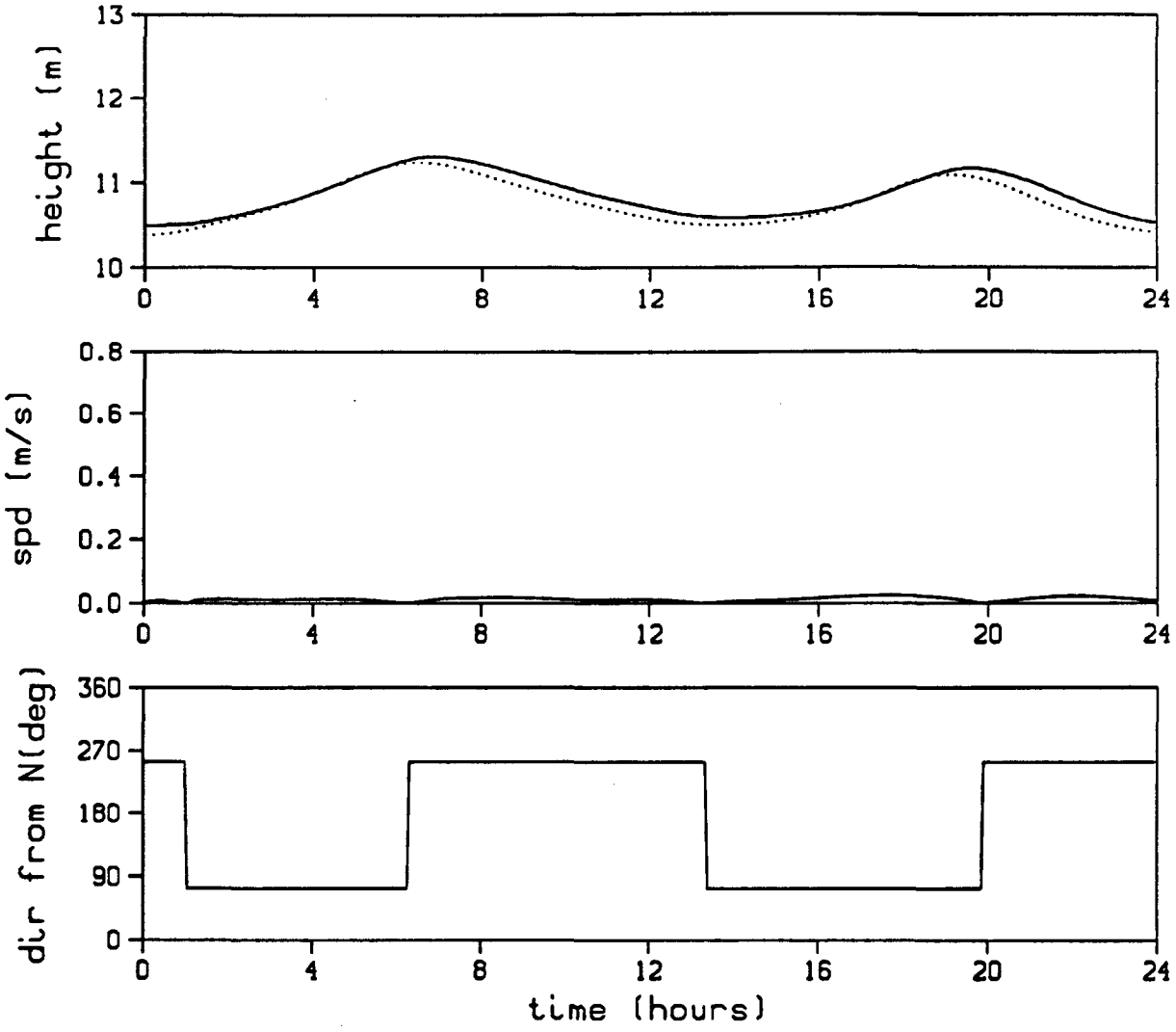

FIGURE 5.56. WATER SURFACE HEIGHT, CURRENT SPEED, AND CURRENT DIRECTION AT WOODS HOLE OCEANOGRAPHIC INSTITUTE (WHOI) STATION D FOR THE JULY 31, 1986 CALIBRATION CASE. (——) = COMPUTED AND (.....) = MEASURED BY WHOI.

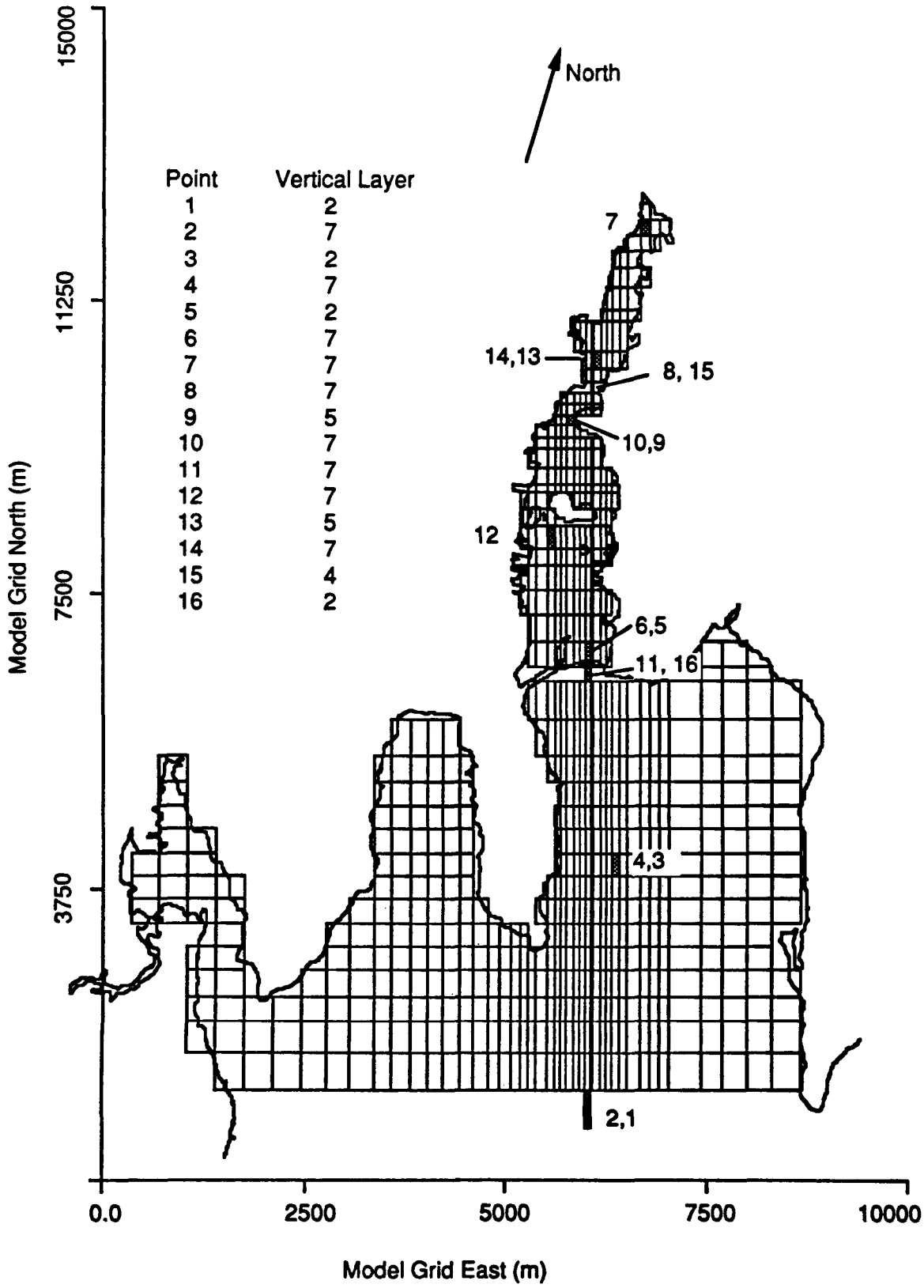

FIGURE 5.57. LOCATION OF MODEL TIME-SERIES OUTPUT POINTS FOR THE JULY 23 AND 31, 1986 HYDRODYNAMICS CALIBRATION CASES

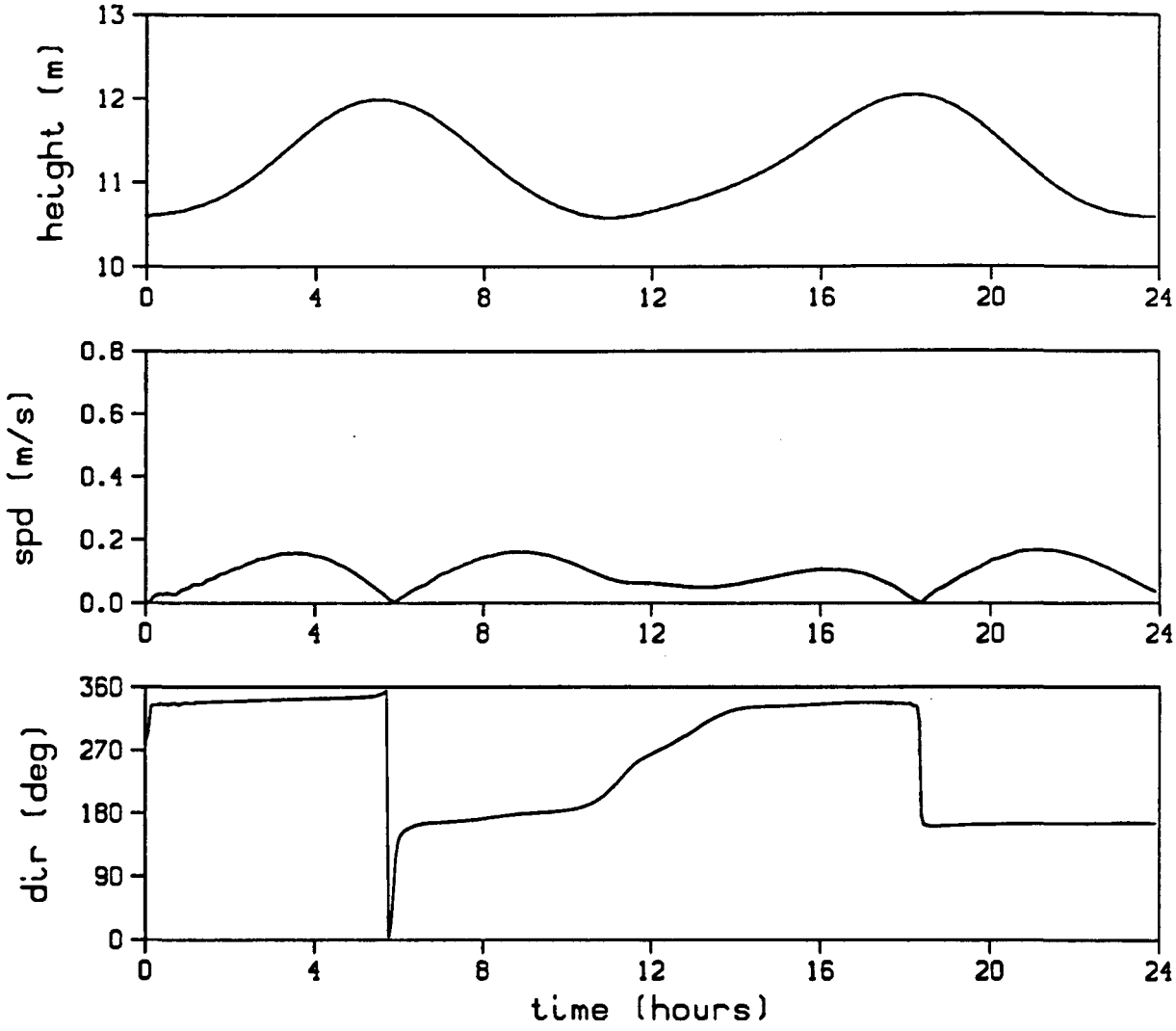

FIGURE 5.58. COMPUTED WATER SURFACE HEIGHT, CURRENT SPEED, AND CURRENT DIRECTION AT TIME-SERIES LOCATION 4 FOR THE JULY 23, 1986 CALIBRATION CASE

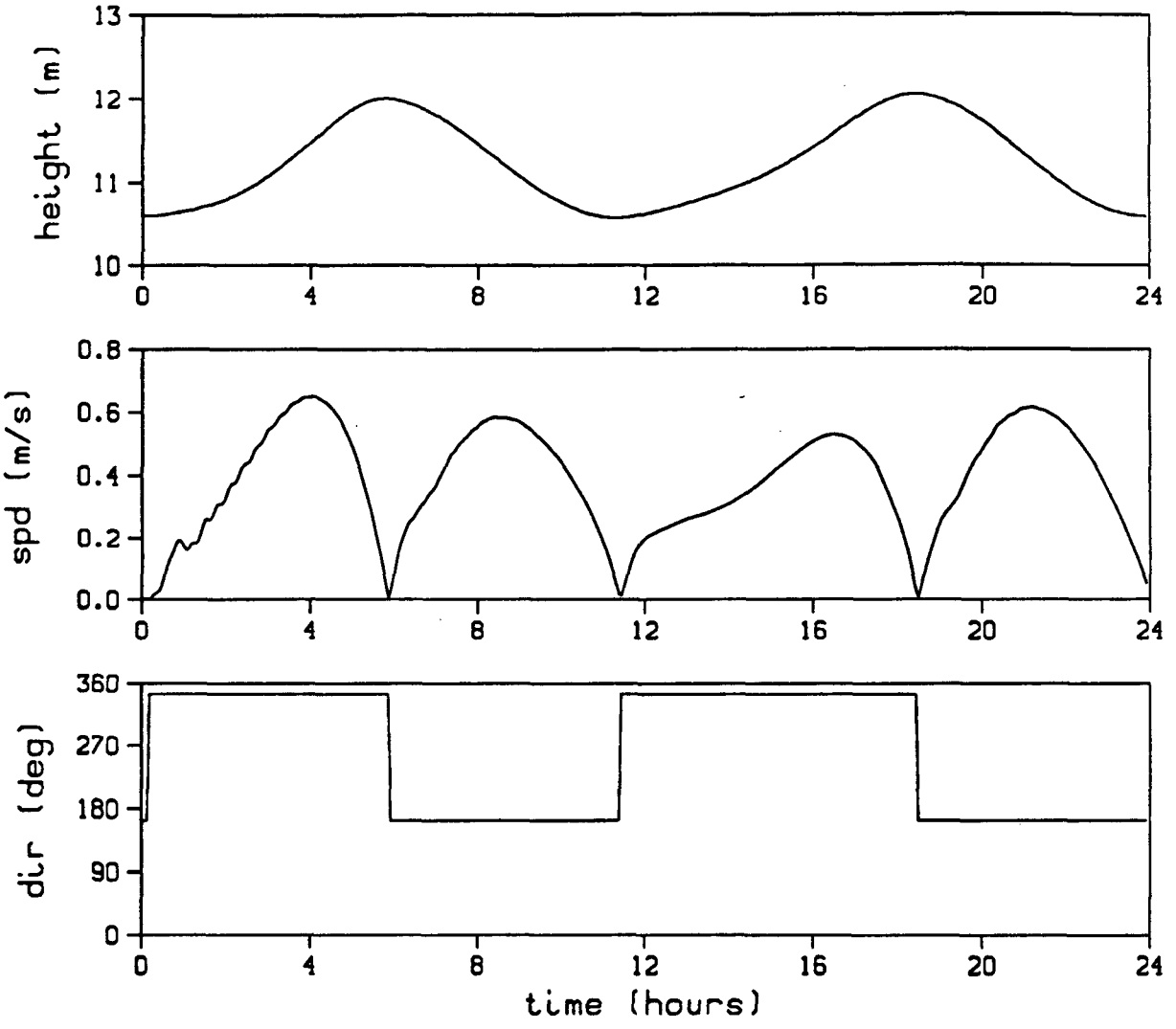

FIGURE 5.59. COMPUTED WATER SURFACE HEIGHT, CURRENT SPEED, AND CURRENT DIRECTION AT TIME-SERIES LOCATION 9 FOR THE JULY 23, 1986 CALIBRATION CASE

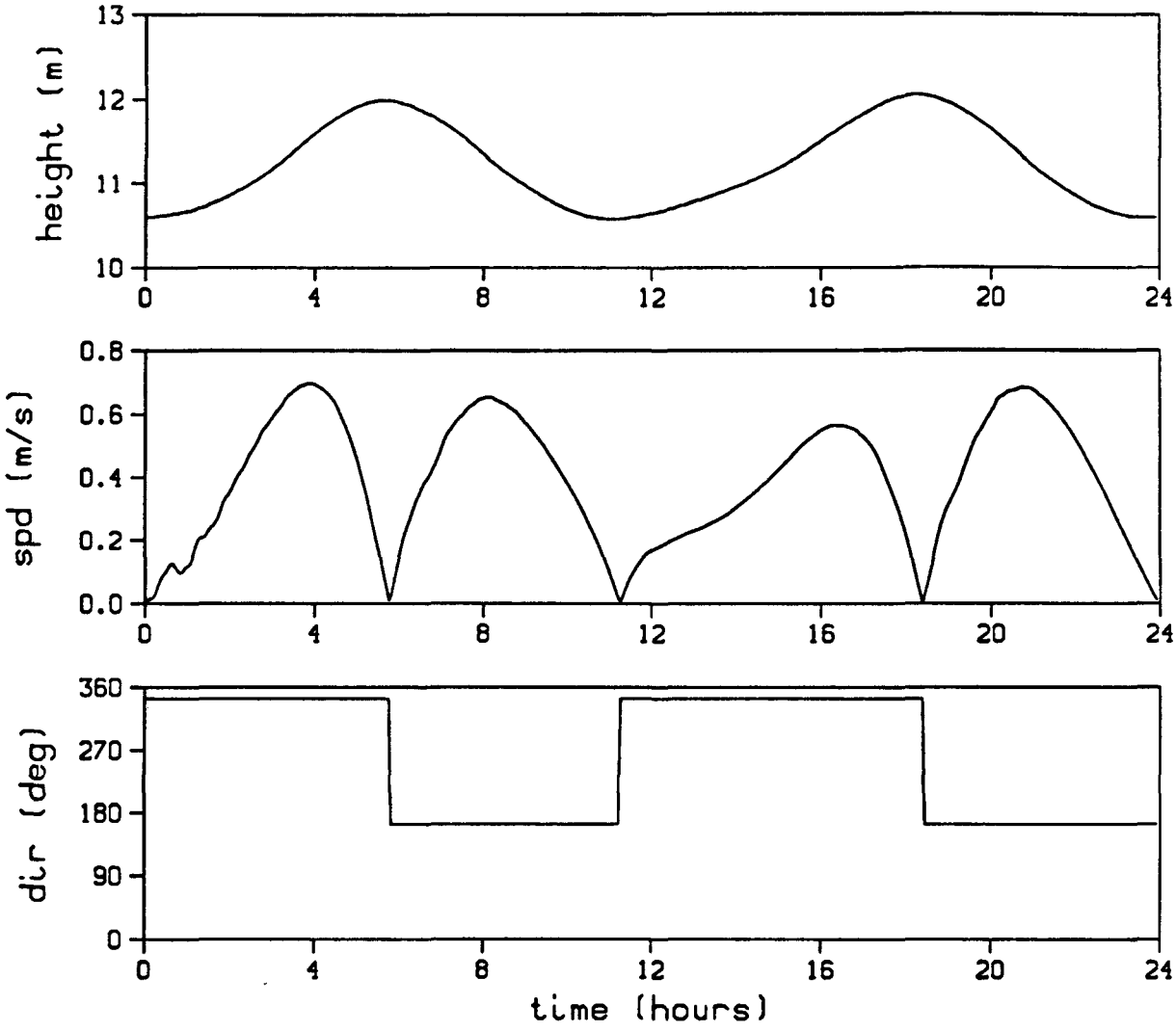

FIGURE 5.60. COMPUTED WATER SURFACE HEIGHT, CURRENT SPEED, AND CURRENT DIRECTION AT TIME-SERIES LOCATION 11 FOR THE JULY 23, 1986 CALIBRATION CASE

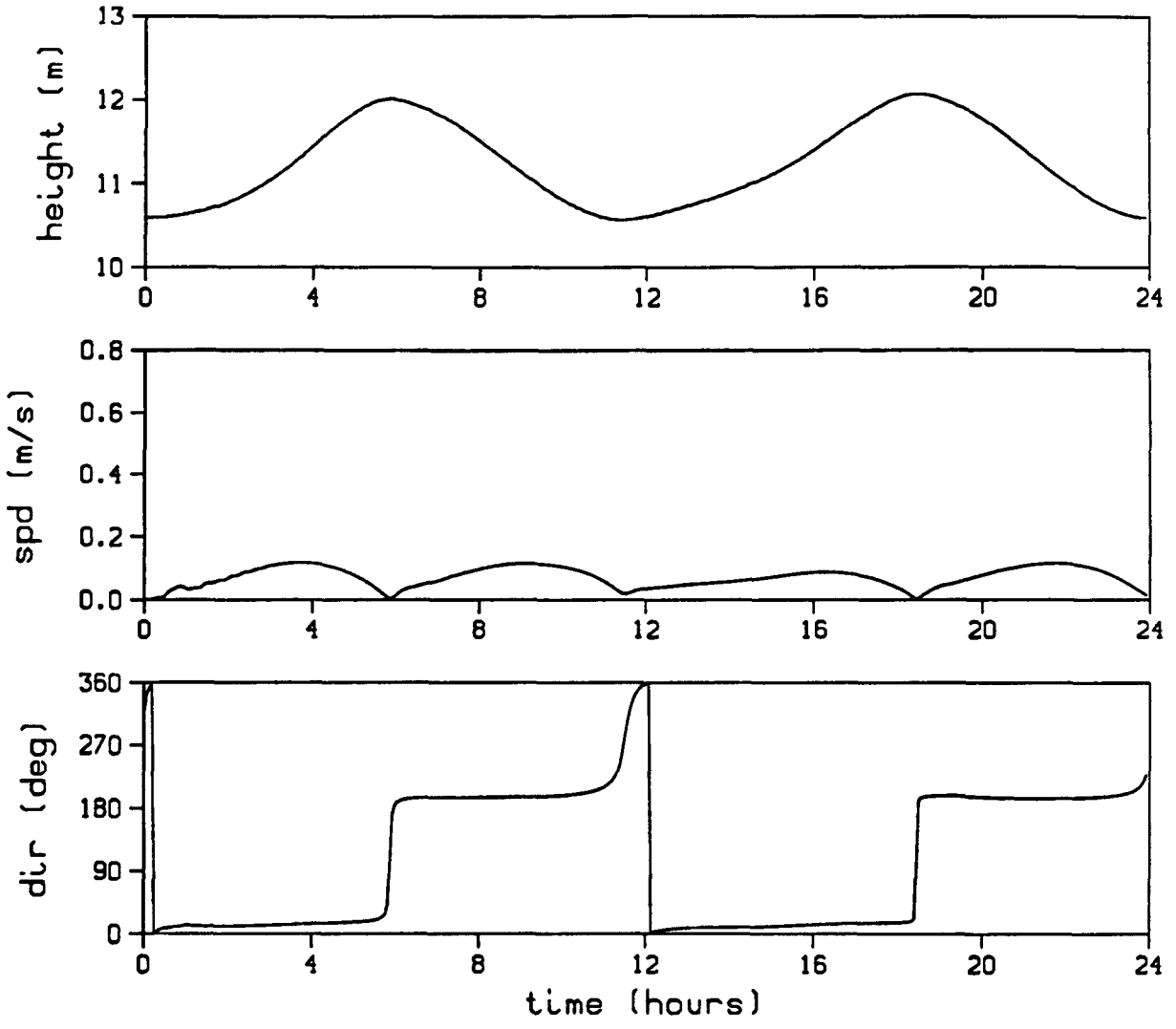

FIGURE 5.61. COMPUTED WATER SURFACE HEIGHT, CURRENT SPEED, AND CURRENT DIRECTION AT TIME-SERIES LOCATION 14 FOR THE JULY 23, 1986 CALIBRATION CASE

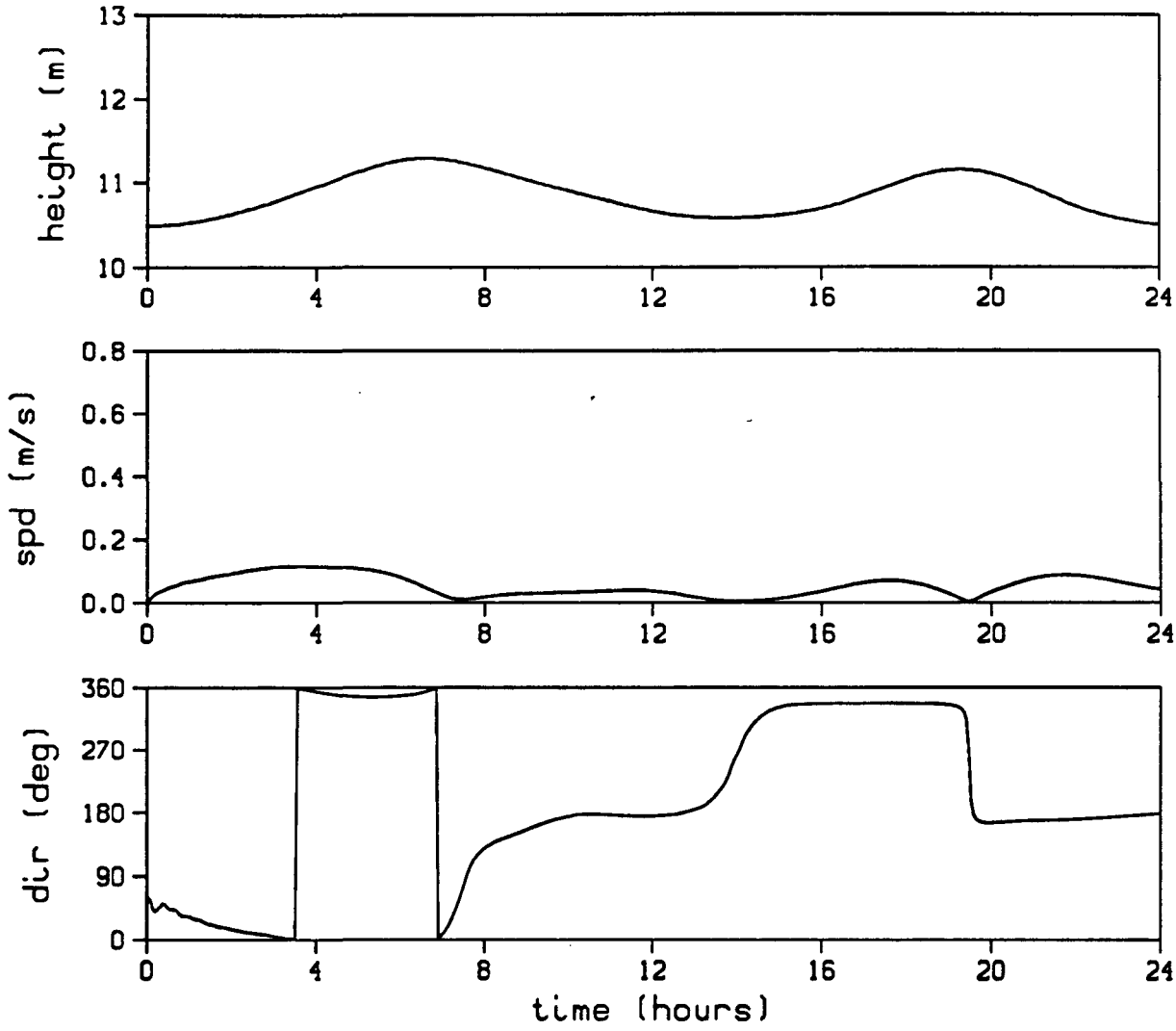

FIGURE 5.62. COMPUTED WATER SURFACE HEIGHT, CURRENT SPEED, AND CURRENT DIRECTION AT TIME-SERIES LOCATION 5 FOR THE JULY 31, 1986 CALIBRATION CASE

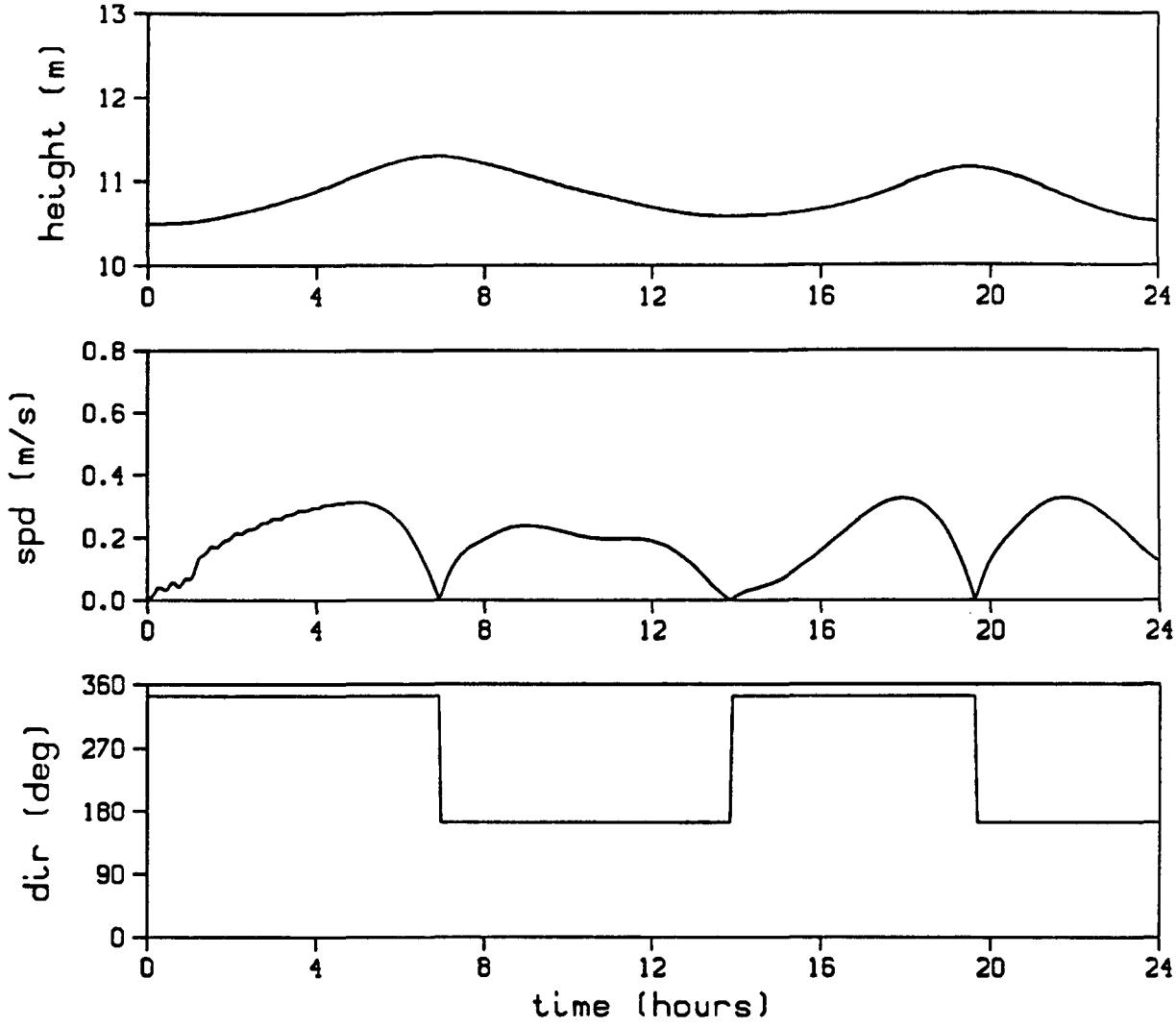

FIGURE 5.63. COMPUTED WATER SURFACE HEIGHT, CURRENT SPEED, AND CURRENT DIRECTION AT TIME-SERIES LOCATION 8 FOR THE JULY 31, 1986 CALIBRATION CASE

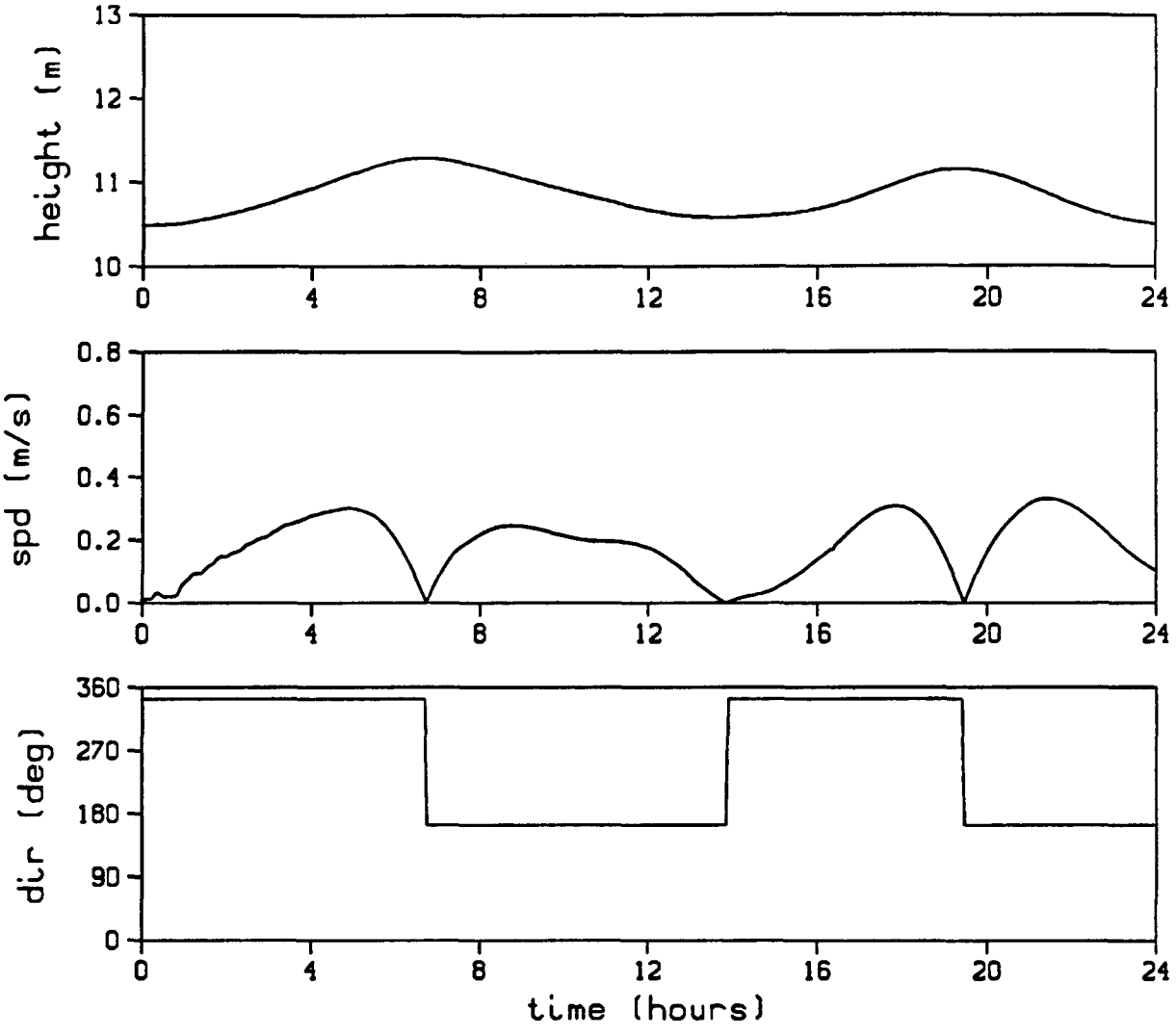

FIGURE 5.64. COMPUTED WATER SURFACE HEIGHT, CURRENT SPEED, AND CURRENT DIRECTION AT TIME-SERIES LOCATION 11 FOR THE JULY 31, 1986 CALIBRATION CASE

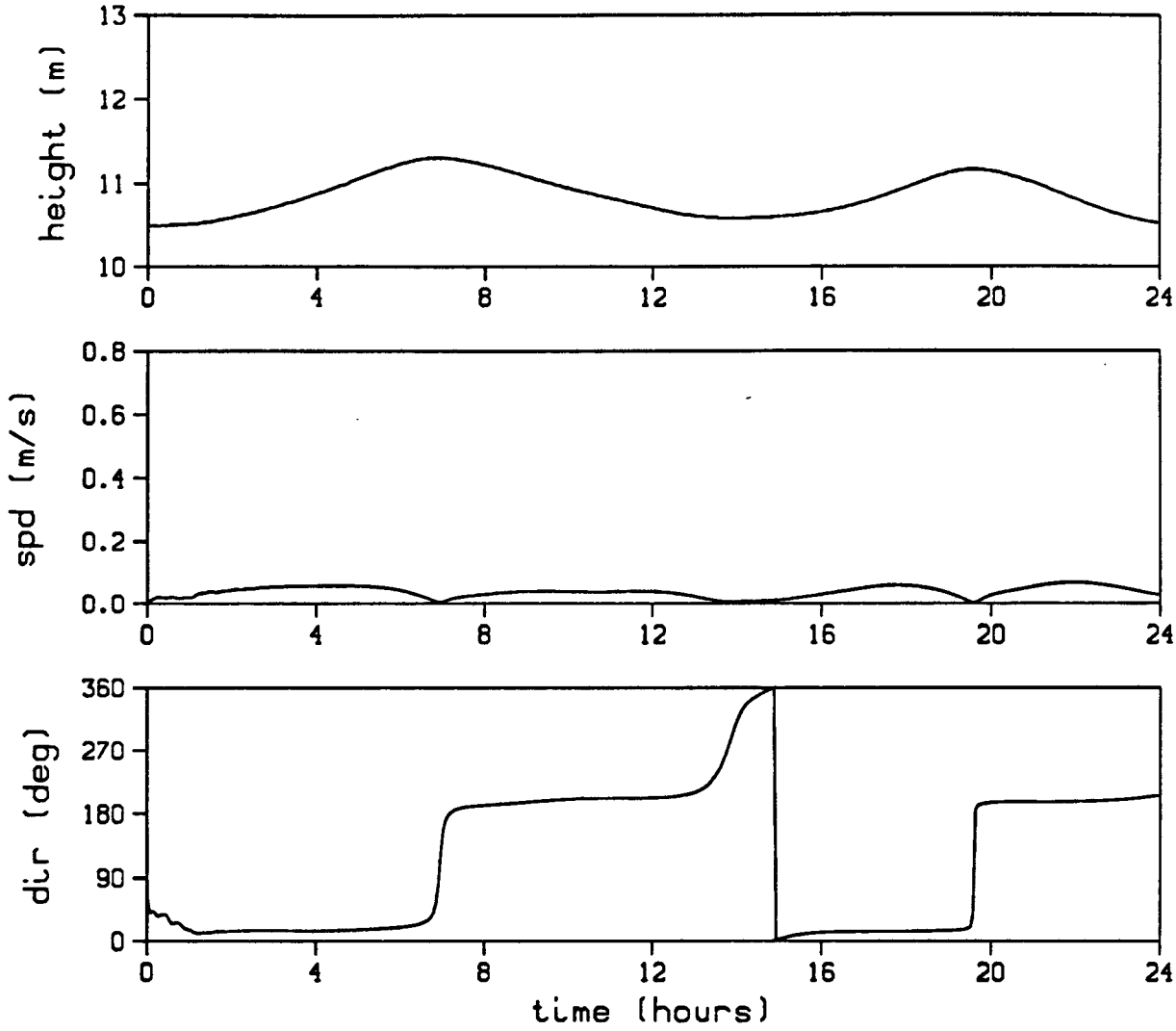

FIGURE 5.65. COMPUTED WATER SURFACE HEIGHT, CURRENT SPEED, AND CURRENT DIRECTION AT TIME-SERIES LOCATION 14 FOR THE JULY 31, 1986 CALIBRATION CASE

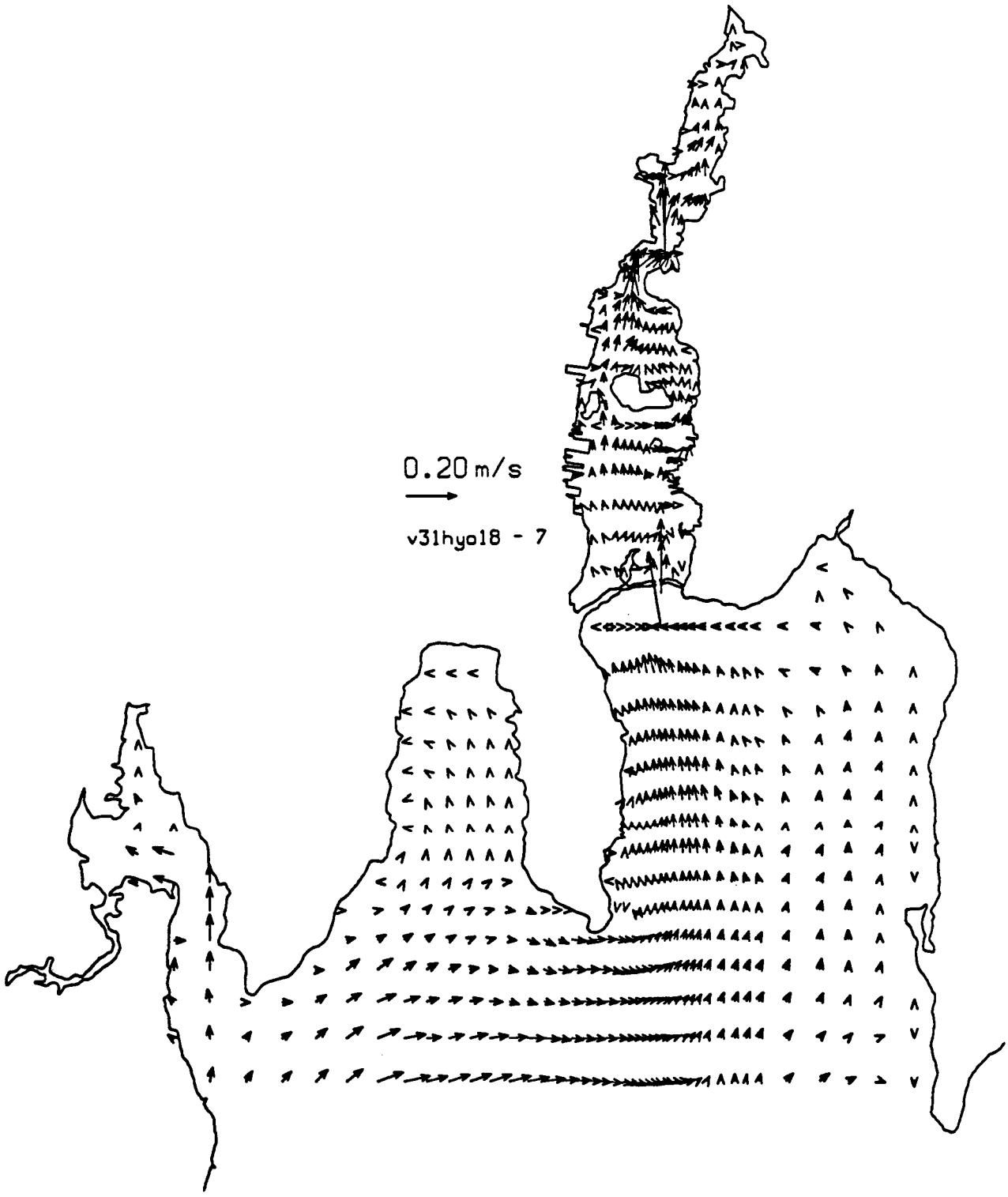

FIGURE 5.66. VELOCITY VECTORS COMPUTED FOR THE JULY 31, 1986 CALIBRATION CASE. CONDITIONS 18 HOURS AFTER THE START OF THE SIMULATION IN GRID LAYER 7.

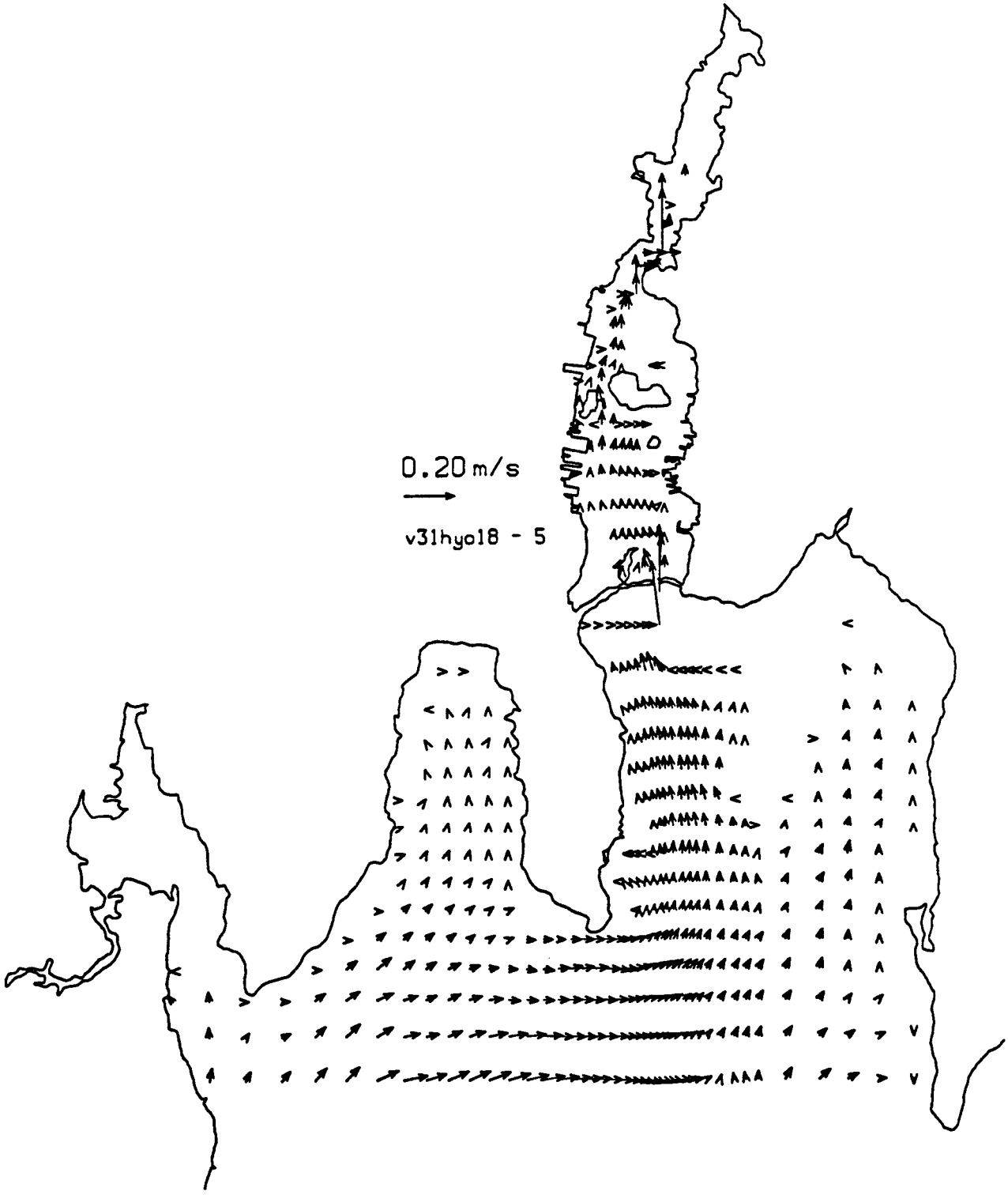

FIGURE 5.67. VELOCITY VECTORS COMPUTED FOR THE JULY 31, 1986 CALIBRATION CASE. CONDITIONS 18 HOURS AFTER THE START OF THE SIMULATION IN GRID LAYER 5.

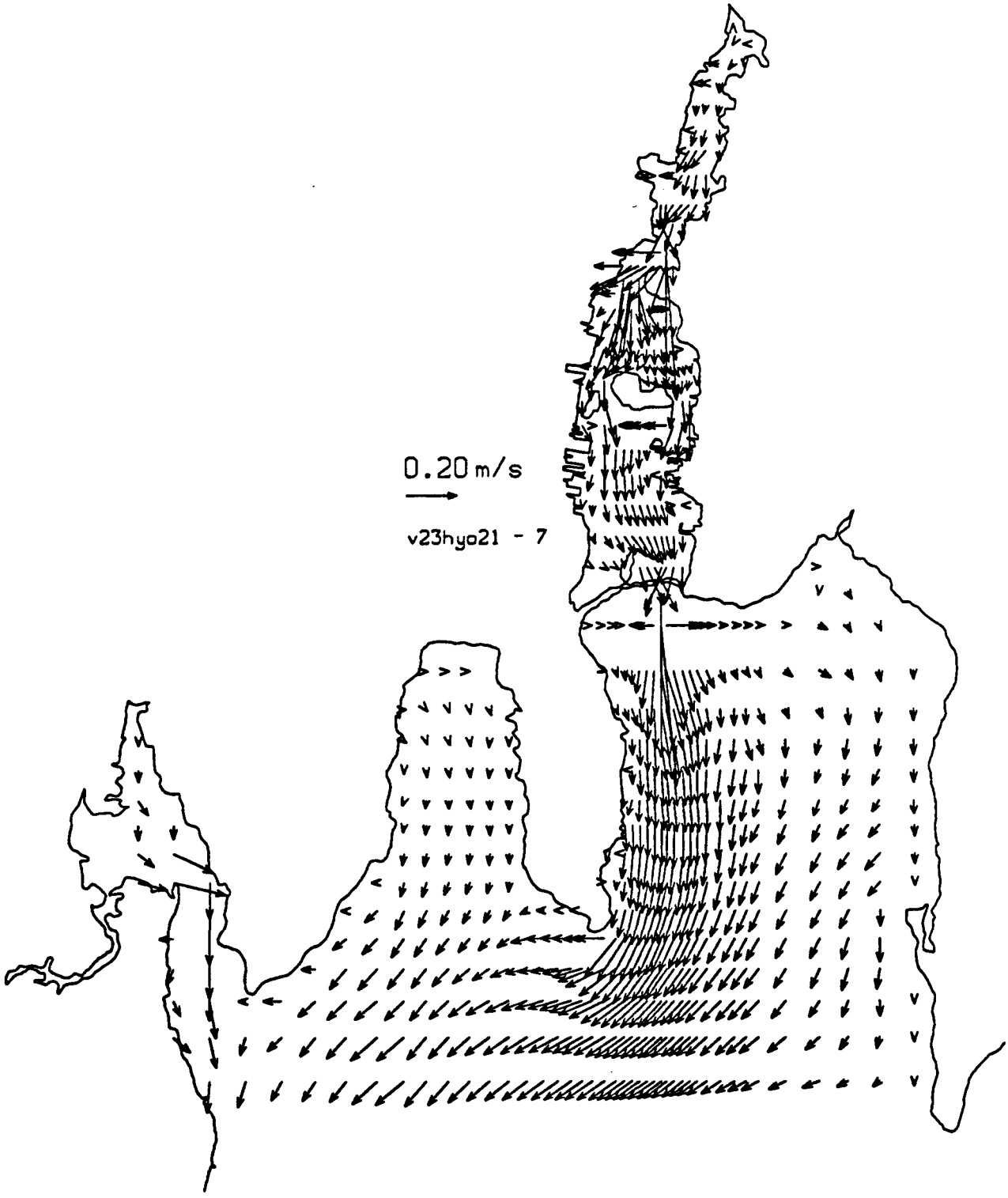

FIGURE 5.68. VELOCITY VECTORS COMPUTED FOR THE JULY 23, 1986 CALIBRATION CASE. CONDITIONS 21 HOURS AFTER THE START OF THE SIMULATION IN GRID LAYER 7.

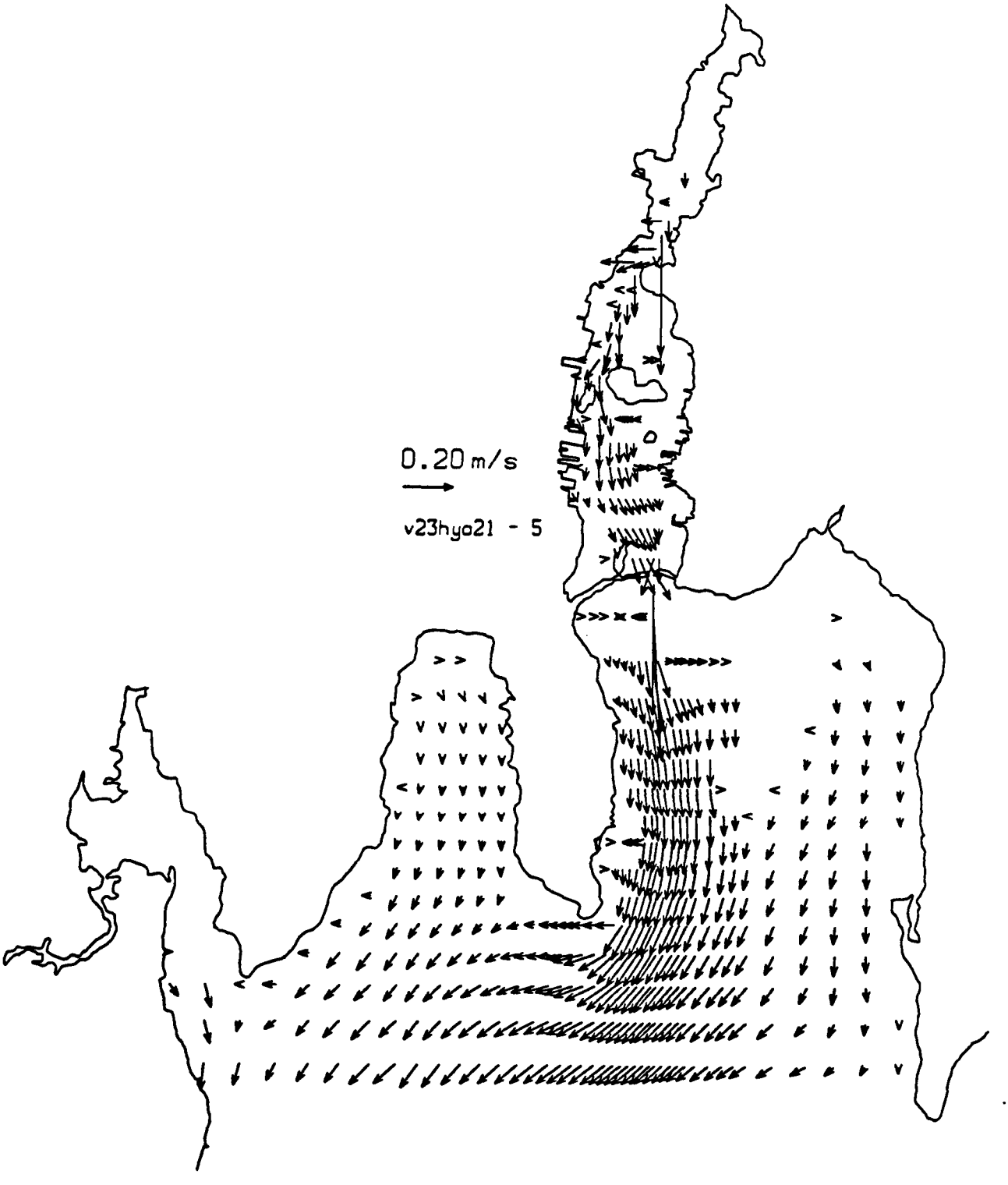

FIGURE 5.69. VELOCITY VECTORS COMPUTED FOR THE JULY 23, 1986 CALIBRATION CASE. CONDITIONS 21 HOURS AFTER THE START OF THE SIMULATION IN GRID LAYER 5.

model requires approximately 70 minutes of Cray-XMP processor time to compute the hydrodynamics for one tidal cycle. These model results are discussed and compared, qualitatively, to field observations below.

Water generally enters and leaves the model domain along a northeast/southwest axis, except in the vicinity of Round Hill Point, where the coastline forces the flow to follow a north/south axis. In the area of Butler Flats, the computed velocity directions are predominately in the grid north/south direction. Computed velocities in the outer harbor are generally in the range of 5 to 20 cm/s. The measurements of Camp, Dresser, and McKee (1983) were made at the locations shown in Figure 5.70. The mean tidal current and direction were as follows: station 1, 6.8 cm/s and northeast/southwest; station 5, 6.5 cm/s (no direction reported); station 6, 6.6 cm/s and north/south-southwest. In addition to these measurements, principal axes of the M_2 tidal ellipses based on harmonic analyses of current meter records were calculated by Geyer and Dragos (1988) and are displayed in Figure 5.71. The computed velocity magnitudes and directions are in fair agreement with both sets of measurements.

The highest computed and measured velocities are observed at the hurricane barrier and Coggeshall Street Bridge constrictions. Computed velocities through the hurricane barrier and Coggeshall Street Bridge are approximately 70 cm/s and 30 cm/s (see Figures 5.59, 5.60, 5.63, and 5.64) maximum flood/ebb for the July 23, 1986 and July 31, 1986 cases, respectively. Velocities at the hurricane barrier reported by ASA (1986) for a tide amplitude equal to the July 23, 1986 case show maximum flood- and ebb-tide currents of 85 cm/s and 75 cm/s, respectively. Ellis (1977) measured even faster peak currents, 122 cm/s, at the hurricane barrier. At the Coggeshall Street Bridge, currents were approximately 183 cm/s maximum ebb, 91 cm/s maximum flood, 52 cm/s average ebb, and 34 cm/s average flood (EPA 1983).

Mean velocities in the lower harbor, defined as the region between the hurricane barrier and Coggeshall Street Bridge, are generally less than 10 cm/s. In the upper estuary, defined as the region between the Coggeshall

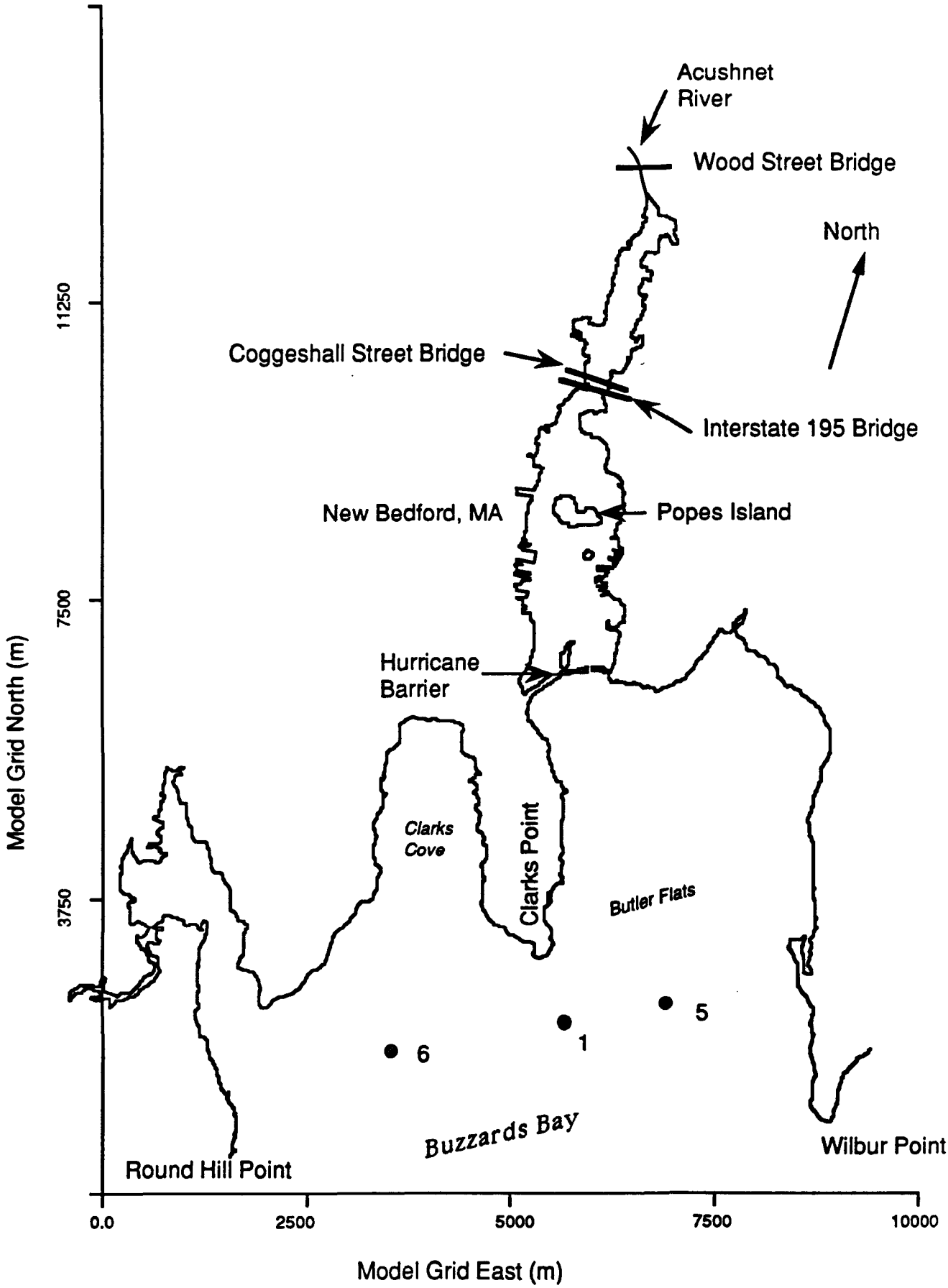

FIGURE 5.70. APPROXIMATE LOCATION OF THE MEASUREMENT STATIONS OF CAMP, DRESSER, AND MCKEE (1983).

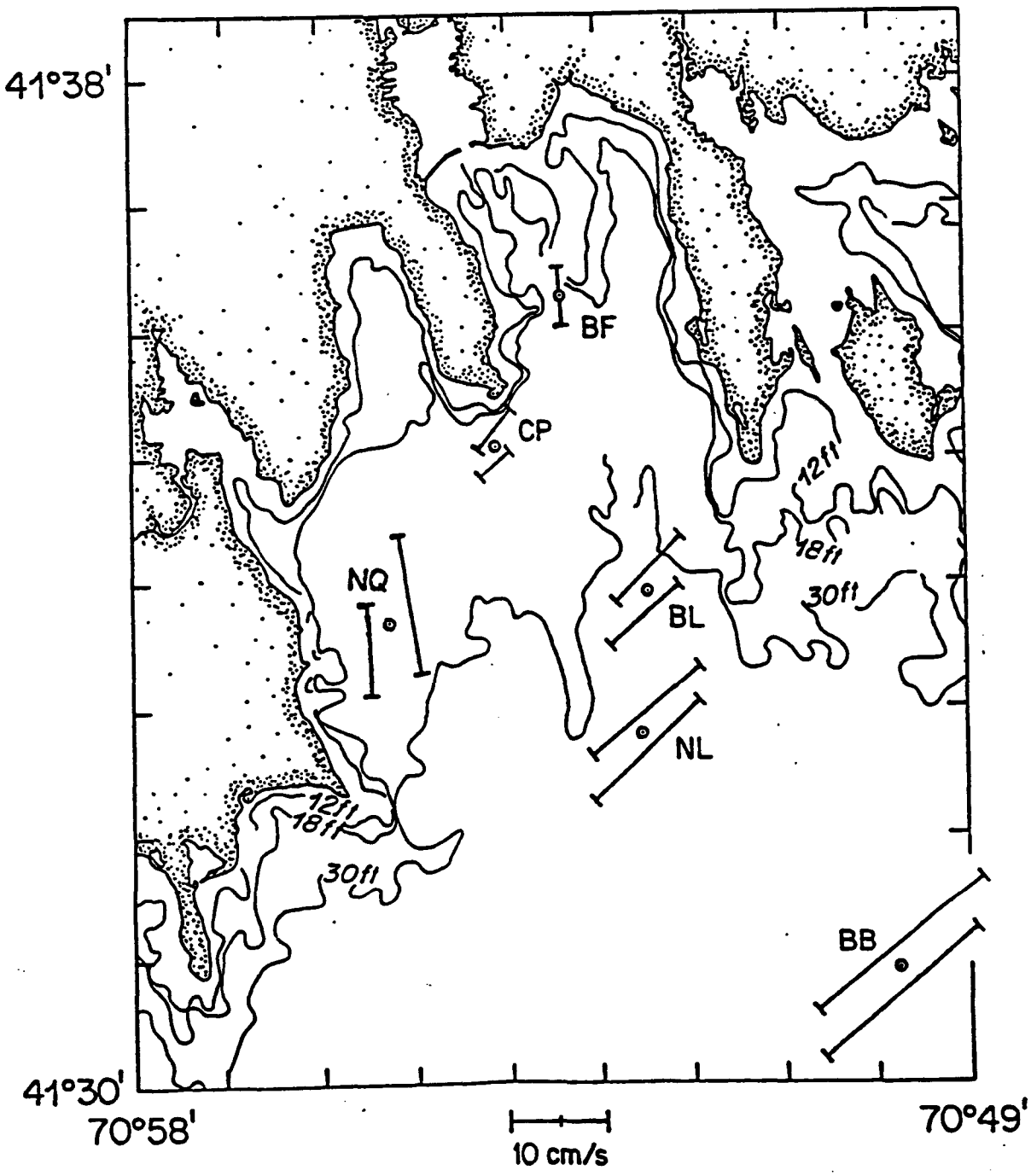

FIGURE 5.71. M_2 MAJOR AXES BASED ON HARMONIC ANALYSES (AFTER GEYER AND DRAGOS, 1988)

Street and Wood Street Bridges, mean velocities are also less than 10 cm/s. Teeter (1988) measured maximum flood/ebb currents of approximately 8 cm/s 400 m north of the Coggeshall Street Bridge. Near the Aerovox facility, computed velocities are less than 5 cm/s, while current measurements by ASA (1986) were in the range of 3 to 5 cm/s.

5.6.2 Sediment/Contaminant Transport

The sediment/contaminant transport portion of the New Bedford Harbor model was calibrated by running the model in the decoupled mode, solving the transport equations using previously computed and stored hydrodynamics. Preliminary model simulations showed that the calculated sediment- and PCB-distributions depended on the initial bed sediment conditions and required 10 to 20 simulation days to reach a quasi-steady state independent of initial water column conditions. To run the model for such long periods required that the decoupled mode be used, because fully coupled simulations, hydrodynamics and sediment/contaminant transport, consumed approximately 90 minutes of Cray-XMP processor time to simulate one tidal cycle. Using the decoupled mode, 30-day simulations could be done in the same amount of Cray time.

The following sections describe the calibration process for the TEMPEST/FLESCOT sediment/contaminant transport model for the New Bedford Harbor site. Section 5.6.2.1 discusses how the hydrodynamics for the decoupled transport calculations were generated. The initial grain size distribution of bed sediments and the sorption of PCBs to bed sediments is presented in Section 5.6.2.2. In Section 5.6.2.3, open boundary conditions for sediments and PCBs and the selection of the volatilization coefficient for PCBs are discussed. The results of the simulation using the final calibrated parameter set and a discussion of the modeled transport and fate processes are presented in Sections 5.6.2.4 and 5.6.2.5, respectively.

5.6.2.1 Hydrodynamics for Transport Calculations

Velocity fields and water surface elevations for use in the transport simulations were computed using the parameter set selected in the calibration of the hydrodynamics. As noted in Section 5.3.4.3, the hydrodynamics were calculated using an M_2 tide with a period of 12.42 h. Using a symmetric tide reduces discontinuities in the water surface elevation when the hydrodynamic record is used repeatedly, as in the present decoupled-transport simulations. In all cases, the amplitude of the M_2 tide is 0.55 m, which corresponds to the mean tidal amplitude at New Bedford. Historical wind speeds and directions measured at the hurricane barrier were used to supply wind forcing. The wind records were not selected to necessarily represent prevailing conditions at the site. Temperature- and salinity-variations were neglected in these hydrodynamic computations.

Two sets of hydrodynamic conditions were created for use in the transport simulations. The first set, referred to as the general-case hydrodynamics, was computed using a 0.55 m amplitude M_2 tide together with northerly, 2 to 10 m/s winds. The tide and wind conditions are shown in Appendix D, Figures D.1 through D.3. The effect of episodic storm events, represented in the model by wind events with approximately a monthly return period, was accounted for in the second set of hydrodynamics, referred to as the storm case. The storm case differed from the general case only in that southerly 2 to 13 m/s winds were specified. This wind record, shown in Figure D.5, contains a 12-h period in which the wind speed is above 10 m/s. As noted in Section 5.2, storm events of this magnitude occur once or twice per month. For each case, calculations were done for two repetitions of the tide and wind boundary conditions. The model was assumed to be sufficiently spun-up after the end of the first cycle, and the hydrodynamics computed on the second repetition were stored at 5-minute intervals for future use during the transport calculations.

The wave-enhanced bottom friction model (Section 5.3) was included in the storm case calculations. Significant wave height and period were estimated for several regions within the model domain using the results of Graber

(1986a) and charts in the Shore Protection Manual (SPM) (Coastal Engineering Research Center 1984). The wave parameters used in the simulations are given in Table 5.1. Bottom roughness, represented by the median grain size d_{50}, was assigned from field survey information described in the following section. The simulation results for the general and storm hydrodynamics are presented in Appendix D as time-series (Figures D.8 through D.39) and vector plots (Figures D.40 through D.43). The results of the simulations were consistent with the previously discussed hydrodynamic calculations.

5.6.2.2 Initial Conditions for Sediments and PCBs

The TEMPEST/FLESCOT model simulates the exchange of sediment and contaminants between the water column and a multi-layered seabed. Initial conditions defining the properties and distribution of sediments and contaminants in the seabed were developed from field measurements. Because no single set of synoptic measurements with adequate spatial extent were available to assign the initial conditions for the model, several sets of data taken at different times had to be used to develop the initial conditions. Therefore, the initial conditions used for the model do not represent a single point in time, but rather a composite bed condition over several years.

TABLE 5.1. WAVE PARAMETERS USED IN STORM HYDROHYNAMICS

Region	Significant Wave Height (m)	Significant Wave Period (s)	Source
South of Clarks Point	0.75	3.0	Graber
Clarks Point to the hurricane barrier	0.50	2.5	SPM
Hurricane barrier to Coggeshall Street Bridge	0.30	1.8	SPM
North of Coggeshall Street Bridge	0.25	1.6	SPM

In the New Bedford Harbor model the bed is represented by a single, 4-cm-thick bed layer. The horizontal distribution and size of the bed cells is the same as that for the surface layer of cells in the water column (Figure 5.22). Because the model assumes that each bed cell is completely mixed at any time step, the bed-layer thickness was selected to be approximately equal to the bioturbation depth (Rhoads 1987).

The model considers the following three sediment size fractions: sand, silt, and clay. Surficial grain size distributions and d_{50} in the bed cells for each class were developed from the field measurements described in Section 5.3. These field data were interpolated onto the computational grid to establish the initial percentages of sand, silt, and clay in the model's bed sediment layer. The model also requires spatially uniform average values of the mean grain size, density, and fall velocity for each sediment size class. Representative values for these properties were selected from information in Vanoni (1975) and Teeter (1988) and are summarized in Table 5.2. A uniform porosity of 0.5 was assigned throughout the model. The remaining sediment parameters, such as critical shear stresses, were used as calibration coefficients, and their final values were the results of the calibration exercise.

TABLE 5.2. SEDIMENT PROPERTIES

Class	Mean Diameter (mm)	Fall Velocity (cm/s)	Density (g/cm^3)
Sand	0.40	0.05	2.65
Silt	0.016	0.0006	2.65
Clay	0.002	0.0002	2.65

The initial concentration and distribution of total PCBs in the bed layer was determined from the field measurements of surficial (less than 8 in depth) concentration described in Section 5.3 and shown in Figure 5.7. For the area north of the hurricane barrier, the field data were interpolated using a distance-weighted quadratic polynomial method onto a uniform grid (finer than the model grid) and then were averaged over each grid cell to yield a concentration estimate. This procedure could not be used for the area between the open boundary and the hurricane barrier because of the sparsity of the available field data. In this region the field data were extrapolated to assign an initial condition. In addition, the field samples in this area are likely to be biased toward higher concentrations, because a uniform sampling grid was not used throughout the entire area and the sample locations tend to be in areas of high PCB concentration, such as the sewage treatment plant outfall. Individual Aroclors were not modeled. The concentrations of total PCBs sorbed to silt and clay were assumed to be equal, and the amount sorbed to the sand fraction negligible.

Initial model simulations showed that the computed water column concentrations of sediments and PCBs were independent of initial water column conditions after approximately 15 simulation days. The resulting quasi-steady water column concentrations depended only on the bed initial conditions and boundary conditions. Therefore, uniform initial water column concentrations for sediments and PCBs were used for all simulations.

5.6.2.3 Boundary Conditions for Sediments and PCBs

Concentration boundary conditions for sediments and PCBs were required at the open boundary. These values were set based on the measurements collected at Battelle Ocean Sciences (BOS) station 18, which, as shown in Figure 5.46, was just outside the open boundary. Table 5.3 shows the sediment and PCB concentrations at the open boundary. The sediment-sorbed PCBs were divided among the sediment size fractions according to the water column partition coefficient. During storm simulations these concentrations were increased by a factor of 3 to account for the resuspension of sediments and PCBs from the Buzzards Bay seabed. The boundary concentration was linearly decreased to its

TABLE 5.3. OPEN-BOUNDARY CONDITIONS FOR SEDIMENTS AND PCBs

Constituent	Concentration
Sand	0.1 mg/L
Silt	3.5 mg/L
Clay	2.5 mg/L
Dissolved PCB	2.5 ng/L
Sediment-Sorbed PCB	2.3 ng/L

former value over a 5-day period following the end of a storm simulation. The five-day period was selected based on the model's relaxation time for suspended sediment concentrations following storm events. Because the Acushnet river was not included in the model, river-inflow boundary conditions were not required.

The flux of PCBs across the air-water interface through volatilization was an important process and that is controlled by the volatilization coefficient. The coefficient was selected as the mean of the values computed using the methods proposed by Bopp (1983), Doskey and Andren (1981), and Atlas et al. (1982). The volatilization coefficient selected use in the model was 1.3×10^{-5} m/s.

5.6.2.4 Calibration Results

The sediment/contaminant transport model was calibrated by adjusting the model parameters and comparing the computed water column concentration of sediments and PCBs to the data collected by BOS. In addition, the computed fluxes of sediments and PCBs through the Coggeshall Street Bridge constriction were compared to the measurements of Teeter (1988) and others. A rigorous validation of the model was not possible because of the strong dependence of

the computed results on the initial sediment and PCB distribution in the bed sediments. Additional field data defining the current bed sediment and water column conditions would be provide a more complete model validation.

The sediment/contaminant calibrations were performed in the decoupled mode using the two sets of hydrodynamics described in Section 5.6.2.1. The calibration simulations covered a 95-day period, repeating the hydrodynamics in the following five sequential stages: 1) 31 days of the general case, 2) 1 day of the storm case, 3) 31 days of the general case, 4) 1 day of the storm case, and 5) 31 days of the general case. This sequence is shown graphically in Figure 5.72. The initial conditions for stage 1 were those described above. The final water column and bed concentrations for one stage served as the initial conditions for the next. This sequence of hydrodynamics was used for all the calibration scenarios because test runs showed that, for simulations longer than 30 days, the computed sediment and PCB concentrations averaged over large areas were not particularly sensitive to different sets of hydrodynamics (velocities and tidal heights).

Sediment calibration parameters included the critical shear stress for erosion and deposition and the erodibility coefficient for cohesive sediments (silt and clay). The only calibration parameter for noncohesive sediments (sand), the mean grain size, was left at the value assigned in the initial conditions. The calibration parameters for PCBs are the water column partition (K_d) and equilibrium rate coefficients and the bed-to-water-column partition and rate coefficient. The primary calibration parameter for PCBs was the bed-to-water-column partition coefficient, the so-called bed K_d term, which controls the mass transfer between the bed sediments and the overlying water column.

Figures 5.73 through 5.76 compare the results of several calibration simulations for varying bed sediment and water column Kd values (Table 5.4) with the BOS field data. The locations of the measurement stations are shown in Figure 5.46. The BOS data in these figures are the average value and the highest and lowest recorded values from all four cruises. The computed mean in the figures is the time-averaged mean, while the upper and lower bounds are

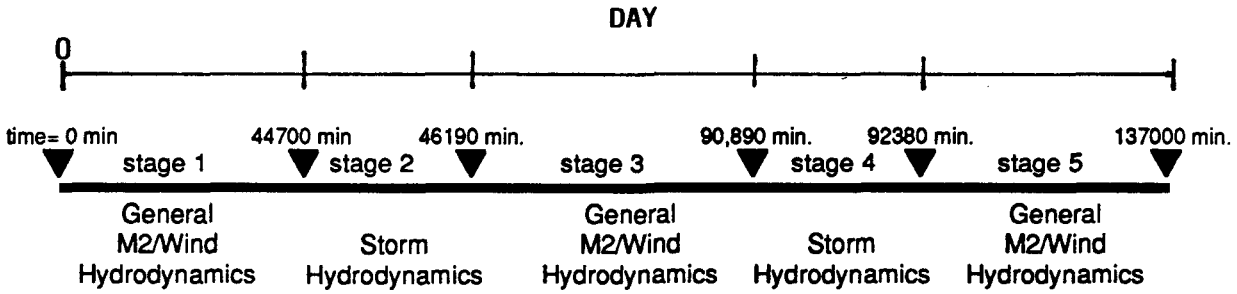

FIGURE 5.72. SEQUENCE OF HYDRODYNAMIC SCENARIOS USED IN DECOUPLED TRANSPORT SIMULATIONS

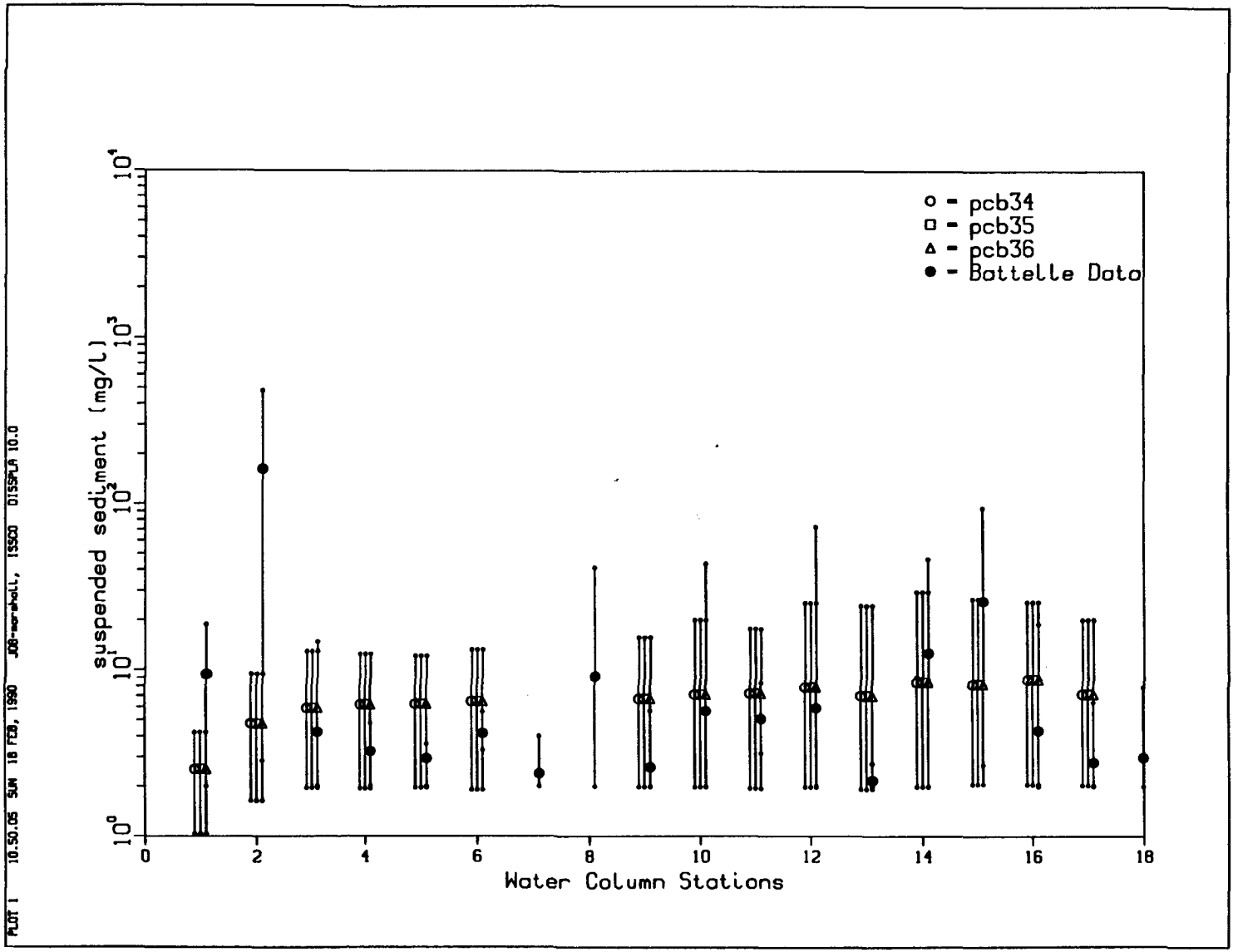

FIGURE 5.73. COMPARISON OF COMPUTED AND MEASURED SEDIMENT-SORBED PCB CONCENTRATION. THE SYMBOLS CORRESPOND TO MEAN VALUES AND THE BAR ENDPOINTS TO HIGH AND LOW VALUES. STATION LOCATIONS ARE GIVEN IN FIGURE 5.46.

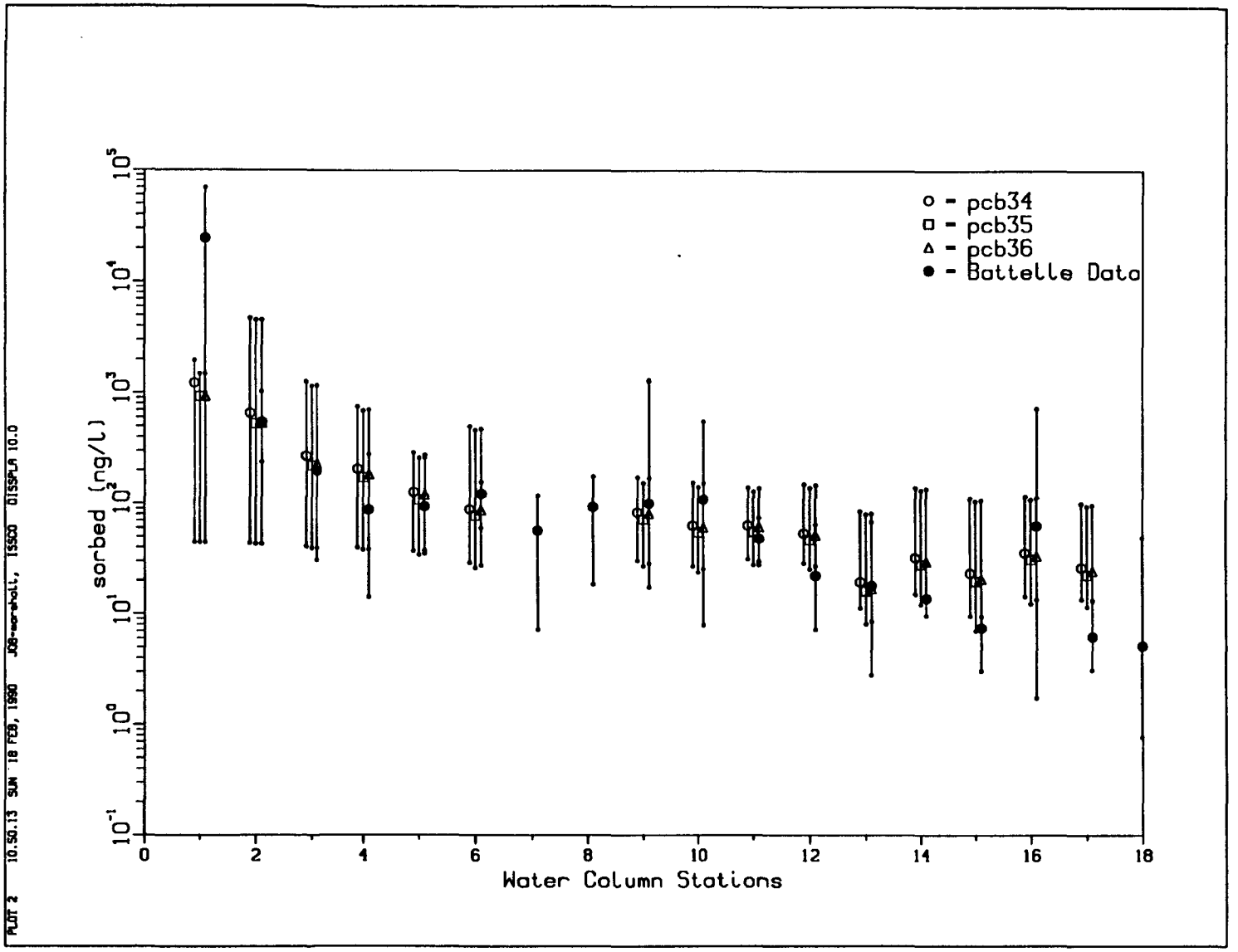

FIGURE 5.74. COMPARISON OF COMPUTED AND MEASURED TOTAL DISSOLVED PCB CONCENTRATION. THE SYMBOLS CORRESPOND TO MEAN VALUES AND THE BAR ENDPOINTS TO HIGH AND LOW VALUES. STATION LOCATIONS ARE GIVEN IN FIGURE 5.46.

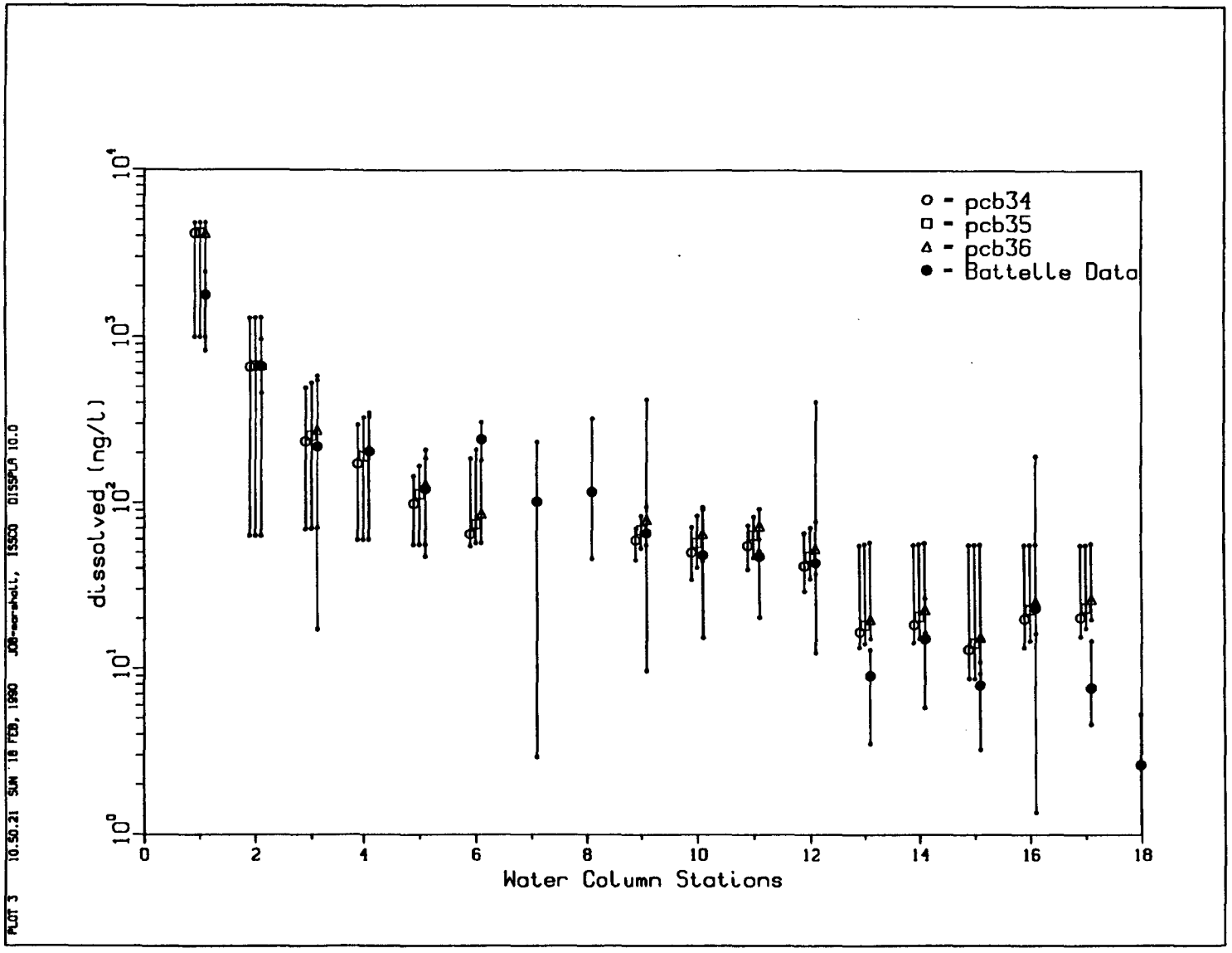

FIGURE 5.75. COMPARISON OF COMPUTED AND MEASURED TOTAL PCB (DISSOLVED + SEDIMENT-SORBED CONCENTRATION. THE SYMBOLS CORRESPOND TO MEAN VALUES AND THE BAR ENDPOINTS TO HIGH AND LOW VALUES. STATION GIVEN IN FIGURE 5.46.

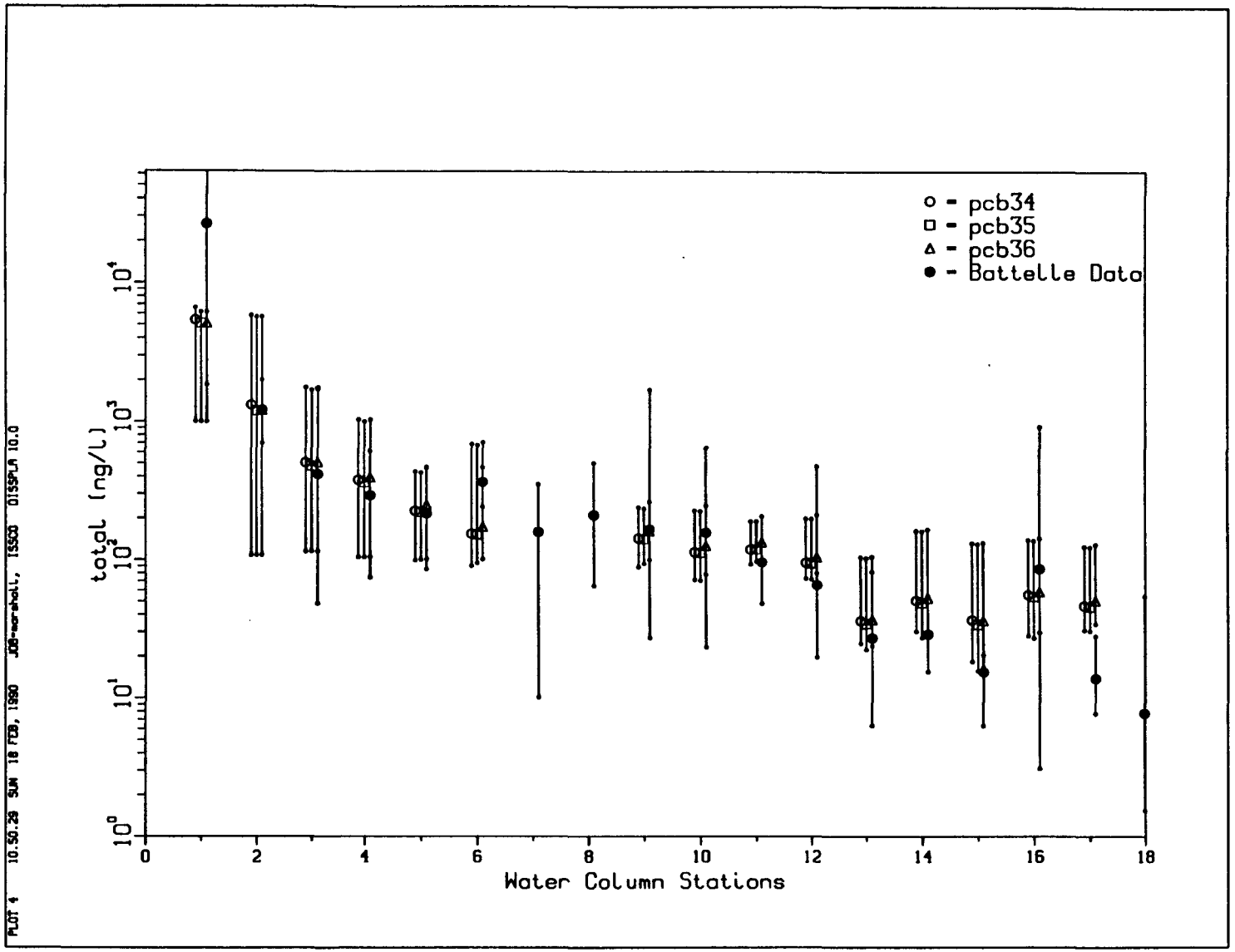

FIGURE 5.76. COMPARISON OF COMPUTED AND MEASURED TOTAL PCB (DISSOLVED PCB SEDIMENT-SORBED) CONCENTRATION. THE SYMBOLS CORRESPOND TO MEAN VALUES AND THE BAR ENDPOINTS TO HIGH AND LOW VALUES. STATION LOCATIONS ARE GIVEN IN FIGURE 5.46.

TABLE 5.4. PCB K_d VALUES

Case	Water Column K_d (m^3/kg)	Bed K_d North of Coggeshall Street Bridge (m^3/kg)	Bed K_d South of Coggeshall Street Bridge (m^3/kg)
pcb34	200.0	500.0	250.0
pcb35	150.0	500.0	200.0
pcb36	150.0	500.0	150.0

the absolute maximum and minimum values. A Schmidt number of 1 was used in all the simulations. The final set of sediment transport parameters are given in Table 5.5. The erodibility coefficient measured by Teeter (1988) for New Bedford Harbor sediments was found to be satisfactory. The critical shear stresses are within an order of magnitude of Teeter's values for these parameters. The computed total sediment concentrations (sum of sand, silt, and clay) fall within the range of the field observations shown in Figure 5.73. Note that Figure 5.73 shows the results obtained using the final set of sediment transport parameter for each PCB calibration case; therefore, the computed results are identical. The results of three calibration simulations using different water column and bed K_d values are shown to illustrate the sensitivity of the calculations to these parameters. The K_d values used in each case are summarized in Table 5.4. The water column partition coefficient

TABLE 5.5. FINAL SEDIMENT TRANSPORT MODEL PARAMETERS

Class	Critical Erosion Shear Stress (N/m^2)	Critical Deposition Shear Stress (N/m^2)	Erodibility Coefficient (kg/m^3-s)
Silt	0.045	0.02	4×10^{-6}
Clay	0.06	0.01	4×10^{-6}

used in the model is within the ranges reported by Baker et al. (1986) and Horzempa and DiToro (1983). An equilibrium rate constant of 1/24 h was used in all the simulations. Different bed K_d values had to be used in the upper estuary than in the rest of the model because of the 2-order-of-magnitude change in the bed PCB concentration between these regions. The computed sediment-sorbed, dissolved, and total (sediment-sorbed plus dissolved) PCB concentrations are compared with the BOS data in Figures 5.74, 5.75, and 5.76, respectively. Each set of K_d values yields results in reasonable agreement with the field data. Figures 5.77 through 5.80 show time-series plots of the computations for selected BOS stations. The time-series plots for the remainder of the BOS stations are shown in Figure E.174 through E.188 of Appendix E. Table 5.6 compares the computed net fluxes of PCBs and sediments through the Coggeshall Street Bridge with the average of the net fluxes reported by Teeter (1988) and with Teeter's corrected values of the EPA (1983) data. A negative flux is in the down-estuary direction (toward Buzzards Bay), while a positive flux is in the up-estuary direction. The computed net fluxes are in the same direction as the measured fluxes, but the magnitudes of the computed ones are lower. It should be noted that the field data were collected under different tide and wind conditions than those used in the model simulations. The computed and measured fluxes show that the upper estuary acts as a source of PCBs to the lower harbor and Buzzards Bay. As is the case for most estuaries (Postma 1967), the flux of suspended sediments is up-estuary, making the upper estuary an area of sediment deposition.

TABLE 5.6. COMPUTED AND MEASURED NET FLUXES OF PCBs AND SEDIMENTS THROUGH COGGESHALL STREET BRIDGE

	Case pcb34	Case pcb35	Case pcb36	Teeter (1988)	EPA (1983)
PCB Flux (kg/tidal cycle)	-0.26	-0.22	-0.20	-1.6	-0.91
Sediment Flux (kg/tidal cycle)	536	536	536	2.202×10^3	6.682×10^3

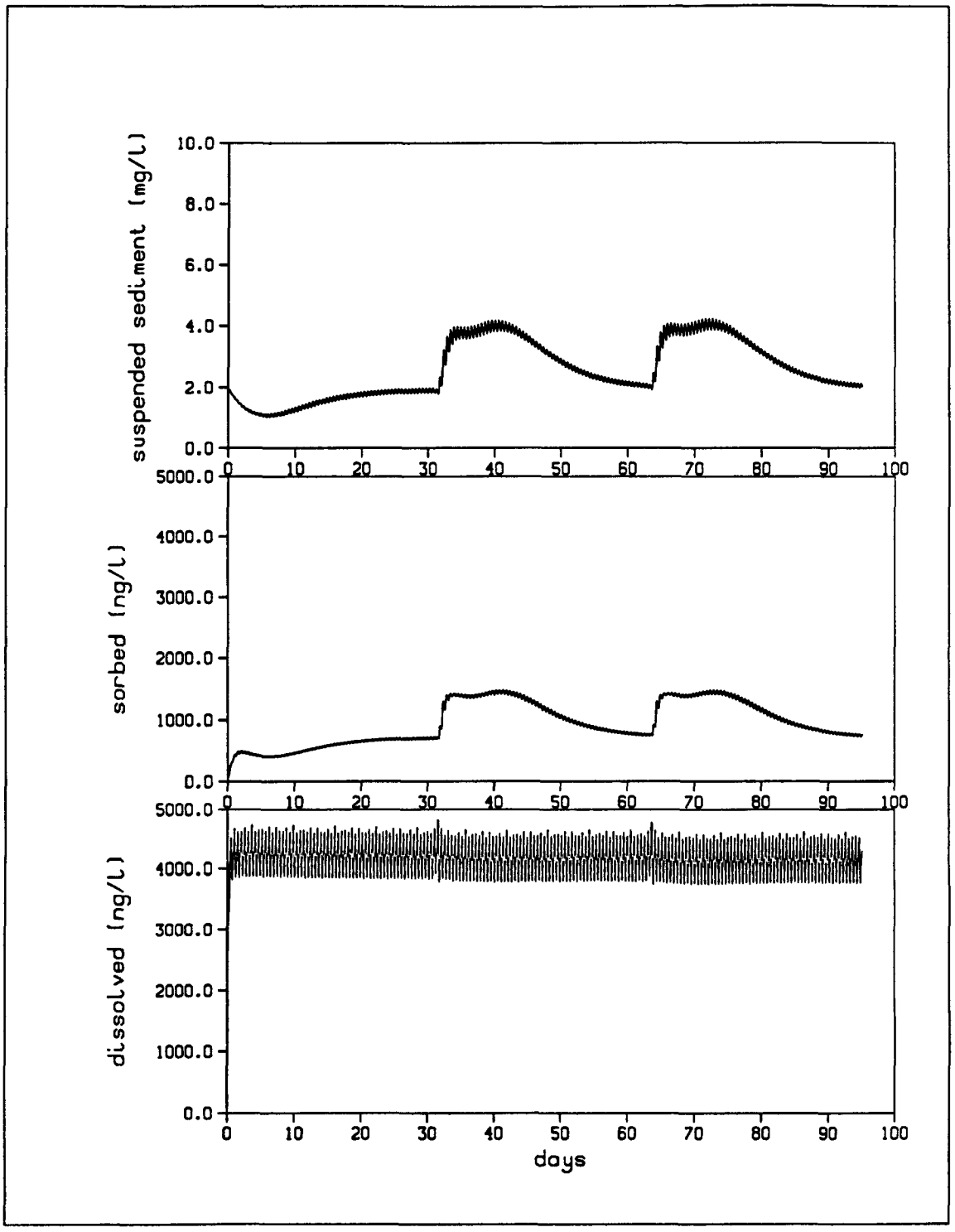

FIGURE 5.77. SEDIMENT AND PCB CONCENTRATION TIME-SERIES COMPUTED USING THE CALIBRATED MODEL. BATTELLE OCEAN SCIENCES STATION 1.

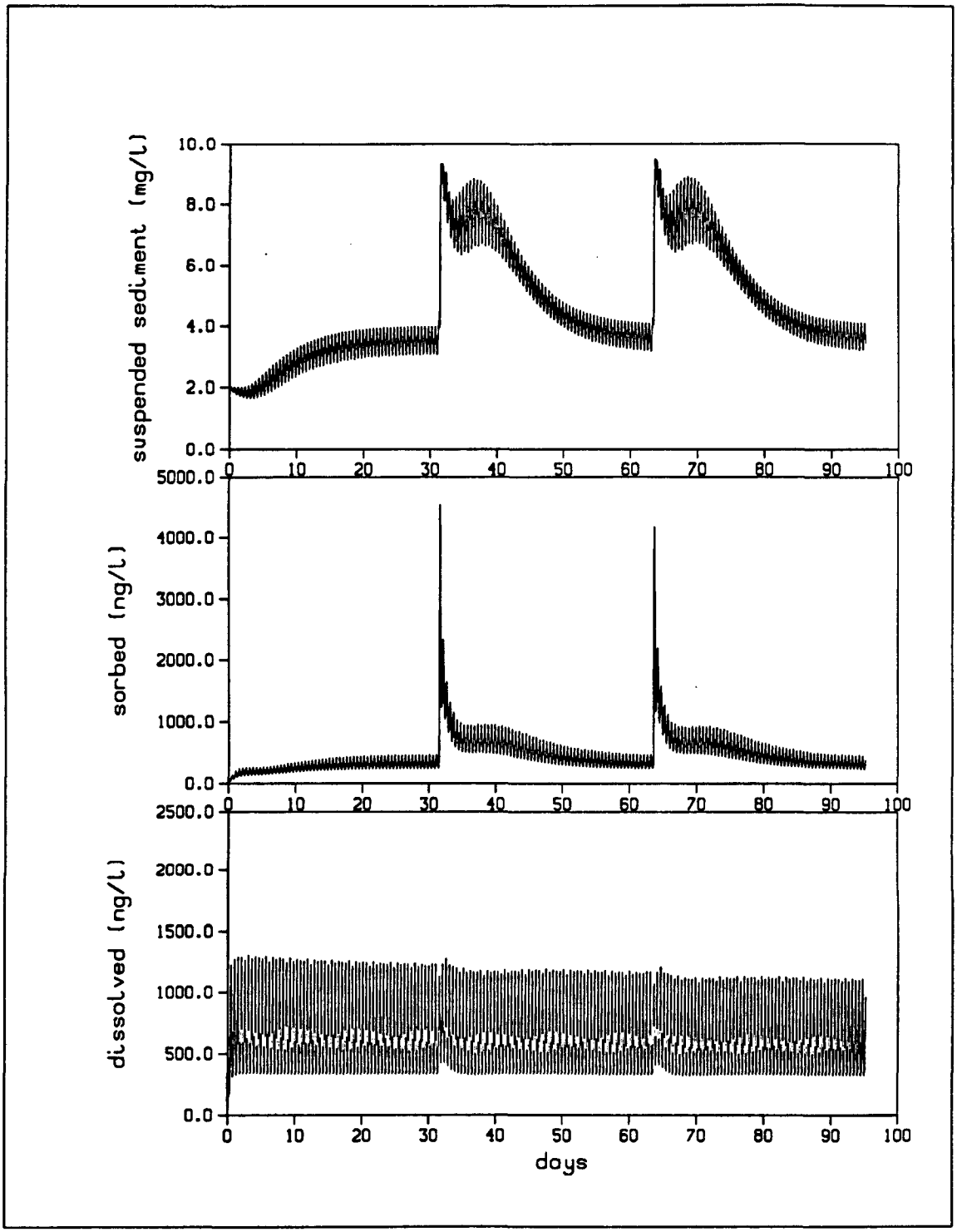

FIGURE 5.78. SEDIMENT AND PCB CONCENTRATION TIME-SERIES COMPUTED USING THE CALIBRATED MODEL. BATTELLE OCEAN SCIENCES STATION 2.

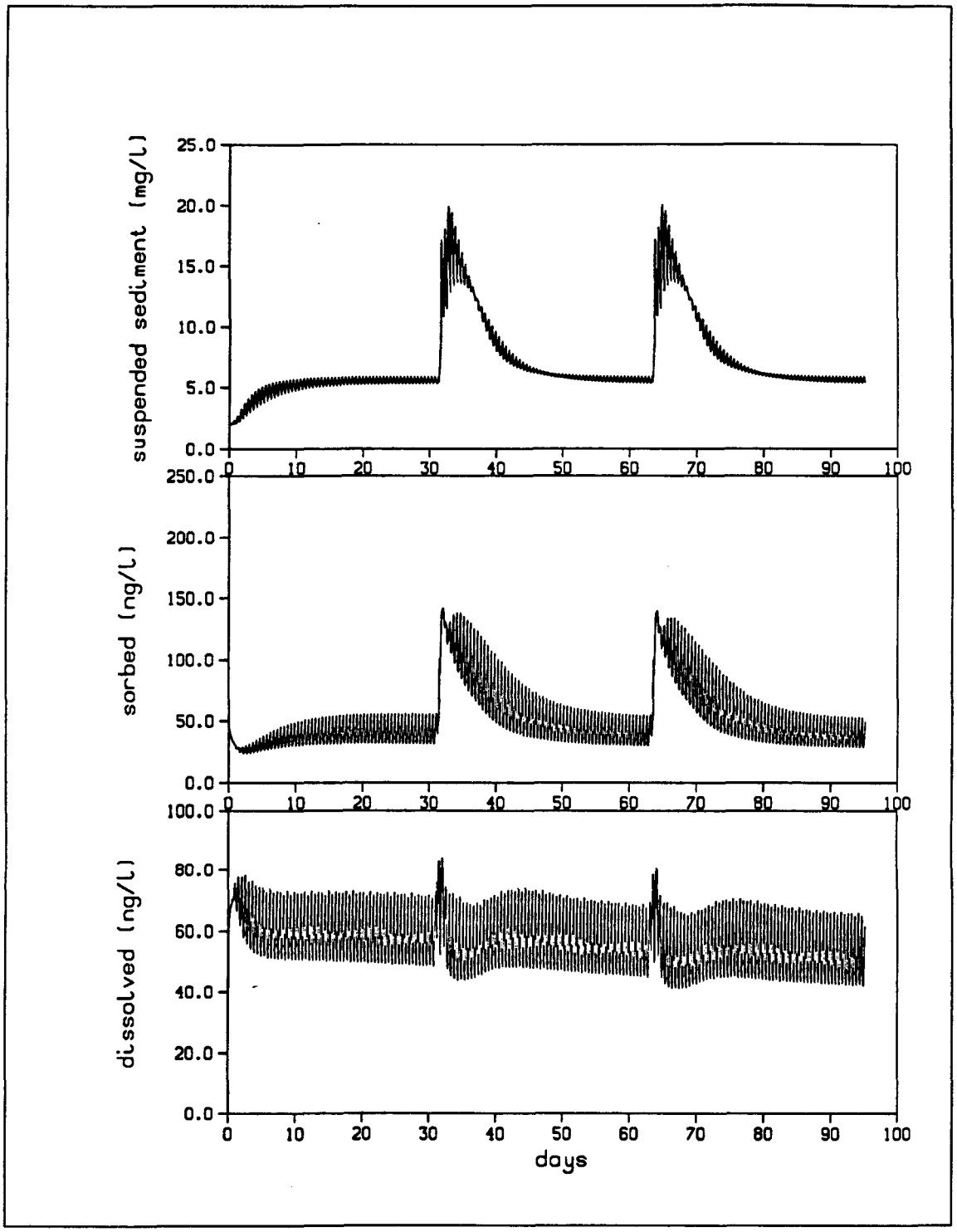

FIGURE 5.79. SEDIMENT AND PCB CONCENTRATION TIME-SERIES COMPUTED USING THE CALIBRATED MODEL. BATTELLE OCEAN SCIENCES STATION 10.

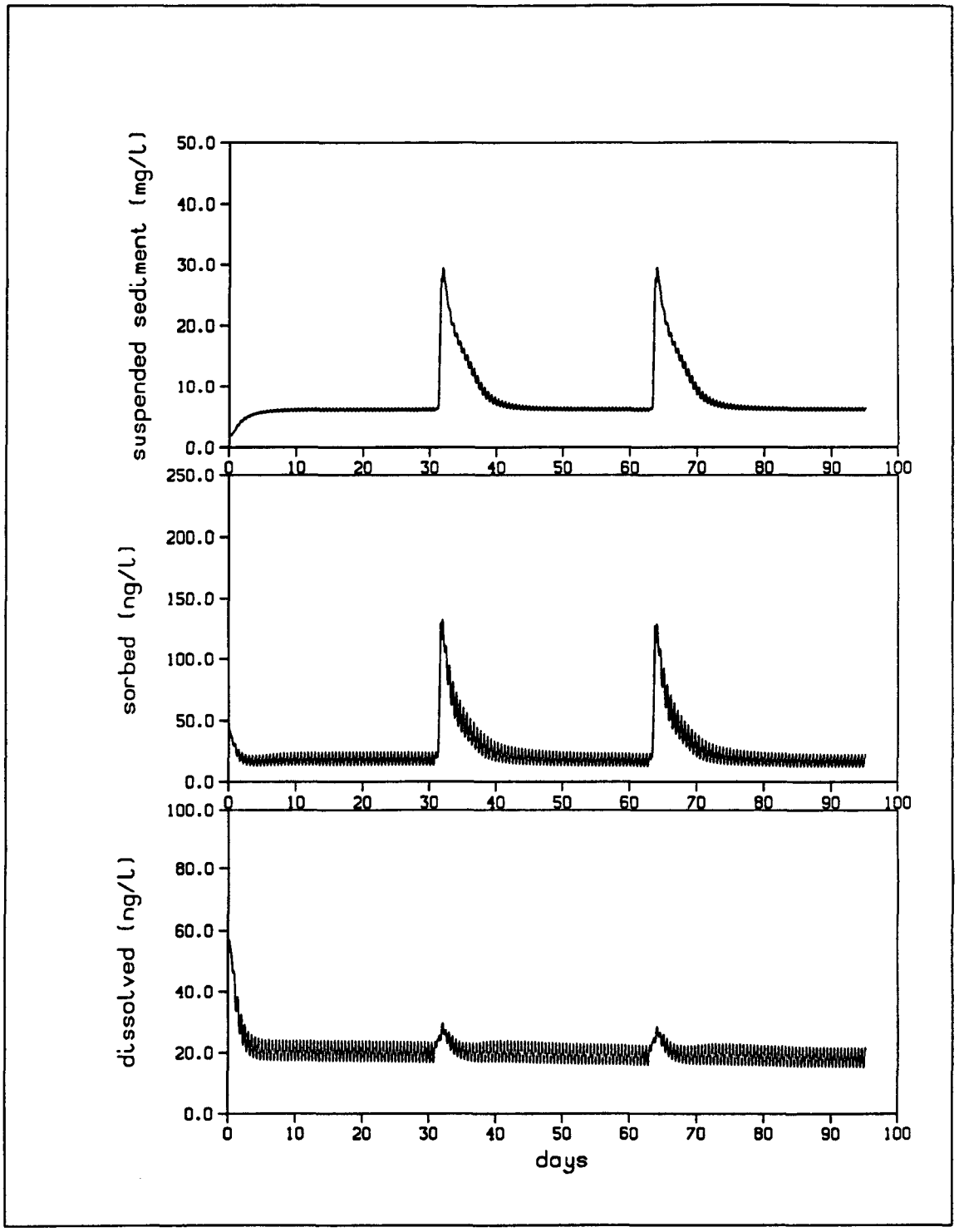

FIGURE 5.80. SEDIMENT AND PCB CONCENTRATION TIME-SERIES COMPUTED USING THE CALIBRATED MODEL. BATTELLE OCEAN SCIENCES STATION 14.

The spatial distribution of PCBs are shown in contour plots in Appendixes B and C. The results at the end of the calibration simulation are equivalent to the results for year 0 of the no-action simulation. The depth-averaged water column concentration for the calibration case in the upper estuary is shown in Figure B.1a, and the concentration of PCBs in the upper estuary bed sediments are displayed in Figure C.1b.

Each PCB calibration simulation yielded reasonable comparisons with the available field data. However, the final calibration parameter set was chosen to be case PCB35, because it showed very little change in the computed PCB concentration in the bed sediments between Popes Island and the hurricane barrier. Concentrations of PCBs in flounder caught in this region have been relatively constant during 1980 to 1986, suggesting that the PCB concentrations in the bed sediments are not changing rapidly.

5.6.2.5 Simulated Transport and Fate Processes

This section further analyzes the calibration simulation results to gain insight into the transport and fate processes simulated by the model.

The net flux of suspended sediments and total PCBs were calculated at several planes in the computational grid. The flux calculation planes, shown in Figure 5.81, were chosen to correspond to the principal constrictions in the system and the open boundary of the model. At the end of each stage the computed sediment and PCB values in each water column and bed cell were averaged over the six boxes. The subsequent box-average water column and bed sediment levels are shown in Figures 5.82 and 5.83, respectively. Over short time periods the box-averaged PCB concentration is relatively constant. Using the computed concentrations of the constituents in each grid cell and the volume of each cell, the total mass of the constituents was computed for the cells residing in each box. The box-averaged water column concentration was then calculated by dividing the box mass by the box volume. The box-averaged bed layer concentration was computed by dividing the bed layer mass by the sediment mass in the bed layer. In the following discussion the model results

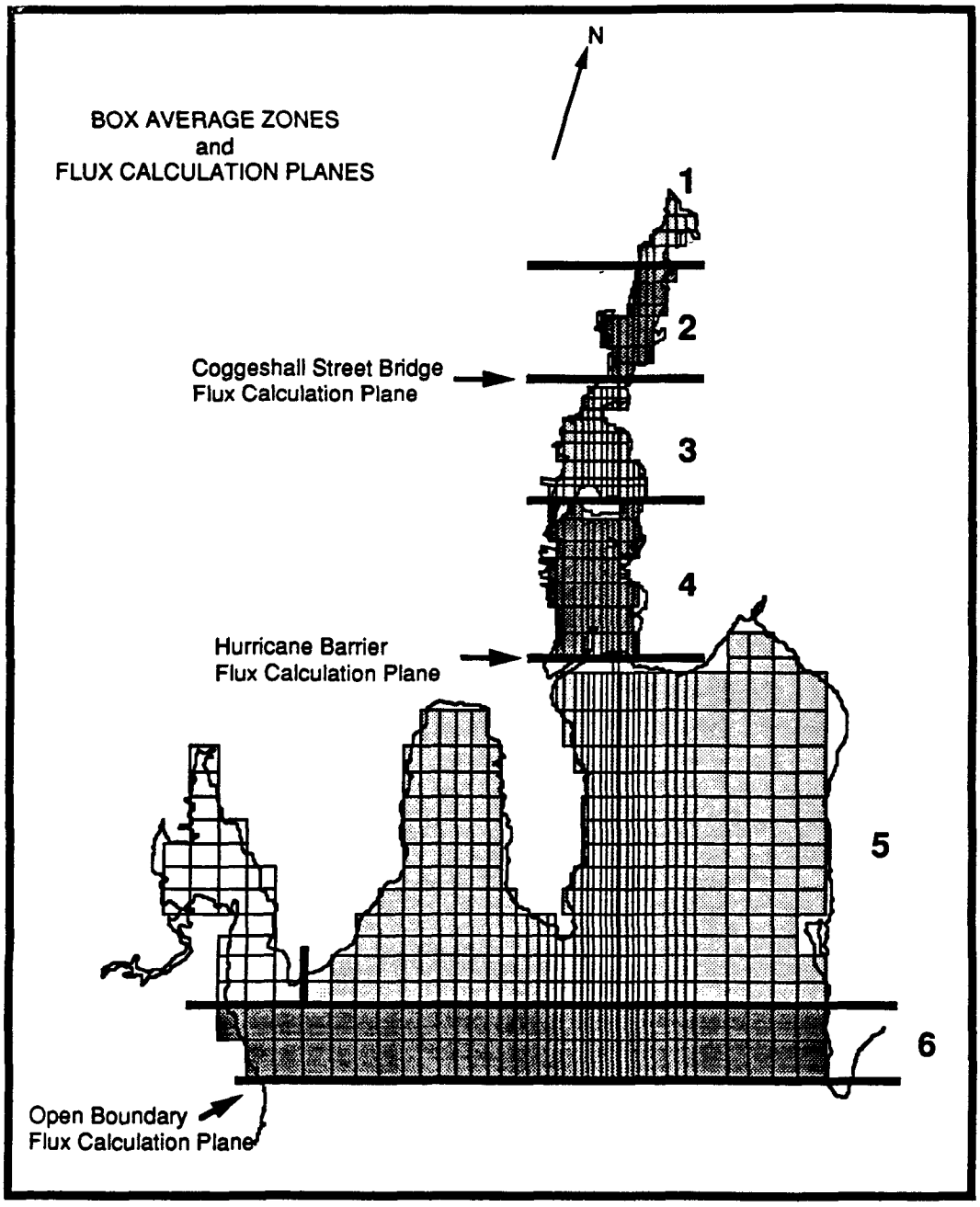

FIGURE 5.81. BOX-AVERAGING ZONES AND FLUX CALCULATION PLANES

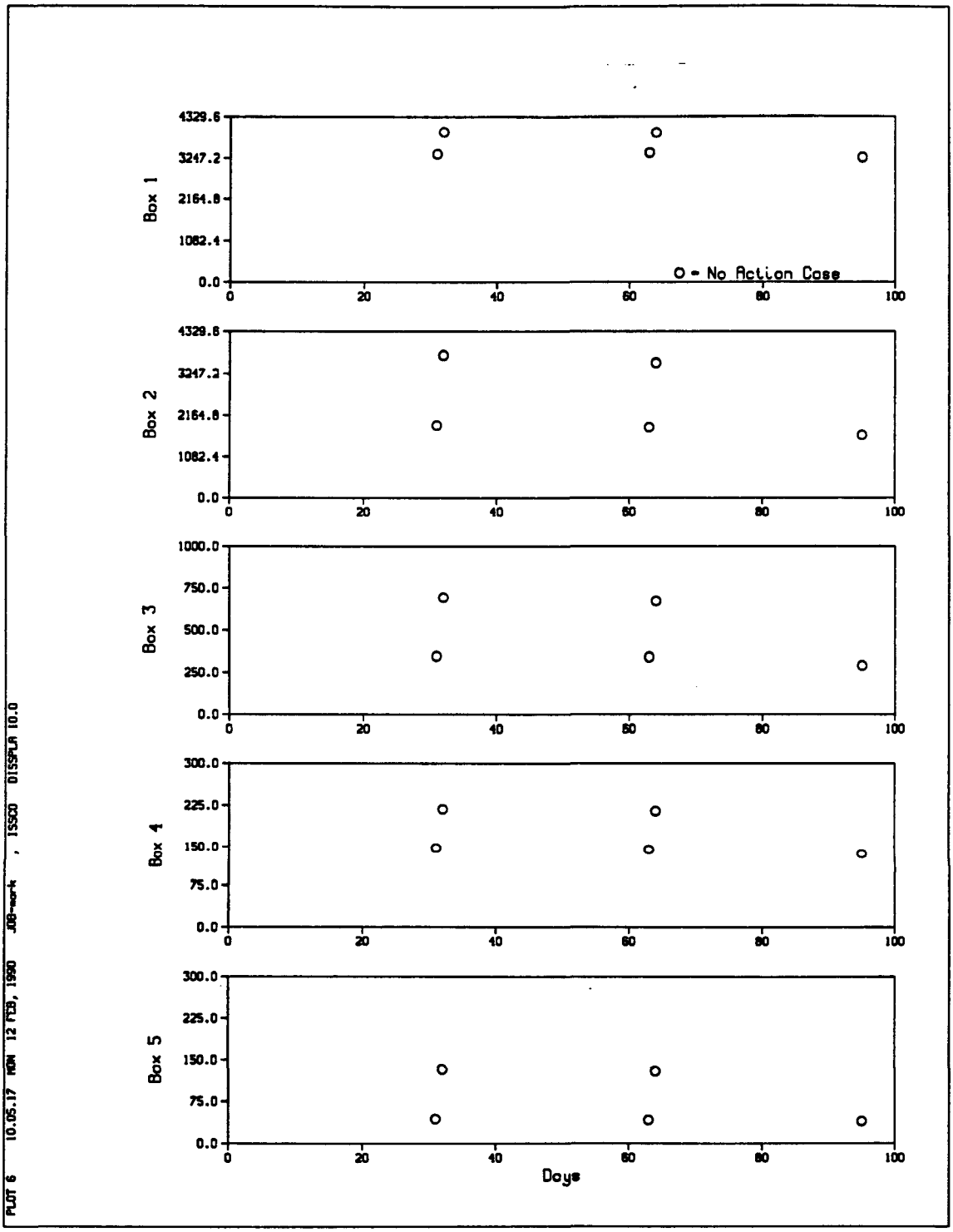

FIGURE 5.82. BOX-AVERAGED MODEL RESULTS FOR THE CALIBRATED MODEL (NO ACTION CASE). TOTAL PCB CONCENTRATION (ng/L) IN THE WATER COLUMN.

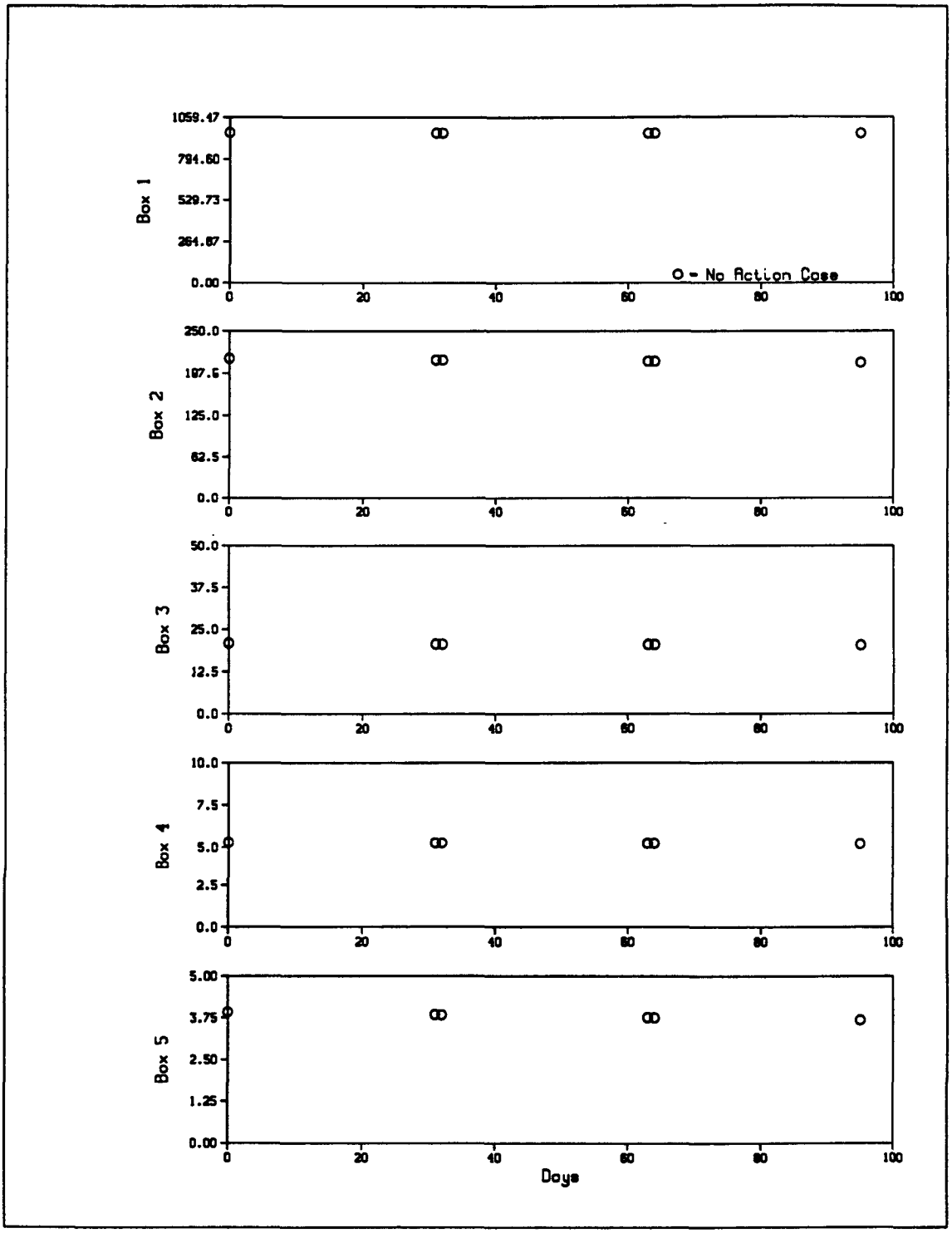

FIGURE 5.83. BOX-AVERAGED MODEL RESULTS FOR THE CALIBRATED MODEL (NO ACTION CASE). TOTAL PCB CONCENTRATION (mg/kg) IN THE BED SEDIMENT LAYER.

are further aggregated into three primary regions: the upper estuary region represented by boxes 1 and 2, the lower-harbor region represented by boxes 3 and 4, and the outer harbor, the area between the hurricane barrier and the open boundary. Using the flux and box-averaged results, one can perform mass balances over the key geographic regions in the study area.

The computed net flux of sediments and PCBs through the three flux planes are shown in Table 5.7. The upper estuary and inner harbor are depositional areas for sediments. This is in agreement with the field measurements of Teeter (1988). In the area outside of the hurricane barrier, sediments are being transported out of the system into Buzzards Bay. This is caused, in part, by the modeled sediment transport for this large area still being in the process of coming into equilibrium with the specified initial bed conditions and the open-boundary condition.

The net flux of PCBs through each plane is toward Buzzards Bay. PCBs are being transported out of the upper estuary through Coggeshall Street bridge into the lower harbor. Similarly, PCBs are moving through the hurricane barrier and the open boundary into Buzzards Bay.

TABLE 5.7. NET FLUX OF SEDIMENTS AND PCBs COMPUTED IN THE CALIBRATION SIMULATION

	Coggeshall Street Bridge	Hurricane Barrier	Open Boundary
Sediment Flux (kg/tidal cycle)	446	1.546×10^3	-2.4641×10^4
PCB Flux (kg/tidal cycle)	-0.22	-0.15	-1.32

Tables 5.8 through 5.13 present a mass balance analysis for the three regions within the model. Each table gives the initial and final mass of sediments or total PCBs in the water column and bed layer. Also included in the tables is

TABLE 5.8. SEDIMENT MASS BALANCE IN THE UPPER ESTUARY

	Initial Mass (kg)	Net Mass Flux (kg)	Final Mass (kg)	Change (kg)
Mass in the Water Column	2.945×10^3	8.2×10^4	4.442×10^3	1.497×10^3
Mass in the Bed Layer	4.972×10^7	N/A	4.98×10^7	8.0×10^4

TABLE 5.9. PCB MASS BALANCE IN THE UPPER ESTUARY

	Initial Mass (kg)	Net Mass Flux (kg)	Final Mass (kg)	Change (kg)
Mass in the Water Column	0.39	-40.0	2.88	2.49
Mass in the Bed Layer	1.9714×10^4	N/A	1.943×10^4	-284

TABLE 5.10. SEDIMENT MASS BALANCE IN THE LOWER HARBOR

	Initial Mass (kg)	Net Mass Flux (kg)	Final Mass (kg)	Change (kg)
Mass in the Water Column	3.2398×10^4	2.02282×10^5	8.046×10^4	4.8062×10^4
Mass in the Bed Layer	1.6567×10^8	N/A	1.6586×10^8	1.9×10^5

TABLE 5.11. PCB MASS BALANCE IN THE LOWER HARBOR

	Initial Mass (kg)	Net Mass Flux (kg)	Final Mass (kg)	Change (kg)
Mass in the Water Column	1.58	13.42	2.62	1.04
Mass in the Bed Layer	1.778×10^3	N/A	1.733×10^3	-45

TABLE 5.12. SEDIMENT MASS BALANCE IN THE OUTER HARBOR

	Initial Mass (kg)	Net Mass Flux (kg)	Final Mass (kg)	Change (kg)
Mass in the Water Column	3.333×10^5	-4.815596×10^6	9.654×10^5	6.321×10^5
Mass in the Bed Layer	1.4023×10^9	N/A	1.3988×10^9	-46×10^6

TABLE 5.13. PCB MASS BALANCE IN THE OUTER HARBOR

	Initial Mass (kg)	Net Mass Flux (kg)	Final Mass (kg)	Change (kg)
Mass in the Water Column	15.53	-215.5	5.15	-10.38
Mass in the Bed Layer	4.492×10^3	N/A	4.206×10^3	-286

the net flux of sediments or PCBs into or out of the region through the flux planes. The net flux is computed using the information in Table 5.7 and the 184 tidal cycles in the 95-day simulation period.

As evidenced by the net flux computations, the upper estuary is a depositional area for sediments. During the course of the 95-day calibration simulation the upper estuary gained an additional 82,000 kg of sediment. Although sediments with sorbed PCB were being transported and deposited into the upper estuary, the mass of PCBs in the bed sediments decreased by 284 kg. This indicates that mass transfer of PCBs from the bed to the water column, modeled as a mass transfer is greater than mass transfer through erosion or deposition. Initially the PCB concentration in the bed sediments was approximately 397 mg/kg. Had all the sediment that was added to the bed layer been deposited with a zero sorbed-PCB concentration and no PCB mass been lost from subsequent desorption, the resulting average concentration would have been 396 mg/kg. The actual final concentration was 390 mg/kg. Thus, even under ideal conditions, deposition of cleaner sediments is not a significant transport process in the upper estuary. Here, volatilization of PCBs is the most significant process. Approximately 283 kg of PCBs were lost from the upper estuary, and of this amount, roughly 40 kg were transported out under Coggeshall Street Bridge. Hence, 243 kg of PCBs were removed from the upper estuary through volatilization.

The importance of volatilization is further evidenced by the mass balance calculations for the lower-harbor region. This area receives a net influx of PCBs from the upper estuary, while a lesser amount of PCBs are transported out through the hurricane barrier. Nevertheless, the lower harbor still experienced a net PCB loss of 44 kg. Although sediment deposition is occurring in the lower harbor, this process does not make a significant contribution to the transport of PCBs. The average concentration of PCBs within the bed sediments changes very little; the initial and final concentrations are 10.7 and 10.5 mg/kg, respectively.

Volatilization accounts for only 81 kg of the PCB transport in the deeper waters outside the hurricane barrier. PCB transport by sediment erosion accounts for approximately 14 kg of the 286 kg that is lost from the bed in the outer harbor. This estimate is based on the mass of sediment eroded from the bed and an average PCB concentration of 3.0 mg/kg. Again, mass transfer of PCBs from the bed to the water column and subsequent transport in the water is the most significant process.

In summary, the most important PCB transport processes occurring in the calibration simulations is the transfer of PCBs from the bed to the overlying water through direct desorption. Once in the water column, PCBs are volatilized in significant amounts in the shallow areas of the upper estuary. PCBs are also transported toward Buzzards Bay through the action of tidally driven flow. Although these observations are in general agreement with field measurements, the estimated concentrations computed by the model should be used as a baseline to compare the relative effectiveness of the modeled remedial actions. The results should not be viewed in an absolute sense, because a rigorous validation of the model was not possible.

6.0 FOOD CHAIN MODEL CALIBRATION AND VALIDATION

6.1 INTRODUCTION

The food chain model used to compute PCB and metals concentrations in the New Bedford Harbor lobster and flounder food chains is formulated from equations that describe the uptake and loss of chemical by species representative of the major predator-prey links from the base of the food chain to the animals of interest. These equations are developed from bioenergetics and consider the uptake of chemical from water and food, the loss of chemical by excretion and the dilution of chemical by growth. The development and application of the model involves the following steps:

1. Determination of the species that form the food chain of the animals of interest (i.e., the lobster and the winter flounder) and the predator-prey relationships between these species,

2. Quantification of the rates of growth and respiration of each species and the dependence of these rates on temperature and animal size or age,

3. Estimation of the efficiency of food assimilation for each predator,

4. Analysis of the water column and sediment chemical concentration data to determine the average concentrations to which animals within a defined region are exposed and analysis of biota concentrations to determine the average concentration in each animal within the defined region,

5. Determination of appropriate ranges for the rates of chemical uptake and excretion for bounding these parameters during model calibration,

6. Calibration of the model by determining the uptake and excretion rate values that result in computed chemical concentrations that quantitatively agree with measured values and are consistent with laboratory and field measurements of these parameters,

7. Projection of the response of the animals to changes in water and sediment chemical concentrations that the physical-chemical model projects will result from various remedial alternatives.

Each of these steps is described in detail in the following sections. The analysis of the water, sediment and biota data is presented first to provide a sense of the magnitude and spatial variability of contamination within the system. This is followed by a presentation and discussion of the equations that form the model. The determination of appropriate values for the parameters describing each process included in the equations is then described.

Finally the calibration of the model for both the PCBs and for the metals cadmium, copper and lead is presented. The projections of the PCB response of the animals to the various remedial actions are presented in Section 7. Since the physical/chemical model only evaluated total PCB fate and transport, the food chain model did not evaluate the metals past the calibration phase. However, the calibrated food chain model is prepared to predict the response of biota to changes in metal exposure conditions should this information subsequently become available.

6.2 ANALYSIS OF PCB AND HEAVY METALS DATA

The PCB and heavy metals measurements conducted as part of this project (i.e., the RIFS cruise data) form the calibration data set for the food chain model. The water column and sediment measurements provide estimates of the contaminant concentrations to which the biota were exposed. The biota measurements provide body estimates against which the food chain model was calibrated. Our analysis of these data was directed to determining appropriate levels of aggregation and averaging, to computing mean and variance at those levels and to evaluating various assumptions made in the development and application of the model. In particular, we evaluated changes in concentrations between cruises and between the RIFS data and earlier measurements. Between-cruise changes were examined to determine if it was appropriate to average concentrations over all cruises. Historical data were compared to the RIFS data to assess temporal trends in biota contamination and evaluate the validity of assuming that the exposure concentrations were constant over each animal's life span. This assumption was invoked to calibrate the food chain model because insufficient data are available to estimate a time history of water column and sediment concentrations.

6.2.1 Segmentation of the Study Area

Historical PCB measurements of water, sediment and biota have demonstrated that a significant concentration gradient exists. Concentrations are highest in the Acushnet River near the Aerovox facility and decline down river and through the Outer Harbor into Buzzards Bay. Consistent with this gradient, the fishery closure established in 1979 by the Massachusetts Department of Public Health is divided into three areas. The area north of the hurricane barrier (i.e., the Inner Harbor, Area 1) is closed to the taking of all finfish, shellfish and lobsters.

The Outer Harbor (Area 2), extending from the hurricane barrier to a line from Wilber Point to Ricketsons Point, is closed to the taking of lobster and bottom-feeding finfish including eel, scup, flounder and tautog. Between the outer harbor and a line from the southern tip of West Island to Round Hill Point (Area 3) only the lobster fishery is closed.

It was considered desirable that predictions of contaminant concentrations in the lobster and flounder and their food chains be applicable to each of the areas of closure. This was to assist in estimating the time until closures may be lifted. Therefore, food chains are considered for each of the closure areas. Initially a fourth area representative of the Buzzards Bay region south of Area 3 was planned to be modeled. However, this region was not modeled past the calibration phase since the physical/chemical model did not extend this far into Buzzards Bay. Area 1 is restricted to the region between the hurricane barrier and the Route 6 bridge, the area assumed to be the habitat of the species of interest. The area locations are shown on Figure 6.1.

6.2.2 Historical Data

The PCB biota measurements made in New Bedford Harbor and Buzzards Bay between 1976 and 1986 were compiled to develop an assessment of the temporal trend in flounder and lobster PCB concentrations. In addition to the RIFS cruise data from this study, data were obtained from two sources:

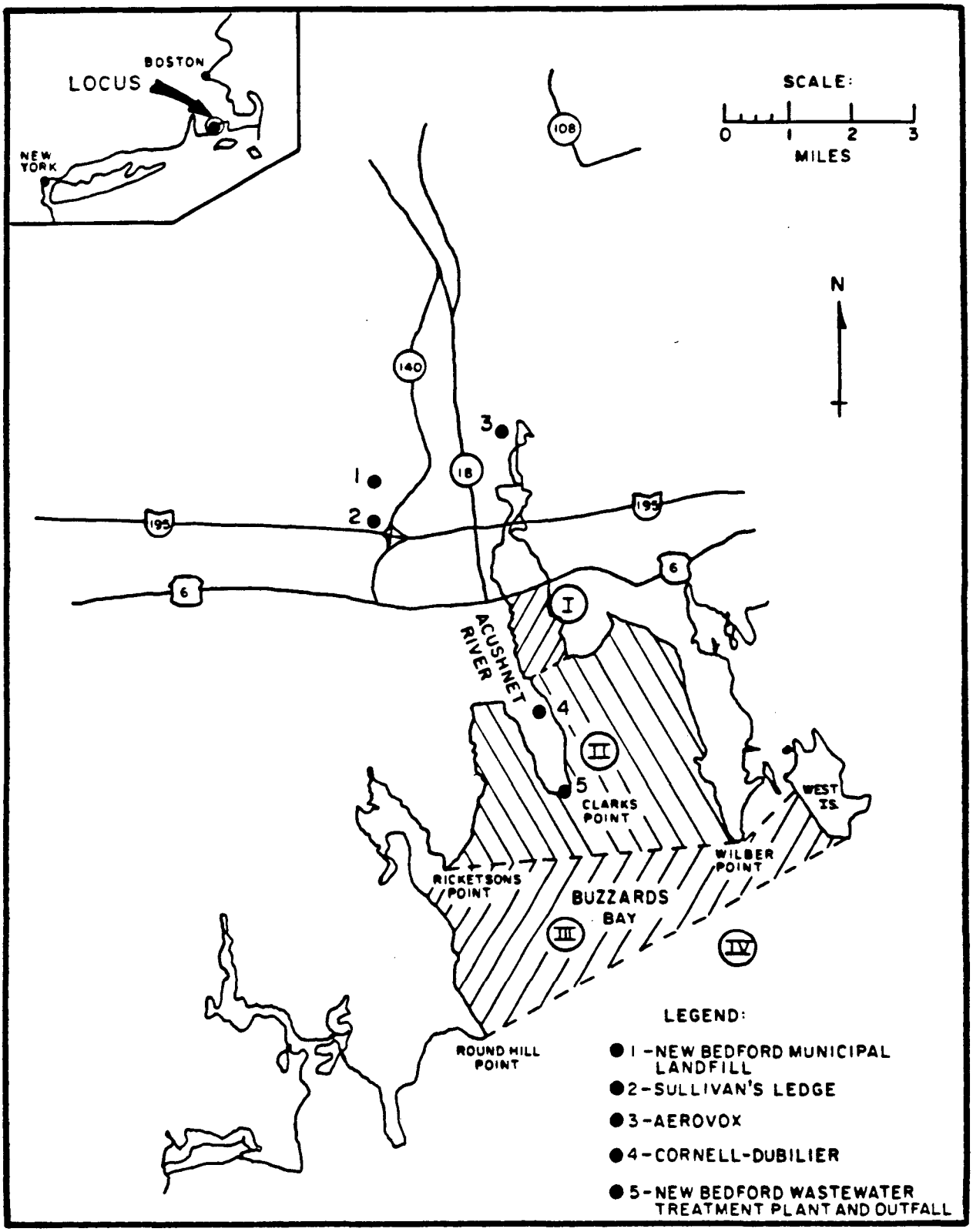

FIGURE 6.1. SEGMENTATION OF THE STUDY AREA FOR FOOD CHAIN MODEL

1. The Acushnet Estuary PCB data base compiled by Metcalf and Eddy, includes data from 1976 through 1982, and

2. Massachusetts Division of Marine Fisheries Data includes data from 1976 through 1986.

Average PCB concentrations in flounder were calculated for each year using data from each data base. For comparison with the Battelle cruise data, historical measurements of PCB in flounder edible tissue were converted to a whole body basis using the muscle-to-whole body ratio developed in this study (see subsequent discussion). Figure 6.2 presents the average flounder PCB concentrations for each area. The data from the Acushnet Estuary and the Division of Marine Fisheries data bases are Aroclor 1254. The Battelle data are total PCB (sum of homologs 2 through 9). Area 1 includes only the area from the Route 6 bridge to the hurricane barrier. A decrease in PCB concentration in all four areas was observed between 1976 and 1980. The concentrations in flounder remained relatively constant from 1980 to 1986.

Average concentrations of PCBs in lobster were calculated for each year data were available. The lobster data from the Acushnet Estuary and the Massachusetts Division of Marine Fisheries data bases are expressed as concentration of Aroclor 1254 in edible tissue. The Battelle data base lobster PCB concentrations are whole body total PCB (sum of homologs 2 through 9).

Historical lobster data were not available for Area 1 between the Route 6 bridge and the hurricane barrier. Figure 6.3 presents the average concentrations. The 1979 values in the three areas are higher than the preceding or following year indicating either an unexplained increase in exposure concentration or a measurement problem. Excluding 1979 there is little variation of concentration from 1977 to 1986. The 1984 and 1985 concentrations, if expressed in terms of edible tissue, may be higher than the whole body concentrations which are plotted.

Four cruises were conducted by Battelle in New Bedford Harbor and Buzzards Bay in 1984 and 1985. Sediment, water column and biota samples were taken

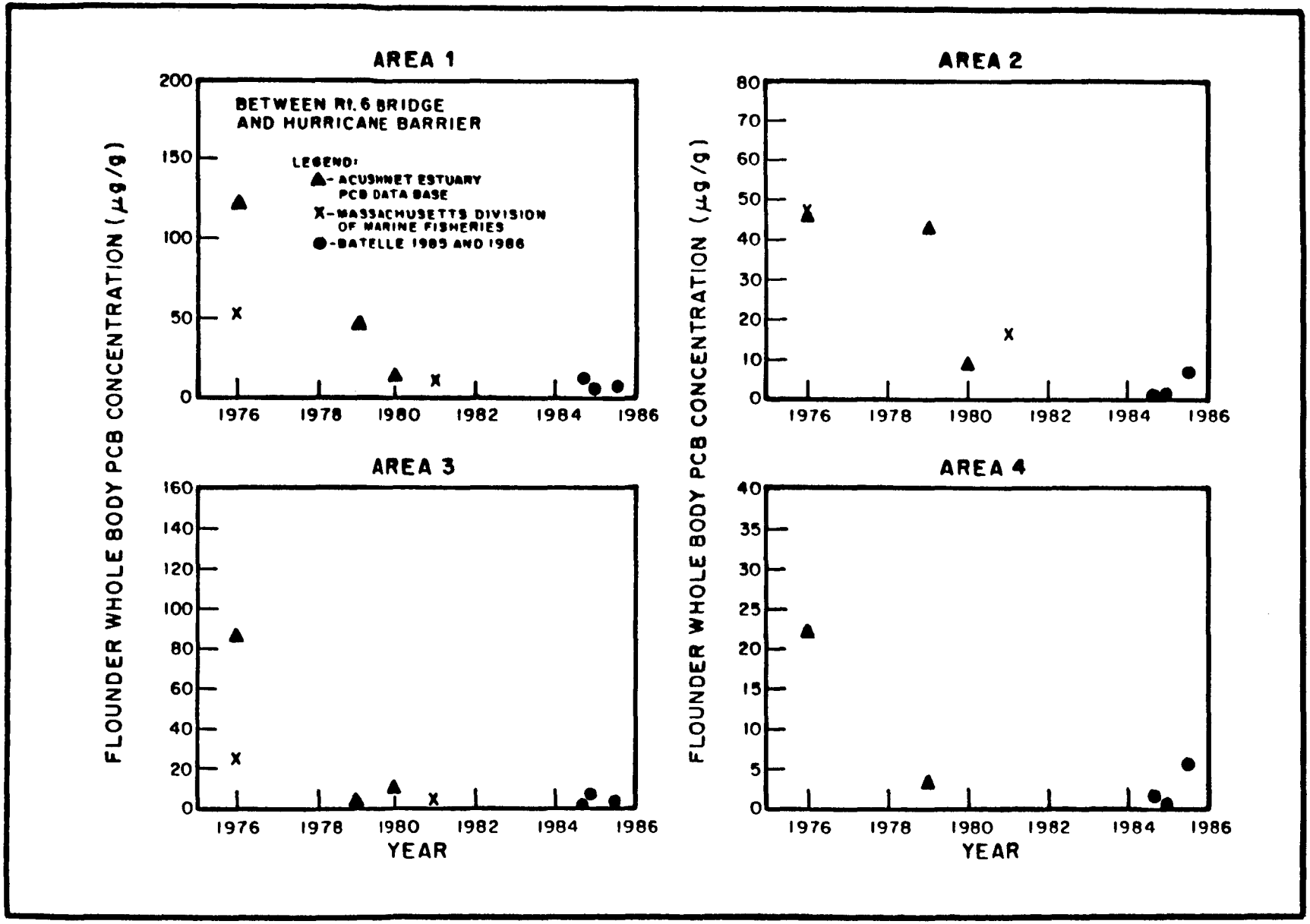

FIGURE 6.2. PCB CONCENTRATION IN FLOUNDER 1976-1986

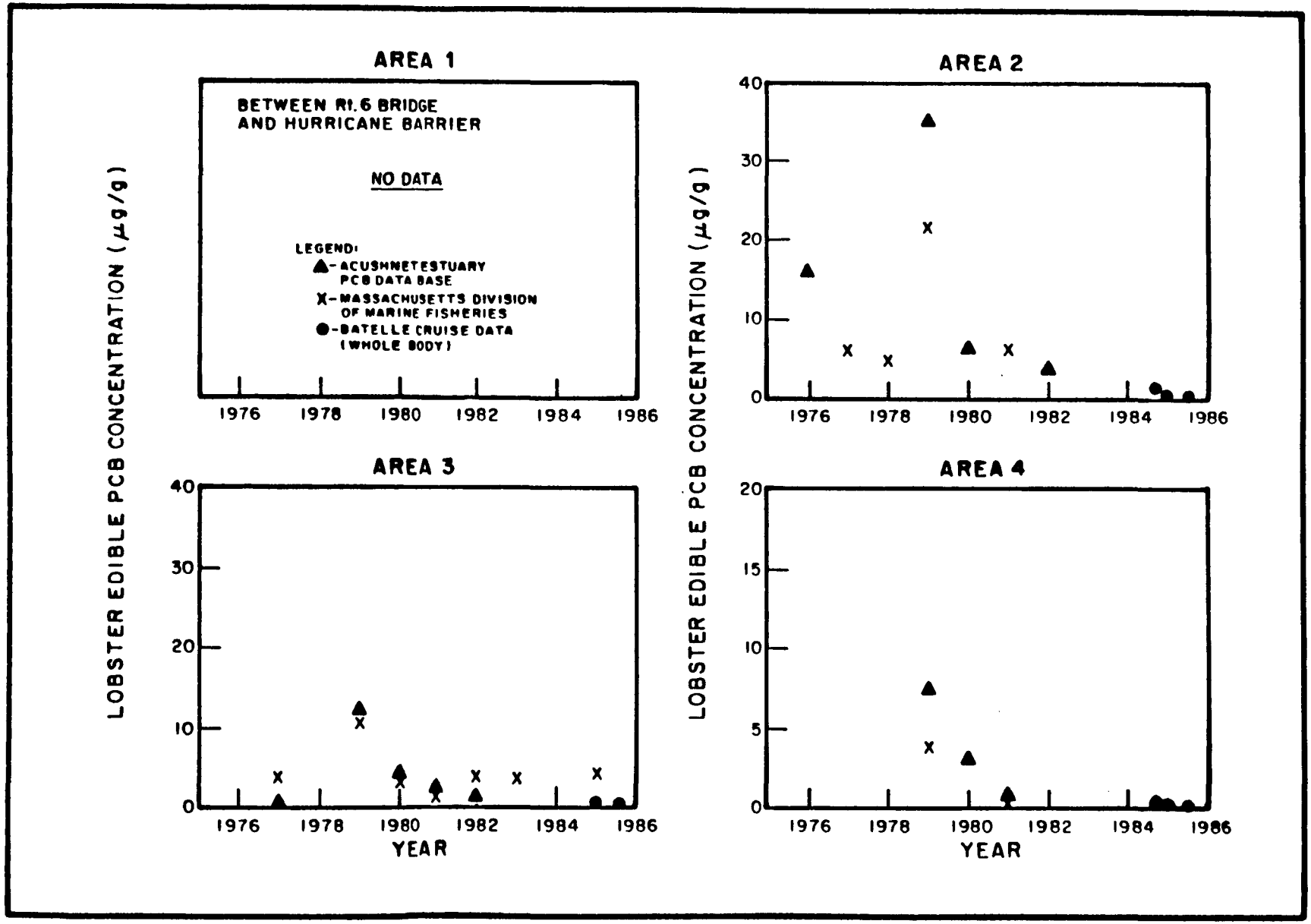

FIGURE 6.3. PCB CONCENTRATION IN LOBSTER 1976-1986

during the first three cruises in September/October 1984, December 1984 and June 1985. Only water column and sediment samples were taken during the fourth cruise which was a storm cruise.

Water column and sediment samples were collected at ten stations in the inner harbor (of which stations 5 and 7 through 10 are in Area 1), seven stations in the outer harbor (Area 2), two stations in inner Buzzards Bay (Area 3), and six stations in outer Buzzards Bay (Area 4) during all four cruises. Trawls were conducted for biota collection in Area 1 between Popes Island and the hurricane barrier and in the other three areas.

Although PCB concentrations were reported for homologs 2 through 9, only homologs 3 through 6 were modeled. A limited number of samples were analyzed for homologs 1 and 10 but were not included in the data analysis. The choice of homologs 3 through 6 was based on the presumption that they represent nearly all of the PCB present in the system. Comparisons of the log-normal probability distributions of the sum of homologs 3 through 6 and total PCB (i.e., the sum of homologs 2 through 9) for dissolved and particulate water column data and sediment data (Appendix J) and biota data (Appendix K) in each of the four areas or segments indicate that the presumption is valid. In all cases the total PCB and sum of homologs 3 through 6 distributions are essentially identical.

The primary objective of the analysis of the cruise data was to establish the area average water column and sediment contaminant concentrations to which the biota were exposed. The data were first screened to determine specific stations or data points that would incorrectly bias an area average. This judgement was made by visual inspection of log normal probability distributions of the PCB and metals data from the four cruises. Data points that deviated significantly from the distribution indicated in the plot (i.e., values that were either unreasonably high or unreasonably low) were not included in subsequent data averaging. Cruise averages were computed for each of the four areas. Finally, area averages over all cruise were computed.

6.2.3.2 Water Column Data

Dissolved and particulate water column samples were typically analyzed for PCB homologs 2 through 9 and the metals cadmium, copper and lead. The particulate samples were also analyzed for particulate organic carbon and silt and clay content.

Samples were collected at the surface and bottom at most stations. Probability distributions of the surface and bottom PCB and metals concentrations indicate little difference between the surface and bottom data (see Appendix G). Therefore, surface and bottom samples were not segregated in the data analysis.

Log probability distributions for the PCB homologs 3, 4, 5, and 6, total PCB and the metals cadmium, copper, and lead are presented in Appendix H. The data conform well to the assumption of log-normality as indicated by the linearity of the plots. Few outlying points are revealed in the distributions.

The data excluded from the averages are indicated by solid symbols in the probability plots. To compute area average concentrations the data were initially assumed to be log-normally distributed and averages of the log-transformed data were computed. Arithmetic means were computed from the means and standard deviation of the log-transformed data by using the equations derived from the relationship of the normal and log-normal probability functions and by a maximum-likelihood estimation technique (Aitchison and Brown, 1981). A comparison of these estimates with the direct computation of the area average is presented for total PCB as Table 6.1, for cadmium as Table 6.2, for copper as Table 6.3 and for lead as Table 6.4. In all cases the three estimates are nearly identical, indicating that the data are approximately normally distributed. In subsequent uses of the area averages the direct arithmetic values are used. Arithmetic averages for each of the PCB homologs are presented in Table 6.5.

TABLE 6.1. COMPARISON OF AREA AVERAGE TOTAL DISSOLVED PCB CONCENTRATIONS (ng/L) COMPUTED FROM ARITHMETIC AND LOG STATISTICS

					Arithmetic Estimates		Log Estimates			
							Direct		Max Likelihood	
		# pts	max	min	mean	CV	mean	CV	mean	CV
Area 1	Cruise 1	22	223.5	23.6	74.7	0.715	73.5	0.618	72.9	0.600
	Cruise 2	20	150.3	9.7	51.8	0.520	52.6	0.534	53.2	0.521
	Cruise 3	22	403.2	28.1	95.9	0.966	91.9	0.754	90.8	0.722
	Cruise 4	4	24.5	14.3	18.4	0.252	18.5	0.247	18.4	0.242
Area 2	Cruise 1	26	177.3	1.5	32.9	1.286	33.1	1.320	32.2	1.190
	Cruise 2	25	58.4	2.2	15.8	0.788	16.1	0.852	15.9	0.812
	Cruise 3	24	60.9	1.4	18.8	1.046	20.2	1.040	19.3	1.410
	Cruise 4	4	17.6	5.3	11.2	0.590	11.9	0.724	11.2	0.630
Area 3	Cruise 1	10	5.3	0.5	2.9	0.575	3.2	0.979	3.0	0.862
	Cruise 2	10	2.6	0.8	1.8	0.350	1.9	0.447	1.9	0.433
	Cruise 3	10	4.5	1.7	3.4	0.261	3.4	0.304	3.4	0.299
	Cruise 4	2	2.9	1.3	2.1	0.528	2.3	0.599	2.1	0.527
Area 4	Cruise 1	24	6.7	0.4	2.1	0.757	2.1	0.854	2.1	0.812
	Cruise 2	23	6.0	0.3	2.1	0.631	2.2	0.784	2.2	0.749
	Cruise 3	23	5.6	0.3	2.4	0.604	2.7	1.060	2.6	0.978
	Cruise 4	4	4.7	1.1	2.6	0.659	2.8	0.814	2.6	0.688

CV: coefficient of variation.

TABLE 6.2. COMPARISON OF AREA AND CRUISE DISSOLVED METALS CONCENTRATIONS FOR CADMIUM (units mg/L)

					Arithmetic Estimates		Log Estimates			
							Direct		Max Likelihood	
		# pts	max	min	mean	CV	mean	CV	mean	CV
Area 1	Cruise 1	19	0.180	0.027	0.087	0.424	0.088	0.487	0.088	0.476
	Cruise 2	21	0.430	0.100	0.200	0.335	0.200	0.307	0.199	0.304
	Cruise 3	22	0.230	0.020	0.109	0.477	0.111	0.500	0.110	0.540
	Cruise 4	4	0.100	0.044	0.075	0.342	0.076	0.307	0.075	0.370
Area 2	Cruise 1	17	0.125	0.024	0.060	0.394	0.060	0.419	0.060	0.411
	Cruise 2	17	0.143	0.030	0.075	0.343	0.075	0.334	0.075	0.330
	Cruise 3	17	0.257	0.010	0.080	0.657	0.081	0.622	0.001	0.599
	Cruise 4	2	0.052	0.020	0.040	0.424	0.042	0.400	0.040	0.425
Area 3	Cruise 1	0	0.110	0.024	0.055	0.050	0.050	0.710	0.055	0.057
	Cruise 2	10	0.147	0.020	0.057	0.049	0.050	0.550	0.050	0.530
	Cruise 3	9	0.151	0.041	0.001	0.539	0.001	0.547	0.000	0.521
	Cruise 4	2	0.042	0.012	0.027	0.700	0.033	1.09	0.027	0.700
Area 4	Cruise 1	21	0.070	0.002	0.027	0.731	0.029	1.070	0.020	0.904
	Cruise 2	22	0.077	0.009	0.035	0.400	0.035	0.520	0.035	0.509
	Cruise 3	23	0.073	0.013	0.044	0.394	0.045	0.504	0.045	0.494
	Cruise 4	4	0.002	0.000	0.035	0.752	0.044	1.400	0.037	0.909

CV: coefficient of variation.

TABLE 6.3. COMPARISON OF AREA AND CRUISE DISSOLVED METALS CONCENTRATIONS FOR COPPER (units mg/L)

		# pts	max	min	Arithmetic Estimates		Log Estimates: Direct		Log Estimates: Max Likelihood	
					mean	CV	mean	CV	mean	CV
Area 1	Cruise 1	19	2.669	0.696	1.826	0.283	1.84	0.337	1.84	0.333
	Cruise 2	22	4.682	1.623	2.562	0.312	2.56	0.293	2.56	0.291
	Cruise 3	22	3.800	1.620	2.446	0.257	2.44	0.268	2.44	0.259
	Cruise 4	4	1.153	1.064	1.115	0.037	1.11	0.037	1.11	0.037
Area 2	Cruise 1	17	2.196	0.903	1.448	0.313	1.44	0.314	1.44	0.311
	Cruise 2	17	2.240	0.536	1.058	0.389	1.06	0.376	1.06	0.371
	Cruise 3	18	2.390	0.530	1.452	0.368	1.47	0.365	1.46	0.361
	Cruise 4	2	1.143	0.835	0.989	0.226	1.00	0.225	0.989	0.226
Area 3	Cruise 1	8	2.260	0.240	0.945	0.690	0.991	0.835	0.954	0.744
	Cruise 2	10	0.658	0.416	0.538	0.146	0.538	0.149	0.537	0.148
	Cruise 3	9	1.200	0.417	0.836	0.312	0.839	0.351	0.833	0.344
	Cruise 4	2	0.601	0.564	0.582	0.045	0.583	0.045	0.582	0.045
Area 4	Cruise 1	22	1.160	0.127	0.511	0.565	0.519	0.652	0.515	0.630
	Cruise 2	24	1.969	0.155	0.572	0.671	0.569	0.593	0.565	0.578
	Cruise 3	24	1.350	0.193	0.646	0.369	0.653	0.426	0.651	0.420
	Cruise 4	4	0.590	0.341	0.474	0.226	0.477	0.234	0.474	0.230

CV: coefficient of variation.

TABLE 6.4. COMPARISON OF AREA AND CRUISE DISSOLVED METALS CONCENTRATIONS FOR LEAD (units mg/L)

		# pts	max	min	Arithmetic Estimates		Log Estimates: Direct		Log Estimates: Max Likelihood	
					mean	CV	mean	CV	mean	CV
Area 1	Cruise 1	17	1.462	0.075	0.373	0.861	0.373	0.887	0.366	0.759
	Cruise 2	21	1.119	0.021	0.262	0.968	0.277	1.000	0.271	0.995
	Cruise 3	22	0.795	0.098	0.263	0.546	0.262	0.467	0.261	0.459
	Cruise 4	4	0.141	0.081	0.104	0.247	0.105	0.235	0.104	0.231
Area 2	Cruise 1	18	0.937	0.029	0.293	0.784	0.318	1.040	0.309	0.953
	Cruise 2	11	0.208	0.012	0.079	0.756	0.087	1.140	0.083	0.900
	Cruise 3	18	0.311	0.027	0.156	0.517	0.162	0.677	0.160	0.649
	Cruise 4	2	0.086	0.057	0.072	0.207	0.073	0.297	0.072	0.207
Area 3	Cruise 1	7	0.795	0.044	0.206	1.092	0.307	1.500	0.272	1.140
	Cruise 2	10	0.170	0.012	0.050	0.900	0.051	1.000	0.049	0.877
	Cruise 3	9	0.814	0.040	0.203	0.951	0.274	1.130	0.259	0.949
	Cruise 4	2	0.060	0.020	0.040	0.500	0.053	0.694	0.040	0.500
Area 4	Cruise 1	19	0.795	0.000	0.101	1.202	0.210	2.020	0.195	2.000
	Cruise 2	13	0.245	0.010	0.001	0.975	0.001	0.917	0.000	0.034
	Cruise 3	23	0.210	0.032	0.100	0.514	0.100	0.001	0.100	0.504
	Cruise 4	4	0.053	0.030	0.045	0.190	0.045	0.190	0.045	0.193

CV: coefficient of variation.

TABLE 6.5. ARITHMETIC AVERAGE DISSOLVED PCB CONCENTRATION (ng/L)

	Area 1	Area 2	Area 3	Area 4
Total PCB				
Cruise 1	74.7 (0.72)	32.9 (1.27)	2.86 (0.58)	2.98 (0.76)
Cruise 2	51.8 (0.52)	15.8 (0.79)	1.83 (0.35)	2.14 (0.63)
Cruise 3	95.9 (0.97)	18.8 (1.05)	3.40 (0.26)	2.42 (0.60)
Cruise 4	18.4 (0.25)	11.2 (0.59)	2.13 (0.53)	2.60 (0.66)
Homolog 3				
Cruise 1	24.8 (0.62)	8.48 (0.96)	0.71 (0.62)	0.55 (0.77)
Cruise 2	17.4 (0.61)	4.82 (0.94)	0.56 (0.44)	0.57 (0.67)
Cruise 3	30.4 (0.86)	6.50 (1.16)	0.81 (0.33)	0.65 (0.61)
Cruise 4	6.63 (0.23)	4.07 (0.76)	0.46 (0.89)	0.77 (0.83)
Homolog 4				
Cruise 1	28.0 (0.67)	11.4 (1.07)	1.00 (0.61)	0.87 (0.77)
Cruise 2	20.7 (0.52)	5.91 (0.78)	0.60 (0.33)	0.71 (0.66)
Cruise 3	35.5 (0.94)	6.90 (1.02)	1.30 (0.29)	0.81 (0.70)
Cruise 4	6.40 (0.32)	3.59 (0.53)	0.82 (0.64)	0.93 (0.69)
Homolog 5				
Cruise 1	11.2 (0.55)	7.02 (1.35)	0.71 (0.55)	0.51 (0.85)
Cruise 2	9.30 (0.41)	3.49 (0.66)	0.43 (0.39)	0.54 (0.65)
Cruise 3	16.9 (0.98)	3.59 (1.04)	0.79 (0.24)	0.59 (0.66)
Cruise 4	3.17 (0.30)	2.03 (0.36)	0.54 (0.35)	0.59 (0.58)
Homolog 6				
Cruise 1	2.20 (0.51)	1.95 (1.37)	0.24 (0.57)	0.18 (1.02)
Cruise 2	2.20 (0.44)	0.99 (0.72)	0.12 (0.37)	0.18 (0.73)
Cruise 3	3.90 (0.94)	0.94 (1.00)	0.25 (0.24)	0.20 (0.57)
Cruise 4	0.63 (0.23)	0.55 (0.35)	0.16 (0.07)	0.17 (0.54)

Numbers in parenthesis are coefficients of variation.

The area averages do suggest some cruise-to-cruise variation in water column concentrations. In most cases the differences in means are not statistically significant (t-test at the 5% level). For the PCBs only two of the twenty four comparisons have significance levels below 5% (area 1 cruises 2 and 4; area 3 cruises 2 and 3). Slightly greater differences exist for the metals. Significance levels below 5% occur four times for cadmium, nine times for copper and eight times for lead. In many of these comparisons the significance level is less than 1%. Because the biota are not sensitive to short-term variations in exposure concentrations it is not necessary to consider cruise to cruise dissolved chemical concentration differences in the model calibration. Average exposure concentrations over all cruises are presented in Table 6.6 for the PCBs and the metals.

Spatial profiles of the concentration average and range are presented in Figure 6.4 for the PCBs and in Figure 6.5 for the metals. A dramatic decline in PCB concentration is evident proceeding from the lower inner harbor (Area 1) to Buzzards Bay (Area 3). A similar but less dramatic decline is demonstrated in the cadmium and copper concentrations, while the lead concentration decreases slightly. Moving out into Buzzards Bay from Area 3 to Area 4, the PCB and metals concentrations remain approximately constant.

Spatial profiles of dissolved PCBs within Area 1 are presented in Figure 6.6. Between station 1, near the Aerovox facility, and station 3, just below the I-195 bridge, concentrations decline significantly. Below this station, concentration declines more slowly. In the region encompassing Area 1 of the food chain model (stations 5, 7-10) concentrations are approximately constant for all of the homologs. Similar plots for cadmium, copper, and lead are presented in Figure 6.7. The lead concentration decreases similar to the PCBs from station 1 to station 3. The cadmium concentration increases from station 1 to station 2 and then decreases from station 2 to station 3. The copper concentration also increases from station 1 to station 2 and remains constant from station 2 to station 3. In general, the average concentrations of cadmium and lead for the stations from the I-195 bridge to the hurricane barrier do not show significant variation. Copper concentrations decline from

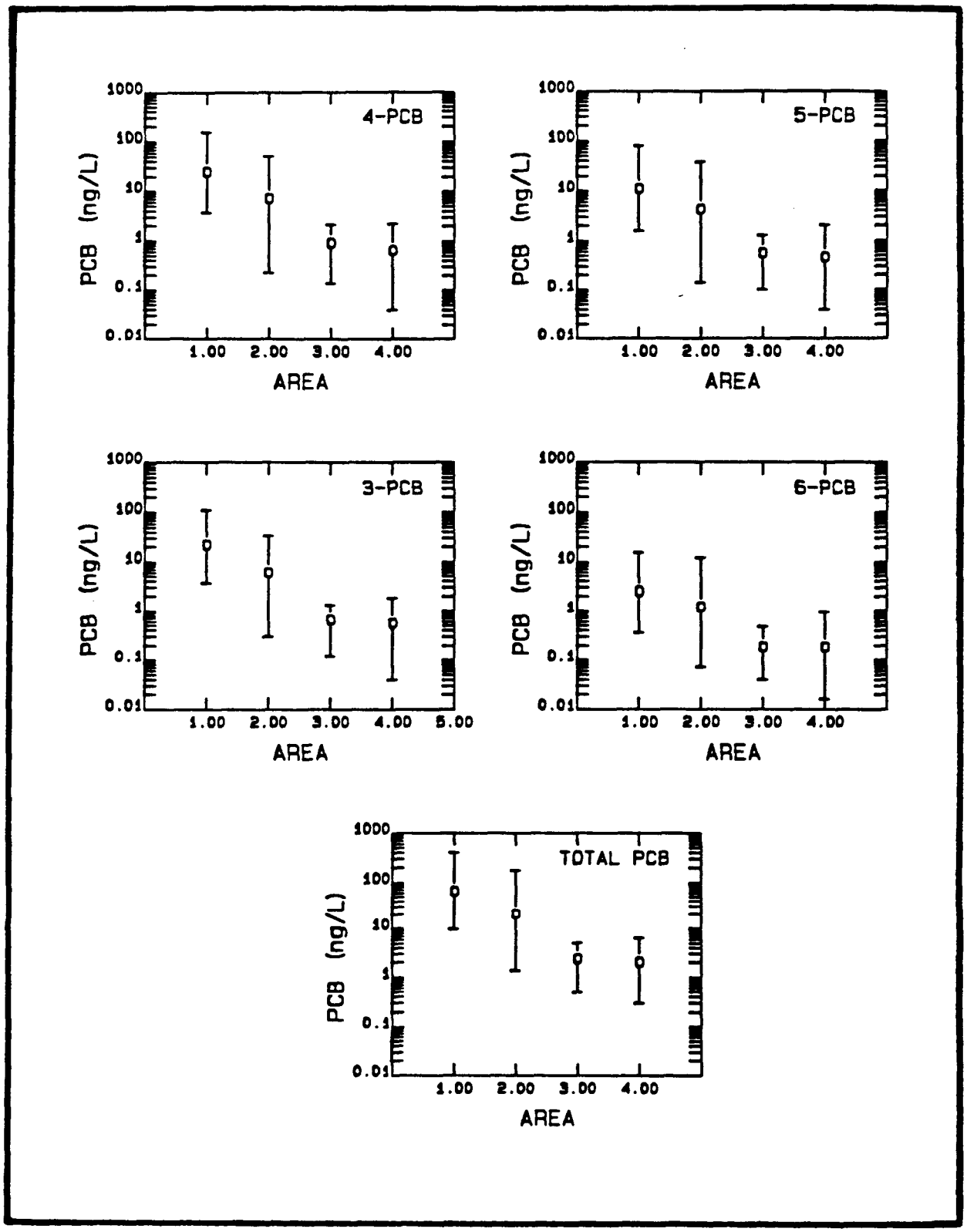

FIGURE 6.4 MEAN AND RANGE OF WATER COLUMN DISSOLVED PCB IN RELATION TO FOOD CHAIN MODEL AREA

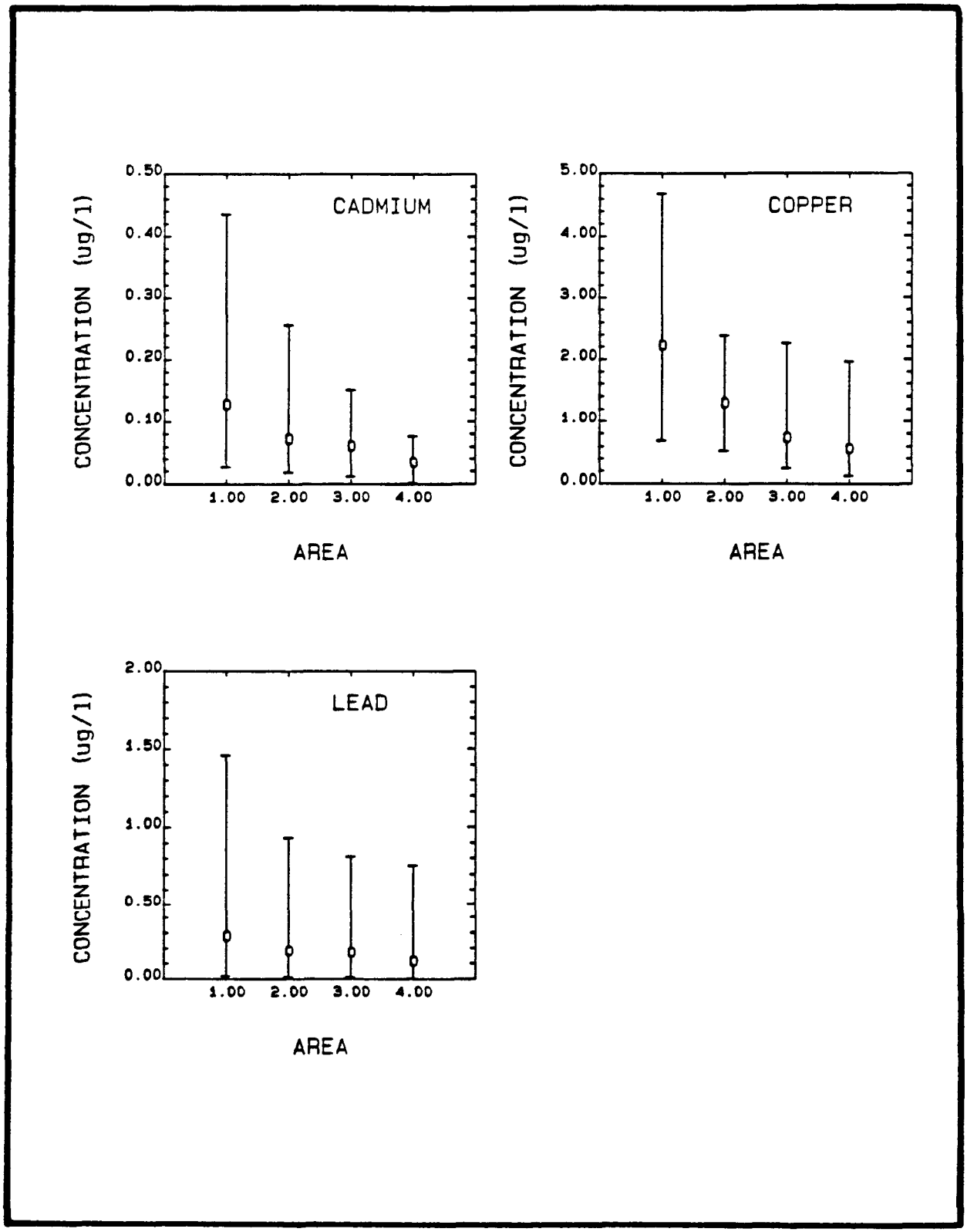

FIGURE 6.5. MEAN AND RANGE OF WATER COLUMN DISSOLVED METALS IN RELATION TO FOOD CHAIN MODEL AREA

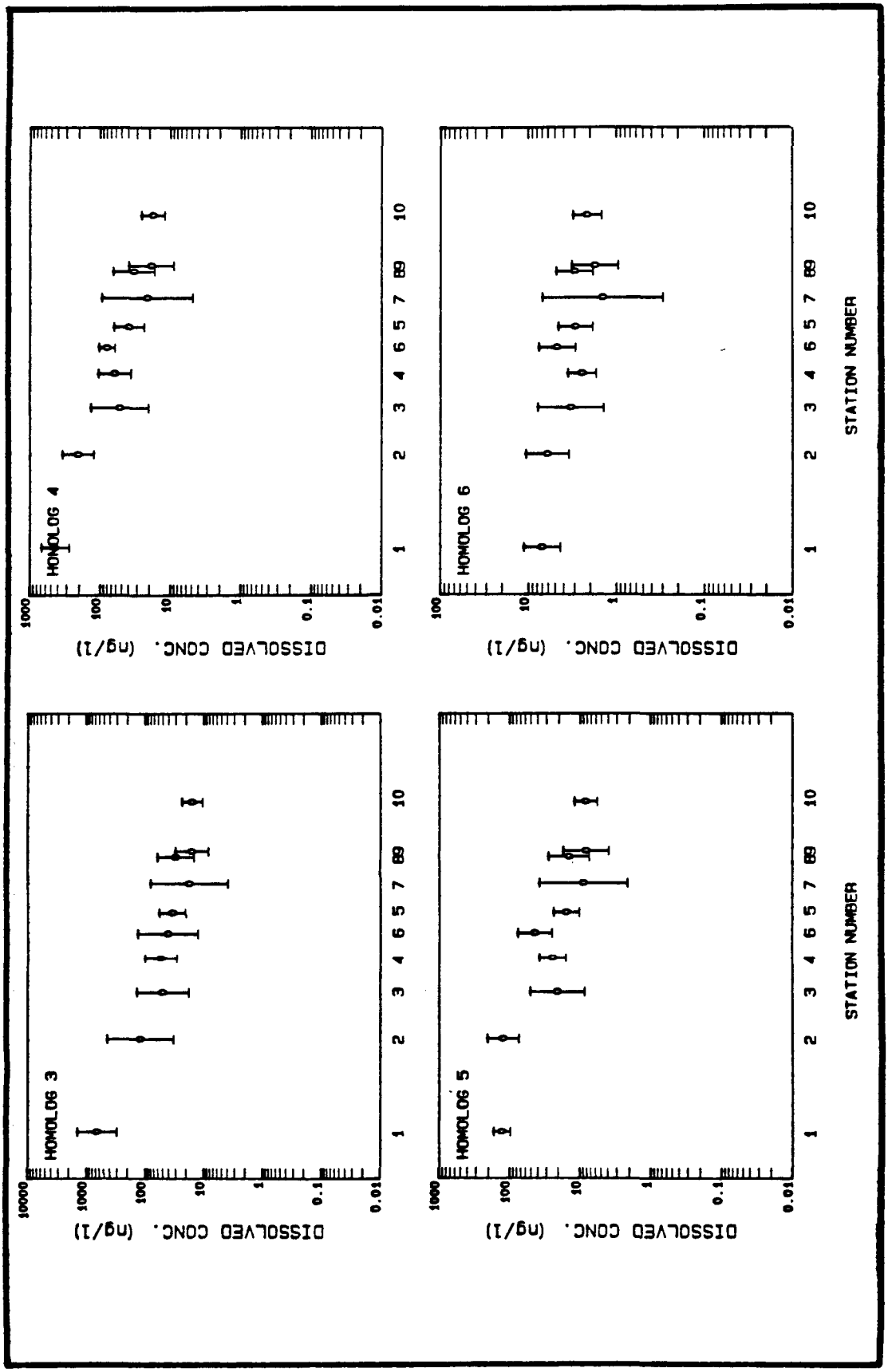

FIGURE 6.6. AVERAGE DISSOLVED PCB CONCENTRATIONS AT AREA 1 STATIONS

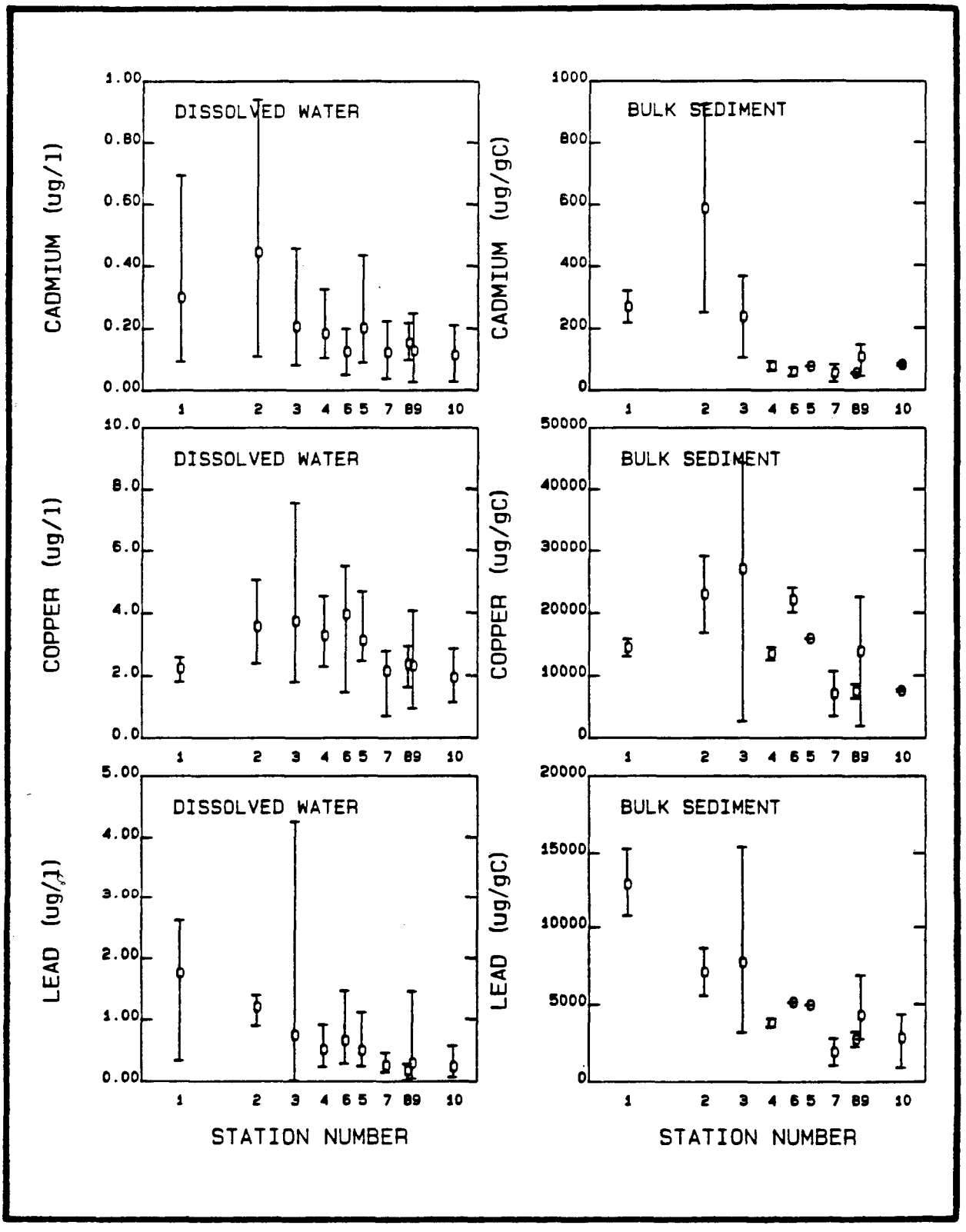

FIGURE 6.7. MEAN AND RANGE OF WATER COLUMN DISSOLVED AND BULK SEDIMENT METALS AT AREA 1 STATIONS

station 3 to station 6, above Pope Island. In the region encompassing Area 1 copper concentrations remain constant.

TABLE 6.6. ARITHMETIC AVERAGE DISSOLVED CHEMICAL CONCENTRATION

	Area 1	Area 2	Area 3	Area 4
PCB (ng/L)				
Homolog 3	23.4 (0.82)	6.5 (1.05)	0.7 (0.50)	0.6 (0.68)
Homolog 4	27.0 (0.87)	7.9 (1.10)	1.0 (0.54)	0.7 (0.70)
Homolog 5	12.0 (0.90)	4.6 (1.33)	0.6 (0.46)	0.5 (0.70)
Homolog 6	2.7 (0.90)	1.3 (1.36)	0.2 (0.52)	0.2 (0.77)
Total	71.5 (0.91)	22.1 (1.27)	2.6 (0.48)	2.2 (0.65)
Metals (mg/L)				
Cadmium	0.129 (0.55)	0.073 (0.50)	0.062 (0.64)	0.035 (0.54)
Copper	2.230 (0.34)	1.310 (0.35)	0.740 (0.54)	0.570 (0.53)
Lead	0.282 (0.84)	0.186 (0.93)	0.176 (1.30)	0.118 (1.24)

Numbers in parenthesis are coefficients of variation.

6.2.3.3 Sediment Data

Surface sediment samples were typically analyzed for PCB homologs 2 through 9, cadmium, copper and lead. Total organic carbon concentrations were also measured. Measurements were made for bulk sediment and for sand, silt and clay fractions. The percent silt, sand and clay were determined for the bulk sediment samples.

The polychaetes used as the representative benthic animal in the food chain take up contaminant directly from the interstitial water and by ingestion of the sediment solids. In the model the sediment ingestion rate is specified in units of grams carbon per gram animal per day. To compute the associated contaminant ingestion rate it is necessary that the contaminant concentration on the solids be specified in units of mass of contaminant per mass of sediment organic carbon. Surface sediment samples collected during the RIFS cruises were analyzed for total mass of contaminant (particulate plus interstitial water) per mass of bulk dry solids (values were also reported for three size fractions representing sand, silt and clay). We converted these data to carbon based units by dividing by the measured total organic carbon in the sample (expressed per mass of dry solids). The use of total contaminant and total organic carbon to compute particulate contaminant per gram of sediment particulate organic carbon is reasonable because at the high solids concentrations existing in sediments the total masses of contaminant and carbon are essentially the masses associated with the solids.

Log probability distributions for the PCB homologs 3, 4, 5, and 6, total PCB and the metals cadmium, copper and lead are presented in Appendix I. As with the water column dissolved concentrations, the data conform well to the assumption of log-normality as indicated by the linearity of the plots. Again, few outlying points are revealed in the distributions. The data excluded from the averages are indicated by solid symbols in the probability plots.

Area average concentrations were computed directly and from log statistics. Comparison of these averages for the PCBs (Table 6.7) indicates some differences, probably due to the log-normality of the data. The averages for the metals (Table 6.8) also show some small differences between the estimates.

The maximum likelihood procedure is presumed to yield the best estimate of the arithmetic mean and these estimates are used in the food chain model.

Spatial profiles of the concentration average and range are presented in Figure 6.8 for the PCBs and in Figure 6.9 for the metals. The decline in

TABLE 6.7. COMPARISON OF AREA AVERAGE CARBON NORMALIZED BULK SEDIMENT TOTAL PCB CONCENTRATIONS (mg/gC) COMPUTED FROM ARITHMETIC AND LOG STATISTICS

					Arithmetic Estimates		Log Estimates			
							Direct		Max Likelihood	
		# pts	max	min	mean	CV	mean	CV	mean	CV
Area 1	Homolog 3	12	137.	16.6	53.3	0.794	55.1	0.986	53.2	0.881
	Homolog 4	12	342.	20.6	108.	0.897	114.	1.160	109.	1.010
	Homolog 5	12	500.	18.5	121.	1.109	124.	1.23	117.	1.050
	Homolog 6	12	132.	4.4	46.8	0.959	53.2	1.600	49.3	1.270
	Total	12	1168.	77.0	357.	0.872	372.	1.050	357.	0.924
Area 2	Homolog 3	12	103.	1.8	23.0	1.230	26.0	1.820	23.8	1.380
	Homolog 4	12	164.	3.6	42.4	1.122	48.6	1.860	44.2	1.400
	Homolog 5	12	174.	4.1	52.1	1.083	60.4	1.850	55.0	1.390
	Homolog 6	12	70.9	0.7	16.7	1.221	19.6	2.100	17.5	1.510
	Total	12	561.	13.7	156.	1.010	176.	1.560	164.	1.250
Area 3	Homolog 3	7	5.3	1.4	2.9	0.446	2.9	0.456	2.9	0.437
	Homolog 4	7	11.3	2.9	6.2	0.446	6.3	0.462	6.2	0.442
	Homolog 5	7	19.5	4.9	10.5	0.472	10.6	0.482	10.4	0.459
	Homolog 6	7	9.4	2.3	5.0	0.478	5.04	0.485	5.0	0.462
	Total	7	48.8	12.3	26.2	0.466	26.5	0.474	26.1	0.452
Area 4	Homolog 3	20	9.6	0.1	1.3	1.654	1.2	1.460	1.1	1.270
	Homolog 4	20	20.7	0.1	2.4	1.840	2.2	1.570	2.1	1.340
	Homolog 5	20	31.0	0.1	3.6	1.847	3.4	1.680	3.3	1.410
	Homolog 6	20	15.4	0.1	1.8	1.840	1.7	1.640	1.6	1.380
	Total	20	88.1	0.5	10.2	1.849	9.5	1.580	9.1	1.350

CV: coefficient of variation.

TABLE 6.8. COMPARISON OF AREA AVERAGE CARBON NORMALIZED BULK SEDIMENT METALS CONCENTRATIONS (units mg/gC)

					Arithmetic Estimates		Log Estimates			
							Direct		Max Likelihood	
		# pts	max	min	mean	CV	mean	CV	mean	CV
Area 1	Cadmium	13	148.0	26.2	84.8	0.43	86.4	0.516	85.6	0.499
	Copper	13	22574.	1865.	10566.	0.56	11144.	0.774	10900.	0.721
	Lead	14	6881.	921.	3476.	0.47	3598.	0.621	3550.	0.594
Area 2	Cadmium	14	337.5	25.0	106.0	0.73	107.2	0.721	105.	0.680
	Copper	14	32679.	2056.	7196.	1.17	6816.	0.947	6620.	0.862
	Lead	14	16125.	1481.	5303.	0.88	5246.	0.857	5120.	0.792
Area 3	Cadmium	7	25.6	6.7	15.1	0.44	15.4	0.491	15.2	0.468
	Copper	7	1912.	820.	1342.	0.30	1350.	0.303	1340.	0.297
	Lead	7	3934.	875.	2154.	0.49	2200.	0.550	2160.	0.524
Area 4	Cadmium	19	138.0	4.1	26.5	1.36	24.7	1.37	23.0	1.200
	Copper	19	15893.	677.	2388.	1.51	2081.	1.00	2030.	0.926
	Lead	19	11964.	1221.	3212.	0.80	3130.	0.610	3100.	0.590

CV: coefficient of variation.

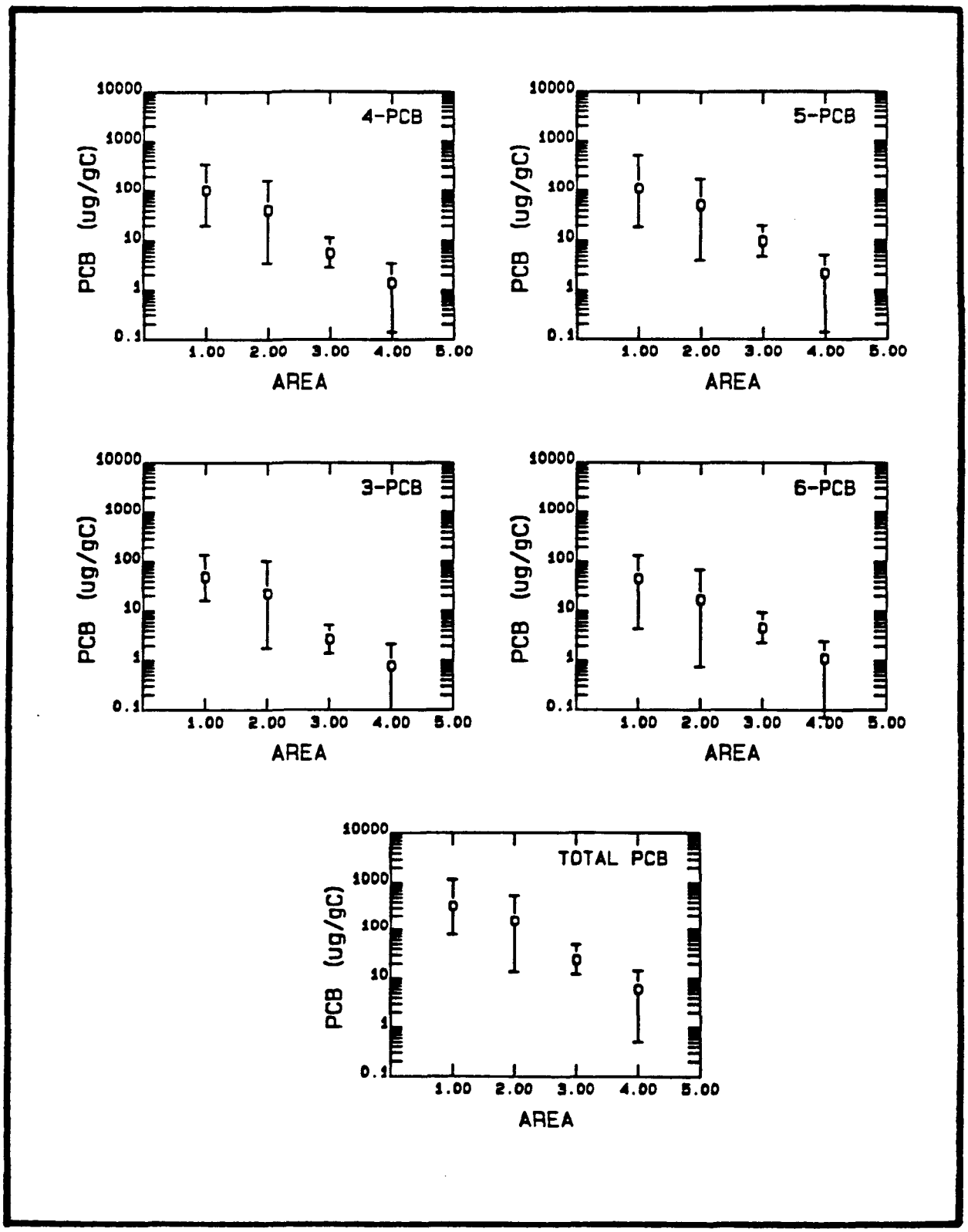

FIGURE 6.8. MEAN AND RANGE OF BULK SEDIMENT PCB IN RELATION TO FOOD CHAIN MODEL AREA

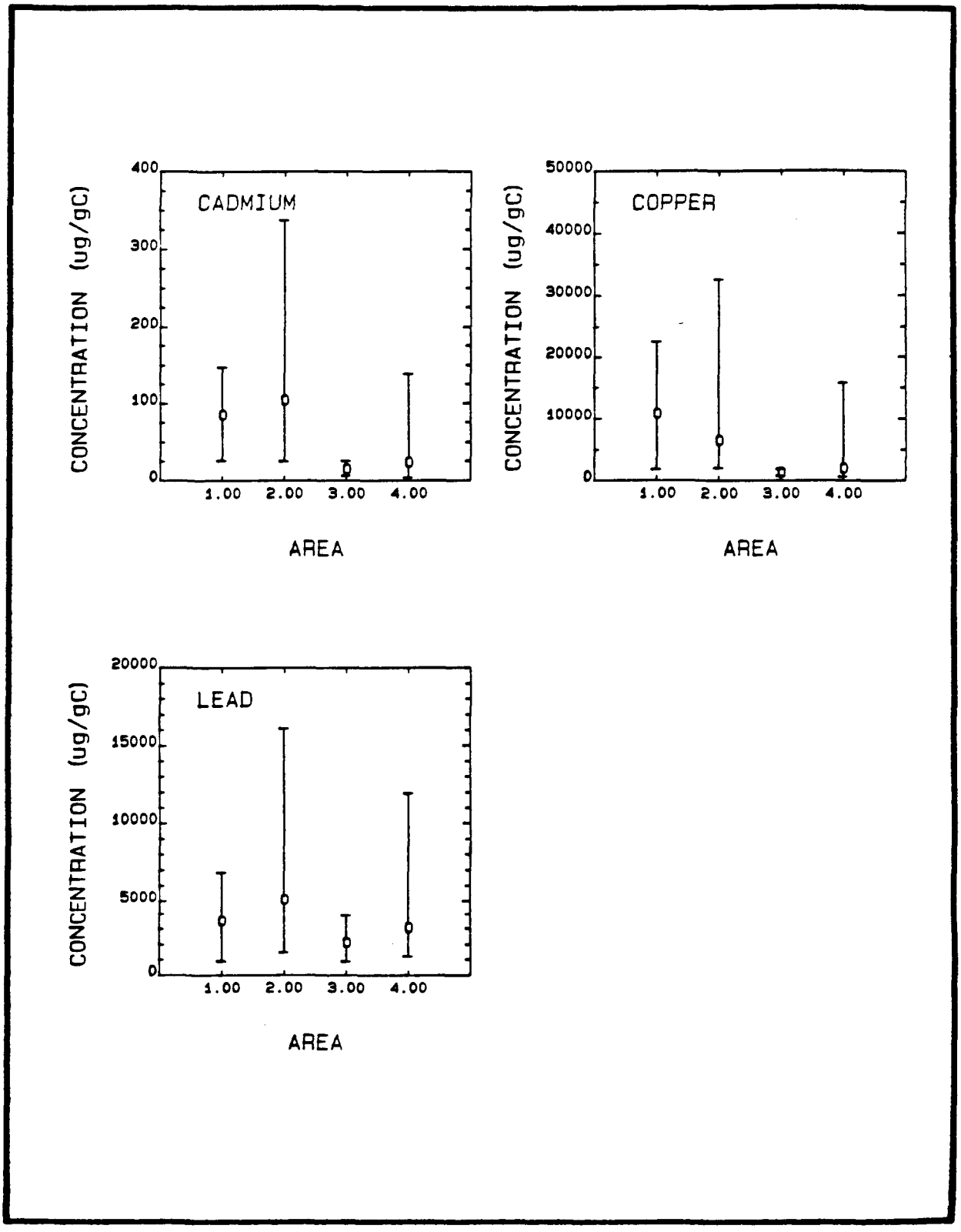

FIGURE 6.9. MEAN AND RANGE OF BULK SEDIMENT METALS IN RELATION TO FOOD CHAIN MODEL AREA

sediment PCBs between Areas 1 and 3 is similar to that exhibited in the water column. An evident difference between the sediment and water column occurs in Buzzards Bay. Whereas dissolved PCB concentrations are similar in Areas 3 and 4, sediment concentrations decline continuously throughout the system from Areas 1 through 4. This may indicate that the water column and sediment are not in equilibrium in outer areas of Buzzards Bay. The metals spatial profiles also indicate a general decline in concentration from Area 1 through Area 3. However, the decline is much less dramatic than that for PCBs and also much less consistent. Lead and cadmium concentrations increase slightly from Area 1 to Area 2. Concentrations in Areas 3 and 4 are about equal for all three metals.

The spatial profile of Area 1 bulk sediment PCB homolog concentrations (Figure 6.10) is similar to that observed in the water column and presented in Figure 6.6. Concentrations decline with distance downstream of station 1. The most pronounced gradients are between stations 1 and 2 and between stations 3 and 4. From station 4 to the hurricane barrier (station 10) concentrations are approximately constant.

The spatial profiles of sediment metals in Area 1 (Figure 6.7) are all similar to the corresponding profiles of water column dissolved concentration (also shown in Figure 6.7). The profiles do differ somewhat from that observed for PCBs. Whereas a dramatic decline in PCB concentration occurs between stations 1 and 2, cadmium and copper concentrations increase and lead concentration is approximately constant. For all of the metals concentrations decrease between stations 2 and 3. From stations 4 through 10 (7 through 10 for copper) concentrations remain approximately constant. The consistency of PCB and metals concentration in the lower inner harbor suggests a high degree of tidal mixing in the water column of this region.

6.2.3.4 Biota

The polychaetes, clams, mussels, spider crabs, flounder and lobsters collected in the trawls were analyzed for PCB homologs 2 through 9 and cadmium, copper

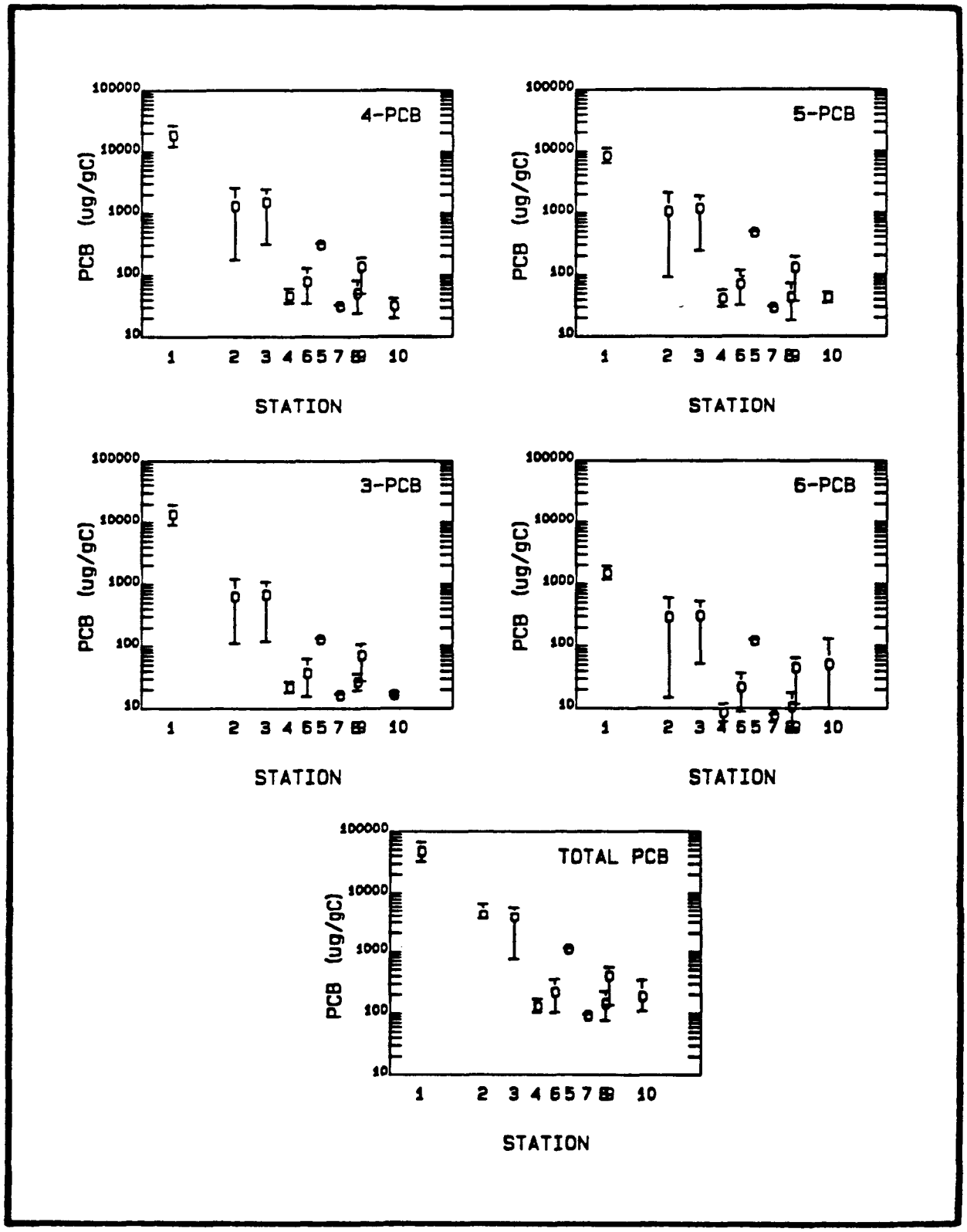

FIGURE 6.10. MEAN AND RANGE OF BULK SEDIMENT PCB AT AREA 1 STATIONS

and lead. The concentration of homologs 1 and 10 were measured in a limited number of the biota samples but were not included in the data review. Lipid content was also measured for each species. All analyses on biota samples were made on whole animals.

Juvenile through adult lobsters, flounder, spider crabs, and clams were collected and divided into size categories representing small, medium and large organisms. Mussels and polychaetes were not separated by size of organism since the weights of these species did not vary significantly. Probability distributions of the concentration of PCB homologs and total PCB (both the sum of homologs 2 through 9 and 3 through 9) for each size class of each species were developed. As with the water column and sediment data little cruise to cruise variation is evident in the plots. Similar plots were developed for cadmium, copper and lead and also showed slight cruise to cruise variation. These plots are included in Appendix K.

Table 6.9 presents the arithmetic average concentration in each species of homologs 3, 4, 5, and 6 and total PCB expressed as the sum of homologs 2 through 9. The arithmetic average cadmium, copper and lead concentrations in each species are presented in Table 6.10. The averages presented are overall species averages and include the small, medium and large organisms. There is some variation in concentrations in each area from cruise to cruise which may be attributed to the location of the trawls, which varied from cruise to cruise and the variation in the size of organisms collected in the cruises.

Trawls for biota in Area 1 were conducted between Popes Island and the hurricane barrier. Water quality and sediment data were collected at stations 1, 2, 3, 4, and 6, located in the upper estuary above Popes Island and at stations 5, 7, 8, 9 and 10 between the Route 6 bridge and the hurricane barrier. The Area 1 spatial plots (Figures 6.6, 6.7, and 6.10) indicate that exposure concentrations in the upper estuary, above Popes Island are in most cases considerably higher than in the lower section of Area 1. Since no biota were collected in the upper estuary the water and sediment data from that part of Area 1 were not included in the average exposure concentrations used in the food chain model. The average dissolved and particulate water column and sediment concentrations used for Area 1 in the model included only stations 5, 7, 8, 9, and 10.

TABLE 6.9. ARITHMETIC AVERAGE BIOTA PCB CONCENTRATION (units mg/kg)

	Area 1			Area 2			Area 3			Area 4		
	Cruise 1	Cruise 2	Cruise 3	Cruise 1	Cruise 2	Cruise 3	Cruise 1	Cruise 2	Cruise 3	Cruise 1	Cruise 2	Cruise 3
Lobster												
Homolog 3	-	-	-	55	35	26	0.64	14	4.4	2.6	1.9	1.7
Homolog 4	-	-	-	261	116	83	17	69	19	14	8.9	8.9
Homolog 5	-	-	-	586	169	148	149	136	43	60	27	27
Homolog 6	-	-	-	416	108	100	175	97	33	70	28	25
Flounder												
Homolog 3	995	574	868	102	75	601	48	815	93	30	9.0	779
Homolog 4	2969	1589	2219	333	368	1816	185	2180	489	190	41	1936
Homolog 5	4068	2087	3091	723	748	2770	392	2780	1642	488	81	1919
Homolog 6	1828	1009	1463	422	453	1458	246	1196	637	337	59	712
Mussel												
Homolog 3	289	400	619	876	201	579	-	23	17	-	0.47	2.5
Homolog 4	619	860	1187	2162	527	1444	-	78	82	-	1.6	11
Homolog 5	517	826	909	2312	574	1461	-	123	127	-	3.8	18
Homolog 6	136	270	223	821	198	482	-	53	58	-	2.7	9.2
Clam												
Homolog 3	68	120	200	4.5	4.8	13	6.7	481	20	0.35	1.6	6.5
Homolog 4	100	250	433	13	18	57	17	1641	67	0.86	4.7	20
Homolog 5	81	217	348	15	21	99	33	2041	101	1.4	6.7	31
Homolog 6	21	77	163	5.5	9.9	58	21	898	60	0.67	3.6	21
Spider Crab												
Homolog 3	427	357	126	-	55	17	20	123	52	-	-	3.0
Homolog 4	1359	832	283	-	161	37	71	313	176	-	-	10
Homolog 5	1753	1102	345	-	380	120	292	599	470	-	-	29
Homolog 6	693	448	136	-	248	79	243	333	270	-	-	22
Polychaete												
Homolog 3	-	-	2785[a]	-	-	173	-	5.7	77	-	48	21
Homolog 4	-	-	4183	-	-	391	-	17	174	-	158	68
Homolog 5	-	-	4385	-	-	771	-	54	355	-	389	137
Homolog 6	-	-	1481	-	-	338	-	46	156	-	244	109

[a] One sample

TABLE 6.10. ARITHMETIC AVERAGE BIOTA METALS CONCENTRATION (units mg/g)

	Area 1			Area 2			Area 3			Area 4		
	Cruise 1	Cruise 2	Cruise 3	Cruise 1	Cruise 2	Cruise 3	Cruise 1	Cruise 2	Cruise 3	Cruise 1	Cruise 2	Cruise 3
Lobster												
Cadmium	-	-	0.002	0.698	0.859	0.188	0.503	0.539	0.075	0.539	0.461	0.002
Copper	-	-	12.505	48.648	32.005	38.300	52.006	29.718	32.600	53.501	25.504	49.329
Lead	-	-	0.757	0.388	0.362	1.977	0.284	0.040	0.001	0.079	0.056	0.524
Flounder												
Cadmium	0.009	0.009	0.011	0.006	0.012	0.011	0.003	0.007	0.008	0.004	0.007	0.018
Copper	2.653	1.301	5.813	4.009	1.014	18.602	2.608	2.818	31.126	2.034	1.168	17.834
Lead	0.392	0.270	2.051	0.242	0.250	2.400	0.161	0.375	1.696	0.145	0.152	1.950
Mussel												
Cadmium	0.246	0.326	0.250	0.230	0.271	0.240	-	0.329	0.433	-	0.140	0.211
Copper	1.902	2.522	1.949	2.700	2.145	1.897	-	0.043	0.742	-	0.731	1.001
Lead	0.702	0.295	1.410	0.995	0.230	1.100	-	0.307	0.040	-	0.130	0.300
Clam												
Cadmium	0.290	0.154	0.120	0.315	0.209	0.224	0.237	0.373	0.290	0.403	0.204	0.224
Copper	7.350	4.941	4.993	6.401	1.919	1.733	2.207	2.300	1.091	1.042	1.233	1.017
Lead	1.937	0.735	0.012	1.370	0.002	0.704	0.070	1.242	1.053	1.030	0.032	1.000
Spider Crab												
Cadmium	0.000	0.003	0.009	-	0.003	0.070	0.070	0.000	0.001	-	-	0.070
Copper	14.400	190.574	103.520	-	100.514	74.250	15.150	200.002	201.000	-	-	227.300
Lead	0.990	0.099	20.232	-	3.941	0.023	0.212	14.040	30.000	-	-	14.030
Polychaete												
Cadmium	-	-	-	-	-	-	-	0.109	0.005	-	-	0.132
Copper	-	-	-	-	-	-	-	2.593	7.194	-	-	7.770
Lead	-	-	-	-	-	-	-	0.400	4.770	-	-	1.000

The exposure concentrations used in the model are presented in Table 6.11 for PCB's and in Table 6.12 for the metals. The dissolved metals concentrations have been adjusted to represent the free ion concentration (see Section 6.5).

In Area 2 the water and sediment concentrations at station 16 located near the wastewater treatment plant outfall were higher than the other stations in Area 2. Because of the station location these data were not included in the calculation of the Area 2 exposure concentrations used in the model.

PCB and metals concentration versus organism weight plots were developed for each species within an area. These plots are presented in Appendix L. In general the biota collected during the three cruises were similar in weight. Based on the concentration versus weight plots and the species concentration probability plots any cruise to cruise differences were considered insignificant and the data from the three cruises were averaged for each chemical.

Lipid Data. The lipid content of the organism is important in the extent of chemical accumulation in the organism. The high lipid solubility of PCBs suggests that accumulation of PCBs should be correlated with the lipid content of the exposed species. The PCB bioconcentration factor (BCF) for each species is calculated in the food chain model from the lipid content and the octanol-water partition coefficient. Lipid content was measured in each species during each of the cruises. Lipid concentration probability plots were developed for each species in each area and are presented in Appendix M. The data from all three cruises are plotted with a distinction made between cruises. Lipid concentrations for each cruise are generally spread throughout the probability distributions indicating no major differences between cruises. Plots of lipid concentration versus organism weight were developed for each species in each area and are also included in Appendix M. During each cruise the distribution of the size of organisms collected was similar. Arithmetic means of the lipid concentrations for each species within an area were calculated and are presented below in Table 6.13. Variations from area to area were not significant, therefore average lipid concentrations were calculated for each species using the data from all areas for use in the model.

TABLE 6.11. PCB EXPOSURE CONCENTRATIONS USED IN MODEL CALIBRATION

	Area 1		Area 2		Area 3		Area 4	
	Dissolved[a]	Sediment[b]	Dissolved	Sediment	Dissolved	Sediment	Dissolved	Sediment
Homolog 3	23	53	6.5	24	0.7	2.9	0.6	1.1
Homolog 4	27	109	7.9	44	1.0	6.2	0.7	2.1
Homolog 5	12	117	4.6	55	0.6	10	0.5	3.3
Homolog 6	2.7	49	1.3	18	0.2	5.6	0.2	1.6
Total PCB	72	357	22	164	2.6	26	2.2	9.1

[a] Dissolved units ng/l.
[b] Sediment units mg/gC.

TABLE 6.12. METALS EXPOSURE CONCENTRATIONS USED IN MODEL CALIBRATION

	Area 1		Area 2		Area 3		Area 4	
	Dissolved[a]*	Sediment[b]	Dissolved[a]*	Sediment[b]	Dissolved[a]*	Sediment	Dissolved	Sediment[b]
Cadmium	0.0032	84.76	0.0018	106.0	0.0016	15.13	0.0009	26.48
Copper	0.2004	10586.	0.1176	7195.	0.0670	1342.	0.0515	2388.
Lead	0.0085	3457.	0.0056	5303.	0.0053	2154.	0.0035	3212.

[a] Dissolved unit mg/l.
* Dissolved water concentrations adjusted to represent free ion concentration:
Cadmium free ion concentration = 2.5 percent total dissolved concentration
Copper free ion concentration = 9.0 percent total dissolved concentration
Lead free ion concentration = 3.0 percent total dissolved concentration.
[b] Sediment units mg/gC.

TABLE 6.13. ARITHMETIC AVERAGE LIPID CONCENTRATION

	Lipid Concentration (g/g)			
	Area 1	Area 2	Area 3	Area 4
Lobster	-	0.0080	0.0082	0.0089
Flounder	0.0172	0.0176	0.0215	0.0177
Crabs	0.0113	0.0058	0.0090	0.0062
Mussel	0.0127	0.0090	0.0055	0.0080
Clam	0.0027	0.0018	0.0040	0.0041
Polychaetes	-	0.0046[a]	0.0181	0.0145

[a] One sample

PCB Tissue Ratios. The contaminant concentrations measured in the field program and computed by the food chain model are on a whole body basis. The relevant measure of contamination for comparison with the FDA action limit for the fishery is the concentration in edible tissue. Consequently, most of the historical measurements are of edible tissue or muscle (flesh). In order to compare the results of the model to the action limit and to compare the field program data to historical data it is necessary to convert from whole body to edible tissue. To determine proper conversion factors a subsample of the lobster and flounder samples collected in the field program were analyzed for the concentration of each PCB homolog in muscle tissue, viscera (lobster hepatopancreas) and whole body. Ratios of specific tissue concentration to whole body concentration were computed for each sample and used to determine an average ratio for each PCB homolog.

The ratios obtained from the PCB analyses were somewhat variable with a range of order 10 for all tissues. To obtain average values the data were assumed to conform to a log-normal probability distribution. Probability plots of the ratios (Figures 6.11 to 6.13) indicate that this assumption is reasonable. Regression analysis yielded estimates of the mean and standard deviation of the log transformed data. The regression line is presented on each of the probability plots. The log statistics were converted to estimates of arithmetic mean and variance using a maximum likelihood estimation technique. The results of this calculation are tabulated in Table 6.14 and presented graphically on Figure 6.14.

The estimates of average tissue ratios are remarkably consistent between homologs. A slight increase in ratio with PCB chlorine content is observed for the lobster muscle-to-whole body and pancreas-to-whole-body ratios. For the 3 through 6 homolog groupings included in the model the ratios are essentially constant. The average ratios for these homologs are 1.35 for lobster muscle-to-whole body, 0.18 for flounder muscle-to-whole body, and 92 for lobster hepatopancreas-to-whole body.

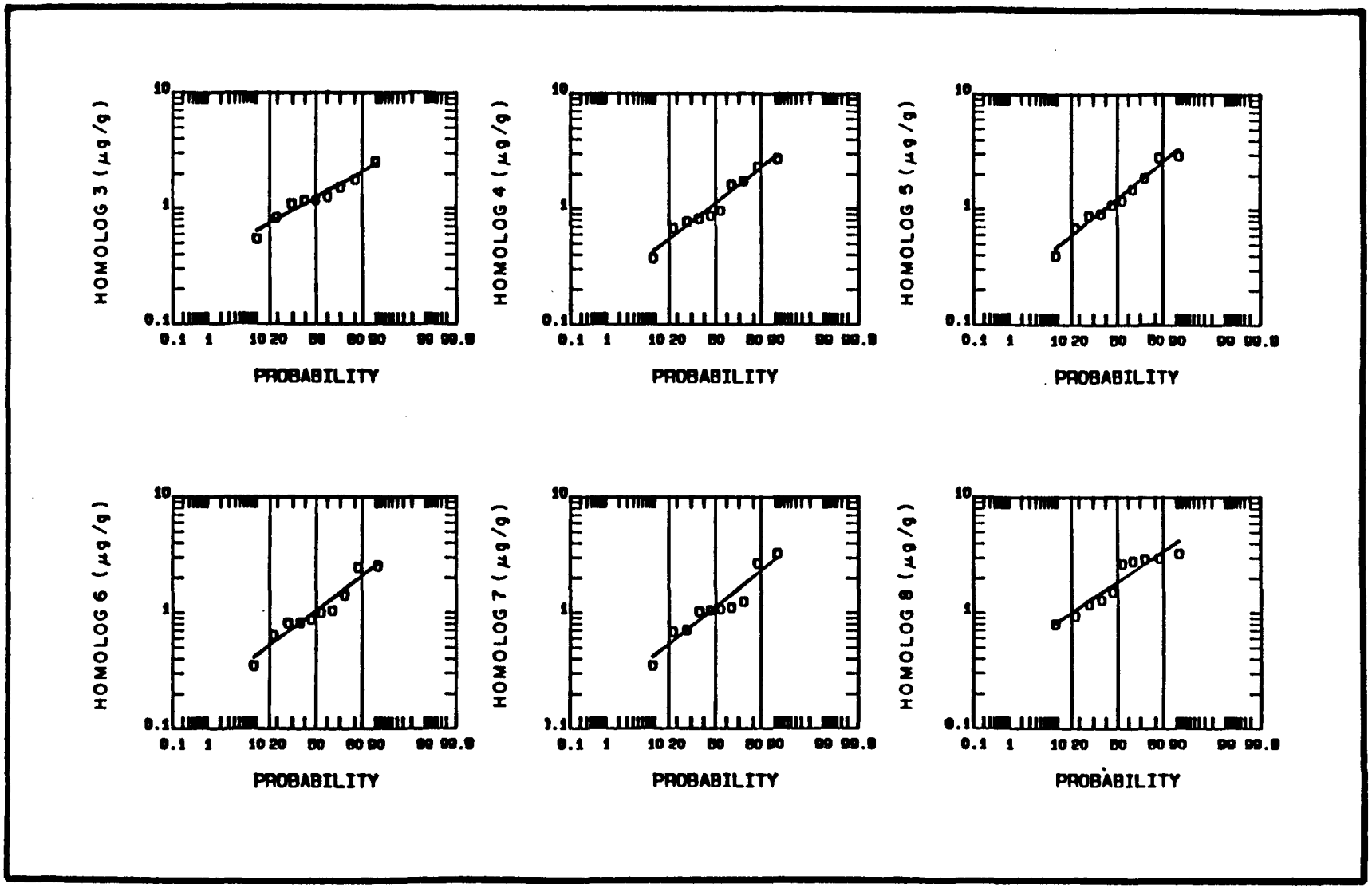

FIGURE 6.11. LOBSTER MUSCLE TO WHOLE BODY PCB RATION

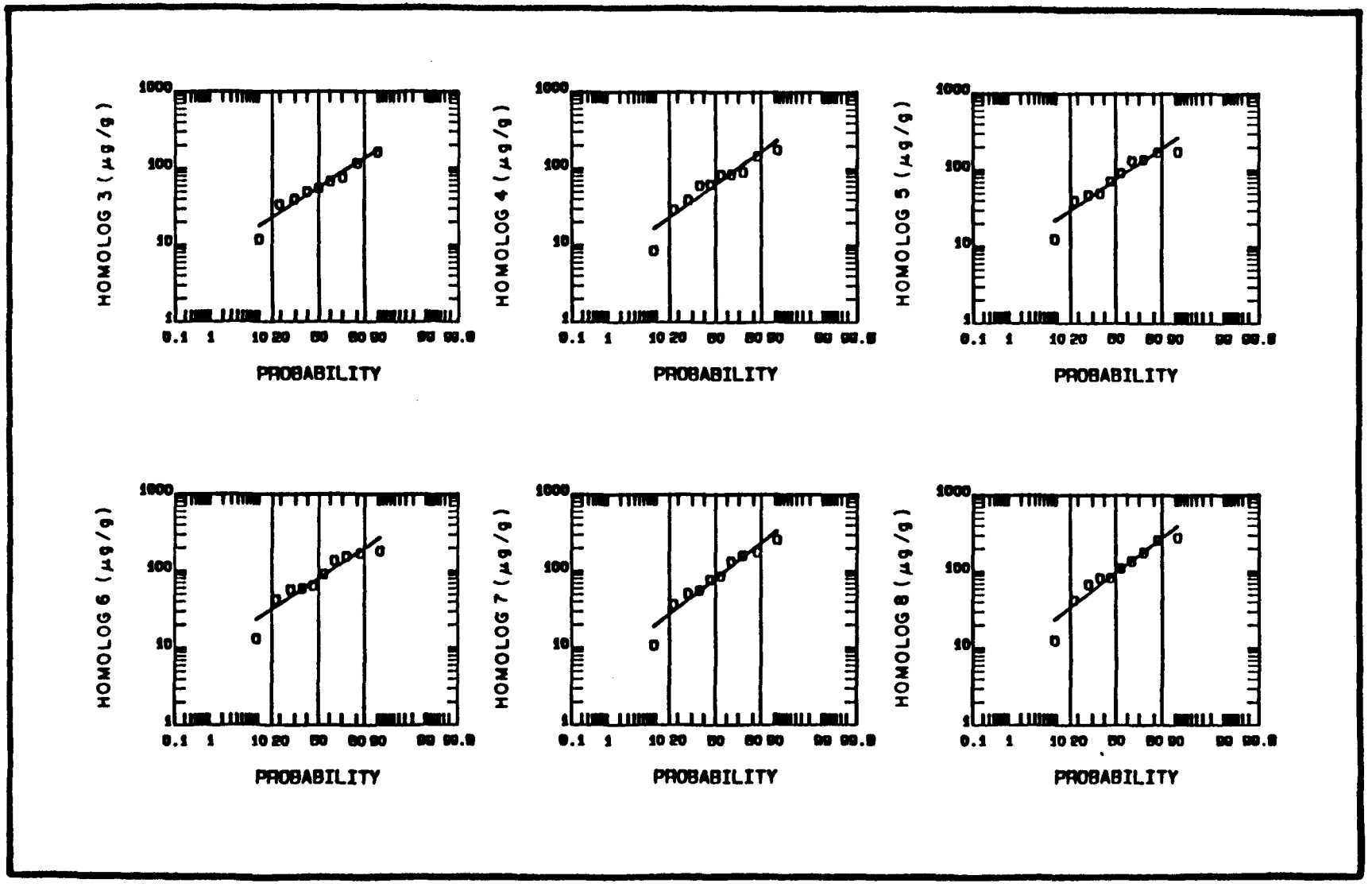

FIGURE 6.12. LOBSTER PANCREAS TO WHOLE BODY PCB RATIO

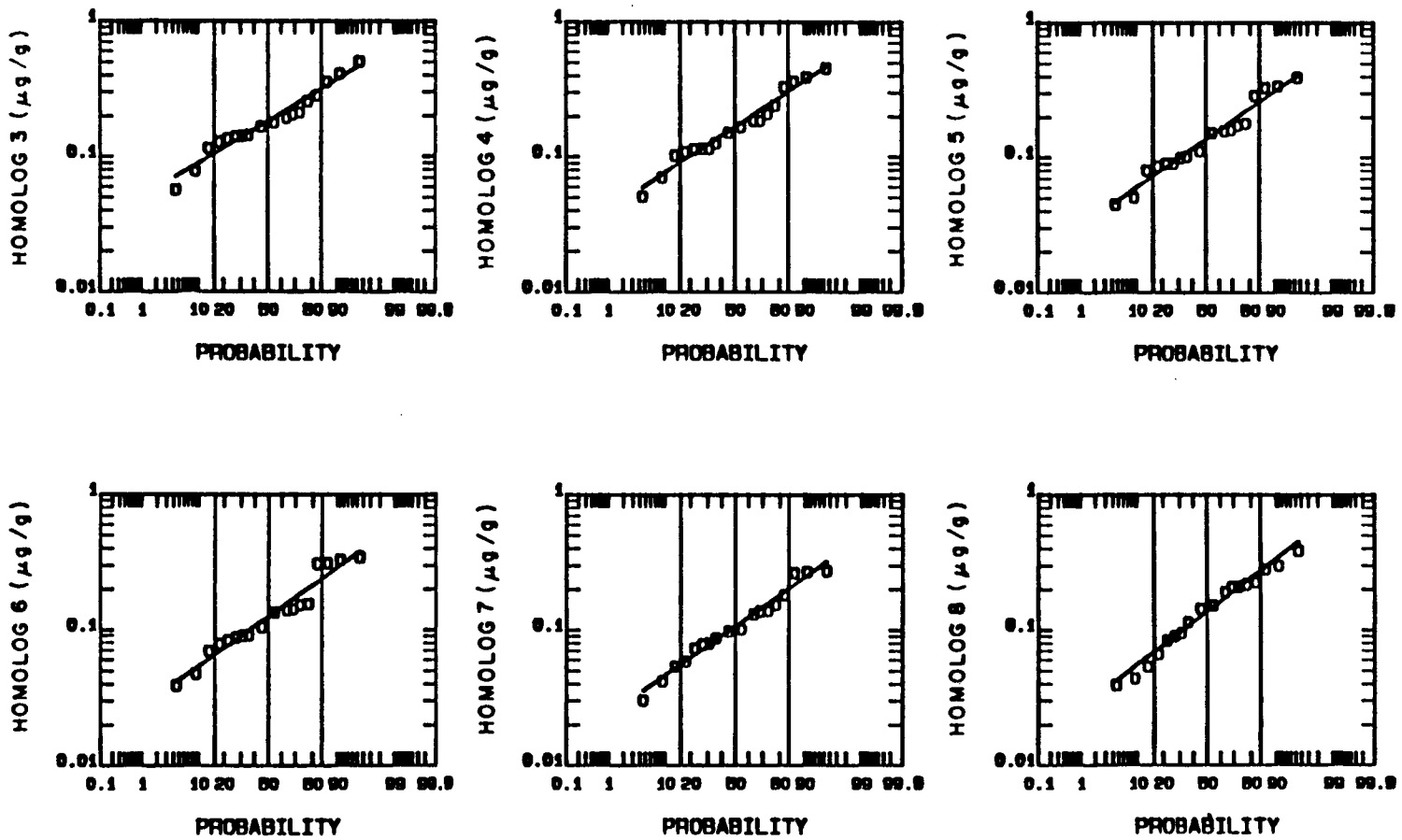

FIGURE 6.13. FLOUNDER MUSCLE TO WHOLE BODY PCB RATIO

TABLE 6.14. LOBSTER AND FLOUNDER TISSUE PCB RATIO STATISTICS

	Homolog Grouping	No. Points	Log Statistics Mean	Log Statistics Standard Deviation	Median	Arithmetic Statistics Mean	Arithmetic Statistics Standard Deviation	Coefficient Variation
Lobster Muscle to Whole Body	3-PCB	9	0.2230	0.4353	1.25	1.38	0.60	0.441
	4-PCB	10	0.1149	0.6129	1.12	1.33	0.84	0.631
	5-PCB	10	0.2202	0.6207	1.25	1.48	0.95	0.639
	6-PCB	10	0.0430	0.5949	1.04	1.22	0.75	0.611
	7-PCB	10	0.1129	0.6439	1.12	1.34	0.89	0.664
	8-PCB	10	0.0158	0.5397	1.05	2.11	1.16	0.552
Lobster Pancreas to Whole Body	3-PCB	9	4.0318	0.7567	56.4	72.3	56.6	0.783
	4-PCB	10	4.1319	0.8749	62.3	87.0	80.5	0.925
	5-PCB	10	4.3274	0.8234	75.7	102	88.3	0.866
	6-PCB	10	4.3805	0.8075	79.9	106	89.9	0.848
	7-PCB	10	4.3907	0.9234	80.7	117	114.9	0.982
	8-PCB	10	4.5726	0.9188	96.8	140	136.8	0.977
Flounder Muscle to Whole Body	3-PCB	21	-1.7079	0.5093	0.181	0.205	0.109	0.531
	4-PCB	21	-1.7918	0.5518	0.167	0.192	0.111	0.579
	5-PCB	21	-1.9887	0.5835	0.137	0.161	0.099	0.616
	6-PCB	21	-2.0784	0.5981	0.125	0.148	0.094	0.633
	7-PCB	21	-2.2383	0.5869	0.107	0.125	0.078	0.628
	8-PCB	21	-1.9901	0.6334	0.137	0.165	0.111	0.675

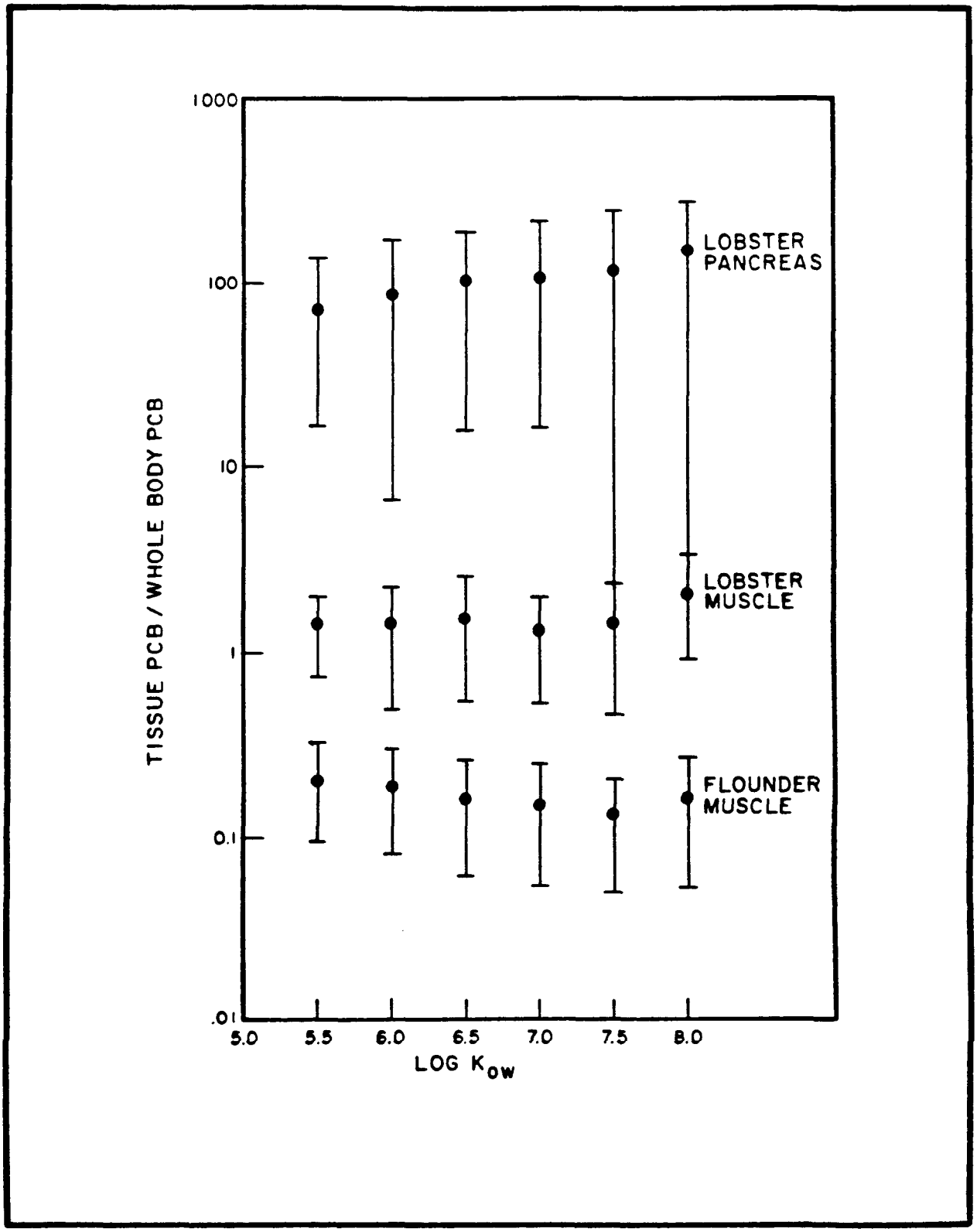

FIGURE 6.14. RATIO OF PCB IN MUSCLE OR PANCREAS TO PCB IN WHOLE BODY OF NEW BEDFORD HARBOR LOBSTERS AND FLOUNDER

The ratios are constant because they are essentially a measure of the ratio of lipid between the tissues. The homologs are predominantly stored in lipids.

The concentration in any tissue is dependent on the lipid fraction of that tissue and the partitioning characteristics of the chemical. The ratio between two tissues is the ratio of the products of lipid mass and chemical concentration in the lipid. Because the chemical concentration in lipid should be equal for both tissues the ratio reduces to the ratio of lipid masses. Thus the ratio is independent of homolog.

6.3 FOOD CHAIN MODEL THEORY

The concentration of a toxic substance that is observed in an aquatic organism is the result of several uptake and loss processes that include: transfer across the gills, surface sorption, ingestion of contaminated food, desorption, metabolism, excretion and growth. These processes are controlled by the bioenergetics of the organism and the chemical and physical characteristics of the toxic substance.

For phytoplankton and detrital organic material representative of the base of the food chain, sorption-desorption controls toxic substance accumulation and the change in the concentration, ν_o (μg/g(w)) may be written as:

$$\frac{d\nu_o}{dt} = k_{uo}c_d - K_o\nu_o \qquad (6\text{-}1)$$

in which k_{uo} is the rate of uptake directly from the water or the sorption rate (L/d-g(w)), c_d is the concentration of dissolved toxicant (μg/L), K_o is the loss rate or desorption rate (d^{-1}), and t is time (d). Because the sorption rates are generally much faster than the uptake and excretion rates of higher levels of the food chain and the transport and transformation rates of the toxic substance, instantaneous equilibrium is assumed. Equation (6-1) then reduces to:

$$\nu_o = N_o c_d \qquad (6\text{-}2)$$

in which N_o, the bioconcentration factor, is the ratio of the uptake to the loss rate.

For species above the phytoplankton/detritus level, uptake of toxicant due to ingestion of contaminated food must be considered. This uptake will depend on (a) toxicant concentration in the food, (b) rate of consumption of food, and (c) the degree to which the ingested toxicant in the food is actually assimilated into the tissues. The rate of consumption of food, C, (g/g-d) is dependent on metabolic requirements and growth rate, and is computed as:

$$C = \frac{R + G}{a} \qquad (6\text{-}3)$$

in which R is the respiration rate (g/g-d), G is the growth rate (g/g-d), and a is the fraction of ingested food that is assimilated.

The uptake of toxicant from water by these species, k_u is determined by the rate of transfer of toxicant across the gills. This rate of transfer is calculated from the rate of transfer of oxygen from water to the fish.

Oxygen transfer is defined by the respiration rate of the animal and the oxygen concentration of the water (C_{O_2}):

$$k_{u_{O_2}} = \frac{r'}{C_{O_2}} \qquad (6\text{-}4)$$

where r' is the respiration rate in units (g O_2/g(w)-d). This uptake is dependent on the mass transfer rate constant at the gill, (K_{L_O}), the gill surface area (A), and the weight of the animal:

$$k_{u_{O_2}} = \frac{K_{L_{O_2}} A}{w} \qquad (6\text{-}5)$$

Similarly, for the toxicant:

$$k_u = \frac{KLA}{w} \qquad (6\text{-}6)$$

If Equations (6-4) and (6-5) are equated, solved for A and substituted into Equation (6-6), the uptake rate of the toxicant may be written as:

$$k_u = \frac{KL}{K_{L_{O_2}}} \frac{r'}{C_{O_2}} \qquad (6\text{-}7)$$

From this equation, it is evident that the uptake rate of a toxicant can be computed from the respiration rate of the animal if the ratio of the mass transfer coefficients for the chemical and oxygen is known. Expressions relating these coefficients to characteristics of the chemical and the physiology of the animal have been developed (Gobas et al., 1986; Gobas and Mackay, 1987; Barber et al., 1988). Estimates of the ratio may also be obtained from measurements of toxicant and oxygen uptake efficiencies. The ratio of mass transfer coefficients is equal to the ratio of uptake efficiencies measured when the body burden of the animal is zero.

Respiration is a function of temperature, T(RC), body weight W(g) and swimming speed m(cm/s) which may be specified as (Weininger, 1978):

$$R = W^{\gamma} e^{\rho T} e^{\epsilon u} \qquad (6\text{-}8)$$

where

$$u = \omega W^{\delta} e^{\phi T}$$

Values for β, γ, ρ, ϵ, w, δ and ϕ are species-specific and are specified from laboratory respiration data.

To convert the respiration rate from units of g(w)/g(w)/d to the units of $g(O_2)/g(w)/d$ used in the uptake rate calculation Equation (6-4): (1) wet weight is converted to dry weight, (2) dry weight is converted to carbon assuming a carbon to dry weight ratio of 0.4, and (3) carbon is stoichiometrically converted to oxygen.

The rate of loss of the toxicant from an organism is the sum of the excretion and detoxification or degradation rates of the chemical. If the organism is exposed to the toxicant in water only, this rate is related to the uptake rate by the bioconcentration factor, N, as specified by Equation (6-2). Assuming no significant weight change during the bioconcentration test, the loss rate, K, is computed as:

$$K = \frac{k_u}{N} \tag{6-9}$$

It has been demonstrated that the bioconcentration factor of neutral organic chemicals measured in laboratory studies can be related to the 1-octanol-water partition coefficient, K_{ow} (Tulp and Hutzinger, 1978; Neely, 1979; Veith et al., 1979; Mackay, 1982). In fact, it appears that the lipid-normalized bioconcentration factor is approximately equal to K_{ow}, at least for log K_{ow} values up to 6. For such chemicals it is, therefore, possible to compute N for a neutral organic chemical from the K_{ow} of the chemical and the fraction lipid of the animal (f_L), i.e.,:

$$N = f_L K_{ow} \tag{6-10}$$

Above a log K_{ow} value of 6 a loss of linearity has been observed in correlations of N and K_{ow} (Bruggeman et al., 1984; Opperhuizen et al., 1985; Gobas et al., 1987). N appears to reach a maximum in the log K_{ow} range 6.5 to 7 and begins to decrease at higher log K_{ow} values. Several hypotheses exist to explain this behavior. Gobas et al. (1989) have reviewed and evaluated these hypotheses and have concluded that the dominant effects are the

increasing importance of fecal elimination and a decrease in freely dissolved chemical (due to complexation with dissolved and colloidal organic material) as K_{ow} increases. The latter efect is an experimental artifact dependent on the concentration of organic matter in the water used in the experiment. Fecal elimination was shown to lower the slope of the N-K_{ow} relationship but not cause a decreasing relationship.

N values for PCB homologs 3 through 5 are computed using Equation (6-9) and assumed log K_{ow} values of 5.5, 6.0 and 6.5, respectively. To reflect the observed loss of linearity of the N-K_{ow} relationship, the value for homolog is assumed to be equal to that of homolog 5. Values for the metals are determined from laboratory measured values.
Combining the above uptake and loss rates, the general mass balance equation for the whole body burden, $\nu'(\mu g)$, may be written as:

$$\frac{d\nu'}{dt} = k_u w c_d + \alpha C w \nu_p - K\nu' \qquad (6\text{-}11)$$

in which w is the weight of the organism (g(w)), a is the fraction of ingested toxicant that is assimilated, and νp is the toxicant concentration in the prey ($\mu g/g(w)$). Because the whole body burden is the product of the toxicant concentration and weight of the organism, the derivative in Equation (6-11) may be written and expanded as:

$$\frac{d\nu'}{dt} = \frac{d(\nu w)}{dt} = \nu \frac{dw}{dt} + w \frac{d\nu}{dt} \qquad (6\text{-}12)$$

Equation (6-12) may then be rewritten in terms of toxicant concentration as:

$$\frac{d\nu}{dt} = k_u c_d + \alpha C \nu_p - k'\nu \qquad (6\text{-}13)$$

where:

$$k' = K + \frac{dw}{dt}/w = K + G$$

and G is the growth rate of the organism (g/g/d).

Equation (6-12) is solved numerically using an Euler Scheme, so that:

$$\nu(t + \Delta t) = \nu(t) + \frac{d\nu}{dt}\bigg|_t \Delta t \qquad (6\text{-}14)$$

The analysis of toxic chemicals in aquatic food chains using Equation (6-2) for phytoplankton and detrital organic material and Equation (6-13) for higher trophic level species requires the bioenergetic and chemical related parameters included in Equations (6-3), (6-4) and (6-5). In addition, the variation of these parameters with age and the feeding habits of each species modeled must be known.

Feeding habits are generally discontinuous functions of age. The prey size or prey species generally change as an organism grows. Thus, Equation (6-13) is not solved continuously over the life span of an organism. Instead, the life span is separated into age classes over which the predator-prey relationships are assumed to be constant. Equation (6-13) is then applied to each age class with the term representing uptake through feeding expanded to allow more than one prey for each predator age class.

The use of age classes also provides a convenient mechanism for computing concentrations in all life stages simultaneously, rather than the direct solution of Equation (6-13). The criteria for age class size is the birth frequency of the organism, thus restarting the first age class of an organism at the proper interval.

Species at the lower end of the food chain tend to exhibit a concentration of chemical that does not vary with age. Their relatively rapid uptake and excretion rates and the lack of a major diet change with age cause them to achieve equilibrium with the chemical in a short time relative to their life span. This fact justifies the use of an equilibrium or steady-state modeling approach for these species. The equation defining the equilibrium concentration is obtained from Equation (6-13) by assuming the uptake and loss rates are constant and setting the derivative, $d\nu/dt$ to zero:

$$\nu = \frac{k_u C_d + \alpha C \nu_p}{k'} \qquad (6\text{-}15)$$

6.4 ESTIMATION OF MODEL FOOD CHAIN INTERACTIONS AND PARAMETERS

6.4.1. Food Chain Structure

Determination of the appropriate species to include in the model is based on a review of published stomach content data for lobster and flounder. From these data species are chosen to represent the next lower level of their food chains. Representative species are then chosen for each lower trophic level in succession to the phytoplankton-detritus level. At any level a single species is sometimes sufficient because the members of that level generally have similar bioenergetic characteristics and chemical concentrations. Additional prey animals are incorporated as necessary to account for differing prey chemical concentrations or multiple vectors of chemical transfer to the predator (i.e., sediment versus water column).

The lobster is the top predator in a three level food chain. Stomach content analyses have indicated that small crustaceans, molluscs, polychaetes and echinoderms are the main constituents of the diet of Homarus americanus. Studies of lobsters in Bonavista Bay, Newfoundland (Ennis, 1973) and in Long Island Sound (Weiss, 1970) indicate that crabs and molluscs (particularly mussels) are the most important prey items. In the Bonavista Bay study crabs composed approximately 50 percent of the food intake and molluscs composed about 11 percent. In the Long Island Sound study prey items were compared based on frequency of occurrence in stomachs. Crustaceans (predominantly crabs) were found in over 90 percent of the stomachs. Bivalve molluscs occurred in 51 percent. Polychaetes accounted for only 2.5 percent of the food intake in the Bonavista Bay study but they were found in 59 percent of the Long Island Sound lobsters.

In the model the lobster food chain is represented by crabs, mussels, polychaetes, phytoplankton and sediment detrital organic material. A schematic diagram of the food chain, showing the fraction of total food consumption assigned to each prey, is presented as Figure 6.15. Polychaetes are included, even though they are a less important food source, because they provide a different route of chemical transfer to the lobster. The small

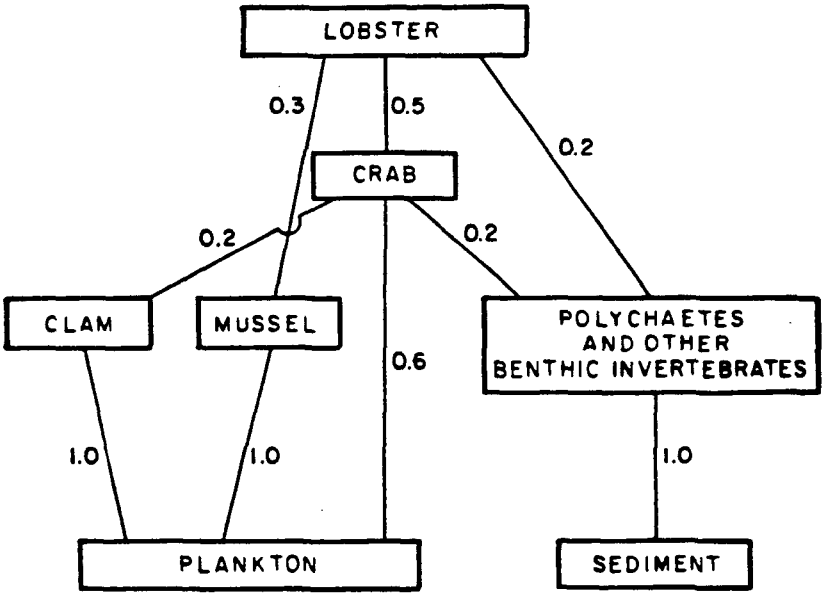

FIGURE 6.15. LOBSTER FOOD CHAIN

crabs and mussels provide a means of chemical transfer from the water column through consumption of phytoplankton. The polychaetes transfer chemical from the sediment to the lobster through their ingestion of sediment particles.

The winter flounder is an omnivore which eats whatever is available. Stomach content analyses indicate a diet that includes polychaetes, amphipod and isopod crustaceans, pelecypods and plant material (Klein-MacPhee, 1978). As part of a quantitative analysis of the food habits of Northwest Atlantic fish, Maurer and Bowman (1975) found that polychaetes were the major food item, composing about 34 percent of stomach content weight. Coelenterates (20 percent) and crustaceans (7 percent) were the next most important food groups.

Polychaetes were also found to be the most important prey item for flounder from Long Pond, Conception Bay, Newfoundland (Kennedy and Steele, 1971) and from mud bottoms of Long Island Sound (Richards, 1963). They were a significant prey item in a Johns Bay, Maine study (Hacunda, 1981), although crustaceans (principally amphipods) were a higher percentage of stomach content weight. These studies clearly indicate that benthic animals form the bulk of the diet of the winter flounder.

In the model young-of-the-year winter flounder are assumed to consume equal percentages of phytoplankton and polychaetes. Older flounder are assumed to consume polychaetes only. In this structure the polychaetes are viewed as representatives of the variety of benthic animals that are prey for the flounder. A schematic diagram of the food chain, showing the fraction of total food consumption assigned to each prey, is presented as Figure 6.16.

Mature flounder exhibit local onshore-offshore migration in response to temperature changes. A study in Quincy Bay by the Massachusetts Division of Marine Fisheries (1961) indicated a pattern of movement between the shoal waters and deeper waters of the harbor and open water. They congregated in shoal water for spawning. As temperature increased in summer they dispersed to deeper waters. Fish up through age 4 remained in the harbor. Fish 5 years old or more tended to move out of the harbor completely. Recaptures from a tagging study conducted in Buzzards Bay (Howe and Coates, 1975) with flounder

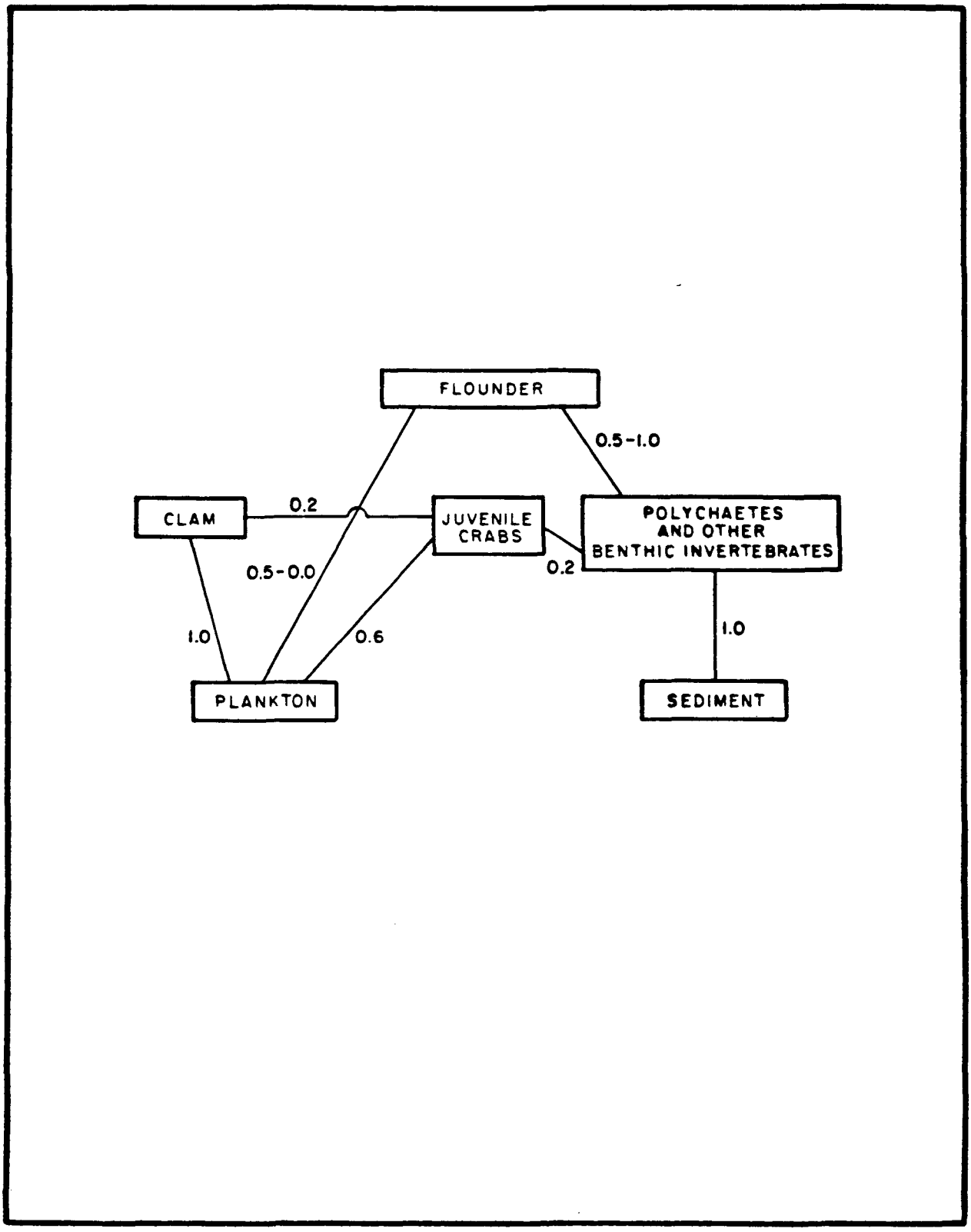

FIGURE 6.16. FLOUNDER FOOD CHAIN

of mean length 342 mm (age 5) (range (190 - 500 mm: age 3 - age 8)) indicate movement out of Buzzards Bay into Nantucket Sound.

The data collected as part of this study show that age I and age II flounder are generally present in all four areas of the study area throughout the year (Figure 6.17). This suggests that spawning probably occurs throughout the study area (in the shoal regions of each area). Data indicate that areas 2, 3 and 4 have approximately the same temperature regime (Figure 6.18). Therefore, it is probable that flounder do not migrate between these regions. A slight thermal gradient exists between the Inner Harbor (Area 1) and the Outer Harbor (Area 2). This may result in some migration between these areas. The absence of flounder greater than age 2 in Area 1 during cruise 2 may reflect this movement. Because age 3 flounder are present in the Outer Harbor and Buzzards Bay at all sampling times it is likely that only a fraction of these young adults migrates into Area 1.

Larger flounder (ages 5 and older) were found in significant numbers only during cruise 2 (Figure 6.19). This probably reflects the migration of these individuals from Nantucket Sound. Their migration pattern is likely such that cruise 1 (September 13 to October 10) was prior to their inshore movement and cruise 3 (June 26 to July 2) was after their offshore movement.

Because the significance of the migration of 2 and 3 year olds between Areas 1 and 2 cannot be determined from available information, it is not included in the model. Also, the potential random movement of animals between Areas 2, 3 and 4 cannot be quantified and it is not considered. Some movement of this type is probable since the PCB body burden gradient between the areas is less for flounder than for the other animals. The lack of data for animals older than age 5 makes analysis of their accumulation and the effects of offshore migration on it problematical. Therefore, the model includes flounder up through age 5 only.

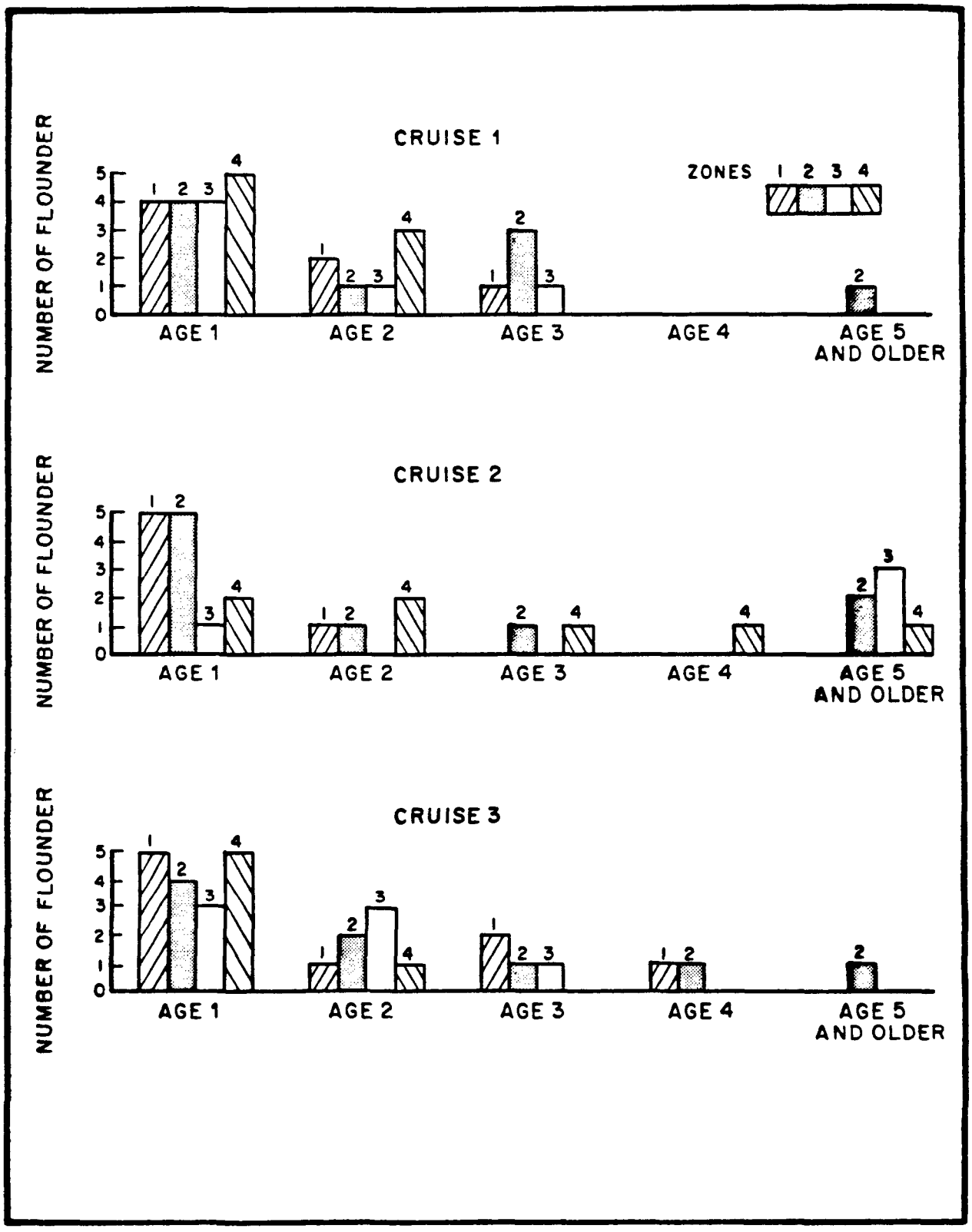

FIGURE 6.17. DISTRIBUTION OF FLOUNDER BY AREA AND AGE FOR EACH CRUISE

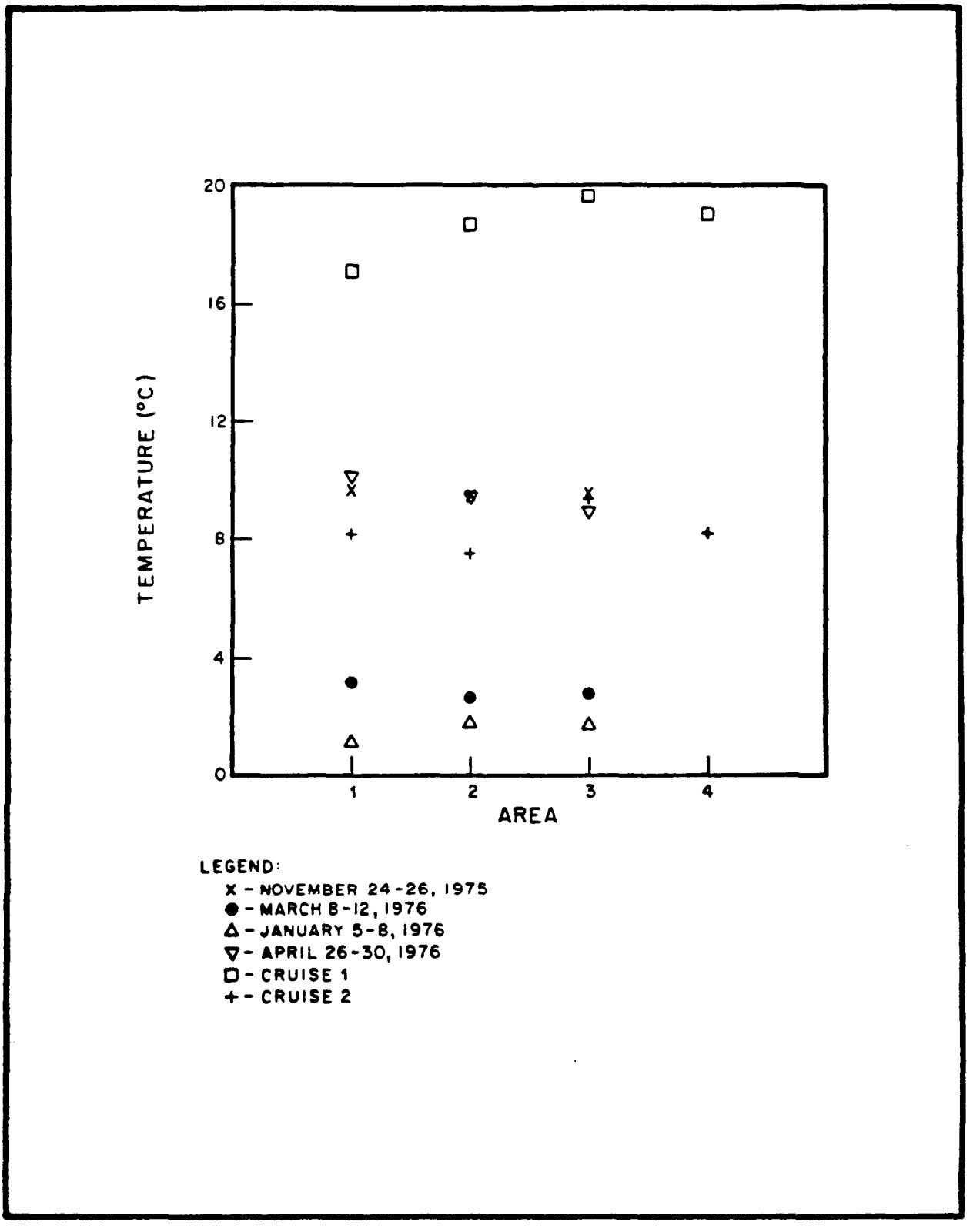

FIGURE 6.18. AVERAGE TEMPERATURES IN EACH AREA

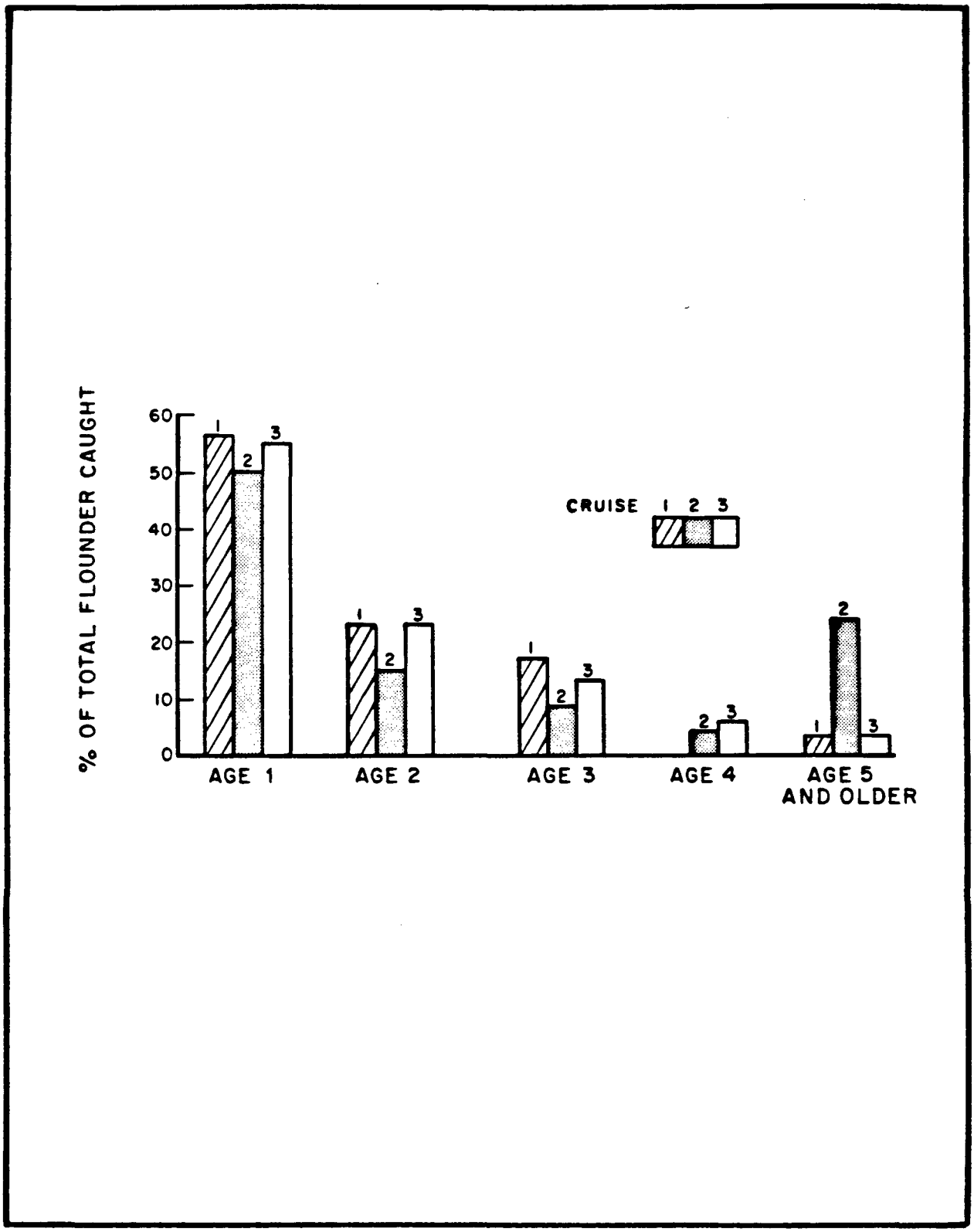

FIGURE 6.19. DISTRIBUTION OF FLOUNDER BY AGE FOR EACH CRUISE

6.4.2 Growth Rate

6.4.2.1 Lobster

The growth of lobsters is a discrete process in which almost all length and weight increase takes place at molt. Tissue accumulation occurs continuously; however, weight increase during intermolt is 2 percent or less (Phillips, Cobb and George, 1980). Frequency of molting and growth at molt are functions of age and size of lobster. Mauchline (1977) found an exponential increase in intermolt period and an exponential decrease in percent increase of carapace length at molt with carapace length. During the first year of life Homarus americanus molts six to nine times. Larvae are planktonic. The lobster stays on the bottom after the third or fourth molt at 10 to 30 days of life.

Weight increase with age has not been determined. Relationships have been developed between weight and carapace length and between carapace length and age. From these a relationship between weight and age may be established. Several data sets are available relating wet weight and carapace length. These data sets are all similar and indicate that the relationship of weight and length is well established (Figure 6.20).

A number of correlations between length and age have been presented. Unfortunately, they yield very different values as shown in Table 6.15. The relationships for male and female lobsters reported by Cooper and Uzmann (1977) was used with the weight-length relationship to establish the weight-age relationships shown in Table 6.16. The average of the male and female weights at each age were used to establish the growth rates used in the model (Table 6.14). The growth rates shown in the table were computed by assuming exponential growth and determining the exponent yielding the yearly weight increase. These rates therefore represent average growth over the year. Within year variability in growth rate is not considered in the model.

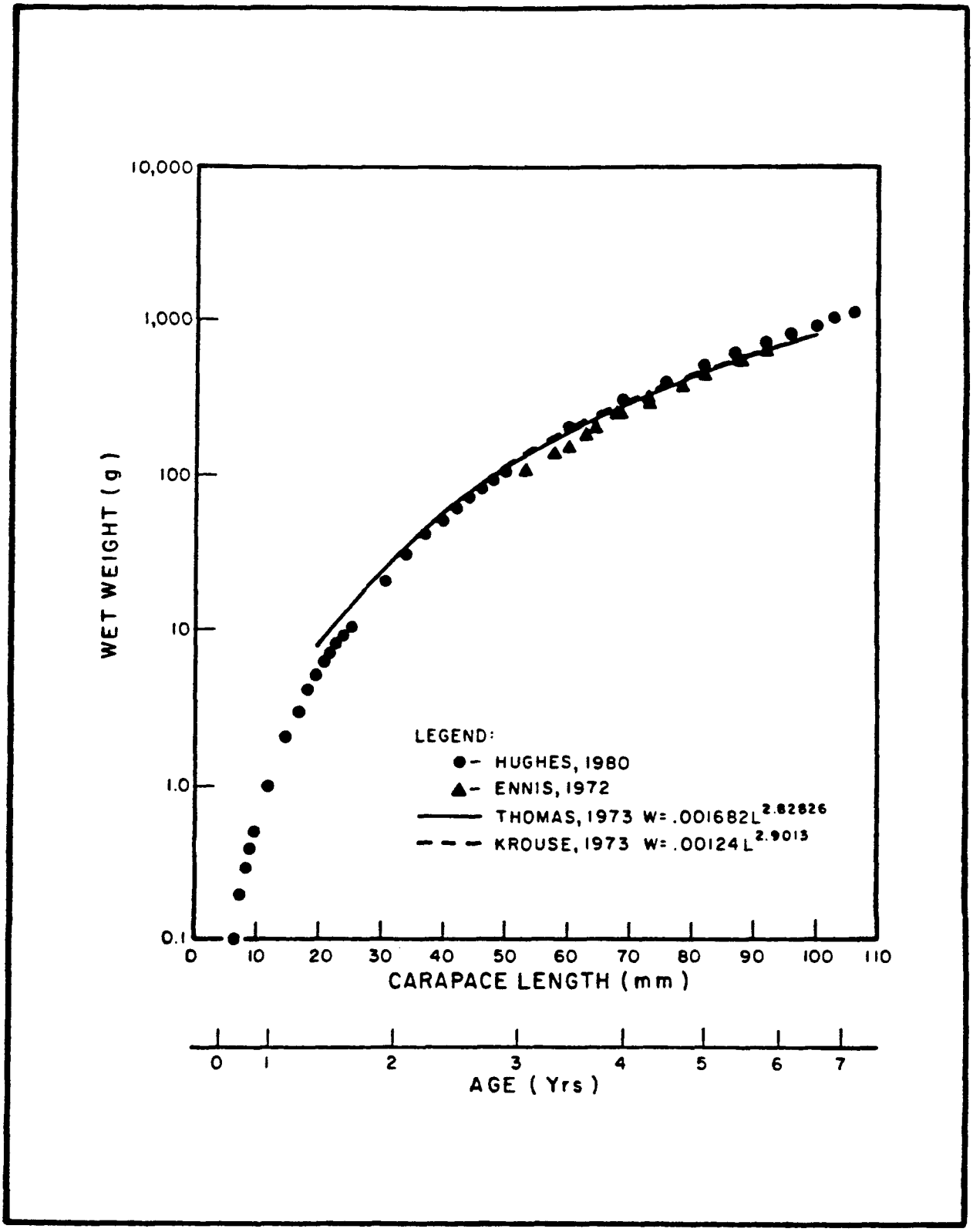

FIGURE 6.20. RELATIONSHIP OF WEIGHT TO LENGTH IN HOMARUS AMERICANUS

TABLE 6.15. COMPARISON OF CARAPACE LENGTHS CALCULATED FOR VARIOUS AGES OF HOMARUS AMERICANUS USING SEVERAL CORRELATIONS

Age (years)	Carapace Length (mm) Thomas[a] (1973)	Cooper & Uzmann (1977) Males[b]	Cooper & Uzmann (1977) Females[c]	Manchline (1977) (using two ages closest to the year values)
1	3	13	12	27-34
4	38	77	57	82-94
8	78	139	104	105-117

[a] = 267 (1 - e-.048 (t - .722)). (Gulf of Maine lobsters)
[b] = 278 (1 - e-.096 (5 - .5)).
[c] = 248 (1 - e-.074 (t - .3)). (Offshore lobster)

TABLE 6.16. WEIGHTS USED TO ESTABLISH GROWTH RATES FOR LOBSTER

Age	Weight (g) Female	Male	Average	Growth Rate (d-1)
0	0.05	0.05	0.05	8.68x10-3
1	1.0	1.3	1.2	8.51x10-3
2	14	40	27	8.51x10-3
3	60	165	113	3.91x10-3
4	170	365	268	2.36x10-3
5	280	665	473	1.55x10-3
6	500	1045	773	1.34x10-3
7	730	1470	1100	9.64x10-4
8	1100	2000	1550	9.37x10-4
9	1586	2525	2056	7.72x10-4
10	2287	3140	2714	7.59x10-4
11	3298	3600	3449	6.55x10-4

6.4.2.2 Winter Flounder

The growth of winter flounder has been evaluated in several studies. Of these, two studies have been conducted in the same region as New Bedford Harbor. Pearcy (1962) reported the weight-age relationship for juvenile flounder in the Mystic River, Connecticut. Berry et al. (1965) presented growth data for adult flounder from Rhode Island waters. The data from both these studies have been compiled and analyzed by Saila et al. (1965), who reported winter flounder weight in relation to age. These data are shown on Figure 6.21 along with a line representing the weight change used in the model.

The growth rates corresponding to the line in the figure are given in Table 6.17.

6.4.2.3 Crab

Crabs are the representative of the crustacean component of the lobster food chain. Juvenile crabs are presumed to be the relevant prey size. The model incorporates a single size crab with steady-state chemical burden. Data for the rock crab (Cancer irroratus) are used to establish the bioenergetic parameters for this component of the food chain.

The growth rate of juvenile crabs was estimated using the weights of 1 and 2 year old crabs as calculated from reported carapace widths (13.7 and 39.9 mm) (Reilly and Saila, 1978) and a relationship between carapace width and weight (Haefner and Van Engel, 1975). The weight increase from 0.3 to 8.5 g corresponds to an exponential growth rate of 0.009/d.

6.4.2.4 Mussel

The blue mussel (Mytilus edulis) is used to represent the mollusc component of the lobster food chain. Consistent with the size of crabs presumed to be prey for lobsters, a mussel length range of 15 to 40 mm was used in the determination of growth and respiration. This size range corresponds to an

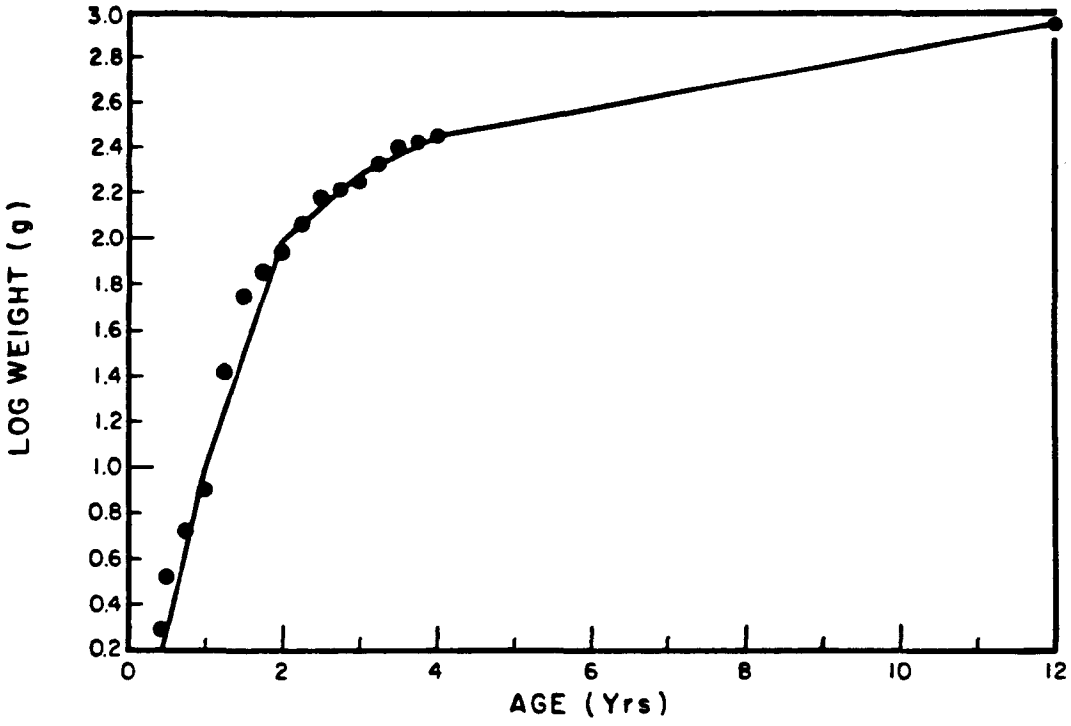

FIGURE 6.21. WINTER FLOUNDER WEIGHT IN RELATION TO AGE

TABLE 6.17. WINTER FLOUNDER GROWTH RATE

Age	Initial Weight (g)	Growth Rate (d-1)
0	0.1	0.01258
1	10	0.00629
2	100	0.00175
3	190	0.00096
4	270	0.0004
5	313	0.0004
6	363	0.0004
7	420	0.0004
8	486	0.0004
9	563	0.0004
10	652	0.0004
11	755	0.0004
12	875	0.0004

age range of approximately 2 to 5 years and a flesh dry weight range of approximately 0.05 to 0.4 g (Bayne and Worrall, 1980). The growth rate was determined from tissue weights reported by Bayne and Worrall for animals from two English estuaries. Figure 6.22 shows the average and range of weight for 3 to 5 year old animals. A seasonal fluctuation in weight is evident in the data. This fluctuation is consistent with other studies (e.g., Dare and Edwards, 1975) and is the result of seasonal variability in food availability. The food chain model is directed to an annual average time scale and the seasonal fluctuation is averaged out by using an exponential growth rate of 0.0019/d as represented by the line on Figure 6.22.

6.4.2.5 Polychaetes

The polychaete growth rate was determined using data for Neries. The bioenergetic parameters for this animal have been reported as part of a food chain modeling study in the James River estuary (Connolly and Tonelli, 1984). The growth rate of 0.007/d derived for that study is used here.

6.4.2.6 Hard Clam

The hard clam Mercenaria mercenaria is included in this study as a potential prey species for the lobster. Although the literature review of lobster stomach content data suggests that it is not a significant prey species, it remains a valuable component of the model because of its importance as a route of contaminant exposure to humans.

Weight-age data is unavailable for hard clams. Growth was determined by combining empirical length-age and weight-length relationships.

Age and length of 6 to 42 month old hard clams in Great South Bay, New York have been measured by Greene (1978). From these data the following length-age relationship was developed for animals less than 30 months old:

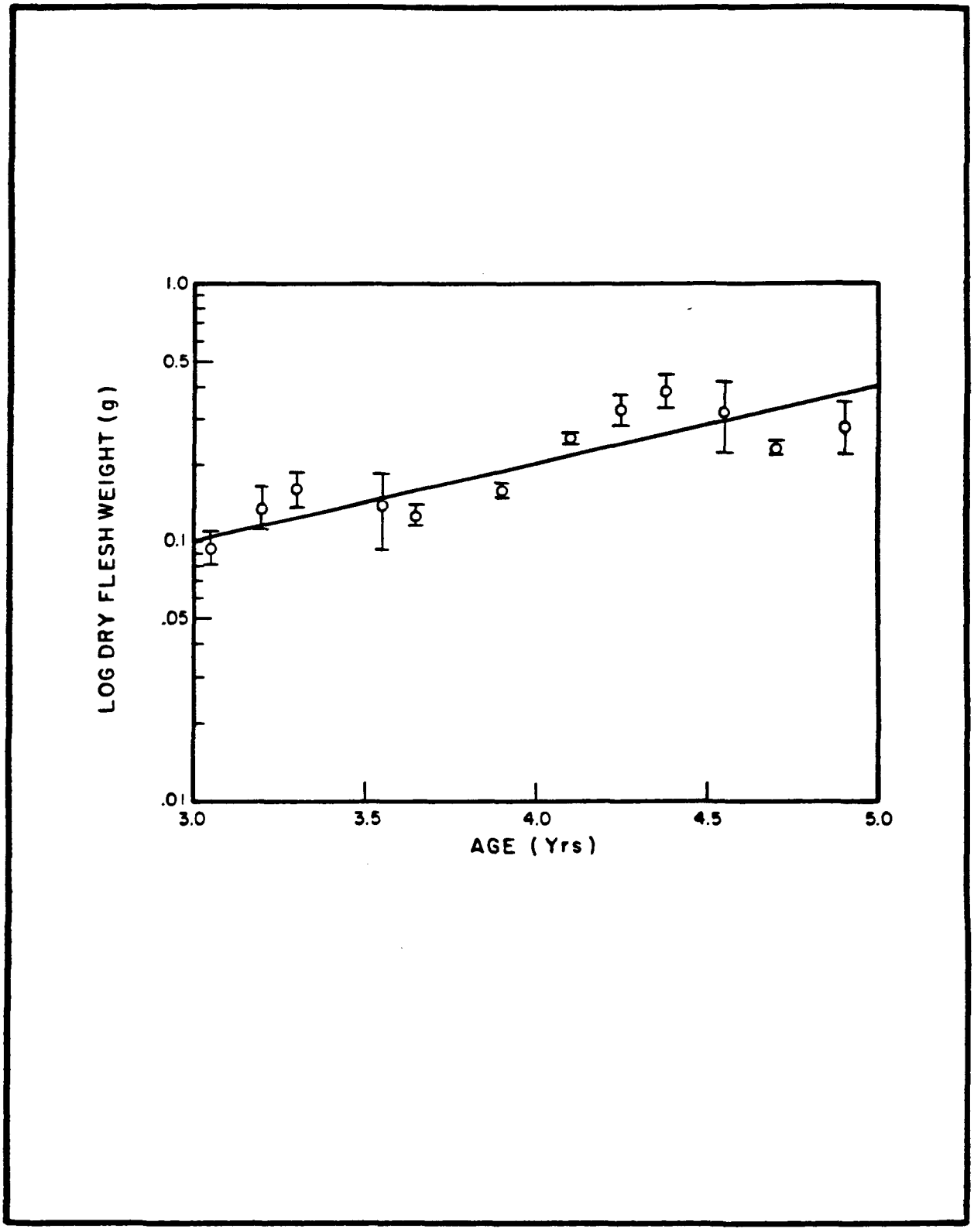

FIGURE 6.22. MYTILUS EDULIS GROWTH IN TWO ENGLISH ESTUARIES (Bayne & Worrall, 1980)

$$\log L = 1.377 \log A - 0.377$$

where:

L = shell length (mm)

A = age (month)

Weight-length relationships for spring and fall collections of Great South Bay clams have been reported by Behrens (1978). Because the spring relationship yields higher weights and may reflect pre-spawning gonadal development, the fall relationship is presumed to be more representative of average conditions.

Combining the length-age and weight-length relationships requires extrapolation of the weight-length relationship to the less than 50 mm shell lengths of animals subject to predation. Justification for this extrapolation is provided by a comparison of weight-length relationships reported for adult and juvenile hard clams from Southhampton, England (Ansell, 1964). When the adult relationship was extrapolated to the 10 to 50 mm length range of interest in this study it yielded values within 20 percent of those given by the juvenile relationship. The weight-age relationship obtained from the Great South Bay length-age and weight-length relationships is as follows:

$$W = 1.52 \times 10^{-5} A^{3.71}$$

where W is the wet tissue weight in g. Wet weight was obtained by assuming a dry weight fraction of 0.2 (Ansell, 1964).

From this relationship the weight normalized growth rate (g/g/d) may be calculated as:

$$G = (1/W)(dW/dt) = 3.71/A$$

The average growth rate over the range of ages included in the length-age relationship (6 to 32 months) is then 0.008/d.

6.4.3 Respiration Rate

6.4.3.1 Lobsters

The respiration of Homarus americanus has been correlated with animal size, temperature and feeding. A comprehensive study of lobster respiration has been published by McLeese (1964). In this study he found that routine respiration of lobster increased with body weight. Regression analysis of his data according to Equation 6-15 yielded:

$$R = 0.105\ W^{0.87} \text{ at } 15°C$$

with an r^2 of 0.96 where R is in units of mg O_2/hour and W is g wet weight.

He also determined oxygen consumption for lobsters 380 to 520 g at temperatures of 12, 15, 20 and 25°C. These data and a measurement at 5°C reported by McLeese and Watson (1968) were used to determine the temperature exponent of Equation 6-15. Regression yielded a value of 0.066 with an r^2 of 0.99 when the 25°C point was excluded.

Respiration rate was converted from mg O_2/hour to g wet weight/d assuming a stoichiometric relationship between oxygen and carbon, 0.4 g carbon per g dry weight and 0.25 g dry weight per g wet weight. The respiration rate on a g/g/d basis is then defined as:

$$R = 0.0035\ W^{-0.13}\ e^{0.066T} \qquad (6\text{-}16)$$

6.4.3.2 Winter Flounder

The coefficient values that define the respiration of winter flounder were determined from a respiration study published by Voyer and Morrison (1971). In this study respiration rate (mg O_2/hour) was measured at temperatures of 10 and 20°C and dissolved oxygen concentrations of 4.3, 6.9 and 8.7 mg/l. They report a weight dependence exponent that is similar for all tests, although slightly lower at 10°C (0.72 - 0.746) than at 20°C (0.785 - 0.792). Dissolved

oxygen concentration had no evident effect on the relationship of respiration to weight, the proportionality coefficients in the relationship at 10°C being 0.093 at 4.3 mg O_2/l and 0.105 at 8.7 mg O_2/l and at 20°C being 0.095 at 4.3 mg O_2/l and 0.196 at 6.9 mg O_2/l. Using the average weight exponent and the average proportionality coefficient at each temperature the respiration equation is defined as:

$$R = 0.051\ W^{0.76}\ e^{0.067T} \qquad (6\text{-}17)$$

where R is in units of mg O_2/hour and W is g wet weight. Respiration was converted to g wet weight/d in identical fashion to the lobster equation. The respiration on a g/g/d basis is then defined as:

$$R = 0.0046\ W^{-0.24}\ e^{0.067T} \qquad (6\text{-}18)$$

6.4.3.3 Crab

Respiration rate for the juvenile crabs included in the model was computed using the lobster respiration equation. Justification for applying the lobster relationship to the crab is based on the correspondence of the only crab respiration measurement obtained from the literature with the lobster relationship. McLeese and Watson (1968) reported a respiration rate for a 760 g spider crab at 5°C equal to 0.0019 when converted to units of g/g/d. The respiration rate given by Equation (6-16) for the same weight and temperature is 0.0020 g/g/d. An average respiration rate was computed for crabs between 1 and 2 years old (0.3 g to 8.5 g). It is 0.0033 g/g/d multiplied by the lobster exponential temperature correction. At the 15°C average temperature used in the model the rate is 0.009 g/g/d.

6.4.3.4 Mussel

The respiration of Mytilus edulis as a function of body weight and temperature has been measured in several studies (Read, 1962; Bayne et al., 1973; Widdows, 1978). In each study the respiration-weight relationship given by Equation 6-15 was used to analyze data at particular temperatures. The reported weight

exponent was similar in all cases, varying from 0.63 to 0.70. We reanalyzed the data using Equation 6-15 to include the temperature effect. Data at temperatures above 20°C were not considered because they consistently deviated from an exponential temperature dependence and are not representative of the range of temperatures expected in this study. Respiration measurements were converted from oxygen volume to dry body weight by assuming 1.38 mg O_2/ml O_2 (ideal gas at 10°C) and the conversion factors described for lobsters. The parameter values obtained for the three studies are given in Table 6.18.

The exponent for temperature dependence varies by a factor of four among the studies. This variation is partially compensated by variation in "α." In the temperature range of 5 to 15 degrees, the computed respirations vary among studies by less than a factor of 1.5. For the food chain model the coefficients obtained from Widdows were used. The average respiration rate between dry weights of 0.05 g and 0.4 g (2 to 5 year olds) of 0.0122 at 0 degrees is used. With the temperature exponent of 0.036 the 15°C rate is 0.021 g/g/d.

6.4.3.5 Polychaete

As indicated for growth rate, the bioenergetic parameters for the polychaetes are taken from a previous food chain modeling study (Connolly and Tonelli, 1984). The respiration rate is 0.02 g/g/d.

TABLE 6.18. RESPIRATION COEFFICIENT VALUES FOR MUSSELS

Reference	Salinity ‰	Respiration Coefficients α	γ	ρ
Read, 1962	24.6-28.8	0.0041	0.62	0.0827
Bayne et al., 1973	33	0.0090	0.69	0.0140
Widdows, 1978	32.5	0.0060	0.65	0.0360

6.4.3.6 Hard Clam

The respiration of the hard clam has been extensively studied by Hamwi (1969). He measured oxygen consumption as a function of size, temperature and salinity. In the analysis of his data he used the generally accepted weight relationship given by Equation 6-15; however, he used a polynomial equation to quantify temperature and salinity effects. These data were reanalyzed using the exponential temperature relationship of Equation 6-15. Using the average oxygen consumption at each temperature the temperature exponent was determined by regression to be 0.085. Combining this with the weight relationship yields the following relationship for respiration (g/g/d) at 21 to 24 ppt salinity:

$$R = 0.028\ W^{-0.622}\ e^{0.085T} \qquad (6\text{-}19)$$

Hamwi's data indicate respiration declines with increasing salinity. A decrease of about a factor of two is observed between salinities of 18 ppt and 32.5 ppt. Unfortunately, the data are not sufficient to accurately quantify the decline.

For the model an average wet weight of 2.5 g (2 year old clam) is used to compute respiration. This value is based on a shell length of 25 mm, which is assumed to be a typical size consumed by larger animals. Shell length was converted to wet weight using length-dry weight data (Behrens, 1978) and a dry weight-wet weight ratio of 0.2 that was computed from data reported by Ansell (1964). The 0 degree respiration rate is 0.014 g/g/d. With the temperature exponent of 0.085 the 15°C rate is 0.050 g/g/d.

6.4.4 Food Assimilation Efficiency

The assimilation efficiency of food is a function of the type of food eaten and the rate of consumption. In general, efficiencies are near 0.8 for carnivorous species and 0.3 for herbivorous species (Brett and Groves, 1979). Deposit feeders appear to have efficiencies in the range of the herbivorous species (Yingst, 1976). Values reported for filter feeders such as the hard clam and the mussel are in the range of 0.3 to 0.6. Tenore and Dunstan (1973)

and Bricelj et al. (1984) have reported organic material assimilation efficiencies for the hard clam in the range of 0.7 to 0.8, which is equivalent to about 0.3 on a dry weight basis. In the model, assimilation efficiencies were assumed to be 0.8 for the lobster and winter flounder, 0.6 for the polychaete (on an organic carbon basis), and 0.45 for the crab, hard clam and the mussel. A low value is used for the crab since the crabs assumed to be prey for the flounder and lobster are the herbivorous to omnivorous juvenile animals.

6.4.5 Chemical Assimilation Efficiencies

The data obtained on chemical assimilation efficiency, bioconcentration factor and excretion rate were used to establish ranges for use in calibrating the food chain model. Whereas the bioenergetic parameter values were established from the data analysis and interpretation discussed above, a choice of values for assimilation efficiency and excretion rate was not made based on the data available. Rather these data provided guidance for the model calibration, i.e., they established a range within which the parameter values may be adjusted to provide the best comparison of field data and model calculation.

6.4.5.1 PCBs

The data from laboratory experiments to determine the assimilation efficiency of PCBs by flounder and lobster (see Section 2.3.1) were not used to parameterize the model. Instead, the assimilation efficiencies used in the model are based on values obtained from published studies.

Several laboratory studies have examined the fraction of ingested PCB that is absorbed. Tanabe et al. (1982) found that small carp (28 g at start of study) fed a commercial food pellet contaminated with PCBs had adsorption efficiencies ranging from 67 to 93 percent. The values decreased with increasing chlorine content of the PCB. Table 6.19 presents the approximate range for the congeners in each homolog grouping.

TABLE 6.19. RANGE OF CARP PCB ASSIMILATION EFFICIENCIES MEASURED FOR THE CONGENERS IN THE 3 TO 8 HOMOLOGS (Tanabe et al., 1982)

Homolog	Assimilation Efficiencies (%)
3-PCB	82 - 91
4-PCB	82 - 88
5-PCB	80 - 88
6-PCB	77 - 87
7-PCB	73 - 79
8-PCB	67 - 79

Goerke and Ernst (1977) fed the sandworm, Neries virens, pieces of Lanice conchilega contaminated with three PCB congeners for a three week period. Based on the PCB in the worms at the end of the exposure period assimilation efficiencies were computed. The values were 58 percent for 2,5,4'-trichlorobiphenyl, 70 percent for 2,2'-dichlorobiphenyl and 93 percent for 2,4,6,2',4'-pentachlorobiphenyl.

Absorption efficiencies of individual PCB congeners by 900 g rainbow trout exposed to a single oral dose administered in a gelatin capsule inserted in the stomach are reported by Niimi and Oliver (1983). The efficiencies were calculated by comparing the administered dose to the PCB estimated to be in the fish after administration. PCB in the fish was computed by extrapolation of body burden versus time data to the day of administration. The efficiencies average about 75 percent and range from 62 to 85 percent. No trend with homolog grouping is evident as indicated by a plot of assimilation efficiency in relation to the K_{OW} of each congener (Figure 6.23).

Analyzing body burden data with a first-order model, Opperhuizen and Schrap (1988) estimated the assimilation efficiencies of 2,2',3,3',5,5'-hexa and 2,3',3,3',4,4',6,6'-octachlorobiphenyl in 70 to 130 mg guppies fed a contaminated diet. Several concentrations of the PCBs in Tetramin fish food

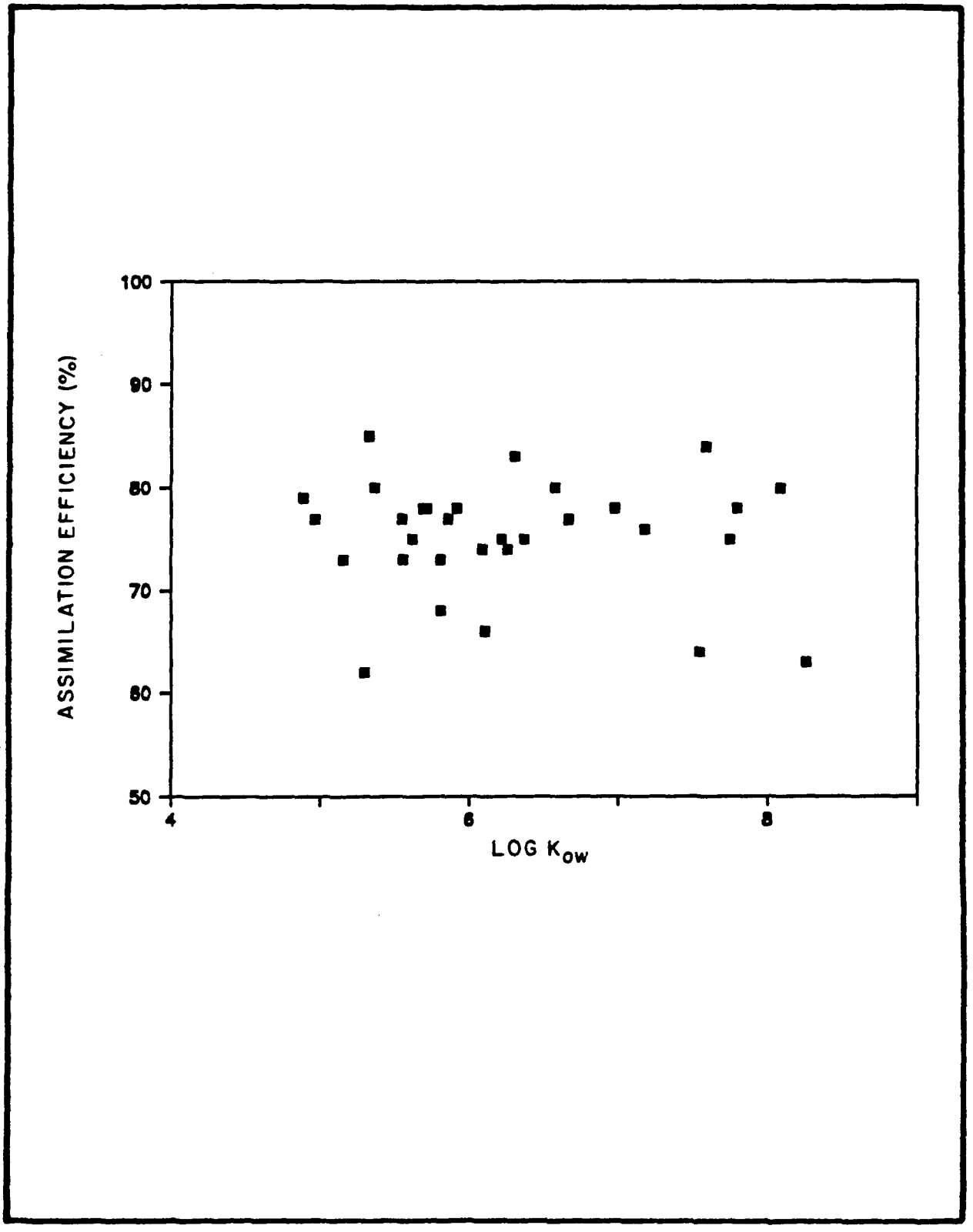

FIGURE 6.23. PCB ASSIMILATION EFFICIENCY IN RELATION TO K_{ow} BASED ON DATA FROM NIIMI AND OLIVER (1983)

were used. The mean assimilation efficiencies at food PCB concentrations up to 150 μg/g ranged from 44 to 53 percent for the hexa- and 45 percent to 50 percent for the octachlorobiphenyl.

In a series of studies with goldfish and guppies (Bruggeman, 1980; Bruggeman et al., 1981; Bruggeman et al., 1984) assimilation efficiencies were measured for several PCB congeners. These data indicate a decline in assimilation efficiency at the highly chlorinated congeners (Figure 6.24). For the di- through hexachlorobiphenyls no trend is evident and the values range from 42 to 67 percent. The measurements for an octachlorobiphenyl range from 31 to 40 percent and for decachlorobiphenyl they range from 19 to 26 percent.

6.4.5.2 Metals

With the exception of cadmium and mercury, little information is available in the literature on the assimilation efficiencies of metals. Because field data show little or no food chain enrichment of metals other than mercury (Forstner and Wittmann, 1979) it is assumed that, in general, the assimilation efficiencies of metals must be low. Low values are attributed to the tendency of metals to be stored in relatively inert components of cells which are not readily digested (Hodson, 1980).

The assimilation efficiency of phytoplankton associated cadmium by marine zooplankton has been found to be approximately 10 percent in one study (Benayoun et al., 1974) and between 13 and 68 percent in another (Sick and Baptist, 1979).

The shore crab (Carcinus maenas) consuming cadmium contaminated Artemia salinia assimilated about 10 percent of the ingested cadmium (Jennings and Rainbow, 1979).

In a study of the accumulation of cadmium by eels fed gammerids only about one percent of the ingested cadmium was retained in the eels (Haesloop and Schirmer, 1985). While this is not a direct measurement of assimilation efficiency because it does not account for excretion of cadmium, it indicates

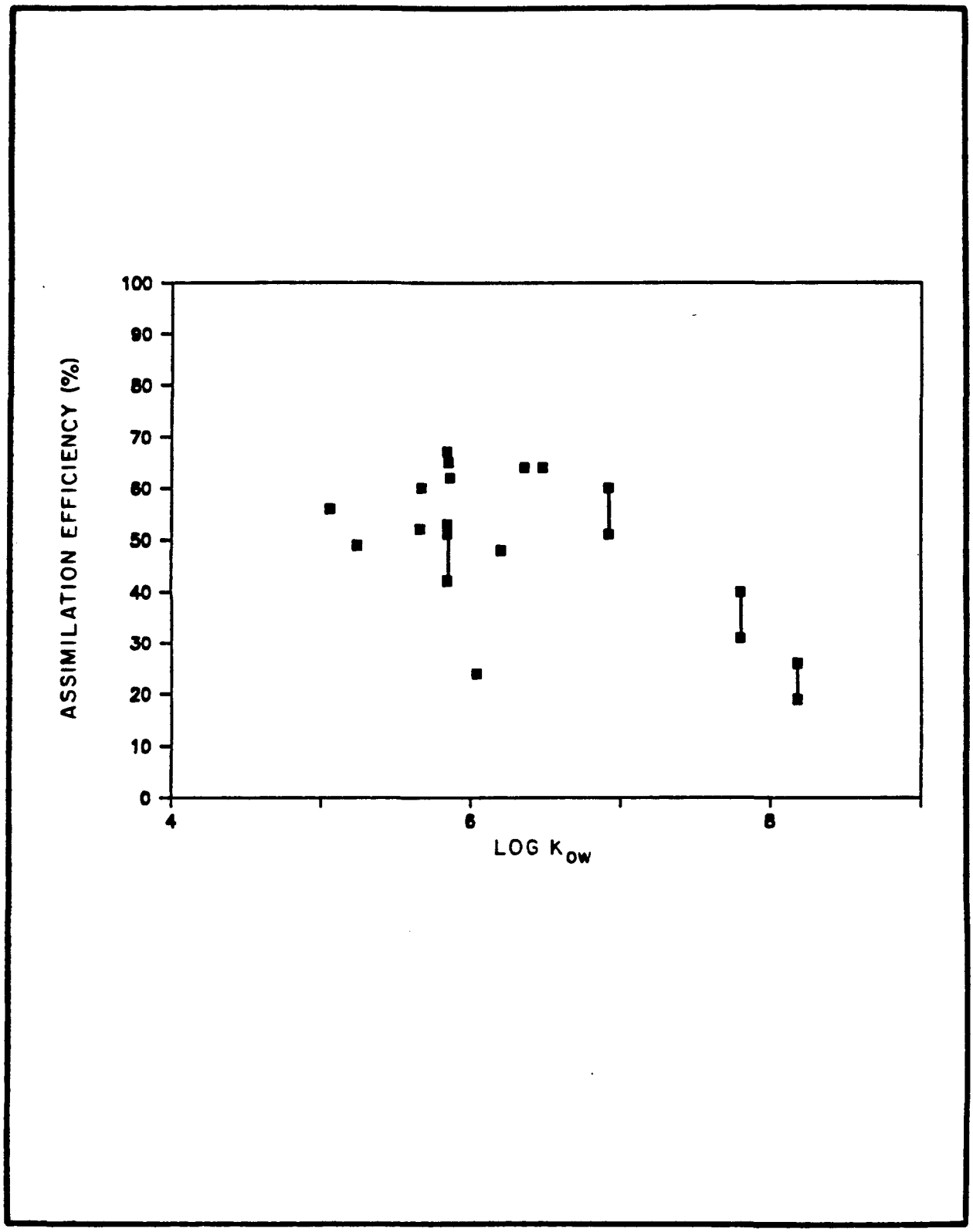

FIGURE 6.24. PCB ASSIMILATION EFFICIENTLY IN RELATION TO K_{ow} BASED ON DATA FROM BRUGGEMAN (1980, 1981, AND 1984)

that the efficiency is very low. The authors also present a summary of published retention values that are also of the order of one percent.

Pentreath (1977) examined the accumulation of cadmium by two marine fish, 45 to 55 g plaice (Pleuronectes platessa L.) and 35 to 50 g thornback ray (Raja clavata L.), fed a single cadmium contaminated Neries. Plaice examined four days after feeding retained about five percent of the ingested cadmium. Thornback ray examined 6 days after feeding retained about 17 percent of the ingested cadmium. For both species most the cadmium was associated with the gut wall.

Assimilation efficiency studies conducted as part of this project are discussed in Section 2.3 of this report. Values for the lobster are highly variable. Cadmium assimilation efficiencies range from 0.33 to 1.52, with 3 of the 8 measurements being greater than 1.0 Values above 1.0 are obviously impossible and indicate errors in the measurement of cadmium concentration.

The data for lead assimilation efficiency by lobsters range from 0.42 to 1.0. The mean value is 0.67 and the standard deviation is 0.22.

The computed assimilation efficiencies for flounder are much less variable than the lobster values. The cadmium values range from 0.38 to 0.62 with a mean of 0.51. The lead values range from 0.74 to 0.92 with a mean of 0.84. The copper values range from 0.05 to 0.13 with a mean of 0.07.

The results suggest differences between lobster and flounder in their abilities to take up the various metals. Cadmium appears to be highly assimilated by the lobster and only moderately assimilated by the flounder. Conversely, lead is highly assimilated by the flounder and moderately assimilated by the lobster. In all cases, the efficiencies for cadmium and lead measured in this study are higher than those reported in the literature or presumed from observations of a lack of food chain enrichment. Although the results are somewhat uncertain because of the variability of the individual measurements, particularly for the lobster, they do suggest real

differences between species that may make direct comparison to literature data inappropriate.

6.4.6 Bioconcentration Factors and Excretion Rates

As discussed in Section 6.3, the excretion rates of the various chemicals can be calculated from the bioconcentration factors. For the PCB homologs bioconcentration factors are calculated from the 1-octanol-water partition coefficient of the homolog and the lipid content of the individual species. For the metals excretion rates are based on the results of the measurements of uptake and depuration discussed in Section 2.3.

Bioconcentration factors (N) and excretion rates (k) were computed from the uptake and depuration data by fitting a first order uptake-depuration model to the data.

$$\nu = Nc\ (1-e^{-kt}) - \nu_0 e^{-kt} \qquad (6\text{-}20)$$

The data for juvenile and adult animals were combined where no differences were evident. In several cases a significant background concentration of chemical (ν_0) was measured. The analysis of the data was performed assuming that the background either was non-excretable or excretable along with chemical taken up during the test (as indicated in the equation). In general, the variability of the data introduced considerable uncertainty into the parameter estimates.

This uncertainty was not quantified because the equation was manually fitted to the data rather than by using a least squares technique. Values obtained for the bioconcentration factor and the excretion rate are presented in Table 6.20.

Large differences between animals and across chemicals is evident. Of particular note is the differences between lobster and flounder. Lobster exhibit a higher bioconcentration factor for lead than for cadmium whereas the flounder have a value for lead that is extremely low and a factor of 40 less

TABLE 6.20. BCF AND EXCRETION RATE VALUES DETERMINED FROM LABORATORY STUDIES

Species	Cadmium		Lead		Copper	
	BCF[a] l/Kg	Excretion Rate	BCF l/Kg	Excretion Rate	BCF l/Kg	Excretion Rate
Adult Lobster	-	-	600	.015	-	-
Juvenile Lobster	-	-	400	.02	-	-
All Lobster	70-130[b]/250	.01-.03[b]/.005	470	.02	-	-
Adult Winter Flounder	1500	.025	40	.035	-	-
Juvenile Winter Flounder	3000	.03	20	.035-.05	-	-
All Winter Flounder	-	-	-	-	20[b]/80	.04[b]/.01
Polychaete	35	.012	1000	.002	2000	.01
Hard Clam	40	.0036	90	.013	200[b]/350	.015[b]/.012

[a] BCF based on nominal exposure concentration of 10 µg/l
[b] Initial body burden is assumed to be an unexcretable background

than their value for cadmium. These relative values are not consistent with the relationships between assimilation efficiencies of these chemicals, as described above. These differences may reflect differences in the ability of the chemicals to be assimilated across the gill and the gut of each species and perhaps differences in gut environment such as pH.

6.5 Model Calibration

The final calibrations are the results of model runs to determine a consistent set of parameters that are in agreement with literature or laboratory values and reproduce the observed average homolog 3, 4, 5, 6, total PCB and metals concentrations reported during the sampling cruises in 1984 and 1985.

Arithmetic average dissolved and particulate water column and sediment concentrations from the four cruises were used as exposure concentrations. As indicated in Section 6.2, the Area 1 averages do not include stations 1, 2, 3, 4 and 6 located in the upper estuary where no biota were collected. Arithmetic averages over all size classifications were used in comparing the observed and computed concentrations. The averages of the computed flounder and lobster concentrations were weighted so that the contribution of any age class to the average was consistent with the contribution of that age class to the average of the observed values. For all other species the steady-state computed concentration was compared to the arithmetic average observed concentration. Six age classes of flounder and lobster were included in the model based on the weights of the animals collected during the trawls. The largest flounder age class included animals weighing up to 363 g and the largest lobster age class included animals weighing up to 773 g. A few larger animals were reported in the trawl data, however, they were not included in the data averages. Lobster were not modeled in Area 1 since only a single lobster was collected during the cruises.

The bioenergetic parameters used in the model are summarized in Table 6.21 for the steady state species and in Table 6.22 for the age dependent species. These parameters are based on literature values (see Section 6.4) and remained constant during calibration. These coefficients are independent of the chemical being modeled.

TABLE 6-21. BIOENERGETIC RELATED PARAMETERS USED IN FOOD CHAIN MODEL CALIBRATION STEADY STATE SPECIES

Species	Growth Rate (1/day)	Respiration Rate (1/day)	Exponential Coefficient for Temperature Dependence of Species Respiration	Food Assimilation Efficiency (%)	Fraction Lipid	Fraction Weight
Polychaete	0.007	0.02	0	60*	0.015	0.2
Clam	0.008	0.014	0.085	45	0.003	0.2
Mussel	0.0019	0.012	0.036	45	0.009	0.2
Crab	0.009	0.009	0	45	0.008	0.25

*Organic carbon basis

TABLE 6-22. BIOENERGETIC RELATED PARAMETERS USED IN FOOD CHAIN MODEL CALIBRATION AGE DEPENDENT SPECIES

Species	Age Class	Growth Rate (1/day)	Initial Weight of Age Class (gw)	Respiration Coefficient	Respiration Weight Exponent	Exponential Coefficient for Temperature Dependence of Species Respiration	Food Assimilation Efficiency (%)	Fraction Lipid	Fraction Weight
Flounder	1	0.013	0.015	0.0046	0.248	0.067	80	0.018	0.25
	2	0.0063	15.0						
	3	0.0017	100.0						
	4	0.00096	190.0						
	5	0.0004	270.0						
	6	0.0004	313.0						
Lobster	1	0.0087	0.05	0.0035	0.13	0.06	80	0.008	0.25
	2	0.0085	1.2						
	3	0.0039	27.0						
	4	0.0024	113.0						
	5	0.0015	268.0						
	6	0.0013	473.0						

6.5.1 PCB

The food chain model was calibrated for homologs 3, 4, 5 and 6 and for total PCB. Total PCB was computed two ways. First, the summation of the concentrations computed for the homologs was compared to the observed total PCB as an additional check on the homolog calibrations. Second, total PCB was calibrated as a separate chemical. The water column and sediment exposure concentrations used in the calibration are presented in Table 6.11. Sediment interstitial water dissolved concentrations were assumed to be equal to the observed water column values. The choice of interstitial water concentrations is not critical since the polychaetes derive a majority of their PCB from ingestion of contaminated sediment. The exposure concentrations determined from the cruise data were assumed to represent the average over the life span of the animals. Such an assumption is reasonable based on the relatively constant body burdens observed between the late 1970s and the time of the cruises (see Section 6.2.2).

Bioconcentration factors (BCFs) were calculated based on average lipid content of each member of the food chain and octanol-water partition coefficients (K_{OW}) of the homologs. Log K_{OW} values of 5.5, 6.0, 6.5 and 7.0 were assumed for homologs 3, 4, 5, and 6, respectively. A value of 6.25 was assumed for total PCB. The BCF values are given in Table 6.23.

TABLE 6.23. BIOCONCENTRATION FACTORS AND CHEMICAL ASSIMILATION EFFICIENCIES USED IN PCB CALIBRATIONS

	Bioconcentration Factor (L/g)					Chemical Assimilation Efficiency (%)				
	Homolog				Total	Homolog				Total
Species	3	4	5	6	PCB	3	4	5	6	PCB
Polychaete	4.7	15.0	47.4	47.4	26.7	60	25	15	15	15
Clam	0.9	3.0	9.5	9.5	5.3	50	30	20	20	20
Mussel	2.8	9.0	28.5	28.5	16.0	50	30	20	20	20
Crab	2.5	8.0	25.3	25.3	14.2	50	40	25	25	25
Lobster	2.5	8.0	25.3	25.3	14.2	50	40	25	25	25
Flounder	5.7	18.0	56.9	56.9	32.0	80	60	40	40	40

During initial calibration the bioconcentration factor (or partition coefficient) for plankton was dependent on K_{ow}, in similar fashion to the higher trophic level animals. This caused computed concentrations in the higher trophic levels to be unreasonably high, even at the lower bounds of observed assimilation efficiencies. Subsequent review of published data indicated that the plankton bioconcentration factor is approximately constant over the full range of PCB congeners. Figure 6.25 shows the bioconcentration factors for various PCB congeners in Lake Ontario plankton. These data were reported by Oliver and Niimi (1988). It appears that the BCF is independent of K_{ow} in the log K_{ow} range of 5 to 8. Laboratory phytoplankton BCF data for PCB congeners (Figure 6.26) and other organic chemicals (Figure 6.27) suggest that BCF is proportional to K_{ow} up to log K_{ow} of about 5 and becomes fairly constant at higher K_{ow} values. Consistent with the Lake Ontario data, a wet weight based log BCF of 4.6 was used in the calibration.

Chemical assimilation efficiencies were adjusted within the range of observed values for the model calibration. This parameter was chosen as the calibration variable because of the uncertainty of its value relative to the other parameters in the model. During calibration we restricted changes in assimilation efficiency to maintain a relationship of assimilation efficiency and homolog that was consistent across all of the species in the food chain. This restriction reflects the fact that the transfer of any homolog across the gut of any animal is controlled by processes that are chemical dependent such as lipid solubility, molecular size and molecular diffusivity. Therefore the relationship of assimilation efficiency and homolog should be similar for all of the animals. This restriction coupled with apriori specification of a constant gill permeability ratio across homologs at a value of one (note that the model is rather insensitive to this assumption because uptake from food dominates accumulation of the higher chlorinated homologs) and apriori calculation of BCF from animal lipid content and K_{ow} allows for little parameter adjustment during the calibration process. The extent to which the model reproduces the observed concentrations is thus viewed as a rigorous test of the modeling framework. The calibration values of assimilation efficiency are presented in Table 6.23.

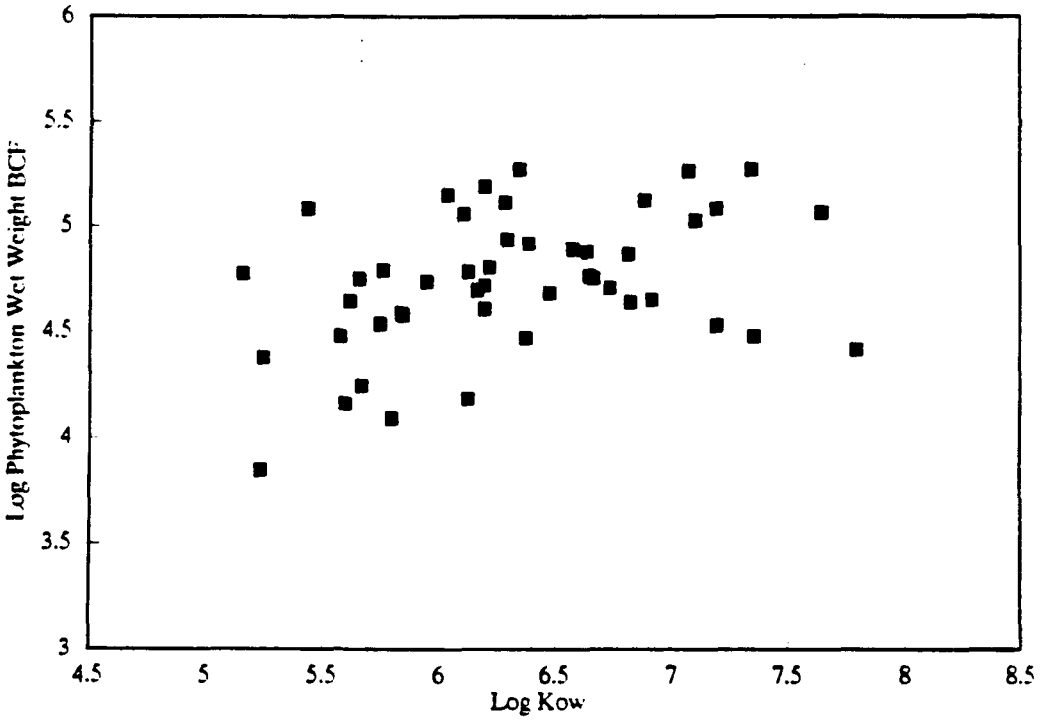

FIGURE 6.25. RELATIONSHIP OF LAKE ONTARIO PHYTOPLANKTON PCB BCF AND K_{OW} (DATA FROM OLIVER NIIMI, 1988)

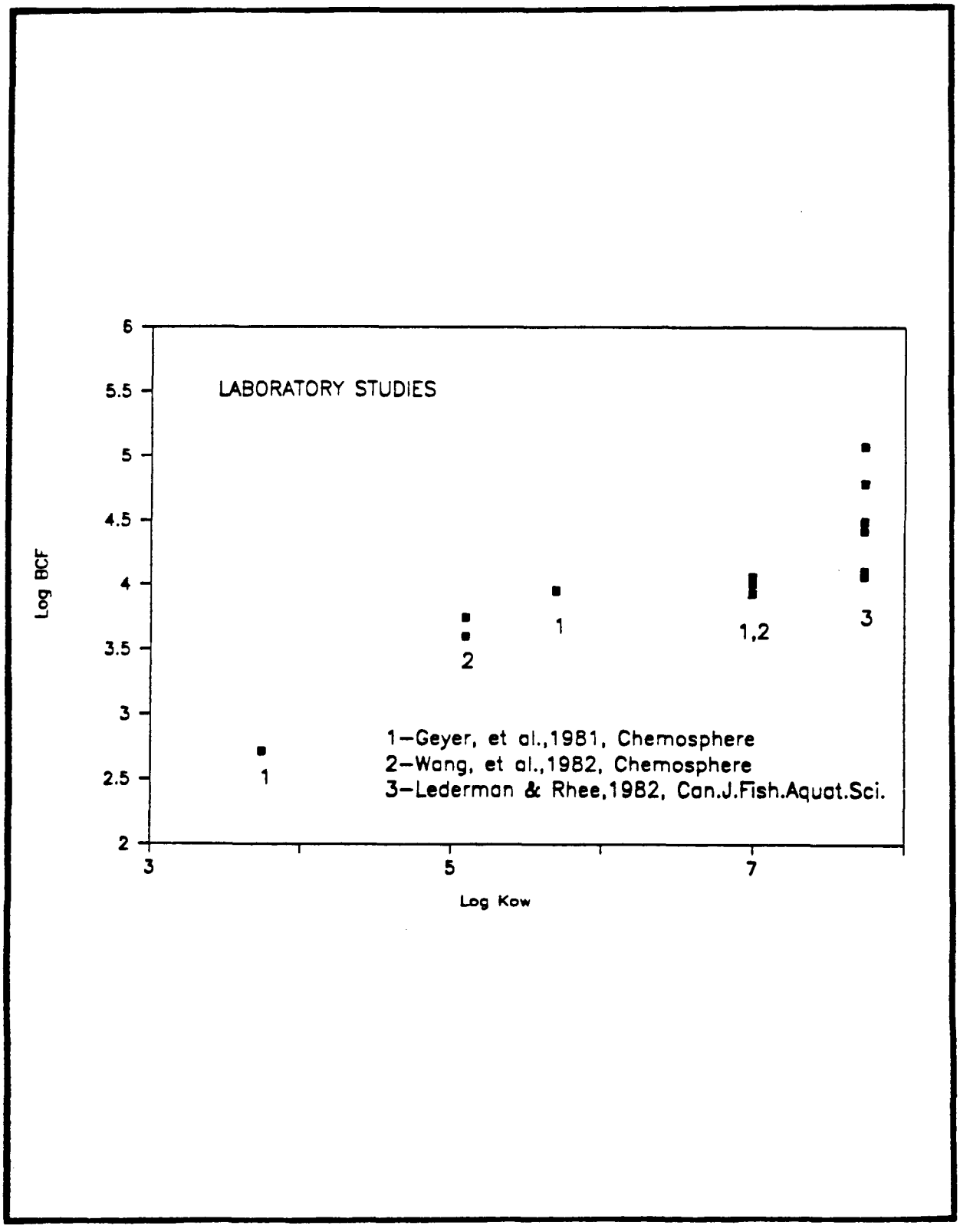

FIGURE 6.26. RELATIONSHIP BETWEEN PHYTOPLANKTON BCF AND K_{OW} FOR VARIOUS PCB CONGENERS

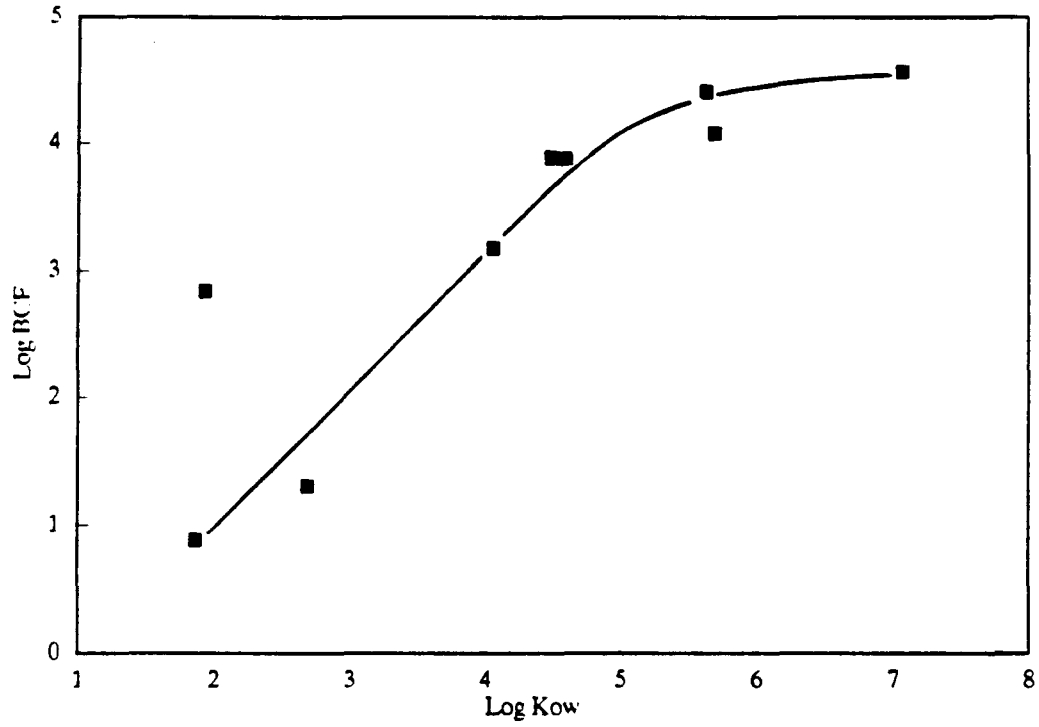

FIGURE 6.27. BCF OF VARIOUS ORGANIC COMPOUNDS IN THE GREEN ALGA SELENASTRUM CAPRICORNUTUM IN RELATION TO K_{OW} (DATA FROM MAILHOT, 1987)

The comparisons between observed and calculated concentrations are presented on Figures 6.28 through 6.32 for homologs 3 through 6 and total PCB as the sum of these homologs and on Figure 6.33 for the separate total PCB calibration. Both the observed and calculated values are averaged over all age classes. The observed values are arithmetic means and standard deviations of the combined cruise data.

There is generally good agreement between the observed data and the calculated concentrations for the homologs and total PCB. The model successfully reproduces the variation in body burdens across the homologs and over the entire food chain. It also reproduces the spatial concentration gradients evident in the data, although some bias is evident in Areas 3 and 4.

In these areas the computed values fall within the error bars of the data but they are consistently below the mean. It was not possible to achieve a calibration that eliminated this bias without computing unreasonably high concentrations in Areas 1 and 2. The data from Areas 3 and 4 may reflect a sampling bias to nearshore or shallow areas which are more highly contaminated than the stations from which water and sediment samples were taken. Because of the greater significance of model calculations in the more contaminated Areas 1 and 2, the calibration was directed to these areas.

Computed and observed whole body concentrations in flounder are higher than in the lobster. The model indicates that this is due to the higher whole body lipid content of the flounder and to differences in the food chain structures of these species. The flounder diet, with the exception of the first age class, is assumed to be exclusively polychaetes, whereas only 20 percent of the lobster diet is polychaetes. The polychaetes are more highly contaminated than the other prey species because of differences in the uptake and loss rates of PCB and the levels of PCB contamination in food. The most significant of these differences are lower excretion rates for the polychaete resulting from a higher lipid content and substantially higher PCB concentrations in the sediment consumed by the polychaetes than in the phytoplankton consumed by the clams and mussels.

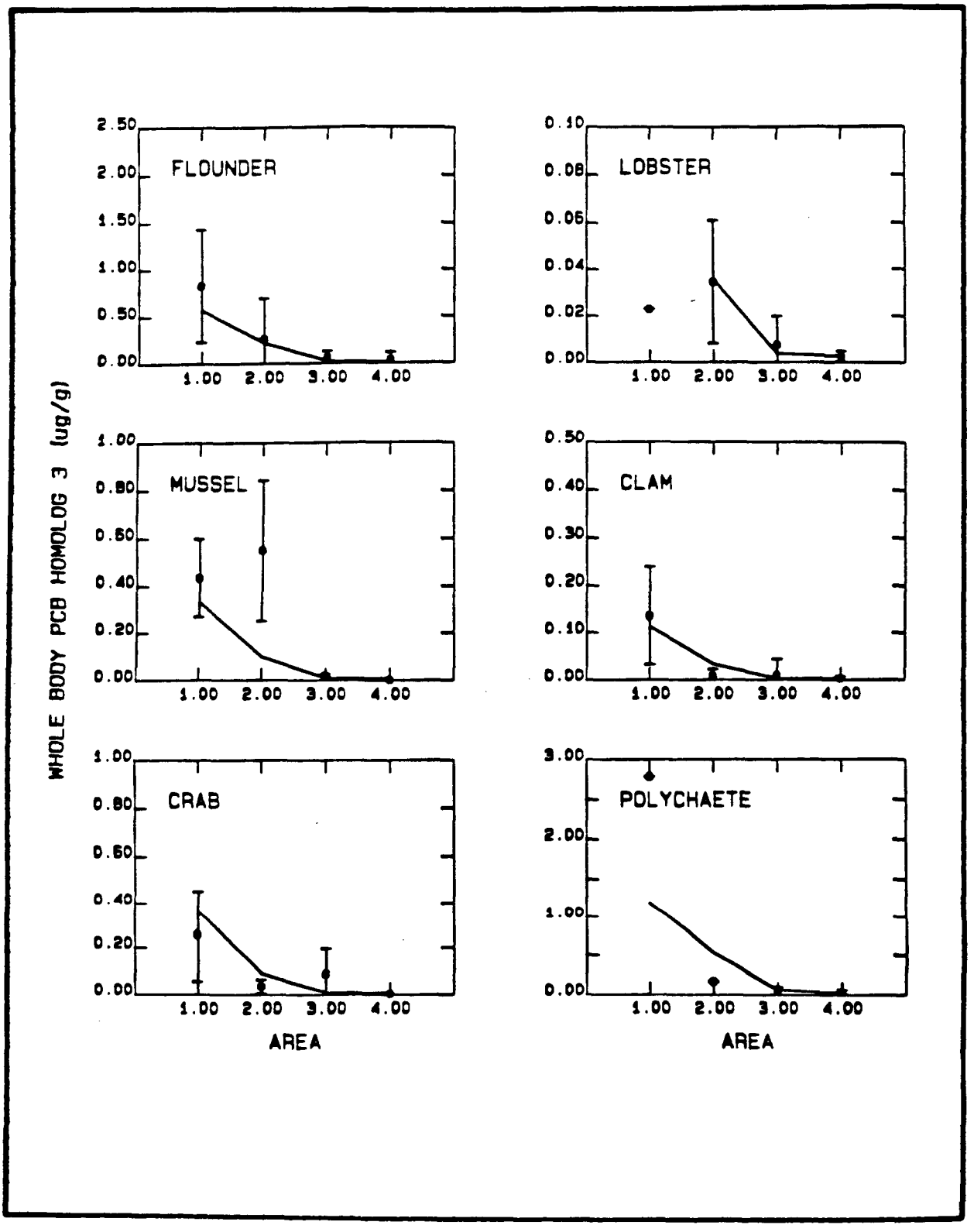

FIGURE 6.28. OBSERVED AND COMPUTED PCB HOMOLOG 3 CONCENTRATIONS IN NEW BEDFORD HARBOR ANIMALS

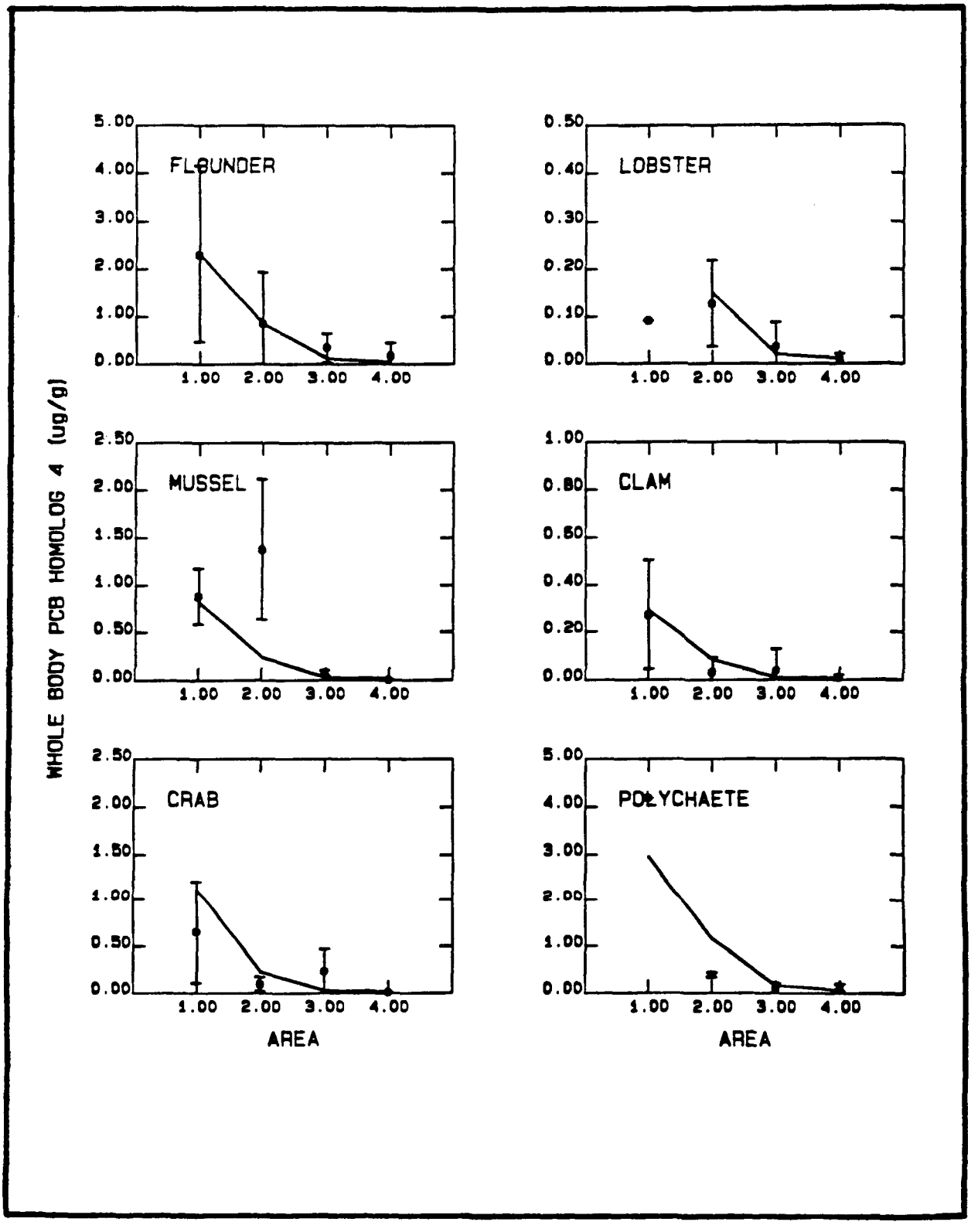

FIGURE 6.29. OBSERVED AND COMPUTED PCB HOMOLOG 4 CONCENTRATIONS IN NEW BEDFORD HARBOR ANIMALS

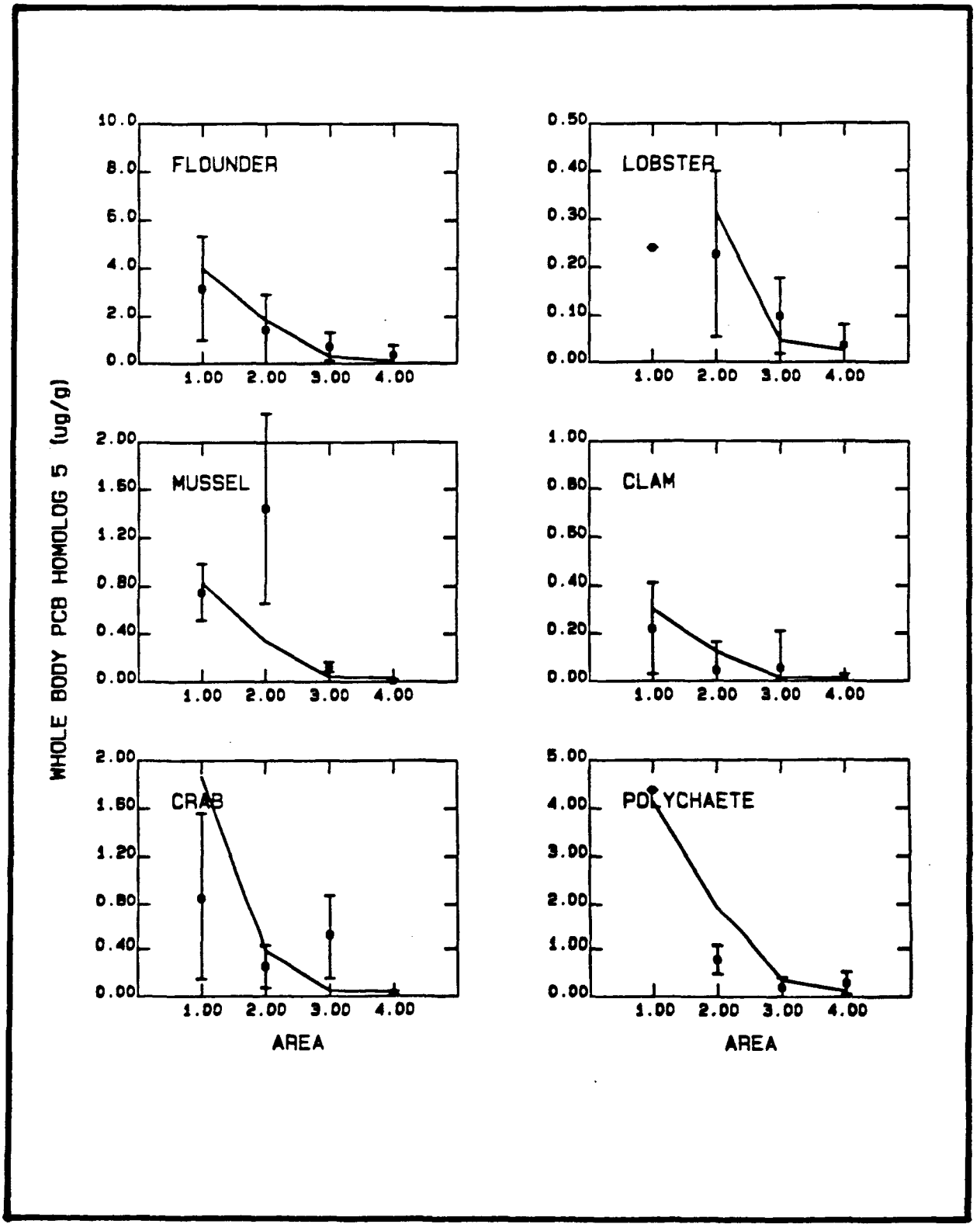

FIGURE 6.30. OBSERVED AND COMPUTED PCB HOMOLOG 5 CONCENTRATIONS IN NEW BEDFORD HARBOR ANIMALS

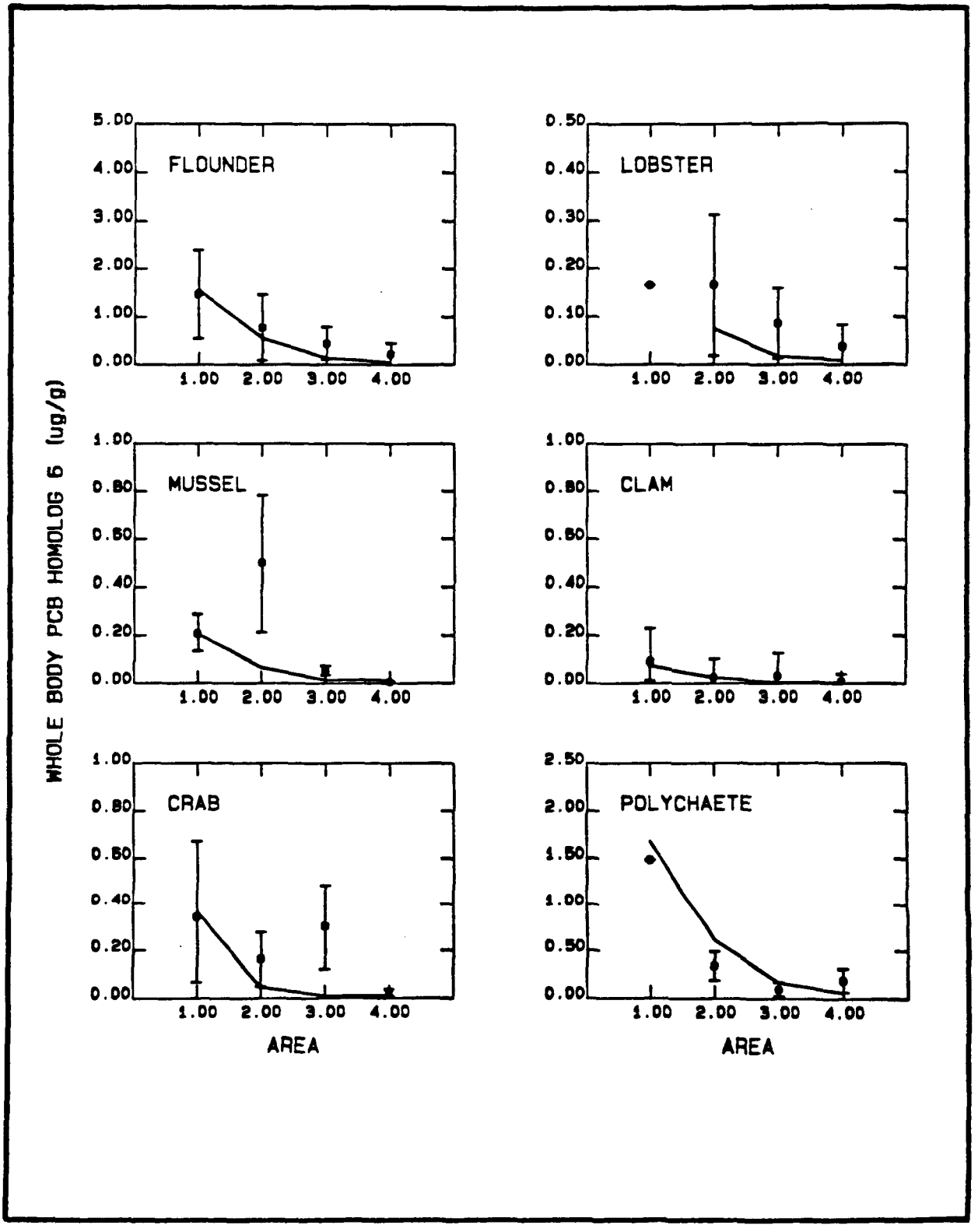

FIGURE 6.31. OBSERVED AND COMPUTED PCB HOMOLOG 6 CONCENTRATIONS IN NEW BEDFORD HARBOR ANIMALS

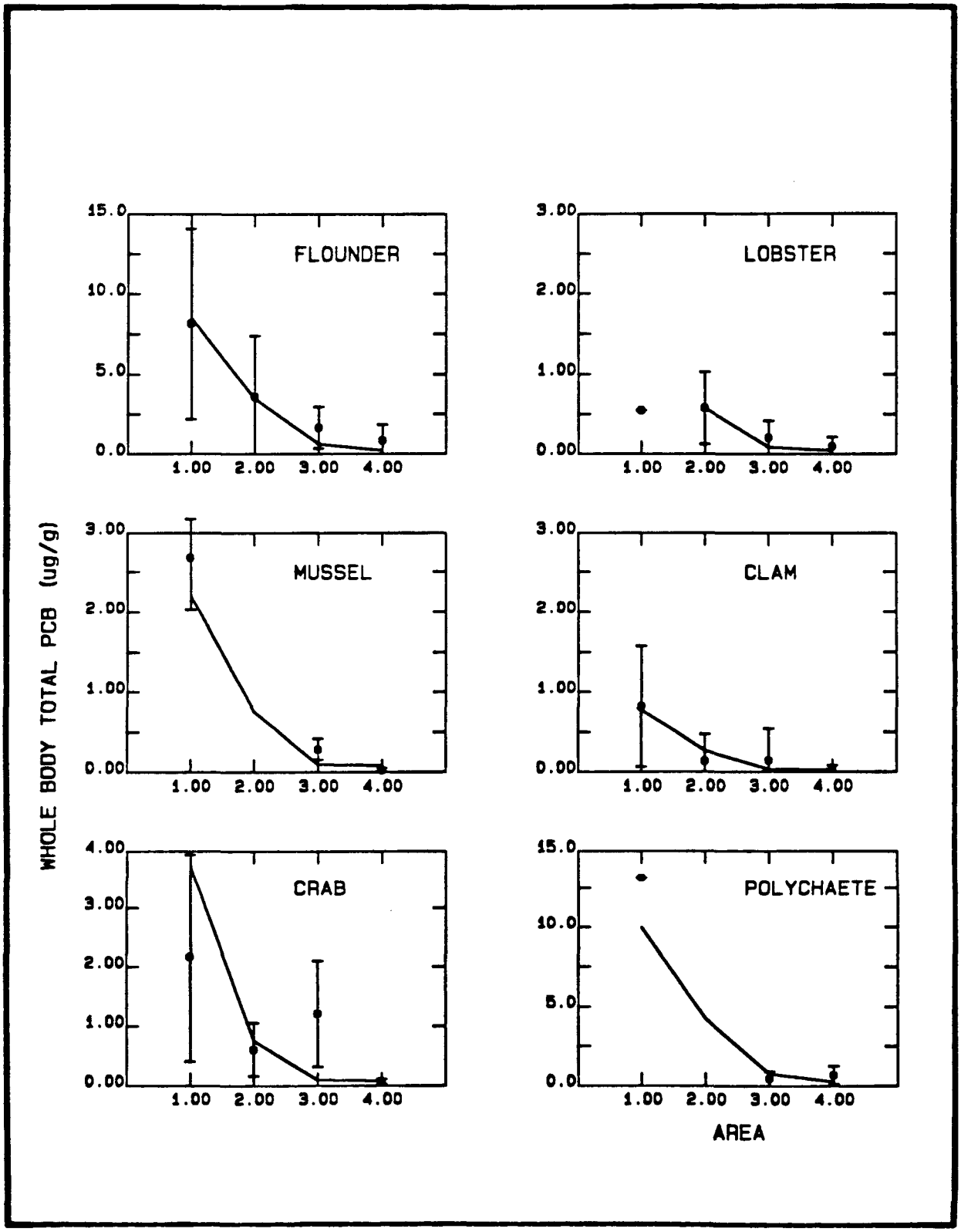

FIGURE 6.32. OBSERVED AND COMPUTED TOTAL PCB (AS SUM OF HOMOLOGS 3 THROUGH 6) CONCENTRATIONS IN NEW BEDFORD HARBOR ANIMALS

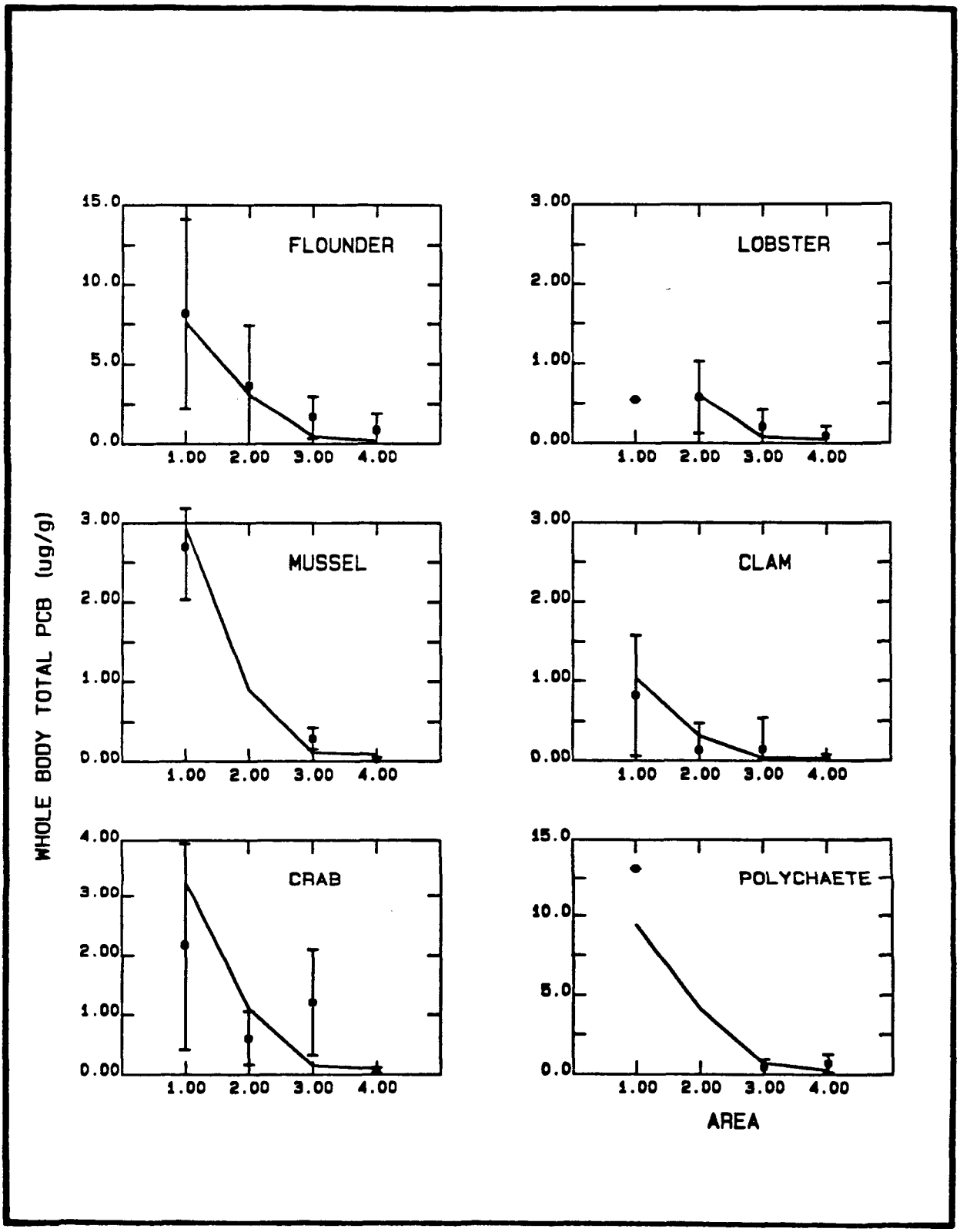

FIGURE 6.33. OBSERVED AND COMPUTED TOTAL PCB CONCENTRATIONS IN NEW BEDFORD HARBOR ANIMALS

6.5.2 Metals

Laboratory studies indicate that for metals such as cadmium, copper and lead it is the free ion concentration that is available for uptake by organisms rather than the total dissolved concentration. In seawater the free ion concentration of most metals is low because of the complexation of the metal with the available chloride ion. In addition, the free ion concentration for copper and lead varies as a function of pH, while the percent free ion concentration for cadmium remains fairly constant (Zirino and Yamamoto, 1972).

Based on analysis of pH data collected by Woods Hole Oceanographic Institute, a pH of 7.5 was used to determine the percent free ion concentration for cadmium, copper and lead. Using the pH dependent model developed by Zirino and Yamamoto and a pH of 7.5 the percent free ion concentration for cadmium, copper and lead was determined to be equal to 2.5 percent, 9.0 percent and 3.0 percent respectively. These percents were used to adjust the arithmetic average dissolved water column concentrations for use as exposure concentrations in the food chain model. The water column and sediment exposure concentrations used in the calibration are presented in Table 6.12. Sediment interstitial water dissolved concentrations were assumed to be equal to the water column exposure concentrations.

Food chain model calibrations for cadmium, copper and lead were performed by adjusting the chemical assimilation efficiencies and bioconcentration factors for the individual species. These parameters were chosen as the calibration variables because of their uncertainty relative to the other parameters in the model. During calibration values were maintained within the ranges defined by the laboratory studies and published references. Table 6.24 summarizes the bioconcentration factors and chemical assimilation efficiencies used in the model for each species.

The model calibration for cadmium, copper and lead are presented in Figures 6.34 through 6.36. As in the PCB calibration, both the observed and calculated concentrations are averaged over all age classes. The data

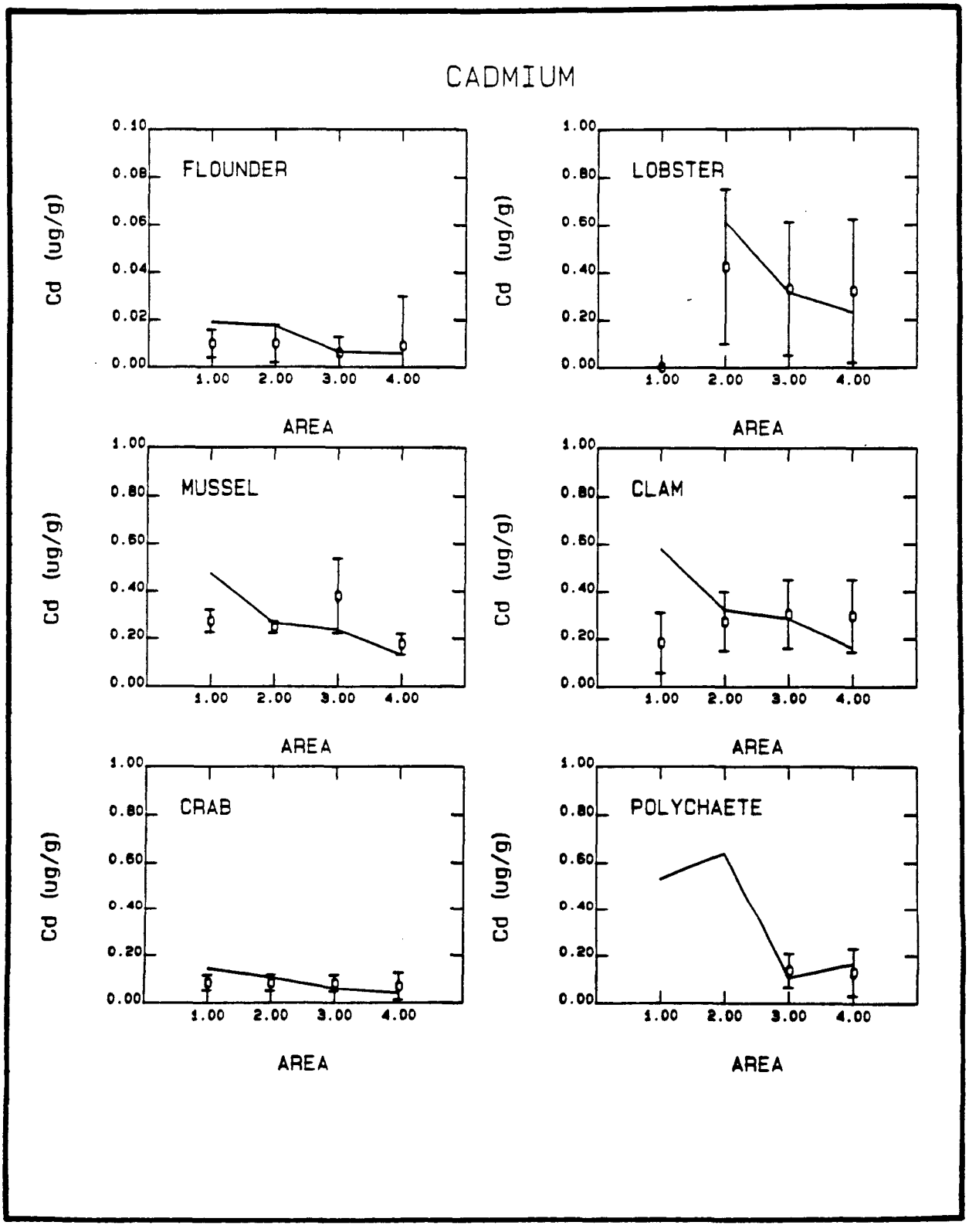

FIGURE 6.34. OBSERVED AND COMPUTED CADMIUM CONCENTRATIONS IN NEW BEDFORD HARBOR ANIMALS

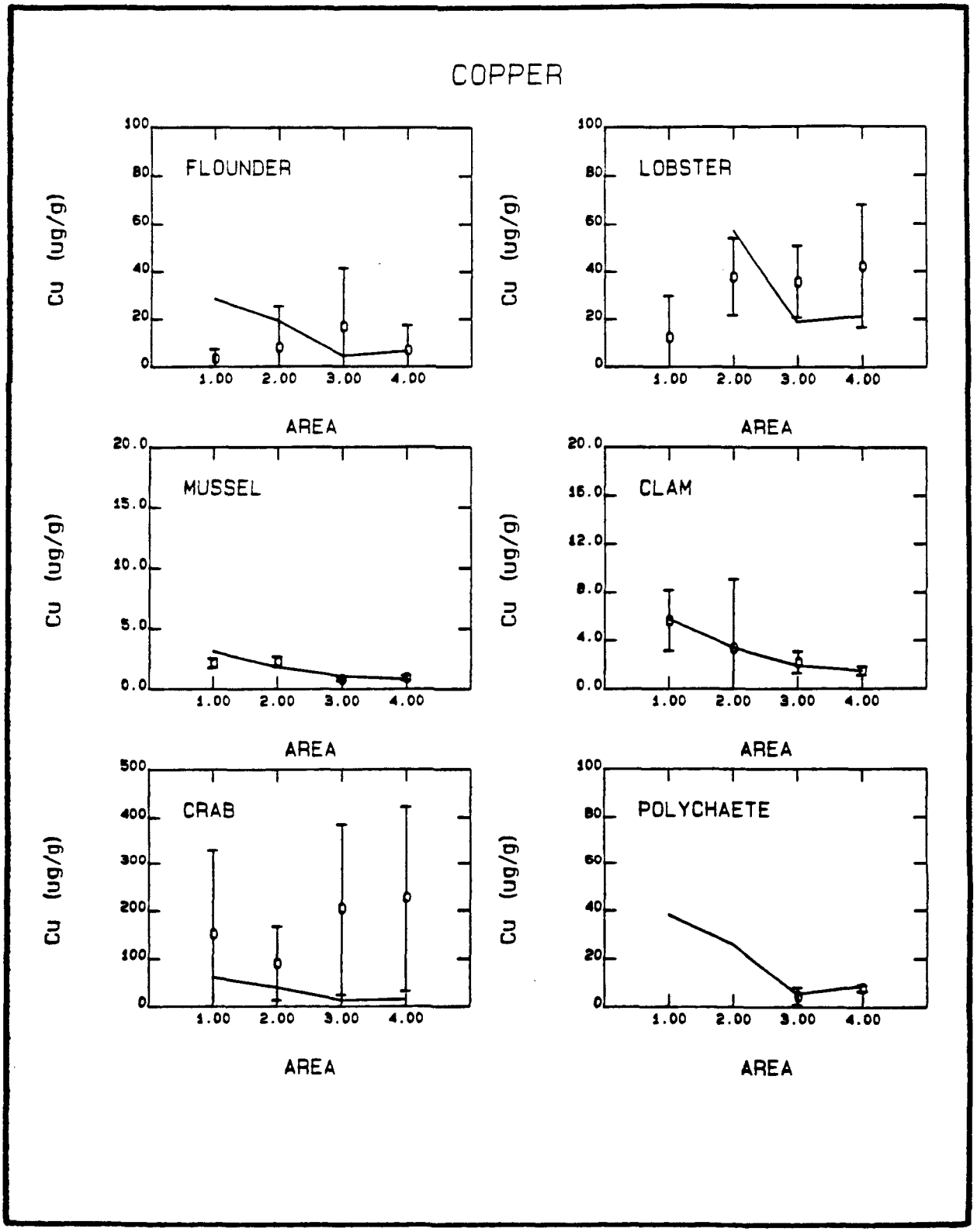

FIGURE 6.35. OBSERVED AND COMPUTED COPPER CONCENTRATIONS IN NEW BEDFORD HARBOR ANIMALS

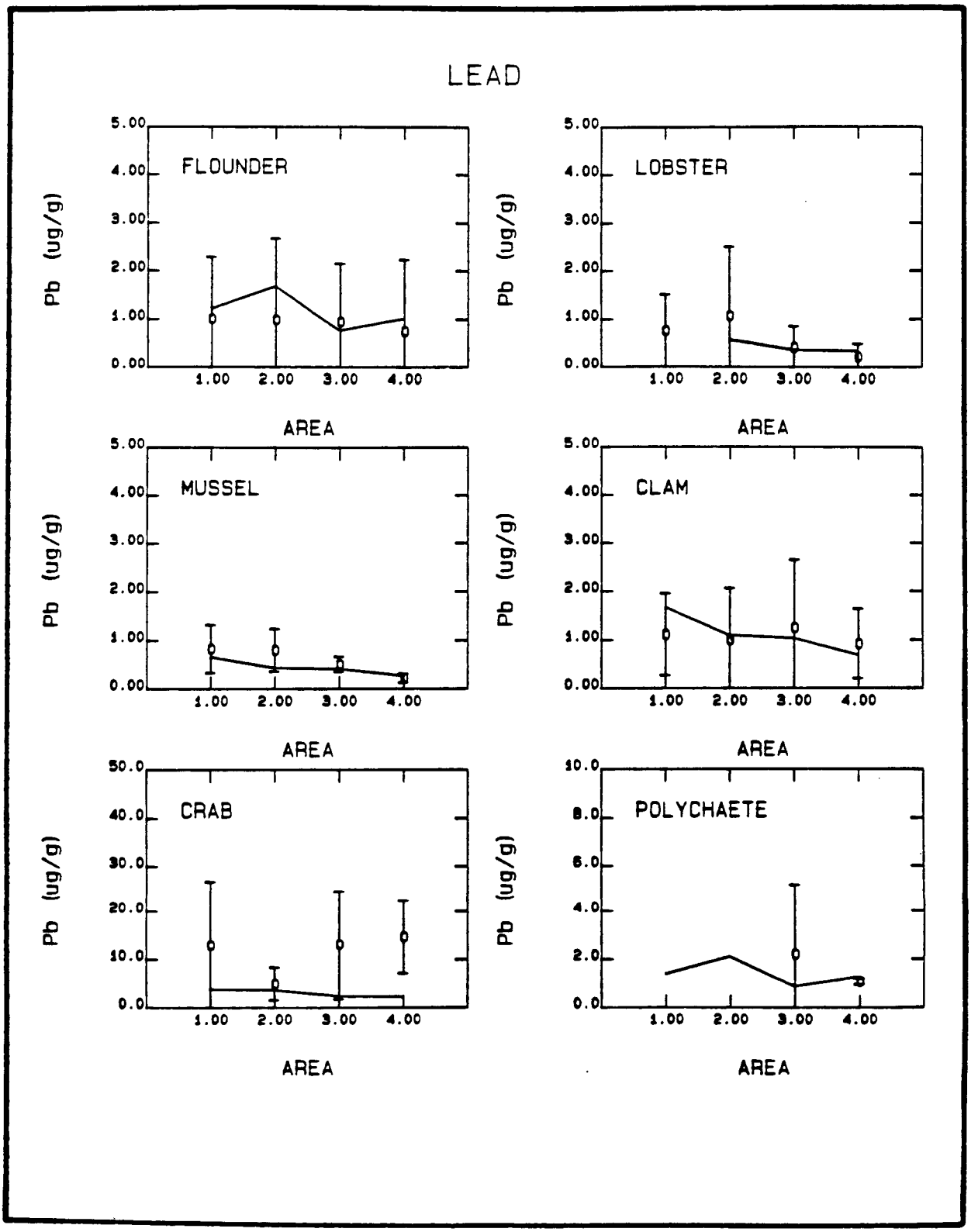

FIGURE 6.36. OBSERVED AND COMPUTED LEAD CONCENTRATIONS IN NEW BEDFORD HARBOR ANIMALS

TABLE 6.24. BIOCONCENTRATION FACTORS AND CHEMICAL ASSIMILATION EFFICIENCIES USED IN METALS CALIBRATIONS

Species	Bioconcentration Factor (L/g) Metal			Chemical Assimilation Efficiency (%) Metal		
	Cd	Cu	Pb	Cd	Cu	Pb
Polychaete	15.0	10.0	5.3	6	5	1
Clam	80.0	8.0	63.0	40	10	55
Mussel	69.3	7.9	27.7	40	10	45
Crab	25.0	2500	2500	15	90	90
Lobster	250.	250.	10.0	60	60	30
Flounder	2.7	20.0	30.0	10	60	50

presented with the model are arithmetic means and standard deviations of the combined data.

Calibration to the metals data was difficult because of inconsistencies between concentrations observed in the biota and those observed in the water and sediment. Water column dissolved metals concentrations decrease from Area 1 through Area 4 by about a factor of 4 for cadmium and copper and a factor of 2.5 for lead (see Figure 6.5). Sediment metals concentrations also decrease by similar factors, although an increase in the concentrations of cadmium and lead occurs from Area 1 to Area 2 (see Figure 6.9). By contrast, the biota concentrations do not exhibit a consistent spatial trend, particularly for cadmium (Figure 6.34) and copper (Figure 6.35). Instead the concentrations are generally uniform and in some cases (cadmium in clams and copper in lobster) even show a reverse trend to that of the water and sediment. In view of the apparent analytical difficulties in measuring biota metals concentrations in the laboratory experiments (see Section 6.4.5.2), it is possible that the biota data suffer from measurement induced statistical uncertainty which may have obscured the expected spatial trends.

Because of the data inconsistencies the calibration effort was limited to establishing general agreement between observed and calculated levels of contamination. To this extent the model was well calibrated particularly for cadmium and lead. The calibration for copper was also satisfactory except for lobster and crabs (Figure 6.35). The poor comparison between the computed and

observed values for these species may reflect the fact that copper is a constituent of blood in these species. The model was also unable to adequately reproduce the lead concentrations observed in the crabs. For both copper and lead the model significantly underpredicted the observed concentrations, even though extreme values of assimilation efficiency (0.90) and bioconcentration factor (2.5 x 106 L/kg) were used. Since the model successfully calculated PCB and cadmium concentrations in this species we are confident that the bioenergetic parameters and feeding habits of this species has been correctly represented. The fact that even with maximal accumulation and minimum excretion the model could not achieve the observed concentrations suggests that the data values are suspect.